

THE UNIVERSITY OF HULL

Finite Element Analysis of Conformal Contacts in Water Hydraulic
Axial Piston Pumps incorporating Advanced Ceramic Materials.

being a Thesis submitted for the Degree of

Doctor of Philosophy

in the University of Hull

by

Jennifer McConnachie, BEng (Sheffield), MSc (Strathclyde)

December, 1995

ABSTRACT

The use of water as a hydraulic fluid in a pump necessitates the use of conformal contacts to reduce the high rates of wear and leakage losses that result from the low viscosity and lubricity of water. Swashplate type axial piston pumps are ideal in this respect because they incorporate such conformal contacts. Furthermore, the development of such a pump for use with water, especially sea-water, critically relies on the correct selection and application of materials.

The purpose of this research work is firstly to examine the contact conditions within an axial piston pump for a range of sleeved and lined components manufactured from a variety of different materials. The use of finite element analysis with gap elements is a useful way of determining the contact pressure distribution between conformally contacting components. It is shown that this method gives excellent agreement with available analytical methods for the two-dimensional cylindrical and axisymmetric spherical cases, and thus can be extended to layered components. Extension to three dimensions, when the contact cannot be accounted for by plane strain or plane stress conditions, is also possible, allowing a much more representative analysis of the contact conditions within an axial piston pump. No single combination of materials is identified as being the most suitable, rather, the method enables the consequences of choosing materials for their tribological characteristics to be examined.

Once the contact conditions are known within the pump it is then possible to more accurately design the pump components. However, conventional deterministic methods are not appropriate for designing ceramic components, due to the inherent scatter of limiting defects, and statistical methods are necessary. Thus the second part of this research work is aimed at reviewing and examining the different probabilistic design methods with the long-term view of determining which, if any, are best suited to the design of ceramic components in this particular application. It is concluded that no single method adequately predicts the probability of failure of ceramic specimens with more complex stress distributions than four-point flexure bars.

ACKNOWLEDGEMENTS

The guidance and encouragement of many people has gone into the production of this thesis and their help is gratefully acknowledged.

Thank you

- to the Science and Engineering Research Council for financial support during part of the project and British Gas plc for their CASE contribution,

- to Lee Jones, my British Gas supervisor, and everyone else at British Gas who gave advice and help, including Adrian Jickells, Bob Conder, Jane Haswell and Mike Kirkwood,

- to Simon Usher and many more from Fenner Water Hydraulics without whom this project could not have happened,

- to Ian Birkby from Dynamic Ceramic for his enthusiasm for the project and the ceramic components,

- to all in the Department of Engineering Design and Manufacture, past and present, who have given encouragement and practical help, including Phil Radcliffe and Phil Kerry.

Special thanks must go to my supervisor Dr Michael Fagan for his advice and support over the years and finally,

To Ian, ο ανδρας μου, for all his love, patience and understanding.

CONTENTS

ABSTRACT	i
ACKNOWLEDGEMENTS	
CONTENTS	i
NOMENCLATURE	vii
	PAGE
CHAPTER 1 - INTRODUCTION	
1.0 INTRODUCTION	1
1.1 THE DEVELOPMENT OF WATER HYDRAULICS	2
1.1.1 Mining	2
1.1.2 Offshore applications	3
1.1.3 Fire and rescue	4
1.1.4 Others	5
1.1.5 Axial piston pumps and motors	5
1.2 WATER AS A HYDRAULIC FLUID	6
1.2.1 Viscosity	7
1.2.2 Bulk modulus	8
1.2.3 Lubrication	9
1.2.4 Thermal properties	9
1.2.5 Cavitation	9
1.2.6 General considerations	10
1.3 WATER HYDRAULICS AT THE UNIVERSITY OF HULL	10
1.3.1 Background	10
1.3.2 Material selection and screening	11
1.3.3 Pump testing	13
1.4 DESIGN AND ANALYSIS	13
1.4.1 Geometry designer	14
1.4.2 Timing analysis	15
1.4.3 Force analysis	16
1.4.4 Finite element analysis and ceramic design analysis	16
1.5 PROJECT OBJECTIVES	18

CHAPTER 2 - CONFORMAL CONTACT ANALYSIS

2.0	INTRODUCTION	19
2.1	DEVELOPMENT OF CONTACT MECHANICS	19
2.1.1	Spherical contact	20
2.1.2	Cylindrical contact	21
2.2	CONFORMAL CONTACT	23
2.2.1	Conformal cylindrical contact	23
2.2.2	Conformal spherical contact	26
2.3	NUMERICAL METHODS	27
2.3.1	Finite element analysis of contact	29
2.3.2	Boundary element analysis of contact	31
2.4	ANALYSIS OF LAYERED COMPONENTS	31

CHAPTER 3 - ANALYSIS OF CERAMIC MATERIALS

3.0	INTRODUCTION	34
3.1	ADVANCED TECHNICAL CERAMICS	34
3.2	DEVELOPMENT OF ADVANCED CERAMIC COMPONENTS	37
3.3	MANUFACTURE OF CERAMICS	38
3.3.1	Powder production and preparation	39
3.3.2	Pre-consolidation	40
3.3.3	Forming	41
3.3.4	Densification	41
3.3.5	Finishing	42
3.4	FRACTURE MECHANICS OF CERAMICS	42
3.5	STATISTICAL METHODS	44
3.5.1	Weibull statistics	44
3.5.2	Principle of independent action	48
3.5.3	Normal stress averaging	49
3.5.4	Flaw density (Batdorf) approach	49
3.5.5	Elemental strength approach	50
3.5.6	Matsuo's approach	51
3.5.7	Assumptions inherent in statistical methods	52

3.6	MECHANICAL PROPERTY DATA	52
3.6.1	Uniaxial testing methods	52
3.6.2	Biaxial/multiaxial tests	56
3.6.3	Fatigue testing	59
3.7	DESIGN OF CERAMIC COMPONENTS	59
3.7.1	Application of statistical methods	60
3.7.2	Component testing	65
3.8	TOUGHENED CERAMICS	65
3.8.1	Transformation toughening	66
3.9	NONDESTRUCTIVE EVALUATION	67
3.10	FAILURE ANALYSIS	68

CHAPTER 4 - FINITE ELEMENT ANALYSES - CONTACT

4.0	INTRODUCTION	69
4.0.1	Model parameterisation and convergence	69
4.1	TWO-DIMENSIONAL VERIFICATION ANALYSIS	71
4.1.1	Models	72
4.1.2	Convergence	72
4.1.3	Analyses	73
4.1.4	Results and discussion	73
4.2	TWO-DIMENSIONAL COMPONENT-SIZED ANALYSIS	80
4.2.1	Models and analyses	80
4.2.2	Results and discussion	82
4.3	AXISYMMETRIC VERIFICATION ANALYSIS	86
4.3.1	Models and analyses	86
4.3.2	Results and discussion	87
4.4	AXISYMMETRIC COMPONENT-SIZED ANALYSIS	92
4.4.1	Models and analyses	92
4.4.2	Results and discussion	93

4.5	AXISYMMETRIC COMPONENT-SHAPED ANALYSIS	95
4.5.1	Models and analyses	95
4.5.2	Results and discussion	97
4.6	THREE-DIMENSIONAL ANALYSIS	99
4.6.1	Models and analyses	99
4.6.2	Results and discussion	100

CHAPTER 5 - FINITE ELEMENT ANALYSES - COMPONENTS

5.0	INTRODUCTION	110
5.0.1	Model parameterisation and convergence	110
5.1	TWO-DIMENSIONAL CYLINDER BLOCK ANALYSIS	112
5.1.1	Model	112
5.1.2	Convergence	114
5.1.3	Analyses	114
5.1.4	Results and discussion	116
5.2	THREE-DIMENSIONAL CYLINDER BLOCK ANALYSIS	117
5.2.1	Models	117
5.2.2	Convergence	119
5.2.3	Analyses	121
5.2.4	Results	121
5.3	PISTON ANALYSIS	121
5.3.1	Models	123
5.3.2	Convergence	123
5.3.3	Analyses	123
5.3.4	Results	125
5.4	AXISYMMETRIC SLIPPER ANALYSIS	127
5.4.1	Models	127
5.4.2	Convergence	127
5.4.3	Analyses	127
5.4.4	Results and discussion	129

CHAPTER 6 - ANALYSIS OF CERAMIC COMPONENTS

6.0	INTRODUCTION	132
6.1	SPECIMEN ANALYSIS	132
6.1.1	Four-point flexure bars	135
6.1.2	Other specimens	136
6.2	FAILURE PROBABILITY OF SPECIMENS	138
6.3	FAILURE PROBABILITY OF COMPONENTS	145
6.3.1	Piston	145
6.3.2	Cylinder block	147

CHAPTER 7 - DISCUSSION

7.0	INTRODUCTION	149
7.1	CONTACT ANALYSIS	150
7.1.1	Cylindrical contact	150
7.1.2	Spherical contact	152
7.2	CYLINDER BLOCK ANALYSIS	152
7.2.1	Aluminium cylinder block	153
7.2.2	PEEK-lined stainless steel cylinder block	154
7.3	PISTON ANALYSIS	157
7.4	SLIPPER ANALYSIS	157
7.5	CERAMIC COMPONENT ANALYSIS	159
7.5.1	Flexure bar specimens	159
7.5.2	Grooved bar and grooved rod specimens	161
7.5.3	Brazilian disc specimens	164
7.5.4	Failure analysis of components	164

CHAPTER 8 - CONCLUSIONS

8.0	INTRODUCTION	165
8.1	CONCLUSIONS	165
8.2	SUGGESTIONS FOR FURTHER WORK	166
	REFERENCES	167
	APPENDIX I	173
	APPENDIX II	176
	APPENDIX III	177
	APPENDIX IV	178

NOMENCLATURE

a	cylindrical half contact width or spherical contact radius
A	constant
An	area
A_n	coefficients
ANG_n	angle
b	width of four point bend specimen
B_V	risk of rupture
CL	radial clearance
d_n	diameter
d	height of four point bend specimen
E_n/E_n	Young's modulus
E_e	Equivalent Young's modulus
F	force
\underline{F}_n	force vector
$g(S)$	flaw distribution function
G	strain energy release rate
G_c	critical strain energy release rate
h	initial separation
$H(\sigma)$	Heaviside function
i	rank of samples
k	flaw density parameter
K_I / K_{II}	stress intensity factors
K_{Ic}	critical stress intensity factor
l	half crack length
L_n	lengths
m	Weibull modulus
m_V / m_A	Weibull moduli from volume/surface flaws
Mn	mesh density
n	ratio of Young's moduli
N	crack density function
N_s	number of samples
p_m / p_{max}	maximum pressure
pn	pressure
p_0	maximum Hertzian contact pressure
$p(x)$	pressure at angular position x

$p(\phi)$	pressure at angular position ϕ
P_f	probability of failure
r_m	mirror radius
r_n	position vector
R_n/R_n	radius
R_e	equivalent radius
\bar{R}	radius of uniform loading
\underline{R}_n	reaction force vector
S	strength
S_E	critical strength
S_n	arc length
t	thickness
THK	thickness of kidney slot
THL	thickness of liner
THS	thickness of sleeve/seat
u_x	displacement constraint in x-direction
u_y	displacement constraint in y-direction
u_z	displacement constraint in z-direction
u_θ	displacement constraint in θ -direction
V_n	volumes
WDS	half width of kidney slot in cylinder block
x	coordinate direction
X_n	dimension in x-direction
XD_n	derived dimension
y	coordinate direction
y_n	dimension in y-direction
Y	dimensionless parameter
Y_n	dimension in y-direction
YD_n	derived dimension
z	coordinate direction
Z_n	dimension in z-direction
ZZ_n	mesh bias
α	contact angle
α	ratio of failure stress in tension and compression
β	trapping angle
χ	Poisson ratio parameter
ϕ	angular position
γ_s	crack specific surface energy

Γ	gamma function
ν_n/ν_n	Poisson's ratio
θ_n	angular dimension
σ	stress
σ_{dp}	Drüker and Prager equivalent stress
σ_e	von Mises equivalent stress
σ_E	equivalent stress
σ_f	fracture strength
σ_{\max}	maximum stress
σ_{nom}	nominal stress
$\sigma_{x/y/z}$	component stresses
$\sigma_{r/t}$	radial/tangential stress
σ_0	characteristic strength
σ_μ	threshold stress
Σ	stress-volume integral
τ	shear stress
ω	angular range
Ω	angle

CHAPTER 1

INTRODUCTION

1.0 INTRODUCTION

This chapter describes the background to the work contained in this thesis: the development of water hydraulics, the advantages and disadvantages of using water as a hydraulic fluid and the Water Hydraulics project at the University of Hull. It concludes by outlining the objectives of the research which is concentrated on conformal contact analysis and ceramic component design, and its relationship to the Water Hydraulics project. The scope of work, including conformal contact analysis and ceramic component design, is outlined.

The development of analytical and numerical solutions to the problem of conformal contact are reviewed in the following chapter. Particular reference is made to the more recent developments of finite element analysis in contact problems and the analysis of layered components. The problems of designing with ceramic materials are then discussed along with a review of the solutions to those problems reached by various authors.

The reviews are followed by two- and three-dimensional finite element analyses of cylindrical and spherical components in conformal contact. This is to allow verification of the method against known solutions and to assess the effects on the contact pressure distribution of using sleeve and liner materials of different properties and thicknesses.

The contact pressure distributions from the above analyses are then used as loading on finite element models of the cylinder block, pistons and slippers of axial piston pumps. Separating the contact analysis from the component models allows more complex models to be created than would otherwise be the case.

The statistical analyses required to design ceramic components demand a knowledge of the stress distribution in the entire component and that the component is discretised into elements of known volume or area. Finite element analysis is ideally suited to this purpose and is applied to a number of ceramic specimens and components allowing a prediction of their probability of failure using a variety of failure criteria and flaw shapes.

The results of all the above analyses are discussed with particular reference to designing components for use in water hydraulic axial piston pumps. Conclusions are drawn and suggestions made for further work which would be useful in these areas.

1.1 THE DEVELOPMENT OF WATER HYDRAULICS

The word *hydraulic* is itself derived from Latin, where *hydro*=water and *aulos*=pipe. In 1876 the first UK public water-based hydraulic power system was installed in Hull and in the late 1800s, Armstrong undertook pioneering work using water for power transmission and developed water powered cranes, lock gates and swing bridges (Routledge, 1876).

However, the pressures used in early water hydraulic systems were relatively low and the size of the equipment usually large. The emergence of the mineral oil industry in the 1900s provided hydraulic fluids with much better characteristics than water. In particular, they offered better lubrication and higher viscosity which meant lower leakage rates and higher allowable contact loads. The risk of fire in high pressure oil systems led to the introduction of water/oil mixtures in the 1940s, allowing existing equipment to be used with minimum modification. Initially these were 40/60 water/oil mixtures, but they have gradually been improved to the 95/5 mixes which are available today. These high water-based fluids (HWBF) contain additives to minimise wear that would otherwise occur but equipment using these fluids must still operate at a reduced level of performance compared to equivalent oil based systems.

The current interest in using raw water as a hydraulic fluid results from its low cost, plentiful supply, low pumping viscosity and numerous safety advantages. However, early experience with high water-based fluids showed that replacing mineral oil with pure water would not be a trivial task. Knowledge of material science and the development of new engineering materials, especially non-metallic materials, has increased significantly over recent decades. In particular, a greater understanding of the tribological properties and performances of the different materials combined with more information on the contact characteristics of different component geometries now means that it is possible to design practical hydraulic systems to accommodate the low viscosity and poor lubricity of water.

1.1.1 Mining

One of the prime movers in the development of water hydraulics was the mining sector, because of the risk of fire with mineral oil-based hydraulics. In addition, some mines have the advantage of abundant natural sources of water at pressures and

flowrates suitable for a wide range of hydraulic power systems. For example, the natural head at the bottom of a coal mine can be 150 bar in some of the deeper UK mines and nearly 400 bar in the deepest South African gold and diamond mines, completely removing the need for hydraulic power pumps.

Wymer (1979) described a variety of prototype machines which were operating on fluids with a high water content in South African gold mines. He recognised that increasing use of mine service water as a hydraulic fluid should be made but reported that, at that time, neither dilute oil-in-water emulsions nor water itself were suitable for use with the majority of conventional hydraulic components. He outlined many of the disadvantages of using water including corrosion, cavitation and wear problems. He recommended the use of hard-on-hard materials to avoid erosion problems and reduce compressibility losses. To reduce cavitation he suggested two approaches: careful design of geometry and appropriate material selection. Wymer said that axial piston pumps had emerged as the most encouraging type for use with dilute emulsions but that they had little chance of operating satisfactorily on water, leaving low speed plunger pumps as the only alternative.

Knight (1977) reported on the potential of using water-based hydraulic systems in the UK coal mining industry where fire risks limit the use of flammable hydraulic fluids. He also emphasised the corrosiveness of water, particularly with ferrous materials and recognised that surface finish and conformity are critical.

1.1.2 Offshore applications

Water hydraulics does not solely include the use of fresh (e.g. tap-, river- or mine-) water but also sea-water. The use of sea-water hydraulics can provide many advantages over conventional oil-based systems in a number of offshore applications, both on surface vessels and platforms and subsea. Oil-based subsea hydraulics can be complex because the viscosity of oil varies with temperature and pressure (i.e. depth subsea), as does the bulk modulus; thus the characteristics of the oil and hence the equipment can vary significantly. In addition, pressure compensation is usually required for all but shallow depths to balance the normal hydrostatic pressure. The use of a sea-water hydraulic system could provide subsea tools for divers or for remote robotic manipulator systems, without the need for hydraulic tanks and umbilicals. There would also be no pressure losses associated with hoses from the surface, no risk of contamination and improved handling by elimination of the return line. Similar sea-water applications under consideration include integrated tool and propulsion systems on submersibles.

Terada et al (1984) reported on the development of a high pressure sea-water pump for use as the power source for an underwater machine system. The study was

undertaken for the Ship Building Research Association of Japan and subsidised by the Japan Foundation for Ship Building Advancement. They employed an axial plunger type of pump with ceramic materials for the cylinders and plungers to 'minimise wear and corrosion caused by silt-contaminated sea-water and to enable high speed pumping with close clearance sealing'. Since the plungers slid at high speed a high wear resistance was required for the materials, as well as corrosion resistance in sea-water, hence the choice of ceramics. They reported that high precision finishing was needed and thus the ceramics were assessed for ease of finishing as well as wear resistance and anti-corrosion characteristics. They chose alumina for the cylinder and alumina-titania for the plunger. Natural sea-water was used for the testing but the pump contained some oil lubricated parts.

Yoshinada et al (1991) reported on a large scale Research and Development project at Komatsu called 'Advanced Robot Technology in the Hazardous Environment', part of which included a sea-water hydraulic actuator system consisting of sea-water hydraulic instruments for a subsea manipulator. The manipulator consisted of a sea-water pump, a joint actuator and a servo valve. They reported that a sea-water hydraulic system cut the size and weight of a subsea robot because the hydraulic tank, drainage pipes and pressurising chambers were eliminated. The pump was tested on raw water and artificial sea-water to a pressure of 200 bar, with the bearings and frictional parts composed of carbon fibre reinforced polymer (CFRP) and ceramics.

Another most promising offshore application is an autonomous subsea control system. Instead of using conventional hydraulics to operate a remote well-head, by pumping hydraulic fluid several kilometres under the sea through an umbilical, a power source and pump could be positioned at the well head to operate on sea-water. There would be no need for the flow and return of the hydraulic fluid, and possibly no need for the umbilical at all if the system were controlled remotely. Loth and Walker (1993) reported that the financial benefits of such a system would be significant, and the exploitation of marginal fields would become attractive.

For surface vessels, and oil and gas process platforms, the introduction of raw sea-water hydraulics has the potential to improve operational safety, with the fluid power system integrating with the high pressure water cleaning system and possibly parts of the fire control system.

1.1.3 Fire and rescue

The use of water hydraulics for fire and rescue systems on land was one of the earliest successful commercial applications of water hydraulics. A high pressure water curtain is used to extinguish the fire and then appropriate water-powered

cutting and spreading tools are attached to the power unit as required. With such a tool the fire service can quickly cut through the roof and door pillars of a car for example and release its occupants (Usher, 1994).

The Firespear™ system has also been developed where a water motor is used to drive a cutter which can penetrate an aircraft's fuselage and then discharge high pressure water inside the cabin. The water is used to power a cutting head which cuts through the skin or windows of the aircraft (in typically 10 seconds); having pierced the skin, water is then sprayed from the tip of the tool in a fine spray to prevent fire from spreading and to suppress the smoke without the additional hazard of oil-based equipment.

1.1.4 Others

Other potential applications of water hydraulic technology include robots in the nuclear industry, food processing machinery, chemical and drug manufacture, the water supply industry, steel and glass production, injection moulding and die casting. However, at the present time, when the costs of water hydraulic systems are still relatively high and components are not so readily available as those of oil hydraulic systems, water hydraulics are generally only considered when there are environmental, safety or contamination risks, or where of course they are expected to outperform oil-based systems.

1.1.5 Axial piston pumps and motors

It has become established that piston type pumps and motors are preferred for water hydraulic systems because of the requirements of high power density and simple symmetric component shapes based on conformal contact. Such a pump is the focus of the work contained in this thesis. The basic geometry of an axial piston pump is shown in figure 1.1.1. A cylinder block containing a number of bores is coupled to a drive shaft with each bore containing a piston supported by a slipper bearing on a swashplate. The swashplate is inclined at an angle relative to the shaft, and as the shaft is turned the slipper slides on the swashplate causing the piston to reciprocate in the bore. As the piston moves out of the bore, fluid is drawn in through the cylinder port from the inlet slot of the port-plate. The situation is reversed as the piston moves in to the bore, and the fluid is forced out of the cylinder port through the outlet slot of the port-plate. A continuous pumping action is established when all the pistons follow this cycle causing pressure to be raised as the outlet line is subjected to restriction. If the action is reversed and water forced into the unit, then it operates as a motor.

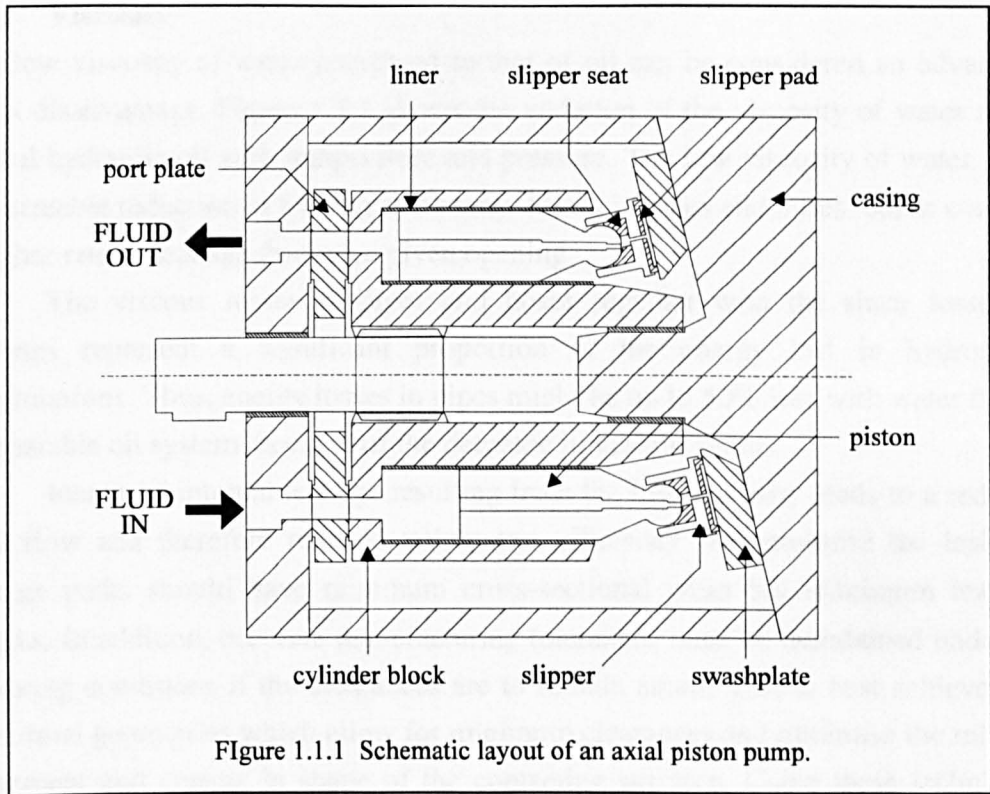


Figure 1.1.1 Schematic layout of an axial piston pump.

1.2 WATER AS A HYDRAULIC FLUID

This section considers the basic physical properties of water and compares them to those of mineral oil. Table 1.1.1 summarises the resulting advantages and disadvantages of raw water used as a hydraulic fluid.

Advantages	Disadvantages
low viscosity plentiful supply non-flammable low cost incompressible fire resistant contamination tolerance non-polluting good heat transfer properties	low viscosity poor lubricity narrow temperature range heavy cavitation bacterial contamination corrosive

Table 1.1.1 Advantages and disadvantages of water as a hydraulic fluid.

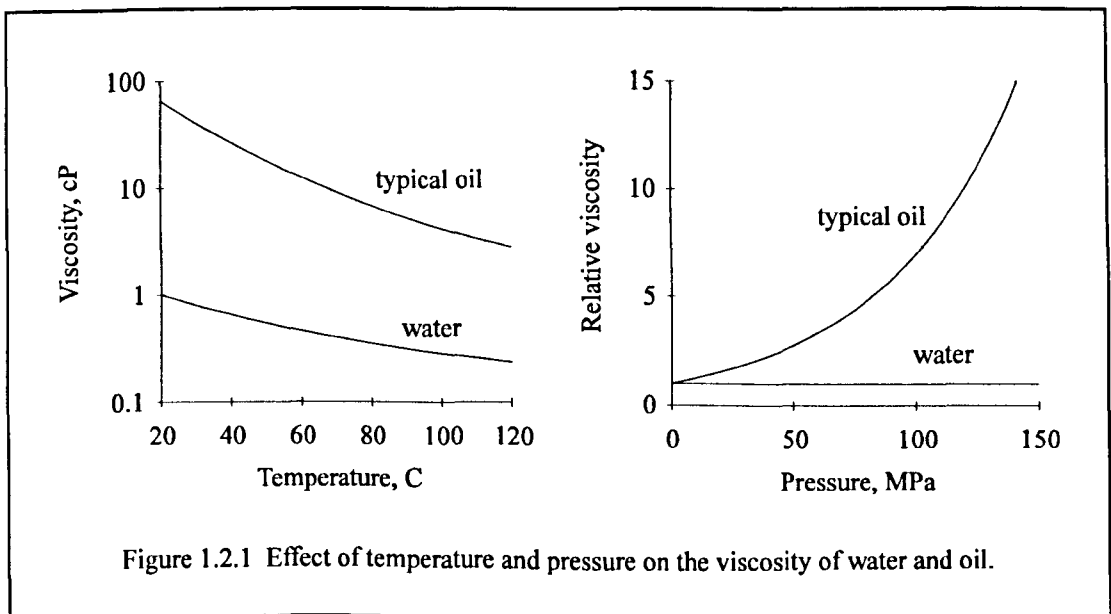
1.2.1 Viscosity

The low viscosity of water compared to that of oil can be considered an advantage and a disadvantage. Figure 1.2.1 shows the variation of the viscosity of water and a typical hydraulic oil with temperature and pressure. The low viscosity of water leads to a sizeable reduction in friction and energy losses in pipes and hoses, but in contrast a higher rate of leakage through a given opening.

The viscous losses in pipes and hoses together with the shear losses in bearings represent a significant proportion of the energy lost in hydrostatic transmissions. Thus, energy losses in pipes might be up to 50% less with water than a comparable oil system, because of the decrease in viscous forces.

Increased internal leakage resulting from the low viscosity leads to a reduced total flow and therefore reduced volumetric efficiency. To minimise the leakage, leakage paths should have minimum cross-sectional areas but maximum leakage lengths. In addition, accurate manufacturing tolerances must be maintained under all operating conditions if the clearances are to remain small. This is best achieved by conformal geometries which allow for minimum clearances and minimise the relative movement and change in shape of the contacting surfaces. Using these techniques volumetric efficiencies of water pumps and motors of more than 95% can be achieved and with the plentiful supply, low cost and non-polluting nature of raw water, reduced efficiency is not the problem it would be with oil-based systems.

Low viscosity also increases the difficulty of developing hydrodynamic films between moving components, particularly at low speeds. Oil has a positive pressure-viscosity coefficient and therefore an increase in its viscosity is seen when it experiences the high pressures generated in non-conformal contacts, such as in gears, cams and rolling element bearings, and this is vital in keeping the contacting surfaces

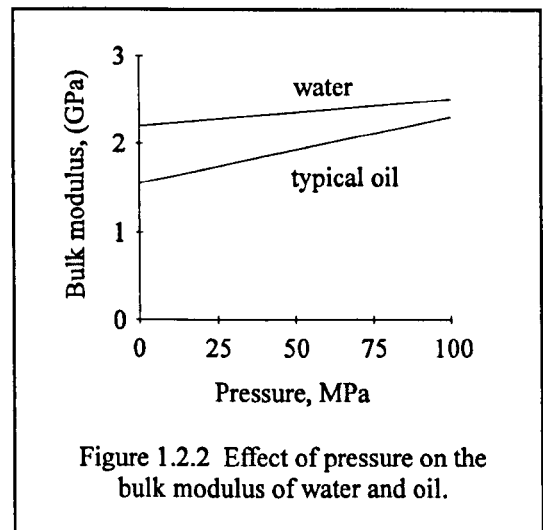


apart. The negligible pressure-viscosity coefficient of water means that such elastohydrodynamic lubrication is unlikely to occur, especially with hard materials.

The different viscosity also directly affects the operating characteristics. For example, the viscosity of the fluid effects the pressure overshoot and undershoot during the opening and closing of the cylinders of axial piston pumps. A 20% reduction in such pressure fluctuations was reported by Edge and Darling (1989) when the viscosity of the fluid was decreased from 100 cSt to 20 cSt. A low viscosity fluid is advantageous however from the point of view of quick response times of the equipment, the necessary pressures are attained significantly faster with systems using water than those using oil-based fluids.

1.2.2 Bulk modulus

Figure 1.2.2 shows that the bulk modulus of water is higher than that of a typical mineral oil, but they both increase marginally with pressure. The higher stiffness of water means that a reduction in the compressibility losses in piston pumps can be expected when water is used, and since much of the total efficiency losses in axial piston pumps is due to the compressibility of the fluid, this effect may be significant. Ifield (1974) reported a reduction in compressibility losses by typically 25% when changing from oil to water.



The stiffness of the fluid also effects the pressure overshoot and undershoot as the cylinders of axial piston units are opened and closed. For example, a phosphate-ester based fluid with a bulk modulus and density similar to that of water was predicted by Edge and Darling (1993) to lead to an increase in these pressure fluctuations of approximately 25% compared to oil but a reduction in the flow ripple of 15%. A related effect is seen when the flow is completely interrupted in water-based systems. A high pressure ripple is experienced which can cause adverse problems for relief valves and seals, and ideally some form of pulsation damping is required.

1.2.3 Lubrication

The poor lubricity of water is clearly one of its major drawbacks, and will lead to increased contact, friction and wear of contacting components. Mineral oils contain additives which aid in the boundary lubrication of contacting surfaces permitting metal-on-metal contact without large amounts of surface damage or wear. Raw water contains no such additives and is very poor in boundary lubrication, so that any metal-on-metal sliding will result in high friction and wear.

Wymer (1979) and other early users of water-based fluids in axial piston pumps reported wear as one of the greatest problems. More recently, this has been overcome for clean raw water systems by careful design and selection of materials but it is still a problem for applications wishing to use 'dirty' water, for example mine-water or sea-water. Carbon fibre reinforced polymers have been used successfully against steel or ceramic materials in raw water provided surface finishes are tightly controlled to reduce contact friction. The polymer-on-ceramic combination has been used with some success in sea-water and it is possible that ceramic-on-ceramic contact may prove to overcome wear and erosion problems in this more aggressive environment.

1.2.4 Thermal properties

The heat generated in water-based hydraulic fluids is significantly less than that generated in oil hydraulic fluid because of the reduction in viscous friction and compressibility losses. In addition, the higher density and specific heat of water compared to oil means that it is more efficient at removing heat from components. These are important considerations if materials with low thermal conductivities such as polymers and ceramics are used to accommodate the poor lubricity of water.

Water has a relatively narrow operating temperature range and this could be a problem in certain applications. The problem of freezing of the water can be overcome by using anti-freeze, but that contradicts one of the primary aims of water hydraulics, i.e. to use raw water without additives. Alternatively, those applications which might experience freezing could use low energy trace heating as required to maintain a minimum temperature, or they could be kept operational at those times when freezing was likely to occur.

1.2.5 Cavitation

Water has a relatively high vapour pressure compared to oil, and cavitation is likely to occur somewhere in a water hydraulic system. Also, because water has a low viscosity and a relatively high bulk modulus, it is particularly prone to cause cavitation erosion damage. The vapour pressure of mineral oils is negligible, and

consequently cavitation damage is not a significant consideration in the design of oil-based systems, and thus oil systems converted to use water often fail prematurely due to cavitation.

Cavitation can be minimised by the use of appropriate materials and suitable geometric design to eliminate bends and sharp corners in the design of components. Using a boost pressure should prevent its occurrence at the port-plate and rear face of the cylinder block of axial piston pumps but this may not be desirable in many operational situations and increases the complexities of the units.

1.2.6 General considerations

In water hydraulic units, individual component parts will perform either a structural or contact function, or quite often a combination of both. From the point of view of manufacture and assembly of the units, the fewer the number of components and the simpler their configuration, the cheaper the units will be. Thus if a material can satisfy both functions, it appears very attractive in the selection process. Of course, those materials required for contact functions cannot be considered in isolation, it is the performance of the material pair that is important and the geometry of the contacting surfaces is critical in determining the contact loads.

1.3 WATER HYDRAULICS AT THE UNIVERSITY OF HULL

This section describes the more immediate background to the water hydraulics project at the University of Hull of which the work contained in this thesis forms a part. A large number of papers and reports have resulted from the work and are listed in Appendix I. Consequently this section summarises the background to the Water Hydraulics project and the principal results which were not central to the research described in this thesis.

1.3.1 Background

Some fifteen years ago the Department of Trade and Industry (DTI) supported a programme of work at the National Engineering Laboratory (NEL) on the introduction of new materials and surface treatments in power transmission systems. The programme of work was oriented towards incorporating plastics in pumps and motors, pumping low lubricity (water) type fluids. The test vehicle used to evaluate suitable candidate material combinations was an adaptation of a conventional nine cylinder axial piston swash plate pump. All moving interfaces were combinations of plastic to either treated or untreated stainless steel.

Shell and Esso then placed a substantial contract with the NEL to develop a range of subsea tools and a subsea power pack, using the technology available. The first tool chosen was a fairly traditional grinding tool with the hydraulic motor integrated into the body of the tool. It was accepted that the motor should work entirely on sea-water, with no oil interface. As the programme developed Shell and Esso extended it to produce a tool that would stretch the current 'state of the art'. An Industrial Exchange Group, consisting of six British companies, was established to advise on details of the programme. J H Fenner plc were one of the companies and after a period of negotiation and assessment, they acquired the rights to both the NEL and Shell technology. In order to transfer the technology to the market place, Scot-Tech, a wholly owned Fenner subsidiary, was set up. Scot-Tech subsequently became Fenner Water Hydraulics.

In 1989, the DTI funded a collaborative project under their Support for Innovation (SFI) involving J H Fenner and the Department of Engineering Design and Manufacture at the University of Hull. The latter was given the particular aim of demonstrating the advantages of using advanced engineering ceramics in water powered pumps and motors for use with plain tap-water and sea-water.

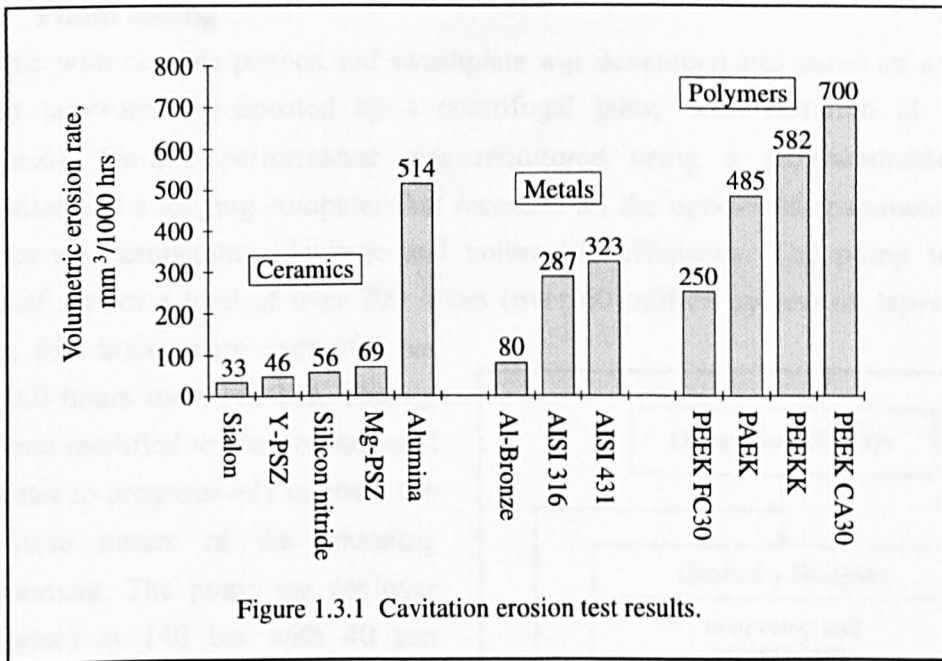
The work at the University was focused in three main areas - the selection and testing of materials and material combinations suitable for use with water, the design and analysis of the pump and components, and pump testing.

1.3.2 Material selection and screening

Selection of the right materials was seen as vital to the development of a successful water hydraulic pump, hence a programme of tests was carried out on specially designed equipment. Existing proprietary tribological equipment was considered but it was eventually decided to design and build testing facilities capable of providing conditions of operation closer to the high speeds and loads in the pump itself.

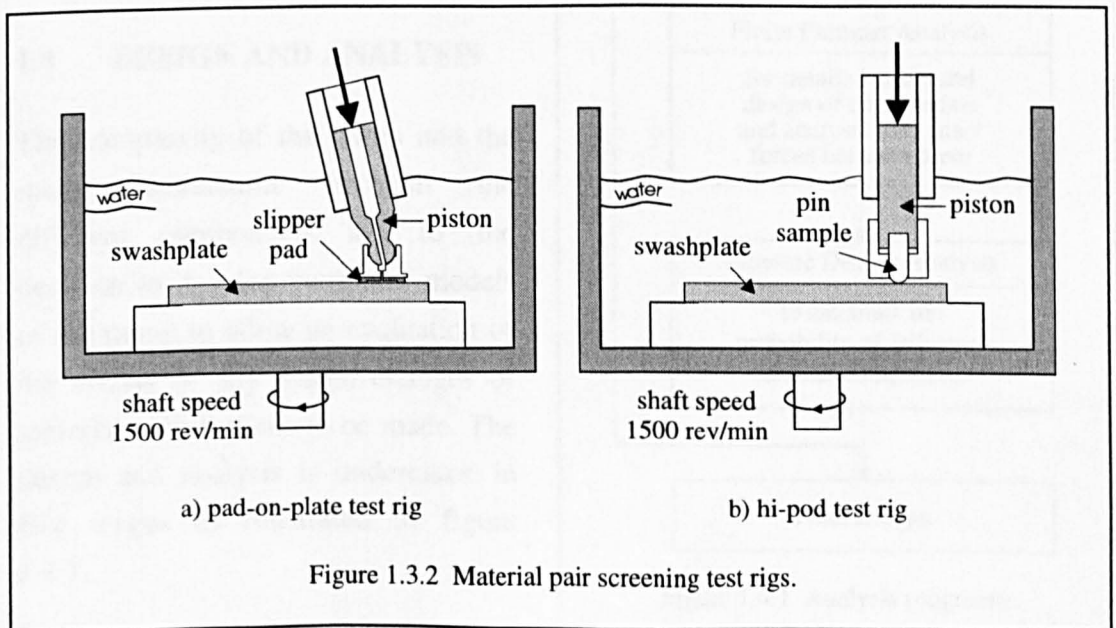
A series of cavitation erosion resistance tests was conducted on potentially useful metallic, ceramic and polymeric materials with an ultrasonic vibratory device. A chart of the results is shown in figure 1.3.1. Apart from alumina, the ceramic materials tested all exhibited good resistance to erosion and there was no significant difference in the erosion resistance of the ferritic or the martensitic stainless steels. Of the polymers tested, polyether-ether-ketone (PEEK) with 30% carbon fibres (FC30 grade) behaved best. Throughout the rest of this thesis this material will be referred to simply as PEEK.

A pad-on-plate test rig as shown in figure 1.3.2a was designed to examine the wear rate of potential slipper pad/swash-plate material combinations under realistic conditions of speed, load and geometry. Actual pump components were used in the



testing programme with the piston/slipper assembly loaded hydrostatically against the rotating swash plate. It was established that PEEK slippers against a PSZ swash plate gave comparable wear performance to that of PEEK on stainless steel under clean fresh-water operating conditions (Brookes et al, 1995).

The pad-on-plate rig design was subsequently modified (figure 1.3.2b) to assess the compatibility and wear rates of ceramic pairs. Specimens were in the form of 10 mm diameter pins with hemispherical ends loaded against a rotating disc submerged in water. Preliminary tests produced several promising pairs (Brookes et al, 1995).



1.3.3 Pump testing

A pump with ceramic pistons and swashplate was developed and tested on a closed-circuit tap-water rig boosted by a centrifugal pump with filtration at 25 μm (nominal). On-line performance was monitored using a programmable logic controller and a logging computer that recorded all the operational parameters such as pressure, temperature, leakage and volumetric efficiency. The pump was run successfully for a total of over 700 hours (over 60 million cycles) on tap-water of which 530 hours were over 100 bar and 260 hours over 140 bar. The rig was then modified to run on untreated sea-water to progressively increase the aggressive nature of the operating environment. The pump ran for over 100 hours at 140 bar with 40 μm filtration and underwent stop:start tests at maximum speed with no significant degradation of the ceramic and polymeric components. After the filtration was increased to 120 μm a catastrophic failure was observed, precipitated by failure of the modified stainless steel cylinder block. However, the ceramic pistons completed over 10^7 cycles with no evidence of degradation.

1.4 DESIGN AND ANALYSIS

The complexity of the pump and the many interactions between the different components led to the decision to develop computer models of the pump to allow an evaluation of the effects of any design changes or material substitutions to be made. The design and analysis is undertaken in five stages as illustrated in figure 1.4.1.

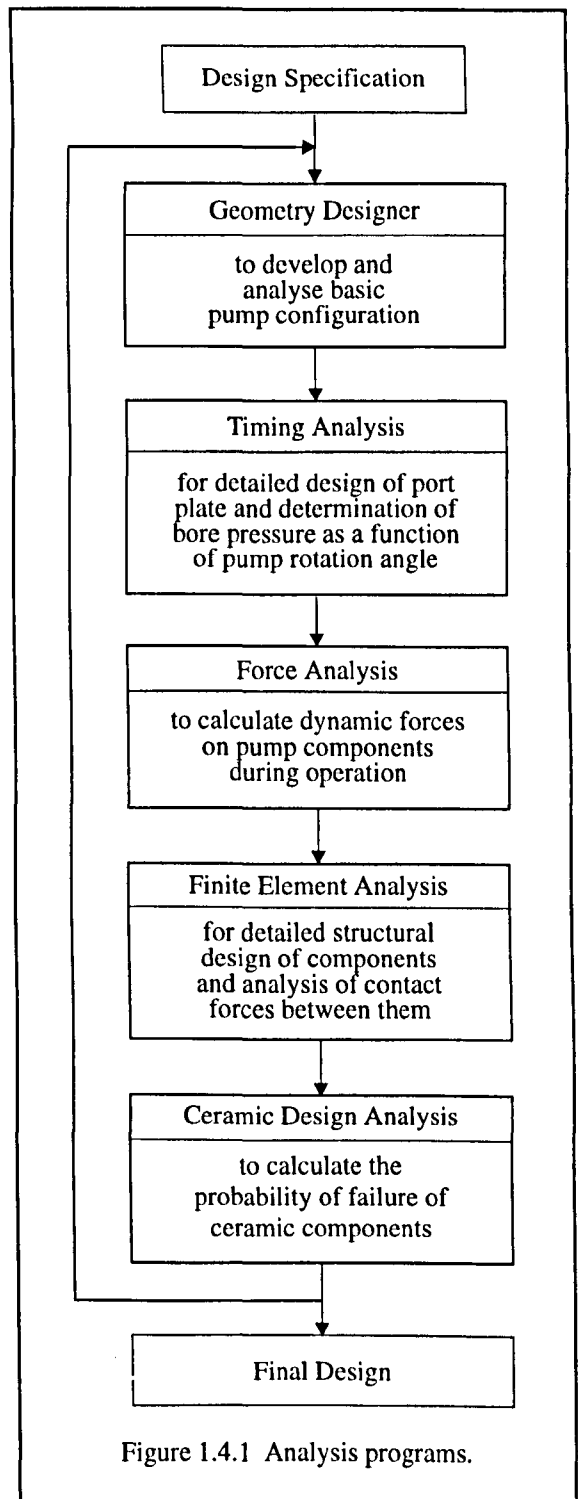


Figure 1.4.1 Analysis programs.

1.4.1 Geometry designer

The geometry designer is the first in the series of programs. It is used primarily to allow the rapid development of geometric information that is required for input to the timing analysis and force analysis. Initially the program was used to avoid erroneous input to the force analysis but it became obvious that whilst basic error checking was valuable the method could be extended to include more sophisticated rules to aid the designer (Radcliffe et al, 1993).

The rules are based on a standard parametric design of axial piston pump, and although each rule is simple, when many are used together they provide a powerful method of design optimisation. When the data is input the program constrains the values within a given range by rules which prevent dimensions being specified which may cause component interference. For example, consider n bores placed around a pitch circle diameter of a cylinder block as in figure 1.4.2. Neglecting the curvature of d_1 ,

$$d_2 n < \pi d_1$$

otherwise the bores will overlap. The wall thickness, t , between the bores is given by

$$t = \frac{d_1 \pi - d_2 n}{n}$$

If the wall thickness around a bore is assumed to be constant then the outside diameter and a maximum inner diameter of the cylinder block can then be calculated as follows

$$d_3 = d_1 + d_2 + 2t$$

$$d_4 = d_1 - d_2 - 2t$$

The geometric information generated is used as input to the timing analysis and subsequent force analysis.

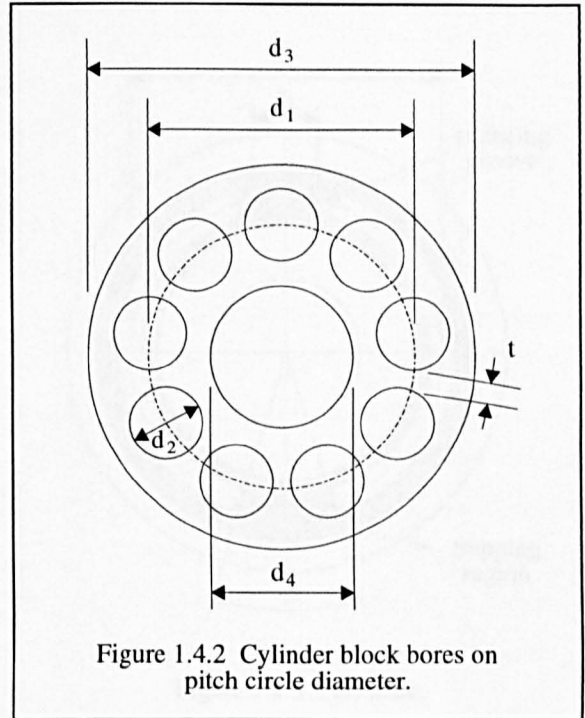


Figure 1.4.2 Cylinder block bores on pitch circle diameter.

1.4.2 Timing analysis

The timing of an axial piston pump controls the transition of cylinder pressure between delivery and boost pressure. The design of the port plate (see for example figure 1.4.3) has a major effect on the pressure cycle of a cylinder. An incorrectly 'timed' pump can lead to large pressure overshoots on the delivery stroke and pressure undershoots, resulting in cavitation on the suction stroke (Edge and Darling, 1986; Martin and Taylor, 1978; Helgestad et al, 1974).

Geometric information from the geometry designer is input directly to the timing analysis program, which uses theoretical considerations and measured leakage to calculate bore pressure against rotation angle for various port plate geometries and operating parameters (Radcliffe, 1992).

Figure 1.4.4 shows a graph of cylinder bore pressure versus rotation angle for two designs of port plate. The dotted line shows an ideally timed port plate, where the pressure rises and falls to the required high and low pressure values without any undershoot or overshoot. When the silencing grooves are omitted, a pressure undershoot and overshoot occurs as illustrated by the solid line. Cavitation damage may occur on the cylinder block or port plate as a result of the undershoot, while the overshoot will lead to unexpectedly high stresses and possible premature failure of the pump's components.

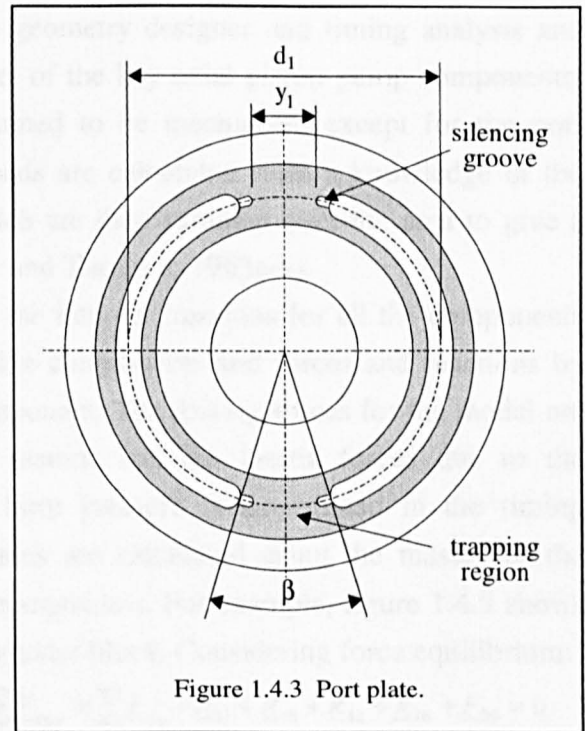


Figure 1.4.3 Port plate.

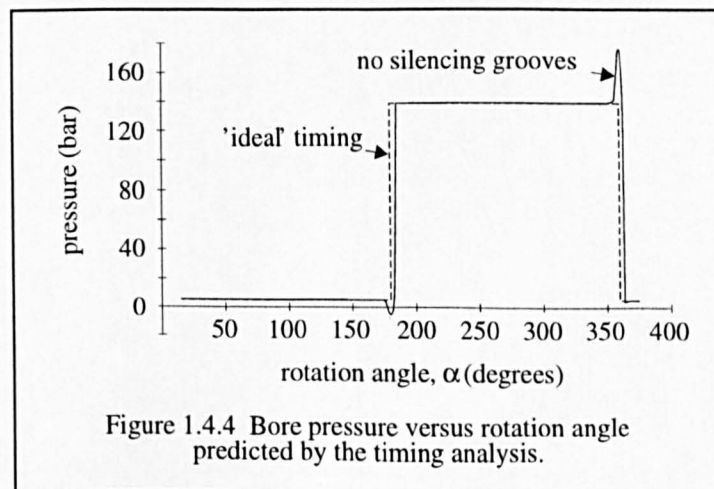


Figure 1.4.4 Bore pressure versus rotation angle predicted by the timing analysis.

1.4.3 Force analysis

The force analysis uses input from the geometry designer and timing analysis and creates a parametric mathematical model of the key axial piston pump components. All contacts within the pump are assumed to be mechanical except for the port plate/cylinder block interface. These loads are calculated from a knowledge of the pressure distributions on the lands, which are then summed over the area to give a resultant force (Saitchenko, 1963; Shute and Turnbull, 1963a/b).

The force analysis thus predicts the internal reactions for all the components and calculates the position vectors of the components and forces and reactions by considering the equilibrium of each component. The driving forces for the model are the pressure in the bores above the pistons and the inertia forces due to the reciprocating and rotating parts. The bore pressure is determined in the timing analysis program whilst the inertia forces are calculated using the masses of the moving parts and the velocities of the components. For example, figure 1.4.5 shows the loading and reaction forces on the cylinder block. Considering force equilibrium:

$$\sum \underline{R}_{16f} + \sum \underline{R}_{17f} + \sum \underline{R}_{20f} + \sum \underline{F}_{3f} + \sum \underline{F}_{10f} + \sum \underline{F}_{9h} + \underline{R}_{37} + \underline{R}_{38} + \underline{R}_{42} + \underline{R}_{46} + \underline{F}_{99} = 0$$

and moment equilibrium:

$$\begin{aligned} & \sum (\underline{r}_{2f} \times \underline{R}_{16f}) + \sum (\underline{r}_{5f} \times \underline{R}_{17f}) + \sum (\underline{r}_{35h} \times \underline{R}_{9h}) + (\underline{r}_{31} \times \underline{R}_{37}) + (\underline{r}_{32} \times \underline{R}_{38}) + (\underline{r}_{36} \times \underline{R}_{42}) + \\ & \sum (\underline{r}_{17f} \times \underline{R}_{20f}) + (\underline{r}_{38} \times \underline{R}_{46}) + \sum (\underline{r}_{18f} \times \underline{R}_{3f}) + \sum (\underline{r}_{18f} \times \underline{R}_{10f}) + (\underline{r}_{99} \times \underline{F}_{99}) = 0 \end{aligned}$$

The above force and moment equations are solved for \underline{R}_{37} , \underline{R}_{38} , \underline{R}_{42} and \underline{R}_{20f}

1.4.4 Finite element analysis and ceramic design analysis

This part of the Design and Analysis program is the core of the research work described in this thesis. The main objectives of the research are outlined in the following section.

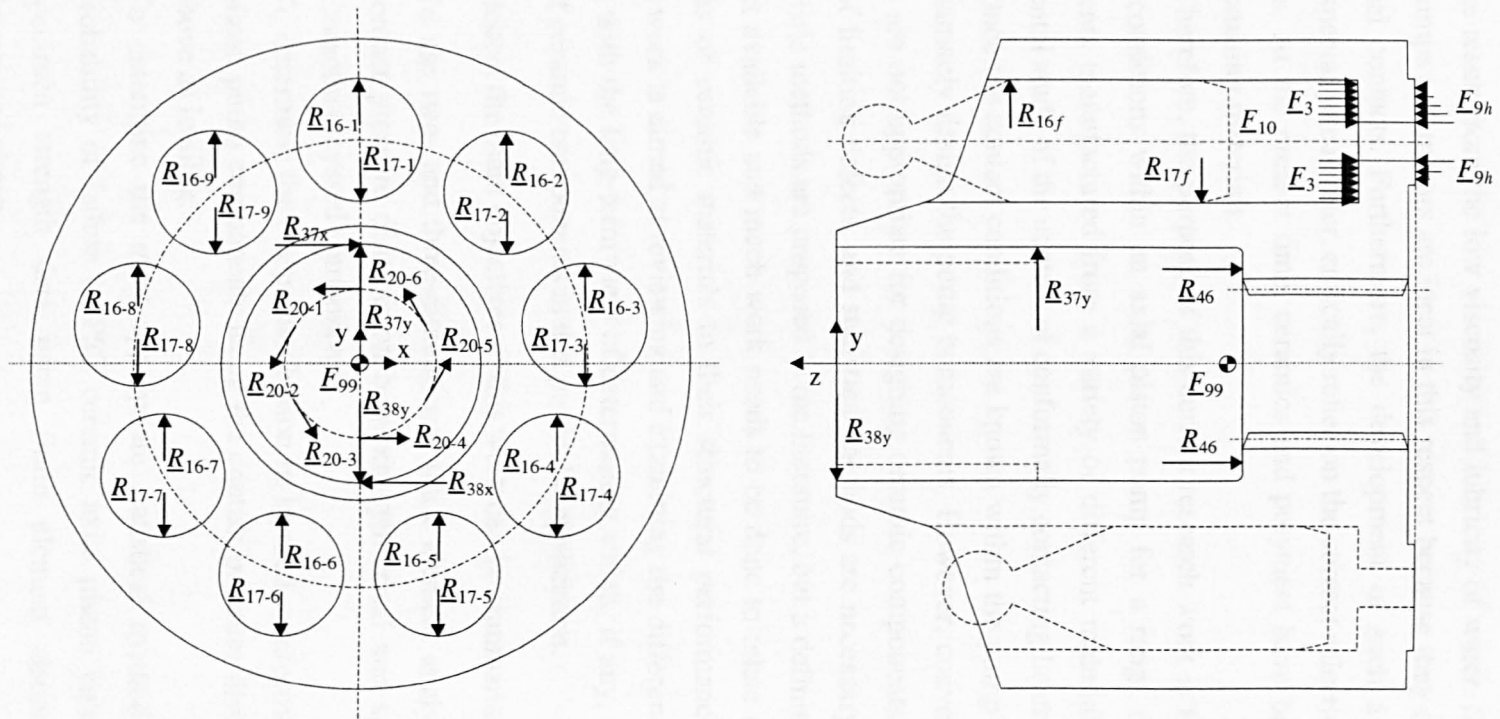


Figure 1.4.5 Loading and reaction forces on the cylinder block.

1.5 PROJECT OBJECTIVES

The use of water as a hydraulic fluid in a pump or motor necessitates the use of conformal contacts to reduce the high rates of wear and leakage losses that would otherwise result from the low viscosity and lubricity of water. Swashplate type axial piston pumps and motors are ideal in this respect because they only incorporate such conformal contacts. Furthermore, the development of such a pump for use with water, especially sea-water, critically relies on the correct selection and application of materials. At the present time, ceramics and polymers have been identified as the most promising materials.

Therefore, the purpose of this current research work is firstly to examine the contact conditions within an axial piston pump for a range of sleeved and lined components manufactured from a variety of different materials, which involves a fundamental study of the contact of conformally contacting layered surfaces.

Once the contact conditions are known within the pump it is then possible to more accurately design the pump components. However, conventional deterministic methods are not appropriate for designing ceramic components, due to the inherent scatter of limiting defects, and statistical methods are necessary. A number of such probabilistic methods are proposed in the literature, but a definitive design procedure is not yet available and much work needs to be done to relate the basic mechanical properties of ceramic materials to their structural performance. Thus part of this research work is aimed at reviewing and examining the different probabilistic design methods with the long-term view of determining which, if any, are best suited to the design of ceramic components in this particular application.

Hence, the main objectives of this work can be summarised as follows:

1. To use two- and three-dimensional finite element analysis to determine the contact pressure distribution between cylindrical and spherical conformally contacting layered components.
2. To determine the stress distribution in layered, conformally contacting, axial piston pump components using the contact pressure distributions determined above as loading.
3. To determine the most appropriate statistical method for calculating the probability of failure of PSZ ceramic axial piston pump components from specimen strength data using finite element stress and volume data determined above.

CHAPTER 2

CONFORMAL CONTACT ANALYSIS

2.0 INTRODUCTION

This chapter considers the development of analytical and numerical solutions to the problem of conformal contact beginning with the introduction of contact mechanics. It reviews the more recent development of the use of finite element analysis in contact problems and considers the analysis of layered components. The literature provides numerous examples of papers relating to all aspects of contact problems but this review will be confined primarily to linear elastic, frictionless, static contact.

2.1 DEVELOPMENT OF CONTACT MECHANICS

Love (1952) presented the classical approach to finding the stresses and displacements in an elastic half-space subjected to surface tractions. These were due to Boussinesq (1885) and Cerruti (1882) who used the theory of potential to obtain equations for the stresses and displacements at any point in the half-space.

For a concentrated force, P , on an elastic half-space bounded by the plane $z = 0$, as shown in figure 2.1.1, the resultant stress perpendicular to the z -axis at a point A is given by

$$\sigma = \frac{3F \cos^2 \theta}{2\pi R^2} \quad (2.1)$$

Thus, for each point on the surface of a sphere of diameter d the resultant stress is constant and equal to $3F/2\pi d^2$. As $R \rightarrow 0$ the resultant stress becomes infinite, a situation which clearly cannot occur in practice.

The problem of a concentrated line load, F /unit length, on the surface of a half-space was first solved by Flamant (1892). For a point A beneath the surface

$$\sigma_R = -\frac{2F \cos \theta}{\pi R} \quad (2.2)$$

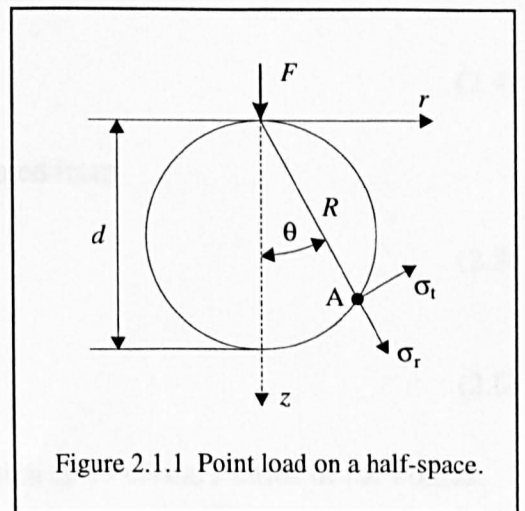


Figure 2.1.1 Point load on a half-space.

$$\sigma_t = \tau_t = 0 \quad (2.3)$$

σ_r , thus has a constant magnitude $-2F/\pi d$ on a circle of diameter d which passes through the origin. Again as $R \rightarrow 0$ the stress becomes infinite.

Using the principle of superposition and Hooke's law the above expressions can be used to find the stresses and displacements due to distributed pressures on a half-space. The subject of contact mechanics itself is often said to have started with the publication by Hertz (1882) of his paper "On the contact of elastic solids". Hertz developed his theory whilst studying interference fringes between glass lenses in contact. His work produced mathematical relationships between the distributed surface pressure and applied load for elastic, frictionless contact of bodies with quadratic surfaces and for small contact areas, an approach which is still used in a great number of contact problems today. However, elastic contact stress problems can really only be classified as Hertzian if they satisfy the following conditions:

- a) The bodies obey the linear theory of elasticity.
- b) The dimensions of the deformed contact area remain small compared with the principal radii of the undeformed surfaces.
- c) The contacting surfaces are continuous and may be represented by second degree polynomials (quadratic surfaces) before deformation.
- d) The deformations are related to the stresses in the contact zones as predicted by Boussinesq's influence functions for half-spaces.
- e) The contacting surfaces are frictionless.

Bodies whose surfaces satisfy these conditions touch first at a point or along a line and, even under load, the dimensions of the contact area remain small compared with the dimensions of the bodies themselves.

2.1.1 Spherical contact

For a sphere in a spherical cavity, as shown in figure 2.1.2a, the radius of the contact circle is given by

$$a = \left(\frac{3FR_e}{4E_e} \right)^{1/3} \quad (2.4)$$

where F is the load and E_e and R_e are calculated from

$$\frac{1}{E_e} = \left(\frac{1-\nu_1^2}{E_1} + \frac{1-\nu_2^2}{E_2} \right) \quad (2.5)$$

$$\frac{1}{R_e} = \left(\frac{1}{R_2} - \frac{1}{R_1} \right) \quad (2.6)$$

where E_1 , E_2 , ν_1 and ν_2 are the Young's moduli and Poisson's ratios of the bodies.

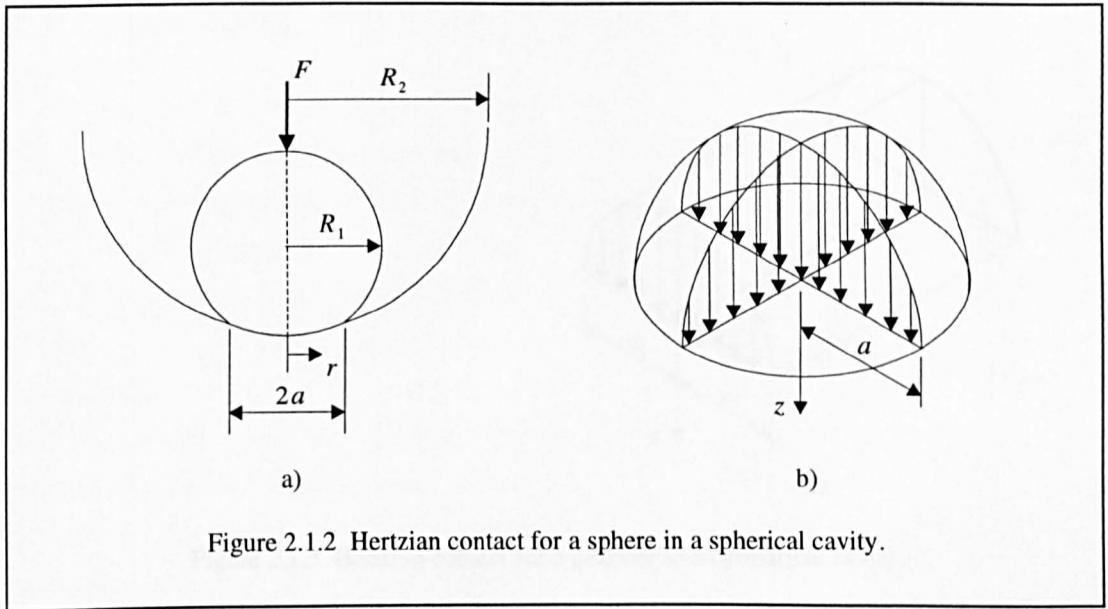


Figure 2.1.2 Hertzian contact for a sphere in a spherical cavity.

The contact pressure between the sphere and cavity is given by

$$p(r) = \frac{3F}{2\pi a^3} (a^2 - r^2)^{1/2}. \quad (2.7)$$

This results in a hemispherical profile (figure 2.1.2b) with a maximum at $r = 0$ given by

$$p_{\max} = \frac{3F}{2\pi a^2} = \left(\frac{6FE_e^2}{\pi^3 R_e^2} \right)^{1/3}. \quad (2.8)$$

2.1.2 Cylindrical contact

For a cylinder in a cylindrical cavity, as in figure 2.1.3a, Hertzian theory gives a contact half-width of

$$a = \left(\frac{4FR_e}{\pi E_e} \right)^{1/2} \quad (2.9)$$

and contact pressure between cylinder and cavity of

$$p(x) = \frac{2F}{\pi a^2} (a^2 - x^2)^{1/2} \quad (2.10)$$

resulting in the profile shown in figure 2.1.3b. The maximum pressure occurs at $x = 0$ and is therefore

$$p_{\max} = \frac{2F}{\pi a} = \left(\frac{FE_e}{\pi R_e} \right)^{1/2} \quad (2.11)$$

where E_e and R_e are the same as for the spherical case.

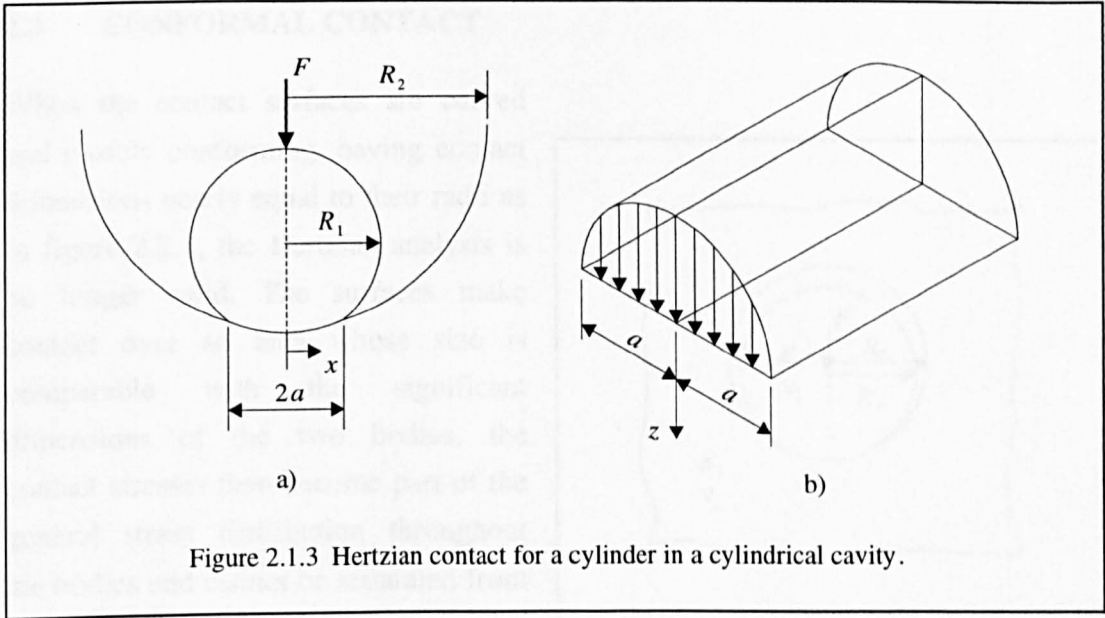


Figure 2.1.3 Hertzian contact for a cylinder in a cylindrical cavity.

The stresses in the bodies due to the contact comprise a local stress concentration that can be considered independently of the stresses in the bulk of the two bodies. These stresses were given by Johnson (1985) for the axis under the centre of contact for both the cylindrical and spherical case and these are shown in figure 2.1.4. Morton and Crose (1922) calculated the stresses elsewhere in the bodies. As can be seen the maximum shear stress occurs beneath the surface: at a depth of $0.78a$ for cylindrical contact and $0.48a$ for spherical contact when $\nu = 0.3$.

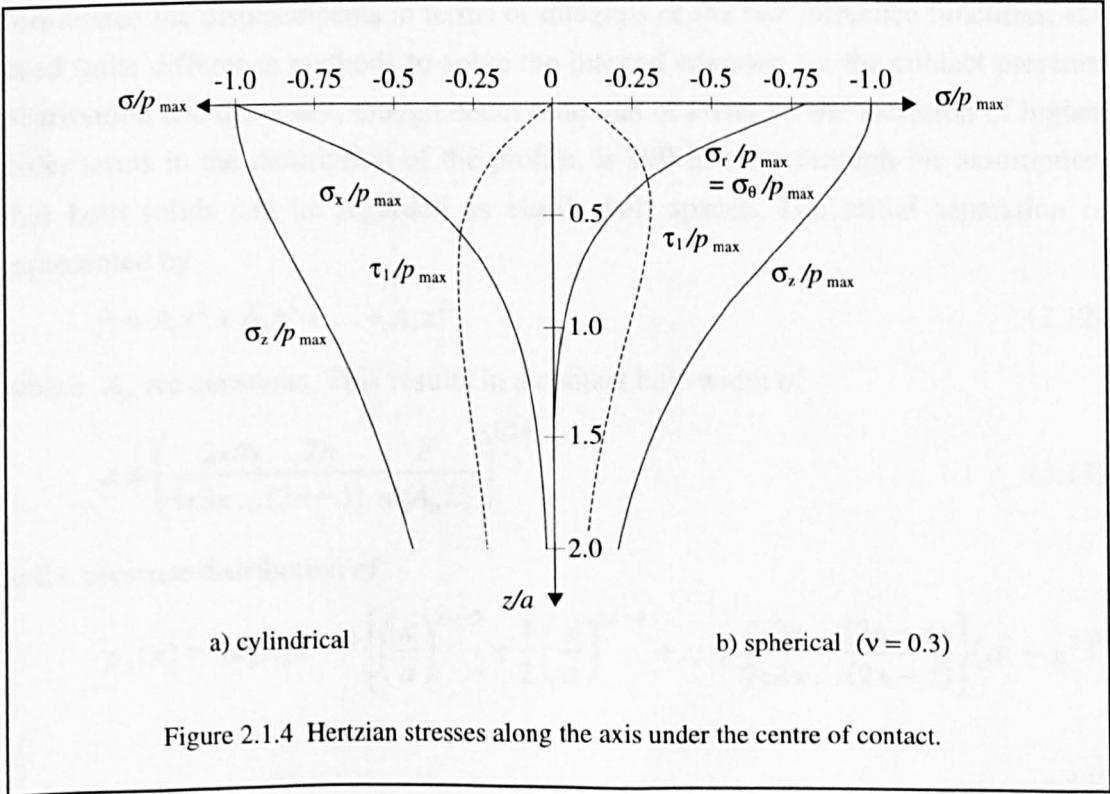


Figure 2.1.4 Hertzian stresses along the axis under the centre of contact.

2.2 CONFORMAL CONTACT

When the contact surfaces are curved and closely conforming, having contact dimensions nearly equal to their radii as in figure 2.2.1, the Hertzian analysis is no longer valid. The surfaces make contact over an area whose size is comparable with the significant dimensions of the two bodies, the contact stresses then become part of the general stress distribution throughout the bodies and cannot be separated from it. Therefore, some of the assumptions made in Hertzian analysis are no longer valid and alternative solutions must be found.

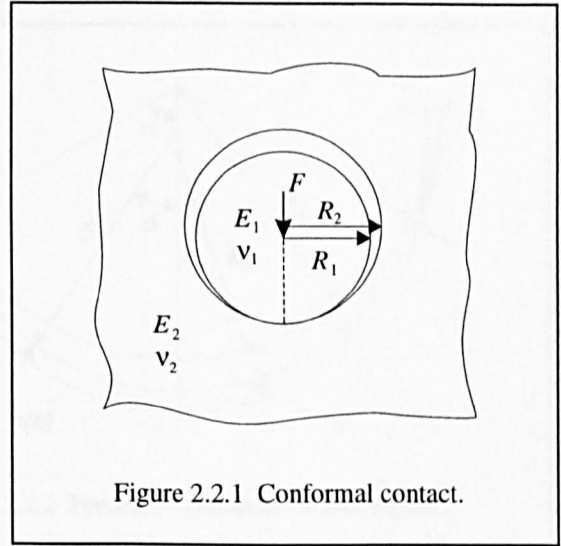


Figure 2.2.1 Conformal contact.

2.2.1 Conformal cylindrical contact

The solution to the problem of the conformal contact of a long elastic cylinder contacting a cylindrical seat was first attempted by Steuermann (1939). He represented the gap between the cylinder and cylindrical seat by a power series and formulated the displacements in terms of integrals of the line influence functions. He used finite difference methods to solve the integral equation for the contact pressure distribution and the result, though better than that of Hertz by the inclusion of higher order terms in the description of the profile, is still in error through his assumption that both solids can be regarded as elastic half spaces. The initial separation is represented by

$$h = A_1 x^2 + A_2 x^4 + \dots + A_n x^{2n}, \quad (2.12)$$

where A_n are constants. This results in a contact half-width of

$$a = \left(\frac{2 \times 4 \times \dots \times 2n}{1 \times 3 \times \dots \times (2n-1)} \frac{F}{n \pi A_n E_e} \right)^{1/2n} \quad (2.13)$$

and a pressure distribution of

$$p_n(x) = n E_e A_n a^{2n-2} \left\{ \left(\frac{x}{a} \right)^{2n-2} + \frac{1}{2} \left(\frac{x}{a} \right)^{2n-4} + \dots + \frac{1 \times 3 \times \dots \times (2n-3)}{2 \times 4 \times \dots \times (2n-2)} \right\} (a^2 - x^2)^{1/2} \quad (2.14)$$

The profiles assumed in Hertz theory correspond to $n = 1$, in which case equation (2.14) reduces to equation (2.10). However, for higher values of n the maximum pressure does not occur at the centre of contact.

The widely accepted standard for the analytical study of conformal contact of cylindrical bodies was conducted by Persson (1964) in Gothenburg. Persson derived an identical contact criterion to Steuermann but proceeded to solve the equation in a different

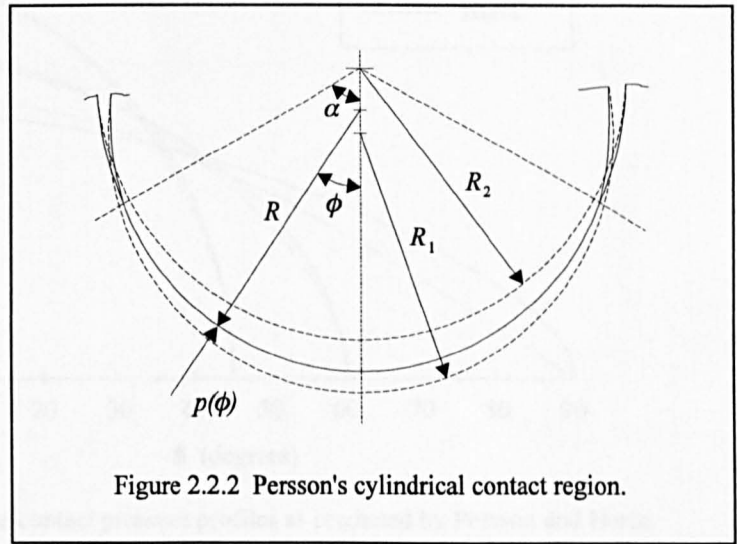


Figure 2.2.2 Persson's cylindrical contact region.

way. He assumed that the contact surface was cylindrical and formulated the contact criterion as an integro-differential equation from which he determined the analytical contact pressure distribution for a plane stress model. i.e. the analysis pertains to a circular disc in a circular hole in an infinite (thin) plate.

Persson calculated the pressure distribution for the case where the elastic constants of the contacting materials are the same:

$$p(\phi) = \frac{2F(c^2 - q^2)^{1/2}}{\pi R(1 + q^2)(c^2 + 1)^{1/2}} + \frac{F(c^2 + 1)^{-1}}{2\pi R c^2} \ln \left\{ \frac{(c^2 + 1)^{1/2} + (c^2 - q^2)^{1/2}}{(c^2 + 1)^{1/2} - (c^2 - q^2)^{1/2}} \right\} \quad (2.15)$$

where $c = \tan\left(\frac{\alpha}{2}\right)$, $q = \tan\left(\frac{\phi}{2}\right)$ and α , ϕ , R and F are as shown in figure 2.2.2.

Figure 2.2.3 shows the pressure profiles thus predicted compared with those from Hertzian analysis. As can be seen, as the contact angle increases the Hertzian analysis results in a higher pressure near the centre of contact, falling off more rapidly at the edges. Persson also determined an expression relating the load, F , radial difference, CL , Young's modulus, E , and contact angle, α which gives

$$\frac{E * CL}{F} = \frac{2}{\pi} \frac{1 - c^2}{c^2} - \frac{I}{\pi^2 c^2 (c^2 + 1)} \quad (2.16)$$

$$\text{where } I = \int_{-c}^c \frac{f(c, t)}{1 + t^2} dt \quad \text{and} \quad f(c, t) = \ln \frac{(c^2 + 1)^{1/2} + (c^2 - t^2)^{1/2}}{(c^2 + 1)^{1/2} - (c^2 - t^2)^{1/2}}. \quad (2.17)$$

Equation (2.16) is plotted in figure 2.2.4 with the equivalent curve from Hertz theory. This illustrates more markedly the difference between the two methods as the contact

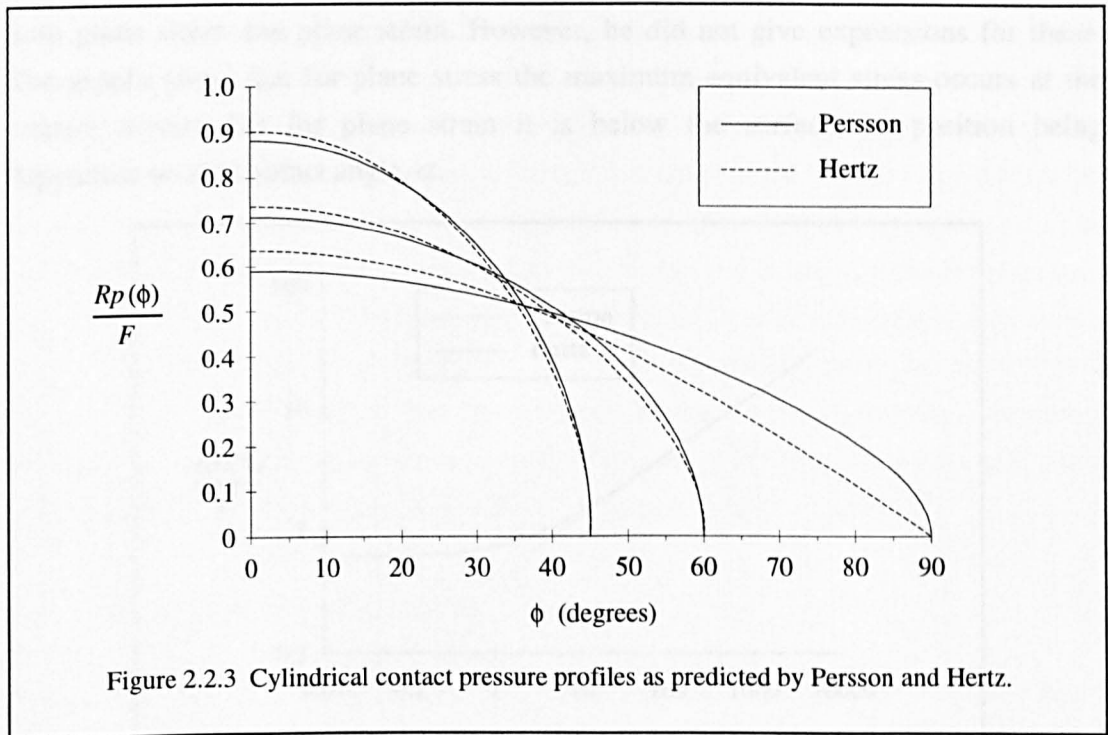


Figure 2.2.3 Cylindrical contact pressure profiles as predicted by Persson and Hertz.

angle increases and the assumption of small contact size in Hertzian analysis is violated. Persson also plotted the expression in equation 2.16 versus the normalised maximum pressure at the centre of contact which is given by

$$\frac{Rp_{max}}{F} = \frac{2c}{\pi(c^2 + 1)^{1/2}} + \frac{\ln[(c^2 + 1)^{1/2} + c]}{\pi c^2(c^2 + 1)}. \quad (2.18)$$

This is shown in figure 2.2.5 again with the curve from Hertzian analysis for comparison. Persson plotted radial and tangential stresses in the plate at the contact interface and Tresca and von Mises equivalent stresses along the symmetry axis for

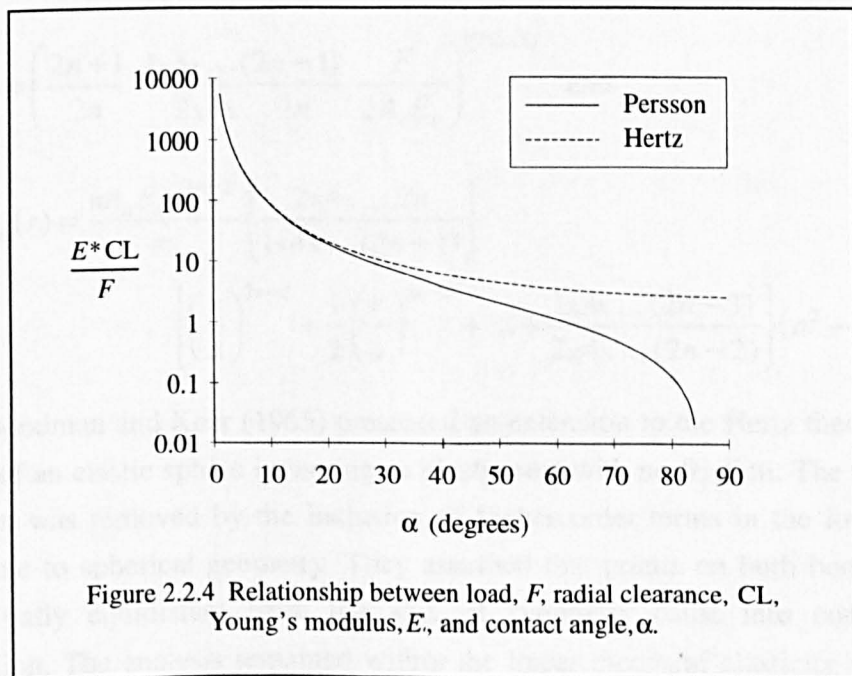
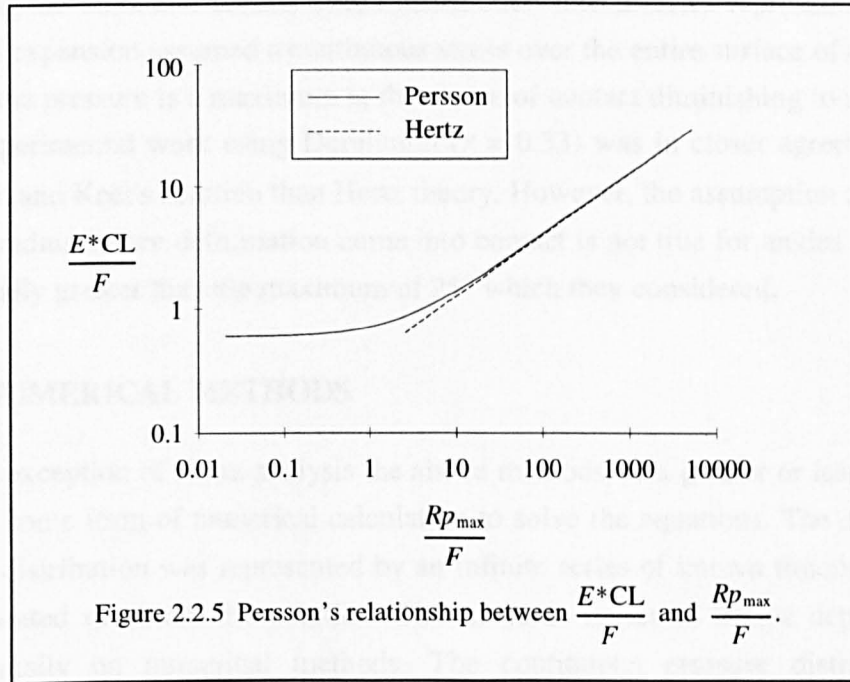


Figure 2.2.4 Relationship between load, F , radial clearance, CL , Young's modulus, E , and contact angle, α .

both plane stress and plane strain. However, he did not give expressions for these. The graphs show that for plane stress the maximum equivalent stress occurs at the contact surface but for plane strain it is below the surface, its position being dependent on the contact angle, α .



2.2.2 Conformal spherical contact

Johnson (1985) gave equivalent expressions for spherical contact to Steuermann's equations (2.12) to (2.14). These are

$$h = A_1 r^2 + A_2 r^4 + \dots + A_n r^{2n}, \quad (2.19)$$

$$a = \left(\frac{2n+1}{2n} \frac{1 \times 3 \times \dots \times (2n-1)}{2 \times 4 \times \dots \times 2n} \frac{F}{2A_n E_e} \right)^{1/(2n+1)} \quad \text{and} \quad (2.20)$$

$$P_n(r) = \frac{nA_n E_e a^{2n-2}}{\pi} \left\{ \frac{2 \times 4 \times \dots \times 2n}{1 \times 4 \times \dots \times (2n-1)} \right\}^2 \left\{ \left(\frac{r}{a} \right)^{2n-2} + \frac{1}{2} \left(\frac{r}{a} \right)^{2n-4} + \dots + \frac{1 \times 3 \times \dots \times (2n-3)}{2 \times 4 \times \dots \times (2n-2)} \right\} (a^2 - r^2)^{1/2} \quad (2.21)$$

Goodman and Keer (1965) presented an extension to the Hertz theory for the solution of an elastic sphere indenting an elastic seat with no friction. The half-space restriction was removed by the inclusion of higher order terms in the formulation, appropriate to spherical geometry. They assumed that points on both bodies which were initially equidistant from the axis of symmetry came into contact after deformation. The analysis remained within the linear theory of elasticity and it was

assumed that the elastic properties of the sphere and cavity were the same. Moreover, by a further assumption which substantially reduced the complexity of the calculation, Poisson's ratio was constrained to be 0.25. Goodman and Keer derived an integral equation from boundary displacement requirements which they solved by expanding the unknown normal stress distribution into a series representation. The choice of expansion assumed a continuous stress over the entire surface of the sphere and that the pressure is a maximum at the centre of contact diminishing to zero at the edge. Experimental work using Duralumin ($\nu = 0.33$) was in closer agreement with Goodman and Keer's solution than Hertz theory. However, the assumption that points of equal radius before deformation come into contact is not true for angles of contact substantially greater than the maximum of 25° which they considered.

2.3 NUMERICAL METHODS

With the exception of Hertz analysis the above methods, to a greater or lesser extent, involved some form of numerical calculation to solve the equations. The continuous pressure distribution was represented by an infinite series of known functions which was truncated to obtain the solution. The methods reviewed below depend more fundamentally on numerical methods. The continuous pressure distribution is replaced by a discrete set of pressures and the solution obtained at a discrete set of points. Two different approaches have developed to obtain the solution: the direct, or matrix inversion, method and the variational method which aims to minimise an appropriate energy function.

Singh and Paul (1974) developed a general method for the numerical analysis of three-dimensional frictionless, nonconformable contact of bodies with arbitrary profiles where the contact region is not known in advance. They introduced an interpenetration curve as the first approximation to the boundary of the contact region and attempted to find the pressure distribution, load and approach. They used the simply discretised method to solve the resulting singular integral equation and described two techniques for overcoming the inherent sensitivity of the manner of discretisation, namely the method of redundant field points (RFP) and the method of functional regularisation (FR). The former method assumes that the errors associated with each of the discretisation or field points are random in nature and hence, instead of solving n equations in n unknowns, m additional field points are generated. The least-squares error criterion is then used to find the solution which best satisfies the $(m+n)$ equations. The FR method aims to keep point-to-point differences in pressure small at the same time as minimising an auxiliary function which is zero when the pressures in all the elements of the discretised mesh are equal. They tested both methods against known Hertzian solutions and obtained good results provided the

problems were within a particular range of applicability. The RFP method was found to give good convergence to the Hertzian solution for contacting cylinders at right angles providing the aspect ratio of the contact ellipse was less than 10.

Later Woodward and Paul (1976) extended the simply discretised method above to the case of conformal contact. Singh and Paul had approximated the contacting surfaces by half-spaces and used the Boussinesq displacement function for a point load on a plane as well as neglecting tangential displacements of the surfaces.

Woodward and Paul initially assumed that points at equal distance around the undeformed curves from the first point of contact, 0, merged after deformation. See figure 2.3.1 where the arcs s_1 and s_2 are the same length. A point-mating procedure was used to iteratively identify mating points from the initial assumption considering deformations normal and

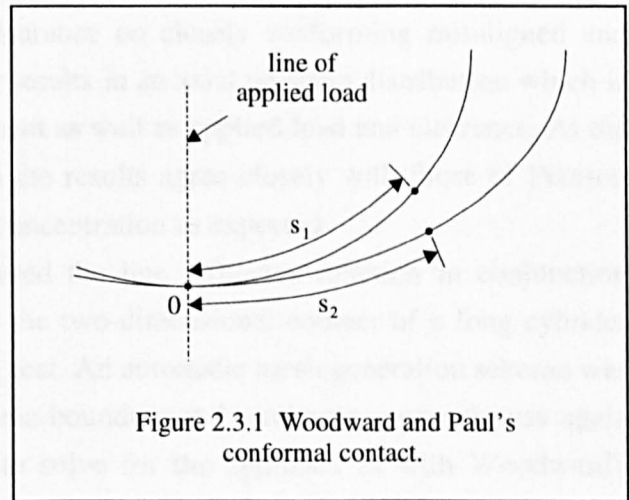


Figure 2.3.1 Woodward and Paul's conformal contact.

tangential to the surface. They also assumed, for ease of computation, that the resultant load passes through 0. The influence functions relating the pressure distribution to the displacements were found numerically. The report restricted the applicability to cylinders indenting cylindrical seats and spheres indenting spherical seats. The cylindrical results are in agreement with Persson's analytical solution and agree well with photoelasticity experiments conducted by the authors. The spherical results agree well with experimental data and are more accurate than those of Goodman and Keer as contacting points are not constrained to be initially on the same cylindrical radius.

Paul and Hashemi (1977) developed a modification to the simply discretised method in which the approach is guessed at, initially for counterformal problems and later (Paul and Hashemi, 1980) for conformal problems with general geometries. They included methods for automatic mesh generation such that the mesh does not have to be uniform and also for contact area boundary determination. They used the method to solve the problem of rail and wheel contact at the flange throat using Boussinesq's influence function.

Hartnett (1978) analysed the axisymmetric contact problem of an elastic sphere indenting an elastic cavity for frictionless and frictional contact. He solved the integral equation by expanding the unknown normal stress into a Fourier-Legendre

series, and employed the method of collocation to form a system of linear algebraic equations. A numerical method, utilising the Gram-Schmidt orthogonalisation principle, was introduced to invert the large scale matrix and minimise computer round-off errors. A prior knowledge of the shape of the contact stress distribution was not required, therefore the influence of surface tractions and geometric distortions upon the distributed stress could be produced more readily.

Chen and Marshek (1986) presented a numerical solution using a modified Boussinesq influence function in conjunction with the discretisation of the integral equation to analyse the effect of clearance on closely conforming misaligned and aligned journal bearings. The former results in an axial pressure distribution which is dependent on the angle of misalignment as well as applied load and clearance. At the centre of the aligned bearing length the results agree closely with those of Persson but at the edge there is a high stress concentration as expected.

Chen and Marshek (1988) used the line influence function in conjunction with the method above to solve for the two-dimensional contact of a long cylinder and a closely conforming cylindrical seat. An automatic mesh generation scheme was described to redefine the pressure area boundary and a relative approach was again guessed at, rather than attempting to solve for the approach as with Woodward's solution. This was with the aim of avoiding the ill-conditioning of the system, as the matrix for the discretised integral equation became diagonally dominant and symmetric. The effects of clearance and material properties on the contact pressure distribution and contact area were examined. The results were compared extensively and favourably with those of Persson's including cases where the contacting materials were dissimilar when it was found that a hard cylinder contacting a soft cylindrical seat will give a higher contact angle than a soft cylinder contacting a hard cylindrical seat.

2.3.1 Finite element analysis of contact

Analysing contact between bodies using the finite element method (FEM) has been a comparatively recent development which has received considerable attention over the past 15-20 years. In early implementations of the finite element method the problems of determining the region of contact between meshes representing the two bodies precluded its use for elastic contact problems. However, more recently there has been a large number of numerical approaches to the problem of applying the correct boundary conditions. The majority allow frictional effects to be considered, making use of either Lagrange multipliers or penalty function methods to impose the displacement constraints at the surface between contacting meshes. Francavilla and Zienkiewicz (1975) were among the first to provide a contact algorithm that became

widely installed in finite element programs. However, this algorithm had the disadvantage of requiring a flexibility, rather than a stiffness, approach.

A significant advance was made by Hughes et al (1976) who used Lagrange multipliers, a method that could be used in finite element displacement solution routines. Node-on-node contact was necessary in the contact zone and much of their work was directed to contact-impact problems. Guerra and Browning (1983) used an incremental loading scheme and showed that displacement constraints could be applied by either Lagrange multipliers or penalty functions and that node-on-node contact was unnecessary.

All methods based on so-called gap elements are based on penalty functions where the gap element stiffness is the penalty number. A gap element which included friction was described by Mazurkiewicz and Ostachowicz (1983). A tangential stiffness was introduced, given by the product of the normal gap stiffness and the coefficient of friction. It is this method which is used in some of the popular general purpose finite element packages including the one used for the work described here.

A general two-dimensional algorithm not requiring node-on-node contact was developed by Bathe and Chaudhary (1985), using linear elements in the contact zone and allowing frictional contact. Linear interpolation formulae were used between the nodes to determine the displacement constraints and contact forces. In a further paper (Chaudhary and Bathe, 1986) the work was extended to allow the solution of three dimensional problems and dynamic contact.

Pascoe and Mottershead (1988) extended the work of Bathe and Chaudhary to include eight-node isoparametric elements using the shape functions to determine displacement constraints and forces in the contact zone. An approach was used whereby the full loads were initially applied. If a change in the contact boundary condition occurred, then scaling of loads and displacements was undertaken until the first new boundary constraint became just operative again. The remainder of the load was then applied with a modified stiffness matrix and the process repeated until the mesh was fully loaded and the contact boundary conditions satisfied. The formulation applied to linear elastic contact but the authors stated that the method could be adapted to deal with material and geometric non-linearities. They compared their (plane strain) results with those of Persson for the analysis of a pin in a hole and obtained a good comparison. However, the method is not restricted to conformal contact.

Pascoe and Mottershead (1989) subsequently provided two further algorithms for frictional contact overcoming the necessity of having a non-symmetric stiffness matrix due to the frictional constraints. Later, Mottershead et al (1992) described the

implementation of further algorithms which could be implemented using either the Lagrange multiplier or penalty function method.

Vijayakar et al (1989) presented a specialised finite element formulation designed to deal with the frictional contact problem in three dimensional conformal contact. They performed three-dimensional analyses of gears and found that because one of the principal relative curvatures is close to zero the contact load distribution is very sensitive to the accuracy of the geometric representation of the surfaces in contact. They stated that the error in the representation must be much smaller than the deformations and that conventional FEA, using linear, quadratic or cubic surfaces, is not adequate unless an inordinately large number of elements is used. They also claimed that a very large number of degrees of freedom of deformation is required in the region of contact if the contact load distribution is to be accurately determined without ill-conditioning of the contact equations. These restrictions do not appear to be valid for conformal cylindrical or spherical contact where adequate results are produced using gap elements available in general purpose commercial FE programs.

An example of the use of FEA to study the effect of the diametral gap between conforming concentric cylindrical components was undertaken by Harrigan and Harris (1991) who used the method to study an uncemented femoral total hip component and a femur. The contact algorithm used was the one described above by Chaudhary and Bathe (1986) assuming no friction.

2.3.2 Boundary element analysis of contact

The boundary element method (BEM) is a more recent technique than the finite element method and it has also been used to analyse contacting bodies numerically. It will only briefly be considered here. In the BEM only the surfaces (boundaries) are modelled rather than entire volumes. Andersson et al (1980) reported on the BEM applied to two-dimensional frictionless contact problems. Becker and Plant (1987) analysed a sphere in a spherical seat using axisymmetric boundary elements and obtained a good agreement with Hertz' solution for the small contact angles which they considered.

2.4 ANALYSIS OF LAYERED COMPONENTS

The analysis of the contact of bodies consisting of layered materials, by analytical or numerical methods, is usually confined to the field of surface coatings where the layer is very thin compared to the dimensions of the bodies. This permits a half-space assumption to be used. Another simplification often made is to assume that the

substrate or indenter are rigid. This is justified as a first approximation if, as in the case of coated rollers, the surface layer is much more compliant than the rollers.

Chen and Engel (1972) considered the indentation of a medium consisting of one or two parallel layers perfectly bonded to an elastic half-space for various combinations of material properties, layer thicknesses and number of layers. They obtained the stress distributions, contact forces and penetrations for rigid, flat ended and parabolic punches which compared well with experiments. The authors said that it would be an easy matter to implement changes in the numerical approximation to take account of the elasticity of the punches but they do not do this themselves.

Gupta and Walowit (1974) obtained a numerical plane strain solution to the problem of a layered elastic solid and a cylindrical elastic indenter for frictionless contact when the elastic moduli of the indenter and substrate were the same. They plotted graphs for a wide range of layer thickness and moduli ratio and found that when the layer was softer than the substrate and indenter the pressure distribution could be approximated from a weighted sum of parabolic and elliptic functions thus

$$p\left(\frac{x}{a}\right) = \frac{3\pi}{3\pi - 8} \left[\left(\frac{a_0}{a} - \frac{8p_m}{3\pi p_0} \right) \left(1 - \frac{x^2}{a^2} \right)^{1/2} + \left(p_0 - \frac{a_0}{a} \right) \left(1 - \frac{x^2}{a^2} \right) \right] \quad (2.22)$$

where a is the contact half-width,
 a_0 is the Hertzian contact half-width,
 p_m is the maximum pressure and
 p_0 is the Hertzian maximum pressure.

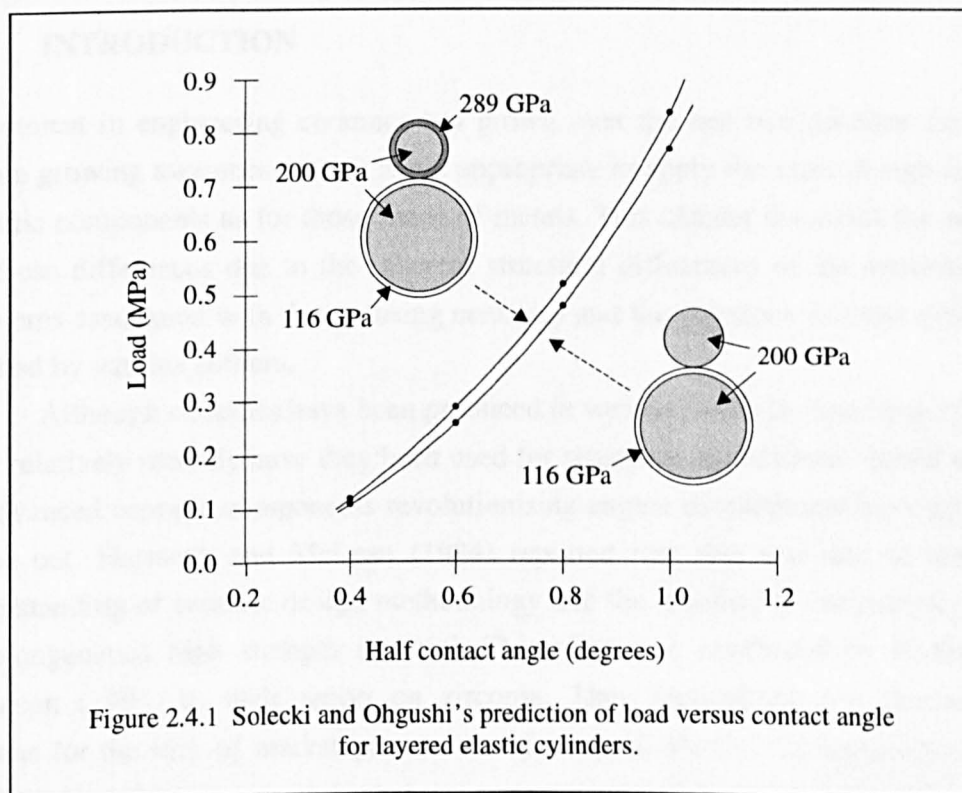
However, when the layer was stiffer than the substrate and indenter it was not possible to determine an equivalent equation for the pressure distribution.

Leveson (1974) obtained approximate analytical solutions to cylindrical and spherical bodies when one is coated with a solid film of lower stiffness, assuming a half-space representation. They compared their results with those of Gupta and Walowit (1974) for the cylindrical case but assumed an elliptic distribution with no parabolic contribution.

An analytical solution for the contact pressure, area, approach and sub-surface stresses was determined for a layered elastic half-space subjected to a uniform distributed pressure over a rectangular area by Chiu and Hartnett (1983). They obtained numerical results for the specific case simulating the contact of a steel rolling element with a steel bearing ring supported by an aluminium housing showing an increase in deformation and a decrease in maximum contact pressure due to the softer substrate.

Solecki and Ohgushi (1984) studied the contact of two layered elastic cylinders taking into account the local curvature of the surfaces. They reduced the integral equation to an infinite system of linear algebraic equations using Fourier

transformation which they solved to obtain the pressure distribution and approach for an assumed contact width. For the fully elastic case they presented only two examples shown in figure 2.4.1. As can be seen the results apply to very light loading and, as expected, the cylinder with the stiff layer resulted in a smaller contact angle for the same load. No attempt was made to determine the stresses in the cylinders or layers.



Tangena and Wijnhoven (1988) used finite element analysis with gap elements to attempt to obtain a correlation between the stresses and wear in a multi-layered system. However, the layers were only several micrometres thick, simulating films of noble metals in non-permanent electrical contacts, and they assumed a rigid indenter despite using gap elements in the model.

No references have been found in the literature to analytical, numerical or finite element analysis of conformal layered contact.

CHAPTER 3

ANALYSIS OF CERAMIC MATERIALS

3.0 INTRODUCTION

As interest in engineering ceramics has grown over the last two decades there has been a growing awareness that it is not appropriate to apply the same design rules to ceramic components as for those made of metals. This chapter discusses the reasons for these differences due to the inherent structural differences of the materials, the problems associated with design using ceramics and the solutions to those problems reached by various authors.

Although ceramics have been produced in various forms for hundreds of years only relatively recently have they been used for structural applications. Initial reports of advanced ceramic components revolutionising engine development have not been borne out. Hartsock and McLean (1984) reported that this was due to the poor understanding of ceramic design methodology and the inability to consistently make a homogeneous high strength material. This view was reinforced by Birkby and Hodgson (1991) in their report on zirconia. They highlighted two fundamental reasons for the lack of market penetration of zirconia. Firstly, the expectations that the benefits of insulation and wear resistance would increase engine performance foundered due to the immaturity of the material, the arduous nature of the application and the lack of tribological data; secondly, ceramics saw low utilisation due to the limited design knowledge and experience of engineers, as it quickly became evident that metal design methods were not appropriate to advanced ceramic materials.

3.1 ADVANCED TECHNICAL CERAMICS

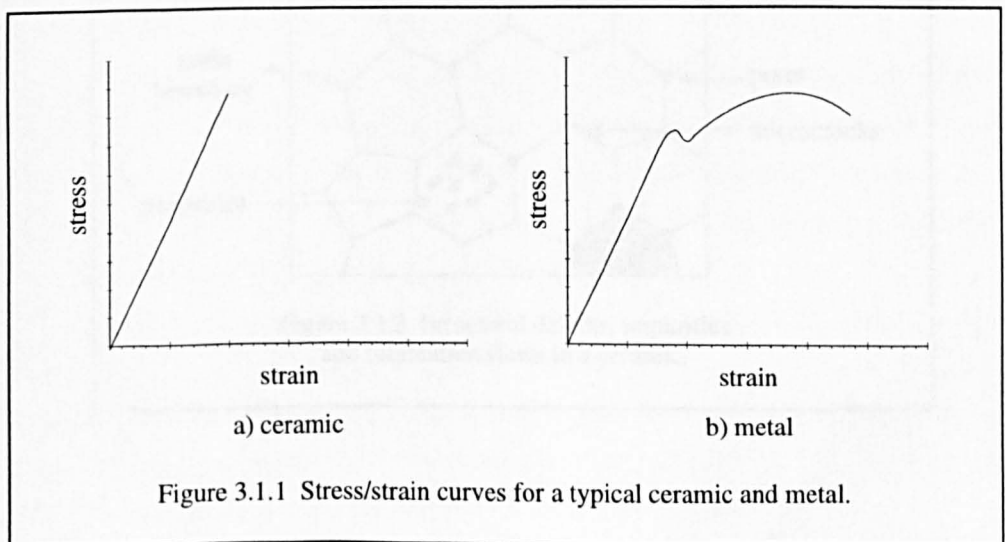
Advanced technical ceramics do not constitute a homogeneous materials group or a single product class, since variations in fabrication and processing techniques result in different properties. However, they do have some characteristics that allow them to be separated from other groups of materials.

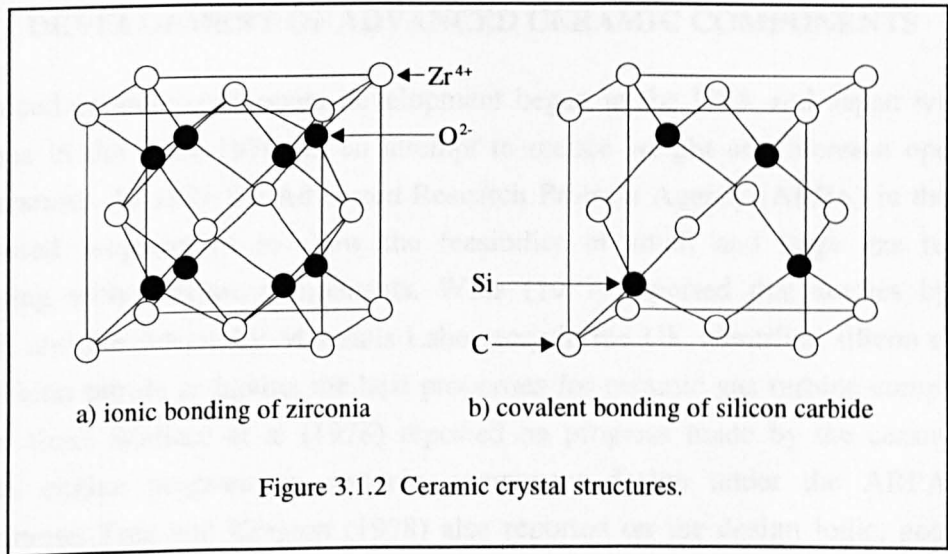
Currently, there is no accepted classification system for advanced ceramics, although there is a general consensus throughout the industry that there is a need for a broad-based, multipurpose classification system (Schneider, 1993). In 1988 the Versailles Project on Advanced Materials and Standards (VAMAS) initiated an effort

to classify advanced ceramics, considering the two basic problems of such a classification system. They saw the first problem as the need to accommodate all the requirements of industry and special national areas of activity; the second as the difficulty of defining a minimum set of information that identifies one material as different from another, while anticipating future developments in this particular group of materials. The additional problems of using computers to store and retrieve appropriate materials property data were considered and reported by Reynard (1993).

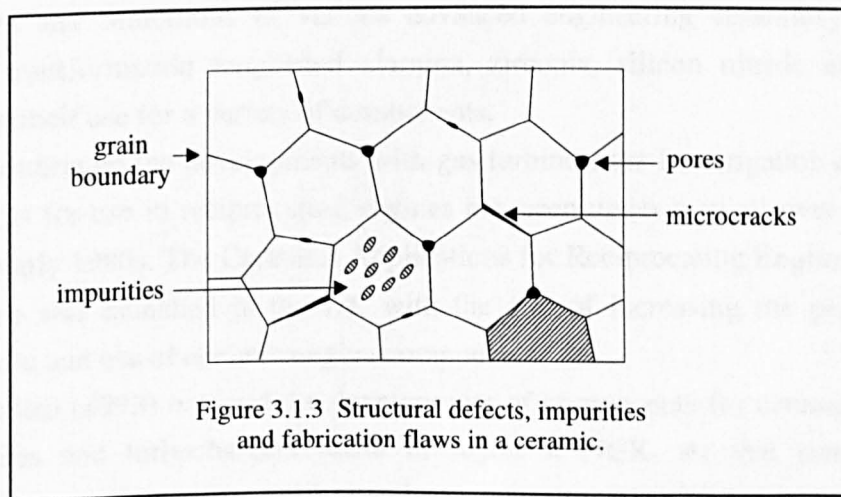
Morrell (1993) reported on the terminology requirements of the VAMAS initiative. He recommended the use of the term "advanced technical ceramics", in English, as a compromise between the multitude of other terms; such as fine, engineering, structural, technical, high-performance, high technology or special ceramics; all of which are in usage in various parts of the world or by different user groups. The recommended definition of advanced technical ceramics resulting from the initial stages of this work (VAMAS, 1993) was "an inorganic, non-metallic (ceramic) basically crystalline, material of rigorously controlled composition and manufactured with detailed regulation from highly refined and/or characterised raw materials giving precisely specified attributes".

Advanced technical ceramics usually possess high temperature strength, thermal shock and fatigue resistance, erosion-corrosion resistance, low density and low thermal conductivity, resulting in their use where metals or polymers would not be suitable. However, the properties responsible for these advantages are also responsible for their disadvantages. Most advanced technical ceramics show negligible plastic strain before failure due to the strong bonds between the atoms which make dislocation movement difficult. Local high stress concentrations therefore cannot be dissipated and reduction of peak stresses by plastic deformation is not possible. Figure 3.1.1 shows typical stress-strain curves for a ceramic and a





metal. The strong covalent and/or ionic bonding and crystalline structure control the intrinsic properties of ceramic materials (figure 3.1.2) whereas the extrinsic or actual properties are controlled by such factors as structural defects, impurities and fabrication flaws (figure 3.1.3). Failure in a ceramic usually occurs by the catastrophic propagation of a crack-like defect, which may be on the surface or in the bulk of the material, when subjected to a sufficiently high stress. The critical defect will vary from specimen to specimen or component to component and, consequently, the strengths of nominally identical specimens or components will vary. This results in a statistical variation in strength assuming a statistical distribution of strength limiting defects. The strength is also sensitive to the size, shape and surface finish of the material.



3.2 DEVELOPMENT OF ADVANCED CERAMIC COMPONENTS

Advanced ceramic component development began in the USA and Japan with gas turbines in the early 1970s in an attempt to reduce weight and increase operating temperatures. In 1971 the Advanced Research Projects Agency (ARPA) in the USA sponsored programmes to show the feasibility of small and large gas turbines operating with ceramic components. Wills (1977) reported that studies by both ARPA and the Admiralty Materials Laboratory in the UK identified silicon carbide and silicon nitride as having the best properties for ceramic gas turbine components at that time. Wallace et al (1978) reported on progress made by the ceramic gas turbine engine program on ceramic component design under the ARPA/Navy programme. Tree and Kington (1978) also reported on the design logic, goals and methodology of the same program from the viewpoint of co-sponsors, AiResearch Manufacturing.

Devendra & Syers (1990) outlined the experience of Rolls-Royce in the development of advanced ceramic components. This began with small components for helicopter engines using monolithic ceramics such as silicon nitride and silicon carbide and progressed to toughened and fibre reinforced ceramics for larger components. The majority of Rolls-Royce experience of ceramic engine components at that time was in a version of the Gem gas turbine used as an advanced mechanical engineering demonstrator. All the ceramic components in that engine were based on silicon nitride.

Dworak and Fingerle (1987) reported that in Europe and the USA ceramic component development was almost all restricted to replacing existing components in conventional engines while in Japan research was also being directed towards a ceramic engine with little in common with existing engines. They outlined the advantages and limitations of various advanced engineering ceramics, including alumina, transformation toughened alumina, zirconia, silicon nitride and silicon carbide, in their use for a variety of components.

Building on the developments with gas turbines, the investigation of ceramic components for use in reciprocating engines has been under way all over the world since the early 1980s. The Ceramics Applications for Reciprocating Engines (CARE) programme was launched in the UK with the aim of increasing the potential for manufacture and use of ceramic engine components.

Matsui (1993) outlined the development of components for ceramic engines, gas turbines and turbochargers made in Japan at NGK. At that time ceramic turbocharger rotors, ceramic swirl chambers, ceramic rocker arm tips, ceramic ball bearings and ceramic cutting tools were all commercially available in Japan. Parts for ceramic gas turbines and ceramic engines were under development.

3.3 MANUFACTURE OF CERAMICS

The small size of the strength-limiting defects in advanced technical ceramics means they are often difficult to detect and control and, hence, one way to increase component reliability is to eliminate flaws as much as possible at the manufacturing stage.

The manufacture of ceramic components can be divided into five steps - powder production and preparation, pre-consolidation, forming, densification and finishing as shown in figure 3.3.1. Kerber and Hoffmann (1993) recognised that each

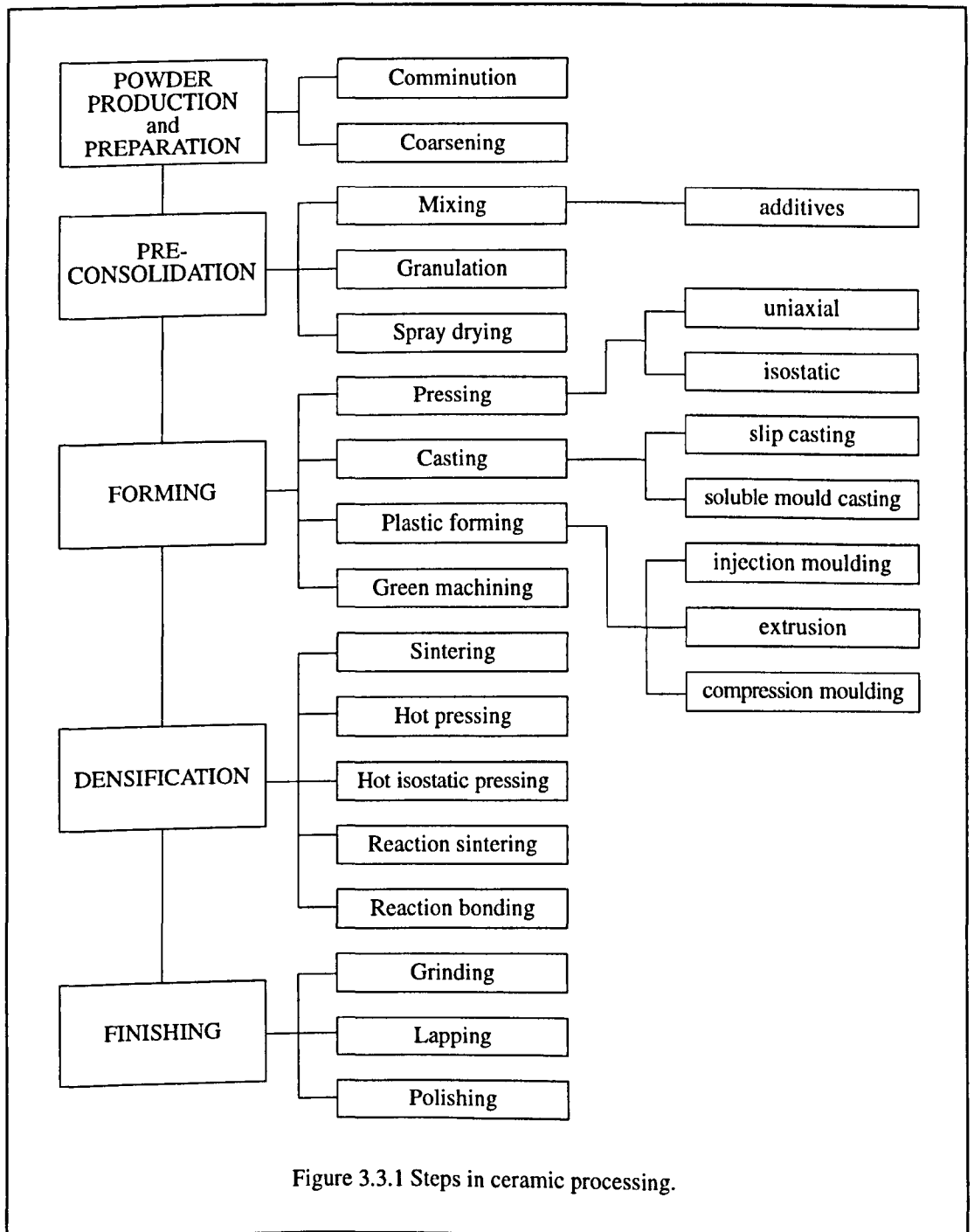


Figure 3.3.1 Steps in ceramic processing.

of the manufacturing steps can lead to different flaw populations which have consequences for the final properties of the material. Schwartz (1992) identified the potential flaws during the first four stages and these are listed in table 3.3.1. He said that the goal in powder production is to achieve the highest degree of intimate mixing; in powder conditioning, to avoid the formation of hard agglomerates; in shaping, to avoid porosity; and in densification, to avoid the formation of glassy phases at grain boundaries. The following sections consider each of the manufacturing steps in more detail.

MANUFACTURING STAGE	POTENTIAL FLAW
Powder production	unfavourable particle size, shape and distribution off composition foreign inclusions hard agglomerates
Powder conditioning (pre-consolidation)	unfavourable agglomerate size distribution hard agglomerates varying agglomerate density distribution insufficient binder organic fibre inclusions
Powder shaping (forming)	porosity, voids and cracks varying density non-uniform binder and additive distribution segregation residual binder organic inclusions
Densification	porosity, micropore clusters, voids and cracks non-uniform grain size and growth harmful grain boundary phases (glassy phases) inclusions rough surface

Table 3.3.1 Potential flaws during ceramic manufacture.

3.3.1 Powder production and preparation

The production of a ceramic powder depends on the ceramic involved. Aluminium oxide powder occurs naturally as the mineral corundum or can be produced in large quantities from bauxite by the Bayer process. Silicon carbide does not occur naturally, except in meteoric iron, but can be synthesised by the Acheson process. Silicon nitride also does not occur naturally and can be synthesised by one of several different processes, resulting in powders of various sizes and purity (Richerson, 1982).

The selection criteria for ceramic starting powders is dependent on the properties required in the finished component. The purity, particle size distribution, reactivity and polymorphic form of the powder can all affect the final properties of

the component material and must therefore be considered. The effect of an impurity on the finished material is dependent on the chemistry and relative stiffnesses of the bulk powder and the impurity and on its distribution. Impurities present as inclusions can cause stress concentrations and therefore a decrease in tensile strength. To achieve maximum particle packing during forming a range of particle sizes is required, the particle size distribution being dependent on which method of forming is used. Clearly it is important that the optimum particle size distribution is controlled and reproducible in order to achieve consistent material properties. The reactivity of the powder is important during the densification process, with very small particles with high surface area having high surface free energy and thus bonding together readily. Many ceramics occur in different polymorphic forms and for most applications one polymorph is preferred over another.

Raw materials are usually not available with the optimum particle size distribution and hence must be further processed to the required specifications. The powder can be separated into particles of a particular size or range of sizes by a process such as screening, air classification or elutriation. Often a particle size reduction step is required or, less often, a coursening step.

Kerber and Hoffmann (1993) showed examples of the possibility of reducing the defect sizes in silicon carbide, zirconia and alumina ceramics by optimising the powder production and preparation processes, thus increasing the reliability of the finished product.

3.3.2 Pre-consolidation

Before the sized powders are formed into the desired shapes they usually require special treatment or processing to achieve the required uniformity. The treatment required will depend on the method of forming used.

Additives are added to the powder for a wide variety of reasons, and can include binders, lubricants, plasticisers, deflocculants, wetting agents, water retention agents, antistatic agents, antifoam agents, foam stabilisers, chelating or sequestering agents, fungicides, bactericides and sintering aids.

Spray drying can be used to achieve a uniform free-flowing powder containing the appropriate additives, and results in a powder in which all the particles have a spherical shape, improving the flow characteristics. An alternative to spray drying is granulation resulting in harder, more dense agglomerates which are irregular in shape but with better packing properties.

3.3.3 Forming

The properly sized and pre-consolidated powders can be formed into the required shapes using one or a combination of several approaches.

Pressing is accomplished by placing the powder into a die and applying pressure to achieve compaction. Uniaxial pressing involves the compaction of powder into a rigid die by applying pressure along a single axial direction through a rigid punch, plunger or piston. Isostatic pressing involves the application of pressure equally to the powder from all sides.

The casting of ceramics is done at room temperature in an operation in which ceramic particles suspended in a liquid are cast into a porous mould which removes the liquid and leaves a particulate compact in the mould. There are a number of variations, the most common being slip casting in which the ceramic particles are suspended in water and cast into porous plaster moulds. Readey (1992) used the slip-casting of zirconia as an example of optimising the processing conditions using statistical reduction of data in a graphical format. Soluble mould casting is based on the technology of investment casting and can be used for more complex shapes.

Plastic forming involves producing a shape from a mixture of powder and additives that is deformable under pressure. About 25 to 50% volume of organic additive is required to achieve adequate plasticity for forming, and heat is usually applied in addition to pressure. The most common methods of plastic forming are injection moulding and extrusion, with the former being used for low-cost, high volume applications. The feed material is forced into a shaped tool cavity until the cavity is full and the material has knit or fused together under pressure and temperature to produce a homogeneous part. Extrusion is used extensively for elongated shapes having a constant cross-section.

Green machining can be done as an additional forming process to those previously mentioned and refers to the machining of a ceramic part prior to final densification by turning, milling, drilling or grinding. The material is much softer at this stage and can be machined much more economically. However, as the material is relatively fragile great care must be taken to avoid overstressing or damaging the material.

3.3.4 Densification

The densification of the formed ceramic part results in the removal of the pores between the starting particles, combined with growth together and strong bonding between adjacent particles. For densification to occur a mechanism for material transport must be present along with a source of energy to activate and sustain the material transport. The primary transport mechanisms are diffusion and viscous flow,

with heat the primary source of energy, in conjunction with energy gradients due to particle contact and surface tension. Richerson (1982) considered the theory and application of sintering to ceramic component manufacture.

Hot pressing uses heat and pressure, providing several processing and property advantages. The application of pressure in addition to heat results in reduced densification time, reduced densification temperature, minimised porosity and hence higher material strength.

Silicon nitride and silicon carbide can be fabricated by a process known as reaction sintering or reaction bonding.

3.3.5 Finishing

Once a ceramic material has undergone densification one or more of the surfaces will often require finishing by machining, lapping or polishing to meet dimensional tolerances, achieve improved surface finish or remove surface flaws. Ceramic materials are difficult and expensive to machine due to their high hardness and brittle nature.

3.4 FRACTURE MECHANICS OF CERAMICS

The quantitative relationships for determining the behaviour of cracked solids were initially stated by Griffith (1920) who noted that when a crack is introduced into a material a balance must be struck between the decrease in potential energy and the increase in surface energy due to the presence of the crack. Thus

$$\sigma = \left(\frac{2E\gamma_s}{\pi l} \right)^{1/2} \quad (3.1)$$

for plane stress and

$$\sigma = \left(\frac{2E\gamma_s}{\pi l(1-\nu^2)} \right)^{1/2} \quad (3.2)$$

for plane strain where

σ is the applied stress,

E is the Young's modulus,

γ_s is the specific surface energy of the crack and

l is half the crack length.

Equations (3.1) and (3.2) assume that the material is elastic and contains a very sharp crack. Irwin (1949) showed that

$$\sigma = \left(\frac{EG}{\pi l} \right)^{1/2} \quad (3.3)$$

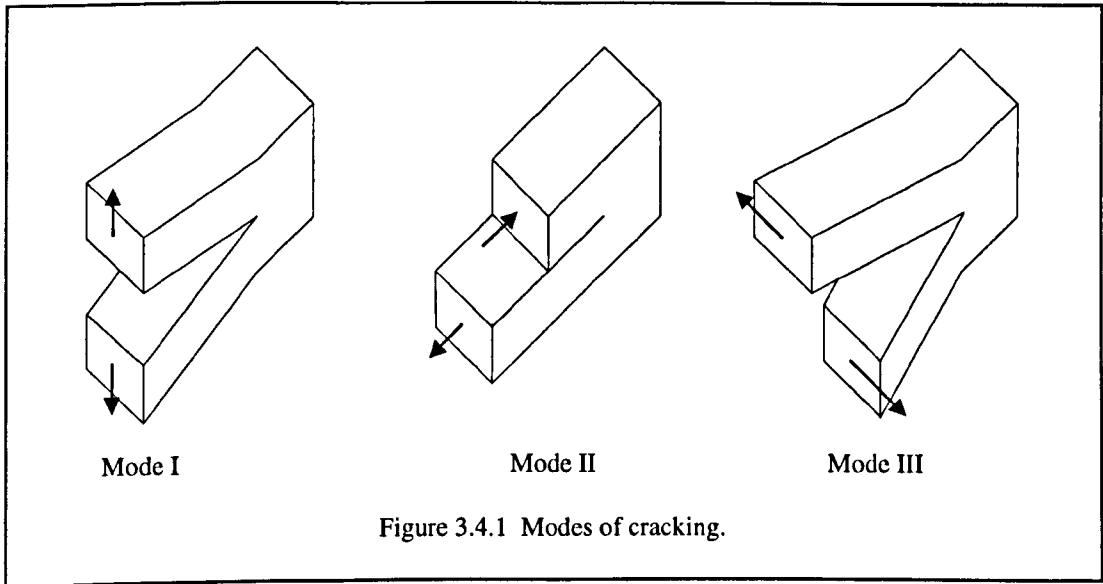


Figure 3.4.1 Modes of cracking.

where G is the strain energy release rate. At the point of instability G reaches a critical value, G_c , and fracture occurs.

Irwin (1958) later published solutions for crack-tip stress distributions associated with the three modes of loading shown in figure 3.4.1. Mode I is an opening or tensile mode, Mode II a sliding or in-plane mode and Mode III a tearing or antiplane shear mode. Mode I loading is encountered in the majority of engineering situations and hence most attention has been given to analytical and experimental methods to quantify stress/crack length relations for this mode. These have the form

$$K_{Ic} = Y\sigma_f(\pi l)^{1/2} \quad (3.4)$$

where K_{Ic} is known as the critical stress intensity factor for Mode I and is a measure of the material's toughness,

Y is a dimensionless parameter dependent on the flaw shape and test geometry,

σ_f is the fracture strength and

l is the flaw length for a surface flaw or half length for an internal flaw.

From equation (3.4) it can be seen that small flaw sizes and large fracture toughness values give high material strengths.

The fracture origin can be characterised by a flat region called the fracture mirror (Hertzberg, 1989). A general relationship between the fracture stress and mirror radius, r , has been found and is given by

$$\sigma_f r^{1/2} = A \quad (3.5)$$

where A is a constant. Combining equations (3.4) and (3.5) gives

$$Y(r/l)^{1/2} = A/K_{Ic} \quad (3.6)$$

Wills (1977) reported that the ratio A/K_{Ic} has a value of 2.35 and is independent of the material, making $Y(r/l)^{1/2}$ material independent also. He said that this is important in the fracture analysis of components where conditions responsible for failure may be known but the stress is not. K_{Ic} is a material constant, measured using fracture mechanics tests, Y calculated from a knowledge of the flaw position and shape and r determined from inspection. However, when designing with ceramic materials the fracture mechanics approach is often impractical due to the difficulty of determining or measuring the critical defect or flaw.

3.5 STATISTICAL METHODS

Statistical or probabilistic methods of failure analysis attempt to account for the scatter in strength data due to the distribution of defects on the surface or in the bulk of a ceramic material. An attempt is also made to relate the data obtained from the simple geometries and uniaxial stress states of test pieces to the more complex situation in real components. This section outlines the main statistical approaches currently being used.

3.5.1 Weibull statistics

The Weibull statistical model (Weibull, 1951) is the most commonly used approach for the analysis of ceramic materials. It is based on the weakest link theory which assumes that there is a local strength associated with each element of volume or surface in a body and that failure will therefore occur at the element with the lowest strength. For a given volume or surface of a ceramic material under uniform stress, failure will occur at the weakest flaw.

Weibull proposed the following distribution function to give the probability of failure, P_f , of a volume or surface element of material as

$$P_f = 1 - \exp \left[- \left(\frac{\sigma - \sigma_\mu}{\sigma_0} \right)^m \right] \quad (3.7)$$

where σ is the applied stress,

σ_μ the threshold stress below which the probability of failure is zero,

σ_0 is the characteristic strength of a unit volume or surface of material and

m is the Weibull modulus.

The Weibull modulus gives an indication of the consistency of the strength data. A high value of m indicates a narrow range of strength values and hence a more reliable material. The Weibull modulus is not a fundamental material property as it depends on such factors as the size and configuration of the test samples.

Equation (3.7) is known as the three-parameter Weibull equation but for most practical analyses σ_μ , the threshold stress, is taken as zero and equation (3.7) is simplified to

$$P_f = 1 - \exp\left[-\left(\frac{\sigma}{\sigma_0}\right)^m\right]. \quad (3.8)$$

This is known as the two-parameter form of the Weibull equation. Using the two-parameter equation gives more conservative results than the three-parameter equation as failure is assumed to be possible at any stress. Equation (3.8) results in a curve as shown in figure 3.5.1a. Alternatively, plotting $\ln\left[\ln\left[\frac{1}{1-P_f}\right]\right]$ versus $\ln(\sigma)$ results in a straight line of slope m as shown in figure 3.5.1b. The characteristic strength then corresponds to $\ln\left[\ln\left[\frac{1}{1-P_f}\right]\right] = 0$ and is the stress at which 63.2% of the samples fail.

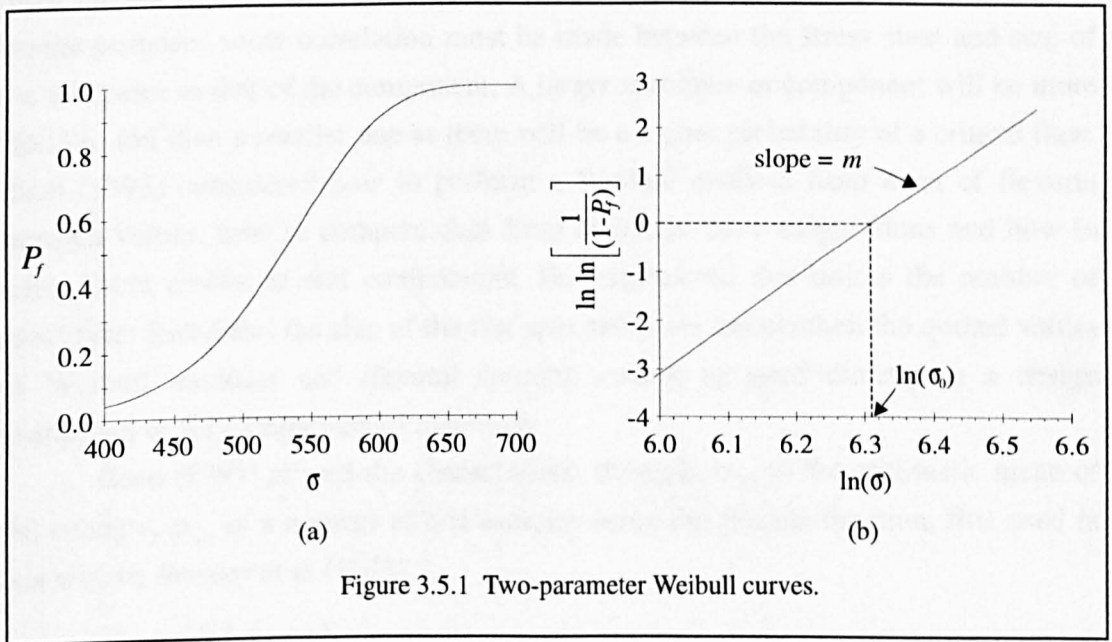
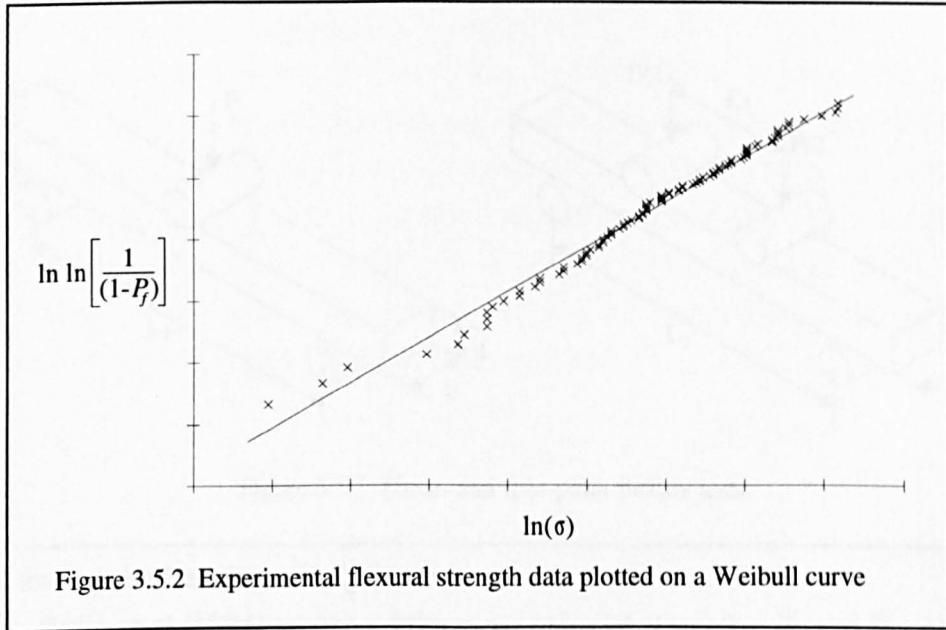


Figure 3.5.1 Two-parameter Weibull curves.

Weibull curves can be plotted from experimental data, usually using the flexural strength for σ , as in figure 3.5.2. Bergman (1986) considered four methods of obtaining the Weibull modulus from the data and concluded that nonlinear least squares analysis was the most appropriate with

$$P_f = \frac{(i-0.5)}{N_s} \quad (3.9)$$

where i is the rank of the sample when they are placed in strength order and N_s is the total number of samples.



The Weibull modulus from the two-parameter form of the equation is the value most often quoted by the ceramic material producer or supplier. However, to use this for design purposes some correlation must be made between the stress state and size of the test piece to that of the component. A larger specimen or component will be more likely to fail than a smaller one as there will be a higher probability of a critical flaw. Bush (1993) considered how to perform a Weibull analysis from a set of flexural strength values, how to compare data from different test configurations and how to relate these results to real components. He emphasised that unless the number of specimens tested and the size of the test specimens are known then the quoted values of Weibull modulus and flexural strength cannot be used directly in a design evaluation or for comparison of materials.

Bush (1993) related the characteristic strength, σ_0 , to the arithmetic mean of the strength, σ_f , of a number of test samples using the gamma function, first used in this way by Stanley et al (1973),

$$\sigma_f = \sigma_0 \Gamma\left(\frac{1}{m} + 1\right) \quad (3.10)$$

where $\Gamma\left(\frac{1}{m} + 1\right)$ is the gamma function, also written as $\left(\frac{1}{m}\right)!$. Bush related the dimensions of the samples and test configuration using the relationship outlined by Hartscock and McLean (1984) to obtain a generalised characteristic strength

$$\sigma_\sigma = \sigma_0 \left(\frac{bd}{2}\right)^{1/m} \left[\frac{L_1 + mL_2}{(m+1)^2}\right]^{1/m} \quad (3.11)$$

where σ_σ is the generalised characteristic strength and b , d , L_1 and L_2 are as shown in figure 3.5.3.

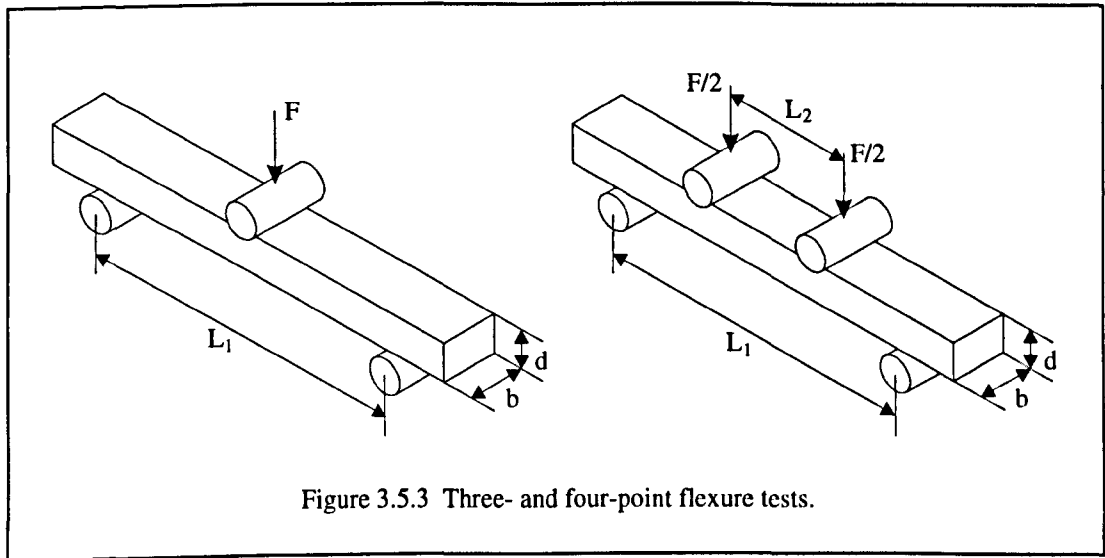


Figure 3.5.3 Three- and four-point flexure tests.

For a three point bending test L_2 is zero.

Rufin et al (1984) compared the mean uniaxial strengths, $\bar{\sigma}_1$ and $\bar{\sigma}_2$, of sets of specimens of the same material but different volumes, V_1 and V_2 , using the relationship

$$\frac{\bar{\sigma}_1}{\bar{\sigma}_2} = \left(\frac{V_2}{V_1} \right)^{1/m} \quad (3.12)$$

which does not, of course, take account of the test method.

Equation (3.8) relates to a unit volume or surface of material. To obtain the probability of failure for a component this must be integrated over the volume or surface such that

$$P_{fc} = 1 - \exp \left[- \int_V \left(\frac{\sigma}{\sigma_0} \right)^{m_v} dV \right] \quad \text{or} \quad P_{fc} = 1 - \exp \left[- \int_A \left(\frac{\sigma}{\sigma_0} \right)^{m_A} dA \right] \quad (3.13)$$

where m_v is the Weibull modulus for specimens failing from volume flaws and m_A that for surface flaws. In general $m_v \neq m_A$ as a different flaw population will control failure in each case. The integral term $\int_V \left(\frac{\sigma}{\sigma_0} \right)^{m_v} dV$ is often referred to as the risk of rupture denoted by B_v .

Hartsock and McLean (1984) said that in general the exponent should include both the volume and surface integral. Only the volume integral will be considered here but the same procedures apply to the surface form.

For uniform uniaxial tension and considering volume flaws, equation (3.13) can be written as

$$P_{fc} = 1 - \exp \left[- \left(\frac{\sigma}{\sigma_0} \right)^m V \right] \quad (3.14)$$

where V is the volume of material.

Equations (3.13) and (3.14) assume that the failure stress is the same in tension and compression which is usually not the case for ceramic materials. Bush (1993) stated that elements in compression should be excluded from any calculation as only elements under tensile stress will contribute to the failure of the component. However, Stanley et al (1973) introduced the Heaviside function, $H(\sigma)$, a step function whose value is determined by the sign of the stress under consideration, to take account of failure under compressive stress. Thus,

$$P_f = 1 - \exp \left[- \left(\frac{\sigma}{\sigma_0} \right)^m V \left(\frac{1}{H(\sigma)} \right)^m \right] \quad (3.15)$$

where $H(\sigma)$ is unity for tensile values of σ and $-\alpha$ for compressive values of σ and α is the ratio of mean failure stress of unit volume in uniaxial compression to that for uniaxial tension.

For ceramics α is usually significantly greater than unity. However, Rufin et al (1984) pointed out that in predominantly compressive stress states crack growth may not be an unstable phenomenon, therefore propagation of a single crack does not necessarily cause catastrophic failure, thus refuting one of the main assumptions of the Weibull weakest link theory.

3.5.2 Principle of independent action

The stresses in a real component will not generally be uniaxial but multiaxial, and can be characterised by three principal stresses. Stanley et al (1973) utilised a failure criterion, the principle of independent action (PIA), which assumed that the failure probability of an element due to one principal stress is independent of the other principal stresses. Therefore, equation (3.13) becomes

$$P_{fc} = 1 - \exp \left[- \int_V \left\{ \left(\frac{\sigma_1}{\sigma_0} \right)^m + \left(\frac{\sigma_2}{\sigma_0} \right)^m + \left(\frac{\sigma_3}{\sigma_0} \right)^m \right\} dV \right] \quad (3.16)$$

where σ_1 , σ_2 and σ_3 are the principal stresses. This further assumed that the material was isotropic. The authors modified the above equation to obtain a combination of non-dimensional factors such that

$$P_{fc} = 1 - \exp \left[- \left(\frac{\sigma_{nom}}{\sigma_0} \right)^m V \Sigma \right] \quad (3.17)$$

$$\Sigma = \int_V \left\{ \left(\frac{\sigma_1}{\sigma_{nom}} \right)^m + \left(\frac{\sigma_2}{\sigma_{nom}} \right)^m + \left(\frac{\sigma_3}{\sigma_{nom}} \right)^m \right\} \frac{dV}{V} \quad (3.18)$$

where σ_{nom} is a nominal stress proportional to the load on the component and Σ is known as the stress-volume integral.

They said that the stress-volume integral characterises the shape of the component and the type of loading but that it is independent of the size of the component and magnitude of the load.

3.5.3 Normal stress averaging

Multiaxial stresses can also be considered using the Weibull normal tensile stress averaging (NSA) method which can be calculated from

$$P_{fc} = 1 - \exp \left[- \int_V \left(\frac{\bar{\sigma}_n}{\sigma_{0p}} \right)^{m_v} dV \right] \quad (3.19)$$

$$\text{where } \bar{\sigma}_n^{m_v} = \frac{\int_A \sigma_n^{m_v} dA}{\int_A dA}. \quad (3.20)$$

The area integration is performed for principal stresses over the surface, A , of a sphere of small radius for regions where σ_n is tensile. The relationship between σ_{0p} and σ_0 is found by equating the failure probability for uniaxial loading to that obtained for the multiaxial stress state when the latter is reduced to a uniaxial condition. Therefore, according to Batdorf (1977),

$$\sigma_{0p}^{m_v} = \frac{1}{2m_v + 1} \sigma_0^{m_v}. \quad (3.21)$$

3.5.4 Flaw density (Batdorf) approach

One of the criticisms of the Weibull approach to predicting the failure of ceramic materials is that it is a wholly statistical approach and takes no account of the actual distribution of flaws within a material. Batdorf and Crose (1974) proposed a physically-based statistical theory which describes the material strength in terms of a flaw density function. They defined both a flaw geometry and distribution. Flaws are assumed to be flat cracks uniformly distributed in position and orientation; thus implying that flaws have associated strengths that depend on their orientations relative to the applied stresses. A crack is assumed to propagate and, hence, failure occurs when a specific stress, σ_e , exceeds a critical value, σ_{cr} , associated with that particular crack. σ_e is a function of the chosen crack configuration.

For surface distributed cracks the probability of failure of area, A , is given by

$$P_f = 1 - \exp \left[- \int_A \int_0^{\sigma_1} \left(\frac{\omega}{\pi} \right) \frac{dN}{d\sigma_{cr}} d\sigma_{cr} dA \right] \quad (3.22)$$

where σ_1 is the maximum principal stress acting in A ,

ω is the angular range in which $\sigma_e \geq \sigma_{cr}$ and

N is the density of cracks having a critical stress $\leq \sigma_{cr}$, the crack density function.

For volume distributed cracks

$$P_f = 1 - \exp \left[- \int_V \int_0^{\sigma_1} \left(\frac{\Omega}{4\pi} \right) \frac{dN}{d\sigma_{cr}} d\sigma_{cr} dV \right] \quad (3.23)$$

where Ω is the solid angle containing the normals to all orientations for which $\sigma_e > \sigma_{cr}$.

Ω depends on the fracture criterion selected, the assumed crack configuration and the applied stress state. Batdorf and Crose (1974) derived closed form expressions for Ω for analytically simple fracture criteria in uniaxial and equi-biaxial stress states. They proposed a Taylor series expression for N and later Batdorf and Heinisch (1978) proposed an expression in a simpler form as a power function of σ_{cr} .

$$N(\sigma_{cr}) = k\sigma_{cr}^m \quad (3.24)$$

where k and m are flaw distribution parameters determined from experimental data, assuming that failure data can be expressed as the two-parameter Weibull distribution.

3.5.5 Elemental strength approach

A multiaxial elemental strength approach was proposed by Evans (1978) based on work by Matthews et al (1976). This approach used concepts of non-coplanar crack extension related to strain energy release rates in fracture mechanics. In this approach the probability of failure is calculated using the following equation

$$P_f = 1 - \exp \left[- \left(\int_V dV \int_0^S g(S) dS \right) \right] \quad (3.25)$$

where V is the volume,

S is the observed strength and

$g(S)$ is the number of flaws with strength between S and $S+dS$.

$g(S)$ characterises the distribution of flaws within the material. It is derived from strength data from specimens with well-defined geometries and stress states and applied to components of the same material. Figure 3.5.4 shows the steps in determining $g(S)$ and the probability of failure using this approach. The local stresses acting on the flaws are determined from the principal stresses, σ_1 , σ_2 and σ_3 , in terms of a normal tensile stress, σ , and a shear component, τ . The response of the flaws to the mixed-mode conditions induced by the local stress field is based on the maximum strain energy release rate, G_{max} , in the direction of crack propagation, given by

$$G_{\max} = \frac{(1+\nu)(1+\chi)}{4E} [K_I^4 + 6K_I^2 K_{II}^2 + K_{II}^4]^{1/2} \quad (3.26)$$

where E is the Young's modulus,

$\chi = (3-4\nu)$ for plane strain conditions and $(3-\nu)(1+\nu)$ for plane stress and

K_I and K_{II} are the mode I and mode II stress intensity factors, respectively.

The fracture criterion uses the equivalent stress, σ_E , as a combination of the local stresses, σ and τ , expressed by

$$\sigma_E = (\sigma^4 + 6\sigma^2\tau^2 + \tau^4)^{1/4}. \quad (3.27)$$

The equivalent stress is then expressed as a function of the principal stresses. Failure is assumed to occur when σ_E reaches a critical value S_E dictated by G_{\max} . The flaw density function, $g(S)$, and the failure probability are derived from the distribution of the equivalent strength, S_E . Lamon and Evans (1983) described this process in greater detail.

Lamon (1988) claimed that the elemental strength approach more accurately predicted the biaxial strength of an alumina ceramic based on uniaxial strength data than either the Weibull/PIA approach or Batdorf flaw density approach. His main criticisms of the latter approach were its complexity and that it failed to take account of multiple flaw populations. However, Chao and Shetty (1990) refuted these conclusions and showed that the flaw density approach and the elemental strength approach give identical predictions of failure despite some fundamental differences in methodology.

3.5.6 Matsuo's approach

Uchimura et al (1992) reported on the comparison of several fracture criteria for multiaxial stress states using Matsuo's multiaxial fracture

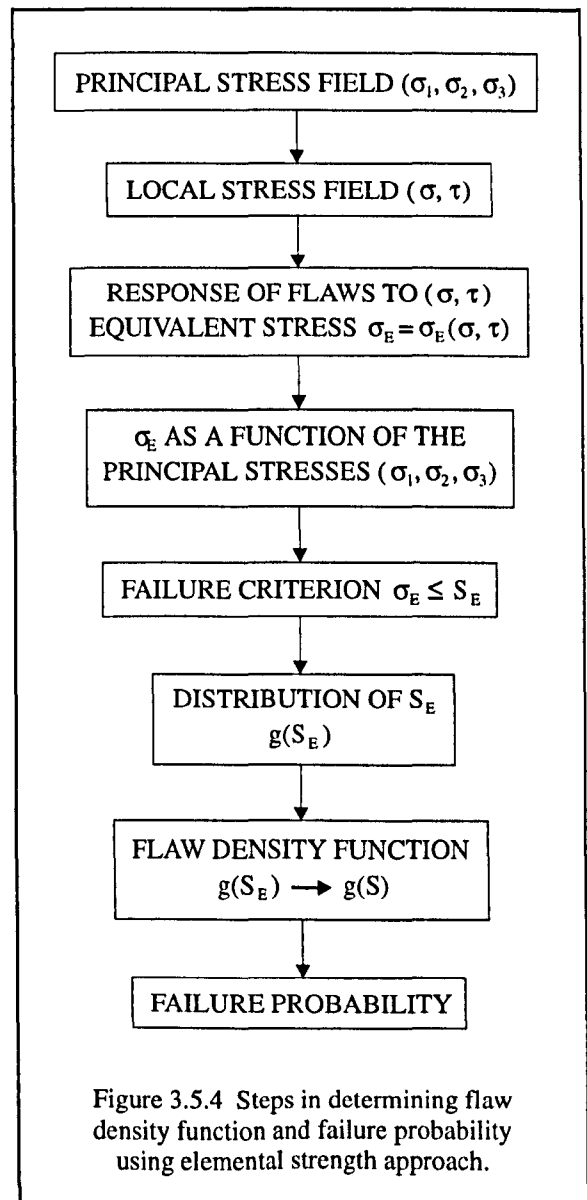


Figure 3.5.4 Steps in determining flaw density function and failure probability using elemental strength approach.

probability distribution function (Matsuo, 1980, in Japanese). Matsuo's function is a modification of the Weibull approach taking the direction of a crack into account and allows different fracture criteria to be used. They considered both surface and volume flaws in silicon nitride tensile-torsional specimens but admitted that for many specimens the fracture origin was difficult to detect.

3.5.7 Assumptions inherent in statistical methods

In principle, the statistical methods described above allow extrapolation of data obtained from test pieces to the calculation of failure probabilities of loaded components of different volumes and areas. Several assumptions are made when using these approaches. All of the methods, with the possible exception of Matsuo's, assume that the strength distribution of the samples can be described by the two parameter Weibull function (equation (3.8)). Other assumptions are that:

- i) the material is isotropic and homogeneous,
- ii) the defects are randomly distributed,
- iii) the defects are small relative to the specimen or component size,
- iv) there is a statistically significant number of defects within the specimen or component,
- v) an initiated crack will propagate without further increase in load,
- vi) flaws do not interact,
- vii) the defect populations do not vary with time,
- viii) the component exhibits the same flaw size distribution as the test bars,
- ix) the component possesses the same mechanical properties as the test bars,
- x) the stress distribution in the entire component is known,

3.6 MECHANICAL PROPERTY DATA

All methods of ceramic component analysis rely on data from test specimens to determine mechanical property data. As a result of the statistical variation of flaws within a ceramic material a large number of strength tests needs to be conducted to obtain statistically valid data. At present the available data on engineering ceramics are generally of inadequate quantity and quality to allow a proper evaluation or comparison between materials. They are generated from a variety of test methods, usually without sufficient supporting information.

3.6.1 Uniaxial testing methods

Flexure testing is the most usual method of measuring the strength of an advanced engineering ceramic. A beam specimen is placed in either a three- or four-point

loading fixture and loaded to fracture. See figure 3.5.3. The maximum stress in the specimen is calculated from simple beam theory assuming linear elastic material properties. For a three-point flexure test the maximum stress in the specimen is given by

$$\sigma_{\max} = \frac{3 FL_1}{2 bd^2} \quad (3.28)$$

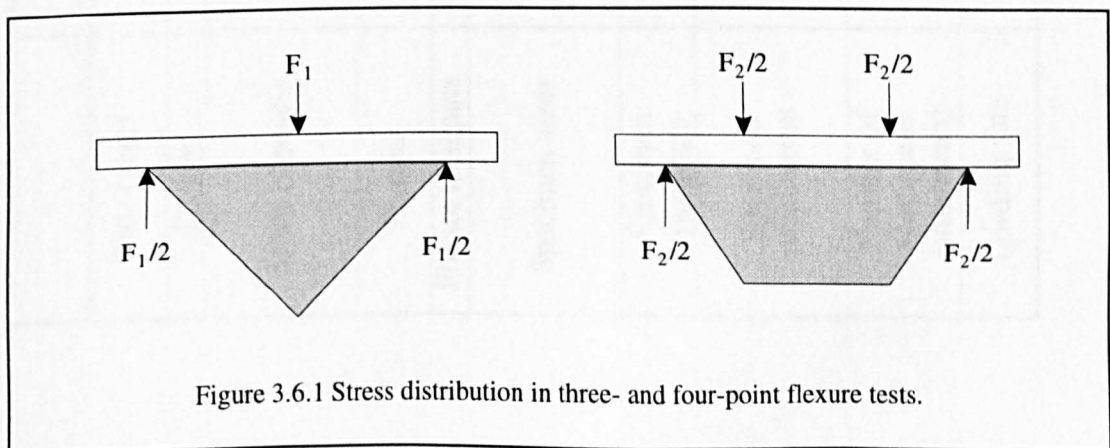
and for a four-point test by

$$\sigma_{\max} = \frac{3 F(L_1 - L_2)}{2 bd^2} \quad (3.29)$$

where L_1 , L_2 , b , d and F are as shown in figure 3.5.3.

Specimen cross-sections differ in size and shape, they are usually rectangular or square, occasionally circular and sometimes trapezoidal or triangular. Quinn and Morrell (1991) reviewed the development of standard test methods which have evolved in different countries for measuring the flexure strength of engineering ceramics. The principal features of the various standards are shown in table 3.6.1. There are many similarities between the standards: the specimen and fixture sizes are quite comparable and many tolerances and specifications are identical. However, there are several important differences and all have the restriction of being applicable only to linearly elastic materials.

The three-point configuration results in higher strength values than the four-point test. Figure 3.6.1 shows the approximate stress distribution on the tensile surface in each case and, as can be seen, a greater amount of material is at the maximum stress in the four-point test and hence the specimen is more likely to fail from a critical flaw. A larger specimen is also more likely to contain a critical flaw than a smaller one. Richerson (1982) compared the results from flexure tests on identical specimens of silicon nitride and reported an average strength of 930 MPa from three-point tests and 724 MPa from four-point tests: an apparent reduction of 22%. Quinn and Morrell (1991) reported that some manufacturers use very small



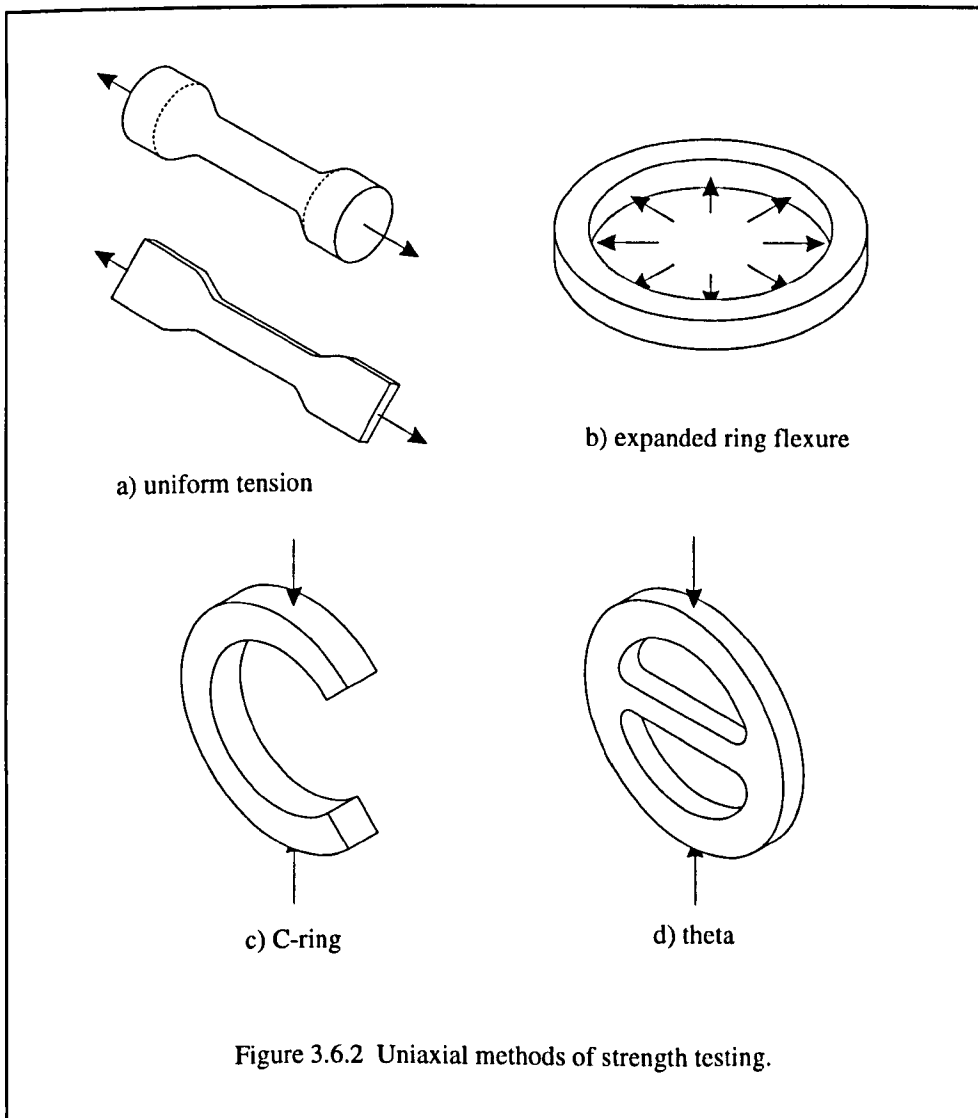
	United States	Japan	Germany	France
Title (year)	MIL-STD 1942 (1983) ASTM C 1161 (1990)	JIS R 1601 (1981)	DIN 51 110 Part 1 (1989)	AFNOR B41-104 (1989, tentative)
Fixture	3 or 4 point	3 or 4 point	4 point	3 or 4 point
Spans (4 point)	10 x 20 mm 20 x 40 mm 40 x 80 mm 0.75 x 1.5 in*	10 x 30 mm	20 x 40 mm	10 x 20 mm 20 x 40 mm
Fixture	Semiarticulating or fully articulating	Fixed	Fully articulating	Fully articulating
Fixture load pins	Rotating	Fixed	Rotating	Rotating
Specimen sizes	1.5 x 2 x 25 mm 3 x 4 x 45 mm 6 x 8 x 85 mm 0.13 x 0.25 x 2 in	3 x 4 x 35 mm	3 x 4 x 45 mm	2 x 4 x 25 mm 3 x 4 x 35 mm
Specimen chamfers	up to 0.15 mm	up to 0.3 mm	up to 0.3 mm	up to 0.3 mm
Specimen preparation	a) as fired b) application matched c) three steps prescribed d) other	a) as fired b) polished	a) as fired b) three steps prescribed (wheels, grits, rates etc)	a) polish, deeply tensile face b) grinding optional c) other
Number of specimens (minimum)	10 for mean, 30 for Weibull analysis	10	15, preferably 30	10
Loading rate	0.5 mm/min	0.5 mm/min	5 - 10 s	0.2 mm/min 0.5 mm/min (or higher)

Table 3.6.1 Flexure testing standards

specimens in three-point loading to give very high strengths for their materials. It is therefore important that until standard testing methods are more widely used manufacturers give details of the specimens and test configurations relevant to their strength data. Bell (1988) reported that of the many published papers giving results from flexural tests of ceramics very few give details of the test apparatus used.

One reason for the popularity of the flexure test method is the difficulty of conducting direct tensile tests on advanced ceramic materials. Tensile specimens are more complex in shape and therefore more difficult and expensive to produce (see figure 3.6.2a). In addition, the test apparatus must be very precisely aligned so as not to introduce any bending stresses into the specimen. However, the specimen experiences a uniform maximum stress throughout the volume and hence is more likely to fail. At present there are no standards for ceramic tensile tests.

Sheshadri and Srinivasan (1981) developed an analytical procedure to determine the Weibull parameters using the expanded ring flexure test shown in figure 3.6.2b. They assumed that the non-uniform circumferential tensile stress



distribution controlled failure and considered both volume and surface flaw populations. They did not assume that the threshold stress, σ_μ , in the Weibull distribution (equation 3.7) was always zero. They showed that this test more closely simulates tensile strengths compared to three- and four- point flexure tests but did not consider how to conduct the tests in practice.

Ferber et al (1986) considered the c-ring specimen configuration shown in figure 3.6.2c. Two different approaches were used to calculate the stress distribution in the c-ring both of which gave very similar results. The tangential component of stress was shown to be dominant, failure occurring approximately 90° from the load points. They compared results from four-point bend bars and c-rings for silicon nitride and found that different flaw populations controlled failure in each case.

Other methods of measuring the uniaxial tensile strength of advanced engineering ceramics reported in the literature include a hydrostatic test and the theta test (figure 3.6.2d). The former consists of a thin-walled cylinder with a hydrostatic load applied to the inside; the latter of a specimen as shown. When a compressive load is applied to the arches the crossbeam is put in uniaxial tension. However, very little testing has been conducted with these configurations, largely due to the difficulty of making the specimens.

3.6.2 Biaxial/multiaxial tests

At present very little data is available for biaxial testing of ceramics. This data is required if confidence in the use of statistical methods is to be increased. The most popular method appears to be biaxial flexure which has the advantage that edge effects are not significant.

Giovan and Sines (1979) tested the uniaxial and equi-biaxial tensile strengths of alumina in order to compare the validity of various fracture theories. They used four-point line loaded plates for the uniaxial tension specimens and concentric ring-on-ring loading to obtain equi-biaxial tension (figure 3.6.3c). Plates were used rather than bars so that both sets of specimens had the same volume, surface area and stress gradient. The maximum equi-biaxial stress inside the inner load ring is given by

$$\sigma_{\max} = \frac{3F}{2\pi t^2} \left[(1-\nu) \frac{R_s^2 - R_l^2}{2R_s^2} \cdot \frac{R_s^2}{R^2} + (1+\nu) \ln \frac{R_s}{R_l} \right] \quad (3.30)$$

where R_s is the radius of the support ring,
 R_l is the radius of the load ring,
 R is the radius of the specimen and
 t is the thickness of the specimen.

They found that the principle of independent action over-estimated the biaxial strength, the Weibull normal stress averaging method under-estimated it but that the Batdorf flaw density approach gave the best agreement with the experimental data.

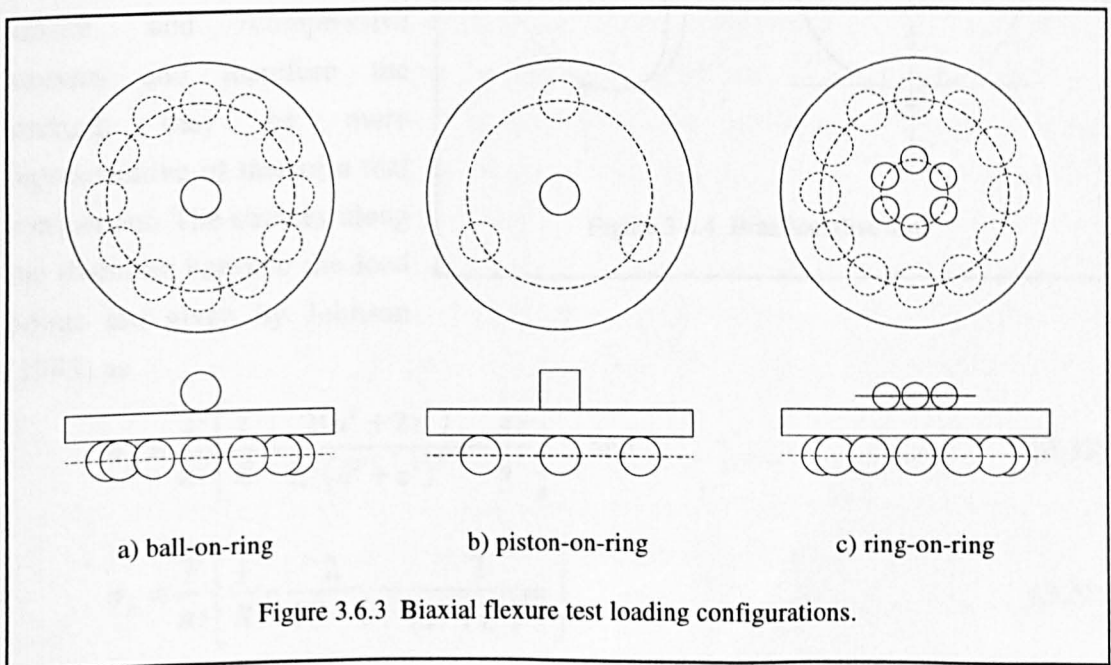
Shetty et al (1980) compared three loading schemes that produce biaxial tension in flat plate specimens. These were: ball-on-ring, piston-on-3-ball and ring-on-ring tests (see figure 3.6.3). In all the tests incorporating a ring a circular ball bearing race with freely moving balls was used to minimise frictional effects. For the ball-on-ring test the maximum equi-biaxial stress occurs at the centre. Shetty et al quoted it as

$$\sigma_{\max} = \frac{3F}{4\pi t^2} \left[1 + 2 \ln \frac{R_s}{\bar{R}} + \frac{(1-\nu)}{(1+\nu)} \left\{ 1 - \frac{\bar{R}^2}{2R_s^2} \right\} \frac{R_s^2}{R^2} \right] \quad (3.31)$$

where \bar{R} is the radius of uniform loading at the centre. In practice the ball does not produce a uniform load but a Hertzian distribution where the pressure is a maximum at the centre and decreases to zero at the edge. They suggested calculating \bar{R} from the Hertzian contact radius, a , using the relationship given by Roark and Young (1975) as

$$\bar{R} = (1.6a^2 + t^2)^{1/2} - 0.675t \quad (3.32)$$

The ball-on-ring test can be thought of as being equivalent to three-point loading and the ring-on-ring as equivalent to four-point loading in the uniaxial case. This would appear to suggest that the ring-on-ring test would be the better test as a greater amount of material experiences the maximum stress. However, Shetty et al (1980) reported that a stress magnification effect occurs in the annular region under the loading ring which is in the region of 20% and therefore the area of the specimen



experiencing the maximum stress is not as great as would appear from equation (3.30) and, more importantly, the maximum stress is impossible to determine analytically. A similar criticism was aimed at the piston-on-3-ball test: the initial uniform load under the piston becomes annular as the plate deflects. They therefore concluded that the ball-on-ring configuration gave the most satisfactory results due to the uncertainties in determining the fracture stresses in the other cases.

Godfrey (1986) used ring-on-ring tests to measure the biaxial strengths of silicon nitride, alumina and zirconia. He compared the experimental results with predictions from three-point bend specimen data and the stress volume integral approach of Stanley et al (1973), using FEA to determine the stress volume integrals. He obtained a poor prediction of biaxial flexure strength concluding that this was due to the weakening effect of biaxial stressing. However, the principle of independent action is inherent in this approach, the results confirming those of Giovan and Sines (1979), that it does not adequately predict failure in biaxial stress states.

Morrell (1989) reported on several other configurations for biaxial bend tests, including a three ball support with a single, flattened ball load and a uniform pressurised loading with ring support. However, he concluded that the variety of biaxial flexure tests needs to be restricted to one or two which are convenient to use and have well-defined stress fields.

Figure 3.6.4 shows a disc specimen loaded in diametral compression, the so-called Brazilian disc test. In this specimen a flaw will be exposed to a combination of tensile and compressive stresses and therefore the strength may be more representative of that of a real component. The stresses along the diameter between the load points are given by Johnson (1985) as

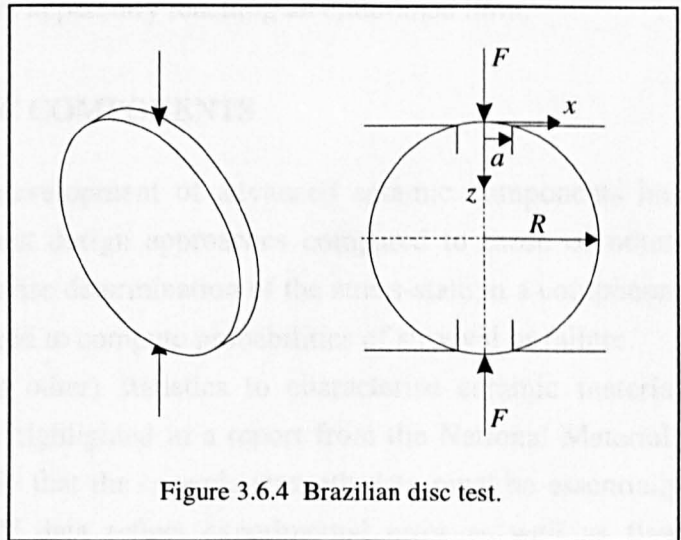


Figure 3.6.4 Brazilian disc test.

$$\sigma_x = \frac{F}{\pi t} \left[\frac{1}{R} - \frac{2(a^2 + 2z^2)}{a^2(a^2 + z^2)^{1/2}} + \frac{4z}{a^2} \right] \quad \text{and} \quad (3.33)$$

$$\sigma_z = \frac{F}{\pi t} \left[\frac{1}{R} - \frac{2}{2R - z} - \frac{2}{(a^2 + z^2)^{1/2}} \right] \quad (3.34)$$

where a is the Hertzian contact half-width and
 z is the distance into the disc.

Other reported biaxial tests include combined tension/torsion and compression/torsion tests on cylindrical silicon nitride specimens by Kokaji et al (1992) and a combined tension/torsion test on thin-walled alumina tubes by Kim and Suh (1992). Impact testing of ceramics has also been reported but is not considered here.

3.6.3 Fatigue testing

Many ceramic components, for example pistons, valves, turbine blades, are subjected to cyclic loading. The relevant design data for numerous metals has existed for many years. However, as with other material properties, there is very little usable fatigue data for ceramic materials as the results are controlled by process route as well as environment and surface condition. Until relatively recently it was generally assumed that ceramic materials were not subject to cyclic damage. However, in the last few years several studies have shown that fatigue damage does occur. See for example Guiu et al (1991), Liu and Chen (1991), Suresh (1991) and Yanagi et al (1992). Buxbaum et al (1994) investigated the fatigue behaviour of several alumina and silicon nitride ceramics and, in common with other authors, their tests resulted in extremely flat S-N curves without apparently reaching an endurance limit.

3.7 DESIGN OF CERAMIC COMPONENTS

Experience gained during the development of advanced ceramic components has highlighted the need for different design approaches compared to those of other, more traditional materials. A precise determination of the stress-state in a component and a statistical analysis is required to compute probabilities of survival or failure.

The use of Weibull (or other) statistics to characterise ceramic material behaviour introduces a problem highlighted in a report from the National Materials Advisory Board in 1980. Namely that the ceramic strength data must be essentially free from experimental error. If data reflect experimental error as well as flaw variability, the resulting statistical description of the ceramic will be incorrect and any stressed component designed on the basis of the description will perform unreliably.

Quinn and Morrell (1991) considered a number of examples of good correlation between flexure test results and component results. They said that these successful studies often were rigorously conducted since they were part of studies to validate brittle material design methodology. The investigations were cognizant of

the limitations of using flexure data for design, and they took precautions to avoid the pitfalls. Fractography was almost always a key ingredient in these studies. The research and development programs attempting to incorporate engineering ceramics into heat engines have gained much useful experience. One of the conclusions of the Ceramic Applications in Turbines (CATE) program was that successful ceramic components for an engine must be designed based upon realistic material properties determined from actual components not solely determined from test bars. Quinn and Morrell (1991) reported that the German advanced ceramics for gas-turbine engines program reached a similar conclusion.

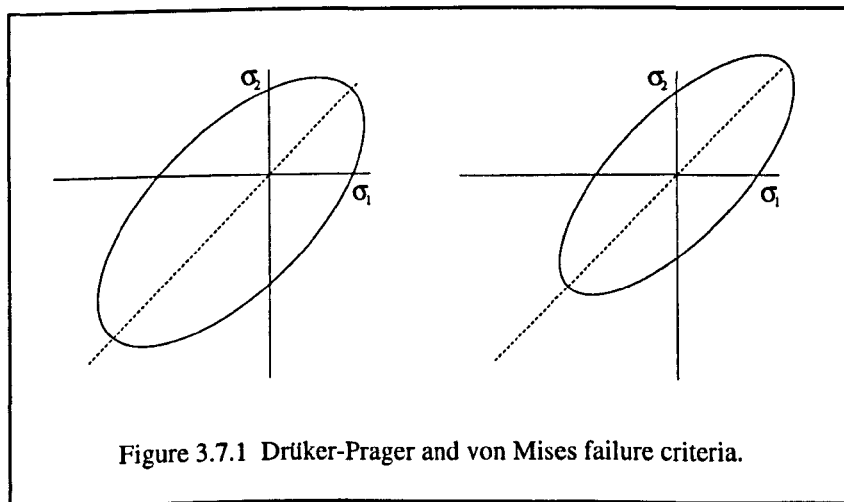
In a failure criterion for ceramics the difference between large uniaxial compressive strengths and relatively low uniaxial tensile strengths must be taken into account. For this reason Sinnema (1989) suggested the use of the failure criterion of Drüker and Prager that has its origin in soil mechanics in place of the more common von-Mises criterion used in metal design. The yield criterion is given by

$$\sigma_{dp} = \frac{\alpha}{3}(\sigma_1 + \sigma_2 + \sigma_3) + \left[\frac{1}{2} \{ (\sigma_1 - \sigma_2)^2 + (\sigma_2 - \sigma_3)^2 + (\sigma_3 - \sigma_1)^2 \} \right]^{1/2} \quad (3.35)$$

where σ_1 , σ_2 and σ_3 are the principal stresses and

α is a factor based on the relative tensile and compressive stresses.

For biaxial stress the material will survive if the stress state is inside the boundary in figure 3.7.1. For comparison the von-Mises criterion will result in the ellipse as shown or, for triaxial stress, a cylinder inclined to the σ_1, σ_2 plane.



3.7.1 Application of statistical methods

The literature provides a number of examples where uniaxial test specimen data is compared with the results from one or more of the statistical methods for more complex test specimens or real components. Finite element analysis (FEA) provides

the ideal method to obtain the stress distribution in a ceramic specimen or component, the material is already discretised into elements of known volume (or area) and stress and several authors have reported on computer programs which perform one or more of the above statistical analyses using the output from FEA as input.

Rufin et al (1984) compared the Weibull/PIA and Batdorf models with experimental data for volume distributed flaws in alumina discs subjected to a uniform pressure and mounted on a ring support. They used the relationship $P_f = i/(n+1)$ to rank the samples and output from finite element analysis as input to the analytical models. They concluded that the Batdorf model produced significantly more accurate results than the Weibull/PIA model for the particular material under the specified state of stress. They said that this confirmed the results of Giovan and Sines (1979) for alumina discs tested in ring-on-ring formation. The Weibull/PIA model produces non-conservative results, probably due to the fact that it neglects shear stresses and combined effects of the principal stresses.

An investigation to compare the results from three-point bend tests and alumina ring specimens of two sizes with predictions using the Weibull/PIA approach was reported by Rolf and Weyand (1985). They obtained a very good agreement for the smaller specimens and good agreement for the larger specimens.

Kawamoto et al (1986) reported on flexural, tensile and torsional tests applied to silicon nitride, giving the configurations of the specimens used. They also tested ring and flexure specimens cut from silicon nitride swirl chambers in order to compare degradation of strength during service but no attempt was made to correlate the data from the different tests.

Kleer et al (1986) performed strength tests on small 4-point bend specimens and larger, tubular components tested in uniaxial tension in an attempt to check the validity of the size effect. All the specimens were of extruded silicon carbide. They found that the fracture strength of the tubes predicted from the bend test specimens was considerably higher than that measured and concluded that different flaw distributions lead to failure in each case.

Analytical failure probability studies for an anisotropic cylinder subjected to internal pressure and a radial temperature gradient were presented by Stanley (1986). In the same paper he combined the failure probabilities from a surface area strength formulation and a volume strength formulation using the following equation

$$P_{fc} = 1 - (1 - P_{fA})(1 - P_{fV}) \quad (3.36)$$

where P_{fA} and P_{fV} are the cumulative probabilities of failure from surface and volume flaws respectively. He presented results from an experiment to determine P_{fA} and P_{fV} using graphite.

Shetty (1987) reviewed several mixed-mode fracture criteria used in reliability analyses of alumina and concluded that no single criterion could adequately account for all experimental results. He conducted tests in an inert N₂ environment and water and found the failure criteria to be conservative in the former case but less clear in the latter, probably due to subcritical crack growth in water. More recently Chao and Shetty (1991) used the uniform-pressure-on-ring configuration to compare results from uniaxial (three and four point bending) and biaxial flexure tests on aluminium and silicon nitride with predictions using the flaw density approach. They obtained good agreement between experiment and prediction but used a different fracture criterion and flaw shape for each material concluding that one method is not applicable to all materials as different flaw populations control failure.

Stürmer et al (1990) reported on the development of the computer code CERITS for the reliability analysis of ceramic components. The code used the Batdorf flaw density approach for volume flaws and was used to calculate the reliability of a silicon carbide flame tube segment.

A further problem was encountered by Thiemeier et al (1991) when they compared the results of several different failure criteria for aluminium nitride four point bend tests and concentric ring-on-ring specimens for surface flaws. They concluded that the selection of a unique fracture criterion for multimodal loading proved to be difficult as the difference between the various fracture criteria was small compared to the statistical uncertainty of the Weibull parameters. They suggest that the use of a test such as the Brazilian disc test, in which one of the principal stresses is negative, may prove to be more useful as the criteria become more discriminative with mixed tension and compression.

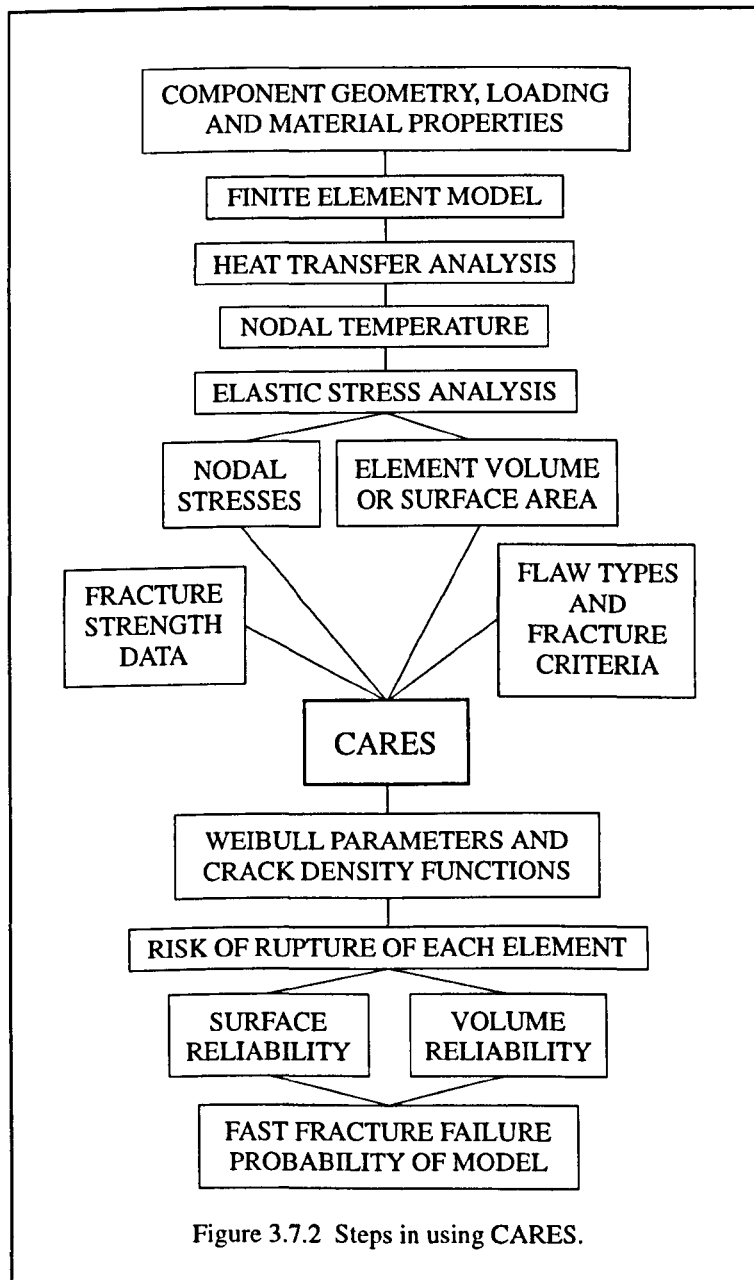
Bush (1993) used finite element analysis to calculate the stresses in a valve seat ring and a computer program to calculate the probability of failure. He then compared two candidate materials their suitability. However, he does not say which stress he used for σ and his example calculations contain several numerical errors.

Andreasen (1994) reviewed the Batdorf approach and the elemental strength model and compared them with the two-parameter Weibull model which included multi-axial stress states and concluded that the methods are equivalent. He used the results from FEA to obtain the probability of fracture for a component of arbitrary shape and loading but concluded that proof-testing components is the best method of obtaining strength data.

Nemeth et al (1989) reported on a public domain computer program developed at the NASA-Lewis Research Centre with the acronym CARES (Ceramics Analysis and Reliability Evaluation of Structures). The program predicts the failure

probability of isotropic ceramic components using test specimen data and finite element analysis output. The three sections of the program consist of: a statistical analysis of the data from the fracture of simple uniaxial or flexural specimens, an estimation of the Weibull and Batdorf (flaw density) parameters from this data and a reliability analysis of the component knowing the stress distribution. The latter uses FEA output from the MSC/NASTRAN or ANSYS programs. The elemental strength approach is not included.

Figure 3.7.2 shows the stages in a typical reliability analysis. Figure 3.7.3 shows the fracture criteria and crack geometries available for surface and volume flaws though the authors recommended the use of the Batdorf method as it combines the use of linear elastic fracture mechanics with the Weibull weakest link theory.



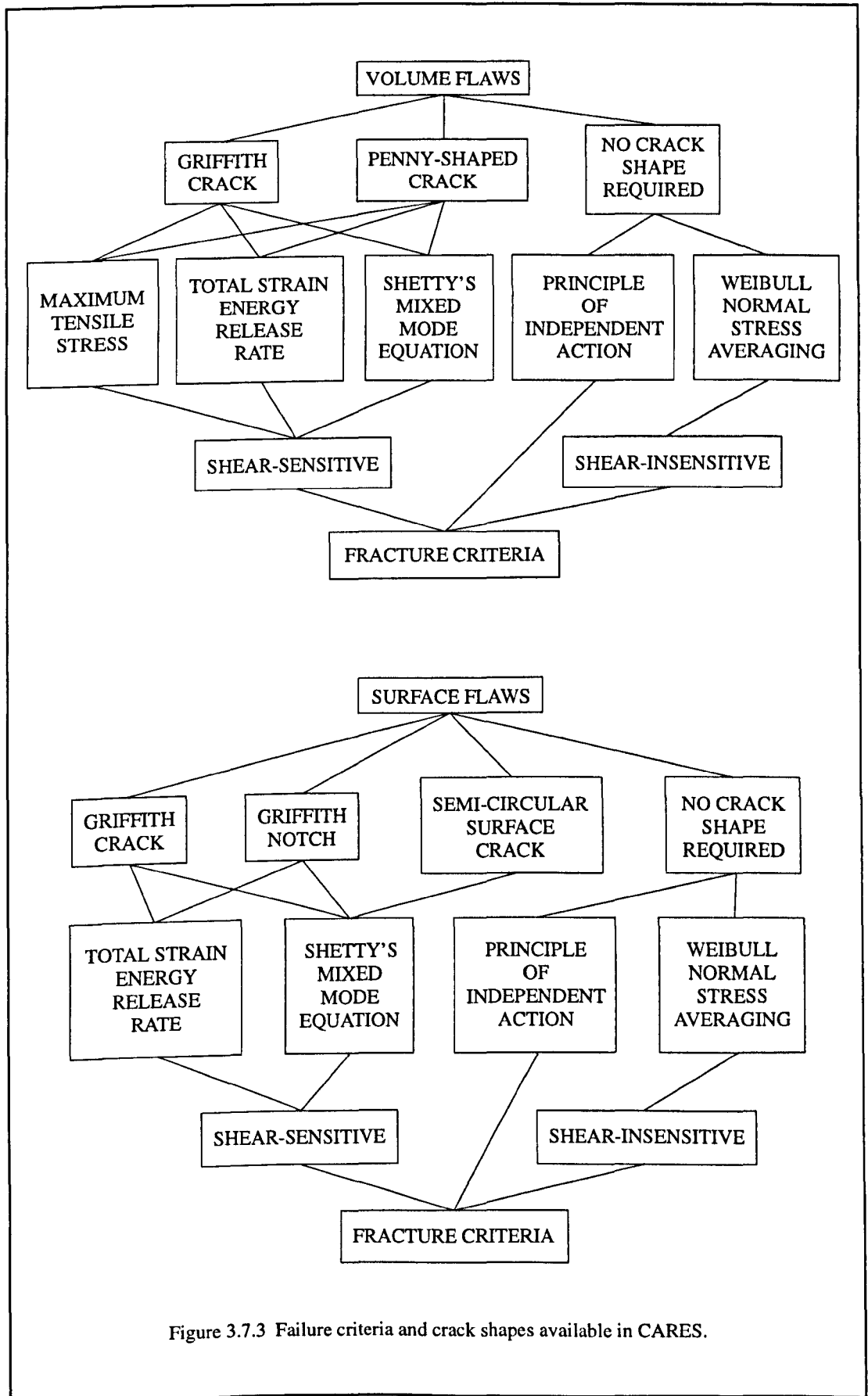


Figure 3.7.3 Failure criteria and crack shapes available in CARES.

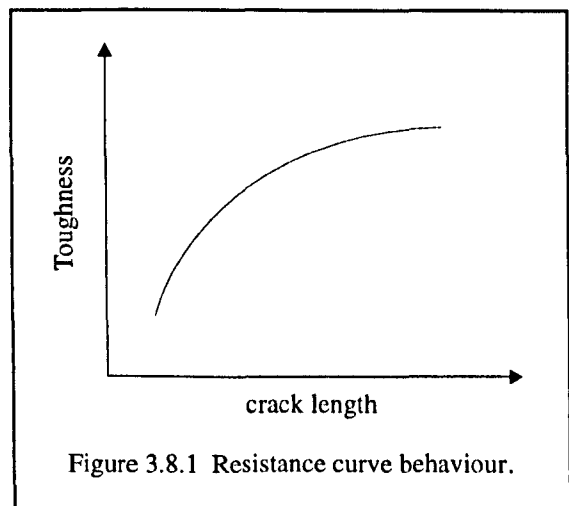
Salem et al (1991) described all the steps in calculating the reliability of a silicon nitride combustor in a ceramic gas turbine engine including materials processing, mechanical property determination, FEA and the use of CARES with various fast fracture criteria. They concluded that censoring of volume and surface flaws was essential but that bend tests did not provide sufficient volume fracture data for the analysis and that tensile testing would therefore be required.

3.7.2 Component testing

Currently the only way to ensure the quality of a component is to actually test it. Until a material has developed a reputation or history of consistency it is necessary to test components, either to failure to verify the design analysis or in a proof-testing mode to assure an operational capability. Several authors have included proof testing as part of their development program. It is essential to load the components in the same mode as they will experience in service but this will not always be feasible. Thermal or vibrational stresses are difficult to simulate. It is hoped that non-destructive evaluation can ultimately play a strong role.

3.8 TOUGHENED CERAMICS

Much of the research concerning advanced technical ceramics is concerned with the improvement of reliability. There are two main approaches to this. The first seeks to control and therefore minimise processing flaws, as described in Section 3.3, and the second to increase the toughness of the material by creating a microstructure with sufficient fracture resistance that the strength is insensitive to the size of the flaws. The latter approach has the advantage that appreciable processing and postprocessing damage can be tolerated without compromising structural reliability. In most cases, toughening results in resistance curve characteristics where the fracture resistance increases with crack extension as shown in figure 3.8.1. The increase in toughness with crack extension causes an increase in crack resistance. This 'resistance curve' or 'R-curve' behaviour profoundly affects the strength of components made from such ceramics and also has consequences for the analysis of such components as non-linear approaches are required to characterise the material behaviour (Evans, 1990). Toughening



mechanisms include transformations, microcracking, twinning, ductile reinforcements, fibre/whisker reinforcements and grain bridging. Evans (1990) considers each of these mechanisms in some detail.

Heuer et al (1988) said that transformation plasticity, being basically irreversible, might be expected to lead to severe fatigue effects and that this has been found to be the case. The ramifications of transformation toughening, in fact of all resistance curve behaviour, on Weibull statistics are as yet unresolved. Only transformation toughening will be considered here.

3.8.1 Transformation toughening.

Transformation toughening can be regarded as a process dominated by a volume increase. Its principle rests on the process of dispersing superfine particles that are able to undergo a stress-induced energy-consuming phase-transformation into a ceramic matrix.

Claussen et al (1976) were the first to investigate on a scientific basis the transformation-toughening of oxide ceramics as a brittleness-reducing principle. Work by Dworak et al (1977, 1978) was the first to document a simultaneous increase in strength and reduction in brittleness while avoiding microcracks by dispersing fine particles of zirconia in alumina. Birkby and Hodgson (1991) described transformation toughening in magnesia-partially-stabilised zirconia (MgO-

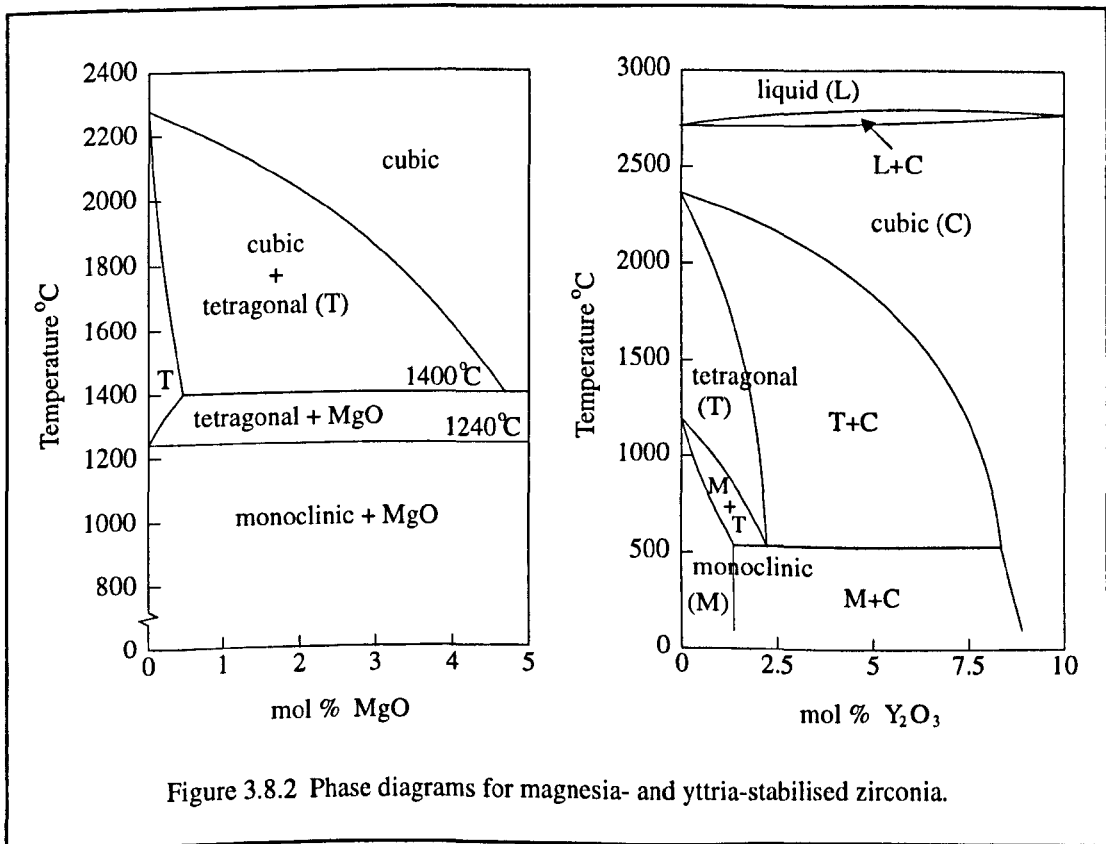


Figure 3.8.2 Phase diagrams for magnesia- and yttria-stabilised zirconia.

PSZ) and yttria stabilised tetragonal zirconia polycrystals (Y-TZP). The high strength and toughness results from the stress-induced martensitic transformation of tetragonal zirconia ($t\text{-ZrO}_2$) precipitates to monoclinic symmetry in the cubic zirconia ($c\text{-ZrO}_2$) matrix (see figure 3.8.2). Heuer et al (1988) described how the high toughness derives from the 'wake' of transformed particles adjacent to crack surfaces. As the crack penetrates the matrix containing transformed particles, the transformation is induced by the high stresses ahead of the crack tip. This wake of transformed particles can extend to a distance of 1-2 mm in the toughest samples and exerts compressive transactions on the crack surface thus shielding the crack from the applied stresses.

3.9 NONDESTRUCTIVE EVALUATION

Nondestructive evaluation (NDE) includes all physical testing methods for detecting defects in a material or component without in any way damaging it. The aim of NDE is to detect defects. Whether the defect is defined as a flaw, creating a substantial risk of failure, is determined by its nature and size.

The applicability of non-destructive tests to ceramic components can be assessed on the basis of four criteria: the nature and size of the defect, the properties of the ceramic material, the type of ceramic component and the test conditions (laboratory or production line). Edwards (1989) considered various conventional and new NDE methods and their applicability in the detection of flaws in ceramic materials. He concludes that neither conventional NDE methods nor the new test methods meet all the requirements for quality control of ceramic components. Conventional NDE methods cannot provide the level of sensitivity required without considerable refinement - he does consider several refinements - while the new methods need to be more practical to meet the needs found in an industrial environment.

X-ray radiography can detect differences in density or thickness of a component or specimen including voids and inclusions. It provides a quick, convenient and cost-effective way of detecting internal flaws in components and can be used to examine complex shapes. The size of defect that can be detected by x-ray radiography depends of various factors such as the thickness of the part, its x-ray absorption, size of flaw compared to the thickness of the part, the relative absorption of the flaw and part and the orientation of the flaw.

Ultrasonic NDE is another technique for detecting subsurface flaws in ceramic materials. It is most easily conducted on material having a smooth, flat surface and a constant cross-section. Penetrant dyes can be used to detect surface flaws. The part is first soaked in a fluorescent dye, dried or cleaned in a controlled

way to remove dye from the surface and then the part is examined under ultraviolet light. Penetrant dyes have different sensitivities and are not suitable for ceramics with open porosity.

Richerson (1982) outlined several other methods of NDE suitable for use with ceramics. These include laser holographic interferometry, acoustic holography, high frequency ultrasonics, microwaves, x-ray tomography and acoustic emissions.

The NDE of ceramic components is as yet poorly developed. The results of NDE cannot simulate service conditions as can (some) mechanical testing. However, the structural integrity of every component can be examined. Edwards (1989) suggested that the conditions for selecting a new test method may include the following: relevance, precision, reproducibility, accuracy and reliability, practicality and cost-effectiveness.

3.10 FAILURE ANALYSIS

Failure analysis is especially important when considering ceramic materials as it is the only means of isolating the failure causing problem. Failure analysis helps determine whether failure or damage occurred due to a design or material deficiency.

Fracture analysis or fractography, an examination of the fractured parts, can be used to reconstruct the sequence and cause of fracture. The path a crack follows as it propagates through a component provides substantial information about the stress distribution at the time of failure. Features on the fracture surfaces provide further information such as the fracture origin, cause of fracture initiation (impact, tensile overload, thermal shock, material flaw etc) and the approximate local stress causing fracture.

Richerson (1982) outlined the expected fracture surface features associated with the different causes/modes of failure and the techniques available to interpret them. Quinn and Morrell (1991) concluded that fractography to characterise fracture origins is essential and they strongly recommended 100% fractography of test specimens as well as failed components. However, due to the large numbers of test specimens required to obtain statistically reliable data and the small size of failure causing defects this is not always practicable.

CHAPTER 4

FINITE ELEMENT ANALYSES - CONTACT

4.0 INTRODUCTION

This chapter describes the finite element models and analyses which were undertaken in two- and three-dimensions to obtain a representation of the conformal contact pressure and distribution between cylindrical and spherical bodies. Two-dimensional and axisymmetric models were used to allow verification of the method against known numerical and analytical solutions for a cylinder contacting a semi-infinite cylindrical cavity and a sphere in a semi-infinite spherical cavity, gap elements being used to model the interface between the bodies. Two- and three-dimensional and axisymmetric analyses were then conducted using models with dimensions appropriate to pump components to assess the effects on the contact pressure distribution of using sleeve and liner materials with different properties and thicknesses.

The contact pressure distributions from the above models were used as loading on models of the cylinder blocks, pistons and slippers with the appropriate sleeve or liner materials as described in Chapter 5. Separating the contact distribution analysis from the component models allowed more complex component models to be created than would otherwise have been the case. Figure 4.0.1 shows the relationship between the contact models and the component models, and indicates how the results from the different analyses were used as input to the next stage of analysis.

Due to the number and complexity of the different finite element models, the results of the analyses and some discussion are included with the model details rather than in a separate chapter, giving a more coherent layout. Specific aspects of the results relating to the performance of the axial piston pump are then included in Chapter 7, the general discussion.

4.0.1 Model parameterisation and convergence

In each case the model was parameterised to allow all input such as dimensions, material properties, loading, mesh density and element type to be varied with the minimum of additional work. The DISPLAY III pre-processor was used to create the models with session file input, the session file containing the appropriate parameters, and the NISA II finite element package was used to run the analyses.

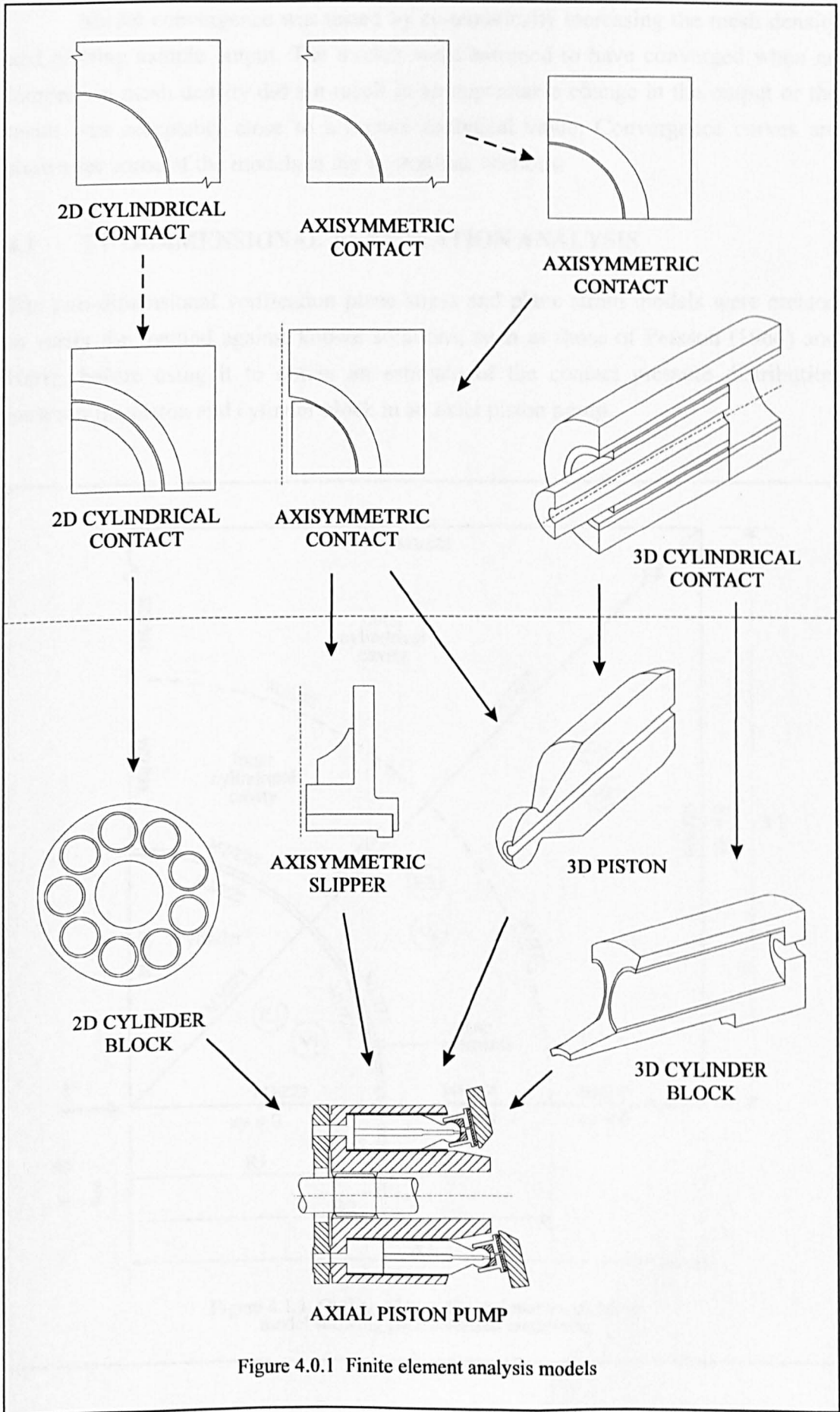


Figure 4.0.1 Finite element analysis models

Model convergence was tested by systematically increasing the mesh density and plotting sample output. The models were assumed to have converged when an increase in mesh density did not result in an appreciable change in the output or the result was acceptably close to a known analytical value. Convergence curves are shown for some of the models in the appropriate sections.

4.1 TWO-DIMENSIONAL VERIFICATION ANALYSIS

The two-dimensional verification plane stress and plane strain models were created to verify the method against known solutions, such as those of Persson (1964) and Hertz, before using it to obtain an estimate of the contact pressure distribution between the piston and cylinder block in an axial piston pump.

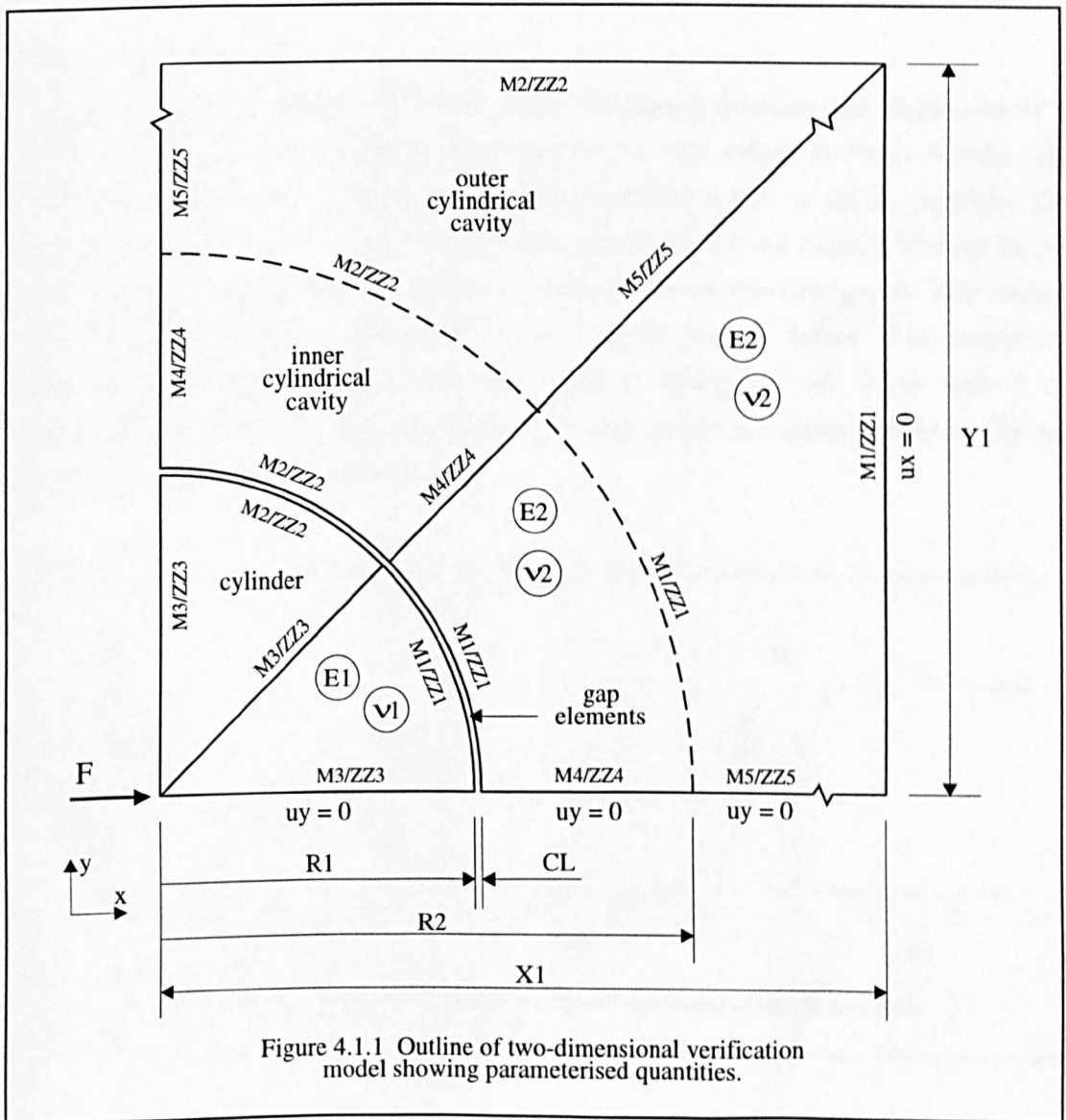


Figure 4.1.1 Outline of two-dimensional verification model showing parameterised quantities.

4.1.1 Models

Figure 4.1.1 shows an outline of the two-dimensional verification model used to compare the method and results against known solutions. It is a quarter representation of a cylinder inside a semi-infinite cylindrical cavity, taking account of symmetry and neglecting the non-contacting half. The model was meshed using first order plane strain or plane stress elements having two degrees of freedom at each node. Gap elements connect nodes across the interface between cylinder and cavity and a force, F , is applied to the model at the centre of the cylinder. Nodes along the symmetry plane are constrained from moving in the y -direction and the nodes along the right hand edge of the cavity are constrained from moving in the x -direction as indicated by $u_y = 0$ and $u_x = 0$. The figure is not drawn to scale: the dimension $X1$ is approximately 1000 times dimension $R1$, in order to simulate an infinitely large cylindrical cavity, and M_n and Z_n indicate the mesh densities and biases respectively.

4.1.2 Convergence

Figure 4.1.2 shows graphs of contact angle, maximum pressure and displacement in the cylindrical seat at the centre of contact for various values of mesh density. The rest of the mesh was varied in the same proportion as $M1$ as far as possible. The contact angle can be compared with the analytical result from Persson (1964) for the same parameters and this is shown as a dashed line on the first graph. The contact angle was calculated as described in the results section below. The maximum pressure and displacement converged with a difference of 0.2% and 0.1% respectively between the last two meshes. For this reason the mesh with $M1 = 36$ was chosen for the rest of the analyses.

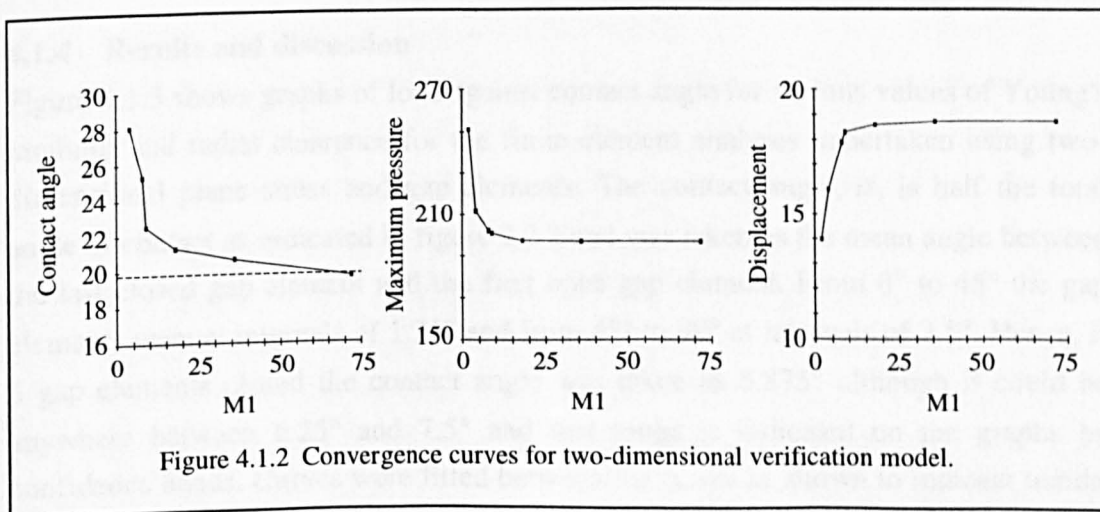


Figure 4.1.2 Convergence curves for two-dimensional verification model.

4.1.3 Analyses

Several series of finite element analyses were undertaken in plane strain and plane stress to establish the effects of load, F , material properties, E_1 and E_2 , and gap width, CL , on the contact size and the forces transmitted between the components and to verify the results against known analytical solutions. Poisson's ratio was 0.3 in all cases. Table 4.1.1 shows the values of F , E and CL for the analyses where the cylinder and cavity are composed of the same material, ie. $E_1 = E_2 = E$; and table 4.1.2 when the cylinder and cavity materials are dissimilar ($E_1 \neq E_2$).

CL (mm)		Young's modulus, E (GPa)					
		10	50	100	200	300	500
Load, F (N)	10	0.1	0.1	0.1	0.1	0.1	0.1
		0.01	0.01	0.01	0.01	0.01	0.01
		0.001	0.001	0.001	0.001	0.001	0.001
	100	0.1	0.1	0.1	0.1	0.1	0.1
		0.01	0.01	0.01	0.01	0.01	0.01
		0.001	0.001	0.001	0.001	0.001	0.001
	500	0.1	0.1	0.1	0.1	0.1	0.1
		0.01	0.01	0.01	0.01	0.01	0.01
		0.001	0.001	0.001	0.001	0.001	0.001
	1000	0.1	0.1	0.1	0.1	0.1	0.1
		0.01	0.01	0.01	0.01	0.01	0.01
		0.001	0.001	0.001	0.001	0.001	0.001
	5000	0.1	0.1	0.1	0.1	0.1	0.1
		0.01	0.01	0.01	0.01	0.01	0.01
		0.001	0.001	0.001	0.001	0.001	0.001

Table 4.1.1 Two-dimensional verification analyses.

4.1.4 Results and discussion

Figure 4.1.3 shows graphs of load against contact angle for various values of Young's modulus and radial clearance for the finite element analyses undertaken using two-dimensional plane stress and gap elements. The contact angle, α , is half the total angle of contact as indicated in figure 2.2.2 and was taken as the mean angle between the last closed gap element and the first open gap element. From 0° to 45° the gap elements were at intervals of 1.25° and from 45° to 90° at intervals of 2.5° . Hence, if 6 gap elements closed the contact angle was taken as 6.875° although it could be anywhere between 6.25° and 7.5° and this range is indicated on the graphs by confidence bands. Curves were fitted between the points as shown to indicate trends. The graphs show that for increased load, a softer material and a smaller radial clearance, the contact angle is increased.

CL (mm)		Young's moduli (GPa)											
		E1	E2	E1	E2	E1	E2	E1	E2	E1	E2	E1	E2
		100	300	300	100	200	100	100	200	500	100	100	500
Load, F (N)	10	0.1 0.01 0.001	0.1 0.01 0.001	0.1	0.1	0.1	0.1	0.1	0.1	0.1	0.1	0.1	
	100	0.1 0.01 0.001	0.1 0.01 0.001	0.1	0.1	0.1	0.1	0.1	0.1	0.1	0.1	0.1	
	500	0.1 0.01 0.001	0.1 0.01 0.001										
	1000	0.1 0.01 0.001	0.1 0.01 0.001	0.1	0.1	0.1	0.1	0.1	0.1	0.1	0.1	0.1	
	5000	0.1 0.01 0.001	0.1 0.01 0.001										
	10000			0.1	0.1	0.1	0.1	0.1	0.1	0.1	0.1	0.1	
	100000					0.1	0.1	0.1	0.1	0.1	0.1	0.1	

Table 4.1.2 Two-dimensional verification analyses for dissimilar materials.

The results from the three graphs can be combined by dividing the load, F , by the clearance, CL , as shown in figure 4.1.4. As the ratio of load/clearance increases the contact angle increases. Figure 4.1.5 shows the results combined further by plotting the non-dimensionalised quantity $\frac{F}{CL * E}$ against contact angle. This is compared with the same quantity as determined analytically by Persson (1964) and, as can be seen, the finite element analysis gives a good estimate of contact angle for given values of load, clearance and Young's modulus.

However, the pressure distribution around the interface and the stresses in the components are undoubtedly of greater interest than the contact angle. Figure 4.1.6 shows the non-dimensionalised pressure distribution, $\frac{Rp(\phi)}{F}$, obtained from three of the finite element analyses, where $p(\phi)$ is the pressure at angle ϕ , R is the radius of the cylinder and F the load. Each closed gap element had an associated load factor which was the force transmitted by the gap element. These forces act at discrete intervals around the contact region and were converted to pressures by assuming that they act over half the area of the adjacent elements as shown in Appendix I. As expected, for a smaller contact area the maximum pressure was greater for a given radius and load. This implies a harder material or a larger radial clearance.

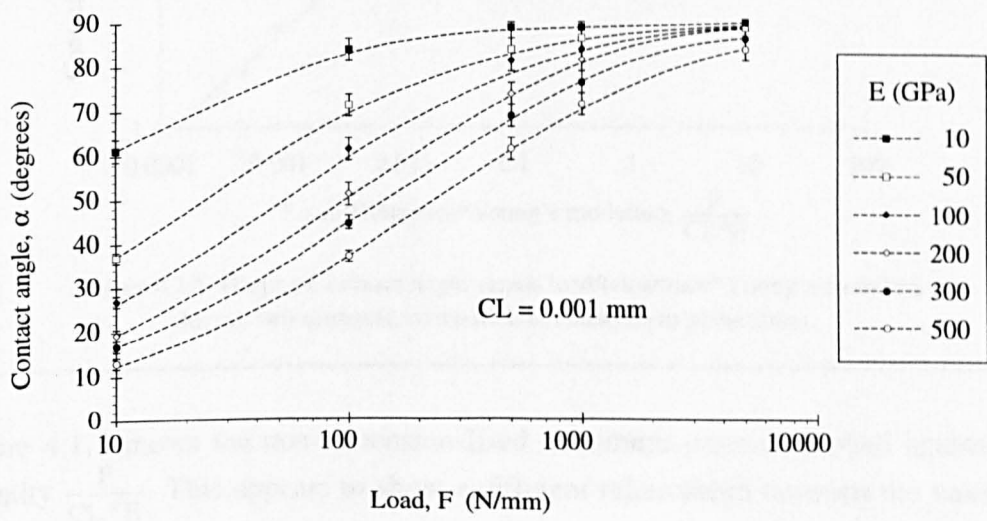
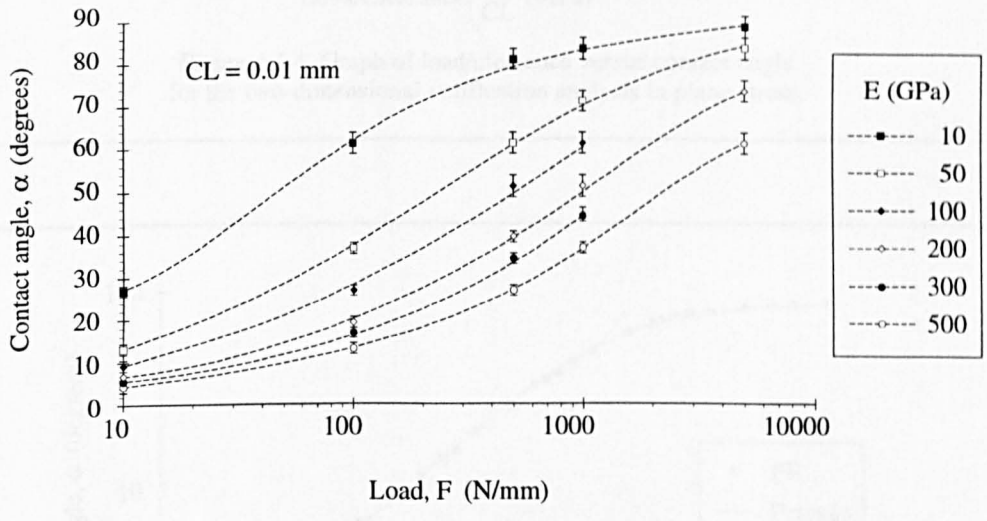
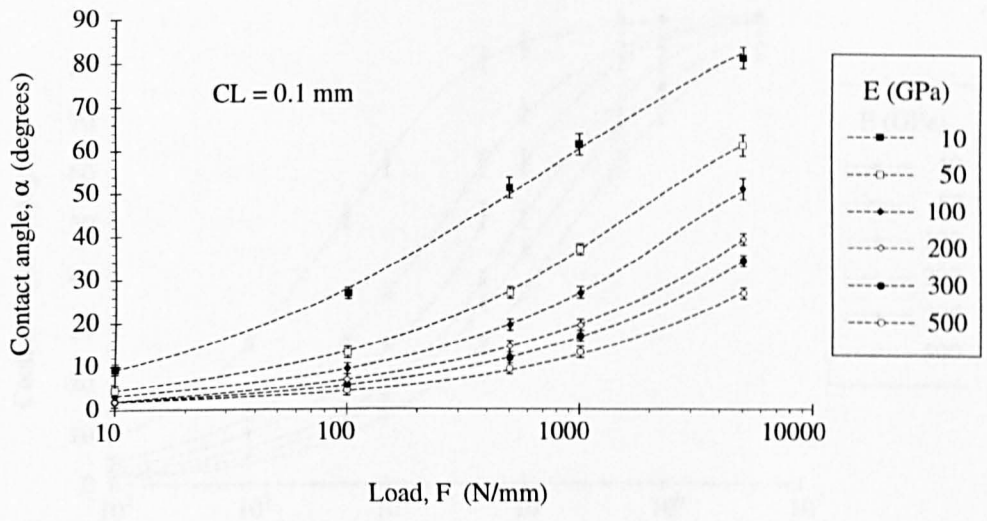


Figure 4.1.3 Graphs of load versus contact angle for the two-dimensional verification analysis in plane stress.

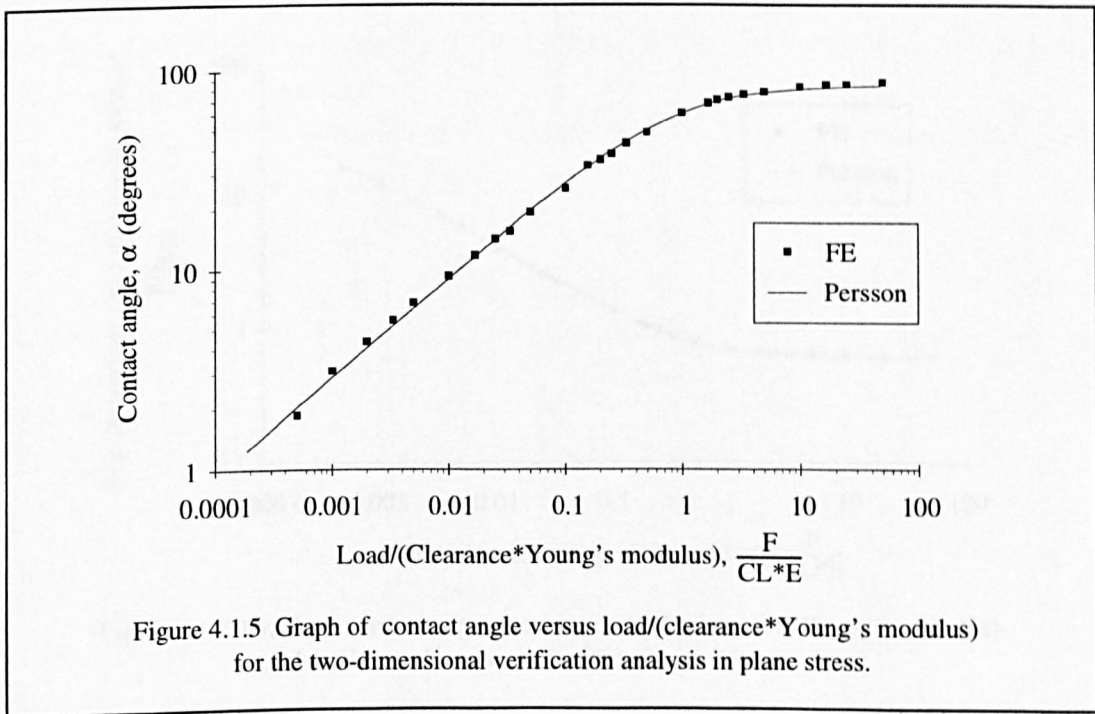
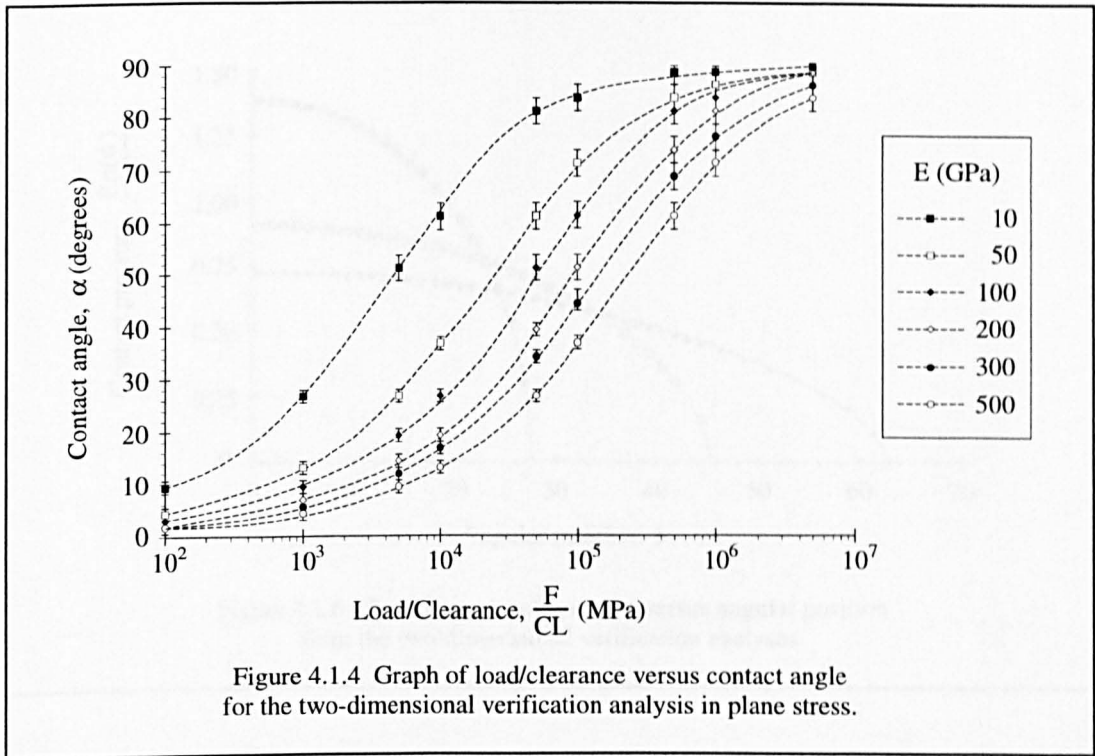


Figure 4.1.7 shows the non-dimensionalised maximum pressure plotted against the quantity $\frac{F}{CL * E}$. This appears to show a different relationship between the variables in different regions of the graph and an empirical equation could be determined for, say, $\frac{F}{CL * E} \leq 0.1$.

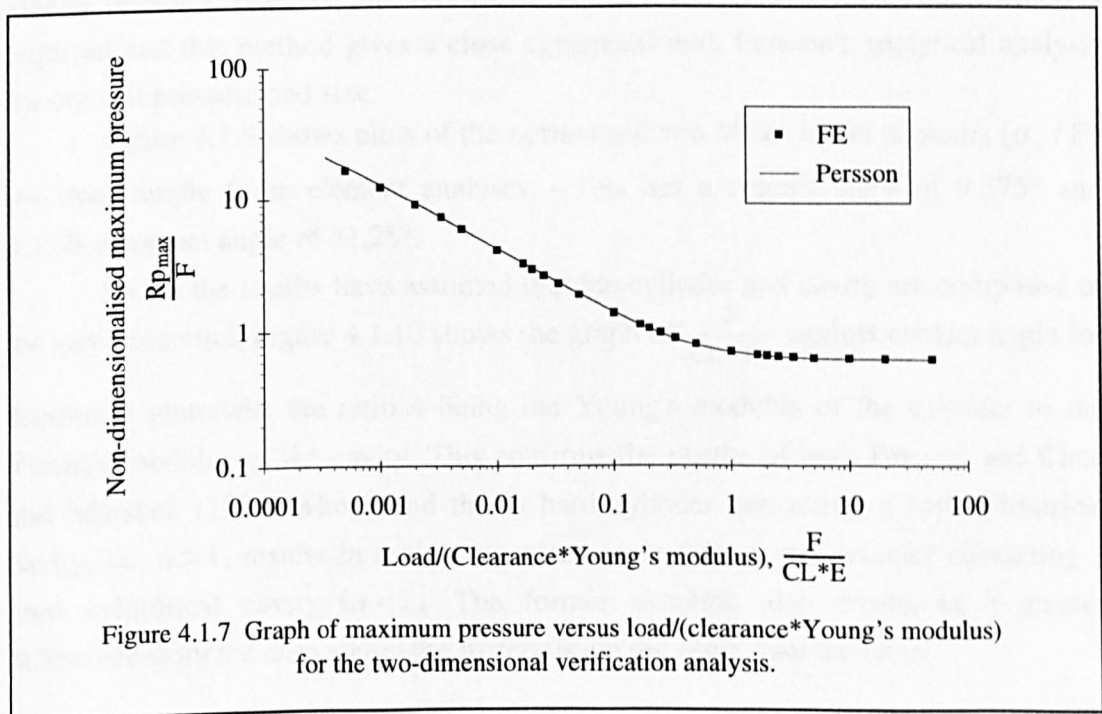
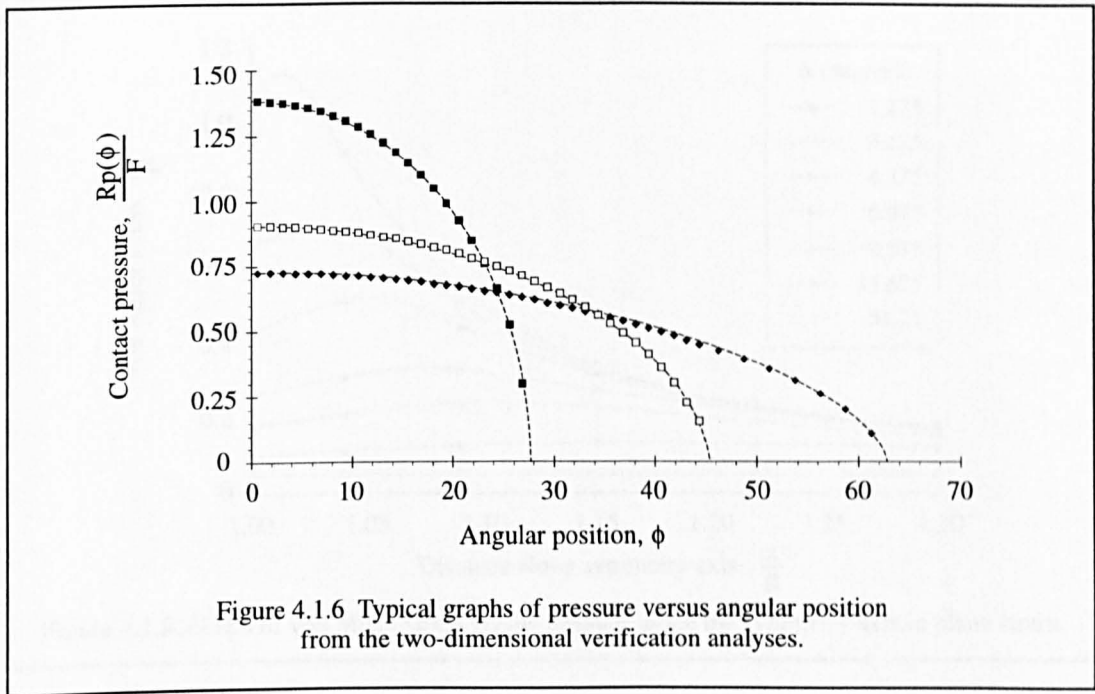
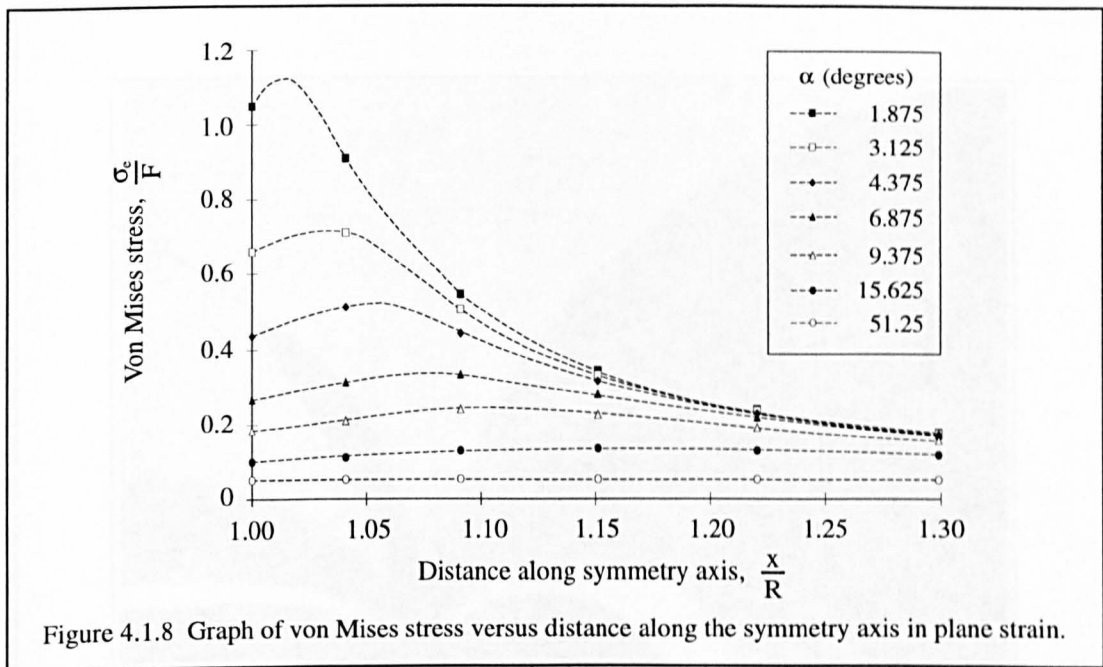


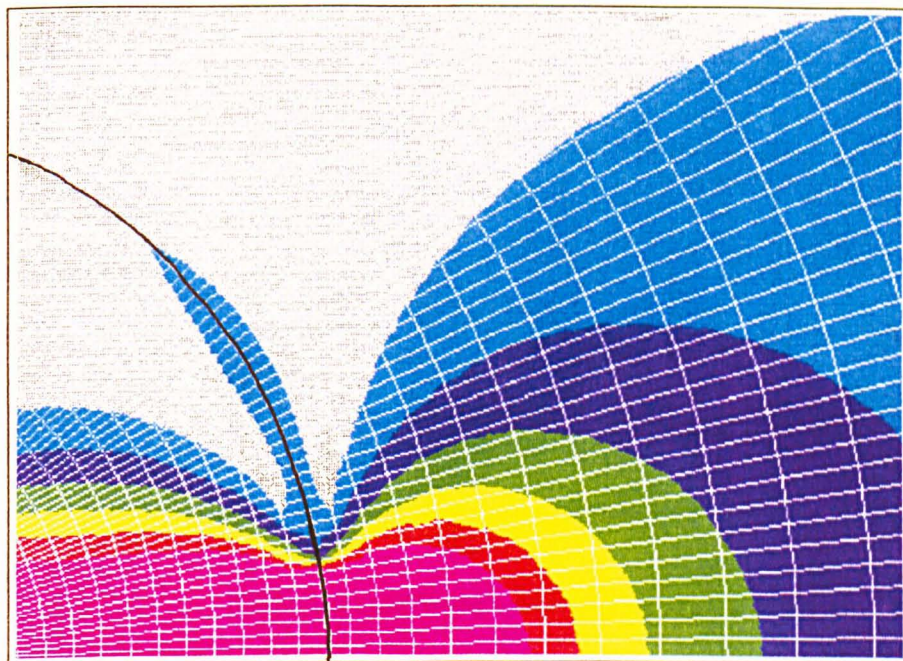
Figure 4.1.8 shows the stress in the cylindrical cavity along the axis of symmetry this time for plane strain. Persson plots these results for both plane stress and plane strain and found that for the former the maximum stress occurs at the surface. For plane strain the maximum stress occurs at a point inside the cylindrical cavity as was also found by Persson. The dashed lines shown are an estimate of the



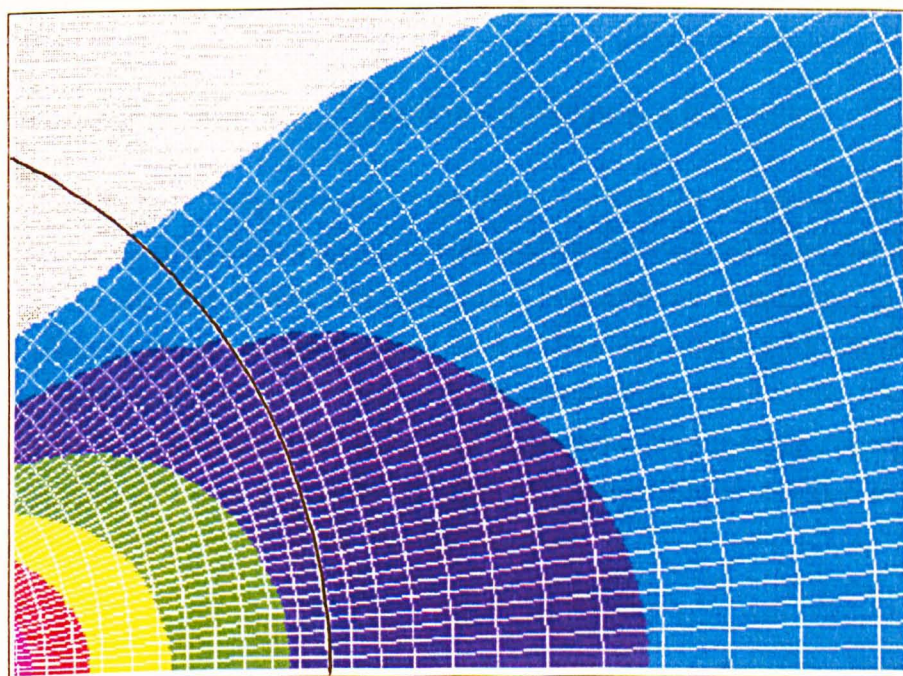
actual situation. It would appear that for small contact angles the mesh density needs to be finer to determine the magnitude and position of the maximum stress with greater accuracy. However, for this application it is the pressure distribution which is required and this method gives a close agreement with Persson's analytical analysis for contact pressure and size.

Figure 4.1.9 shows plots of the normalised von Mises stress contours (σ_c / F) for two sample finite element analyses, 4.1.9a has a contact angle of 9.375° and 4.1.9b a contact angle of 51.25° .

So far the results have assumed that the cylinder and cavity are composed of the same material. Figure 4.1.10 shows the graph of $\frac{F}{CL * E_1}$ against contact angle for dissimilar materials, the ratio n being the Young's modulus of the cylinder to the Young's modulus of the cavity. This confirms the results of both Persson and Chen and Marshek (1988) who found that a hard cylinder contacting a soft cylindrical cavity, i.e. $n > 1$, results in a higher contact angle than a soft cylinder contacting a hard cylindrical cavity ($n < 1$). The former situation also results in a greater difference from the case where the materials are the same than the latter.



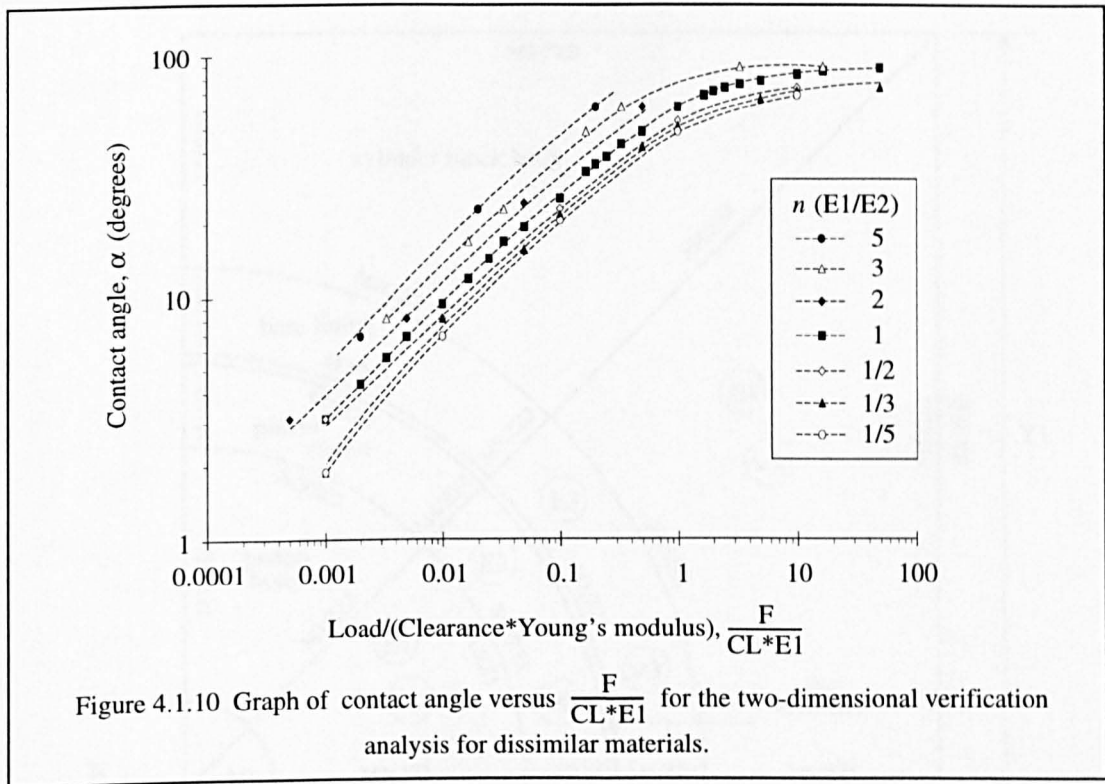
a) $\alpha = 9.375^\circ$, $E = 100 \text{ GPa}$, $CL = 0.1 \text{ mm}$



b) $\alpha = 51.25^\circ$, $E = 100 \text{ GPa}$, $CL = 0.1 \text{ mm}$



Figure 4.1.9 Stress contours in the two-dimensional verification model .



4.2 TWO-DIMENSIONAL COMPONENT-SIZED ANALYSIS

The two-dimensional component-sized models were created to obtain the contact pressure distribution between a piston and the cylinder block of an axial piston pump. The verification models proved that using plane strain or stress and gap elements to model contacting concentric components gave a close agreement with the analytical method of Persson (1964) for a cylinder in an infinite cylindrical cavity. Hence, the same method and elements were used, with dimensions and loading appropriate to pump components, to model a cross-section of the conformal contact between a piston and the cylinder block of an axial piston pump.

4.2.1 Models and analyses

Figure 4.2.1 shows an outline of the two-dimensional component-sized contact model. It was essentially the same as the two-dimensional verification contact model, the addition of two further regions enabling the effects of varying the piston sleeve or bore lining material properties and thickness to be assessed. The loading was representative of that in an axial piston pump assuming a unit thickness slice through the piston and cylinder block at the top of the piston.

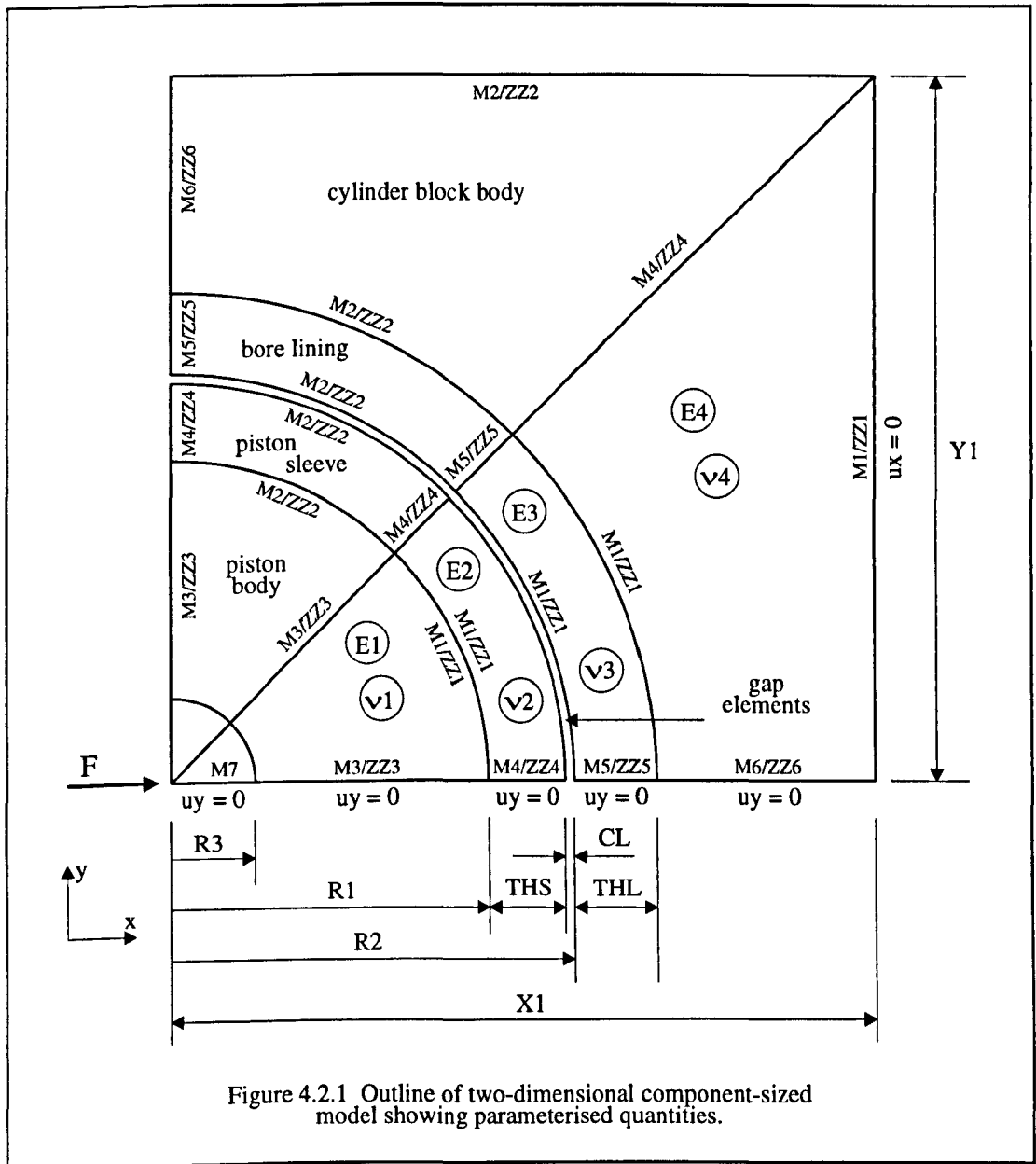


Figure 4.2.1 Outline of two-dimensional component-sized model showing parameterised quantities.

The model was meshed using plane strain and gap elements using the same cylindrical mesh density as was used for the 2D verification models, i.e. $M1 = 36$ and $M2 = 18$. Again, several series of finite element analyses were undertaken to establish the effects of load, material properties and clearance on the contact size and the forces transmitted between the components and these are summarised in table 4.2.1. For each combination in the table four load cases were analysed, corresponding to bore pressures of 5 bar (boost pressure), 100 bar, 140 bar (2000 psi) and 210 bar (3000 psi) bar.

	E1 (GPa)	v1	E2 (GPa)	v2	E3 (GPa)	v3	E4 (GPa)	v4	CL (mm)	THS (mm)	THL (mm)
all materials the same	200	0.3	200	0.3	200	0.3	200	0.3	0.0125	1.0	1.0
	210	0.25	210	0.25	210	0.25	210	0.25	0.0125	1.0	1.0
	70	0.3	70	0.3	70	0.3	70	0.3	0.0125	1.0	1.0
	310	0.28	310	0.28	310	0.28	310	0.28	0.0125	1.0	1.0
different sleeve materials	200	0.3	210	0.25	200	0.3	200	0.3	0.0125	1.0	1.0
	200	0.3	70	0.3	200	0.3	200	0.3	0.0125	1.0	1.0
	200	0.3	310	0.28	200	0.3	200	0.3	0.0125	1.0	1.0
	200	0.3	10	0.4	200	0.3	200	0.3	0.0125	1.0	1.0
	210	0.25	10	0.4	210	0.25	210	0.25	0.0125	1.0	1.0
different liner material	200	0.3	200	0.3	210	0.25	200	0.3	0.0125	1.0	1.0
	200	0.3	200	0.3	70	0.3	200	0.3	0.0125	1.0	1.0
	200	0.3	200	0.3	310	0.28	200	0.3	0.0125	1.0	1.0
	200	0.3	200	0.3	10	0.4	200	0.3	0.0125	1.0	1.0
	210	0.25	210	0.25	10	0.4	200	0.3	0.0125	1.0	1.0
different sleeve thickness	200	0.3	10	0.4	200	0.3	200	0.3	0.0125	0.5	1.0
	200	0.3	10	0.4	200	0.3	200	0.3	0.0125	1.5	1.0
	200	0.3	10	0.4	200	0.3	200	0.3	0.0125	2.0	1.0
	200	0.3	10	0.4	200	0.3	200	0.3	0.0125	3.0	1.0
	200	0.3	10	0.4	200	0.3	200	0.3	0.0125	4.0	1.0
	200	0.3	10	0.4	200	0.3	200	0.3	0.0125	5.0	1.0
different liner thickness	200	0.3	200	0.3	10	0.4	200	0.3	0.0125	1.0	0.25
	200	0.3	200	0.3	10	0.4	200	0.3	0.0125	1.0	0.5
	200	0.3	200	0.3	10	0.4	200	0.3	0.0125	1.0	0.75
	200	0.3	200	0.3	10	0.4	200	0.3	0.0125	1.0	1.25
	200	0.3	200	0.3	10	0.4	200	0.3	0.0125	1.0	1.5
different radial clearance	200	0.3	200	0.3	200	0.3	200	0.3	0.001	1.0	1.0
	200	0.3	200	0.3	200	0.3	200	0.3	0.01	1.0	1.0
	200	0.3	200	0.3	200	0.3	200	0.3	0.015	1.0	1.0
	200	0.3	200	0.3	200	0.3	200	0.3	0.02	1.0	1.0
	200	0.3	200	0.3	200	0.3	200	0.3	0.025	1.0	1.0

Table 4.2.1 Parameter combinations for the two-dimensional component-sized models.

4.2.2 Results and discussion

Figure 4.2.2 shows a graph of non-dimensionalised maximum contact pressure versus bore pressure for 1 mm piston sleeves and bore liners of different stiffnesses. In each case the other three material areas had identical properties and the ratio n refers to the Young's modulus of the sleeve or liner to the Young's modulus of the rest of the material. The graphs indicate that a 1 mm liner or sleeve of the stiffness of silicon nitride does not markedly affect the maximum contact pressure of a stainless steel piston in a stainless steel cylinder block. However, a more compliant liner or sleeve, for example, of a polymer, will result in a reduced maximum contact pressure from, of course, an increased contact angle.

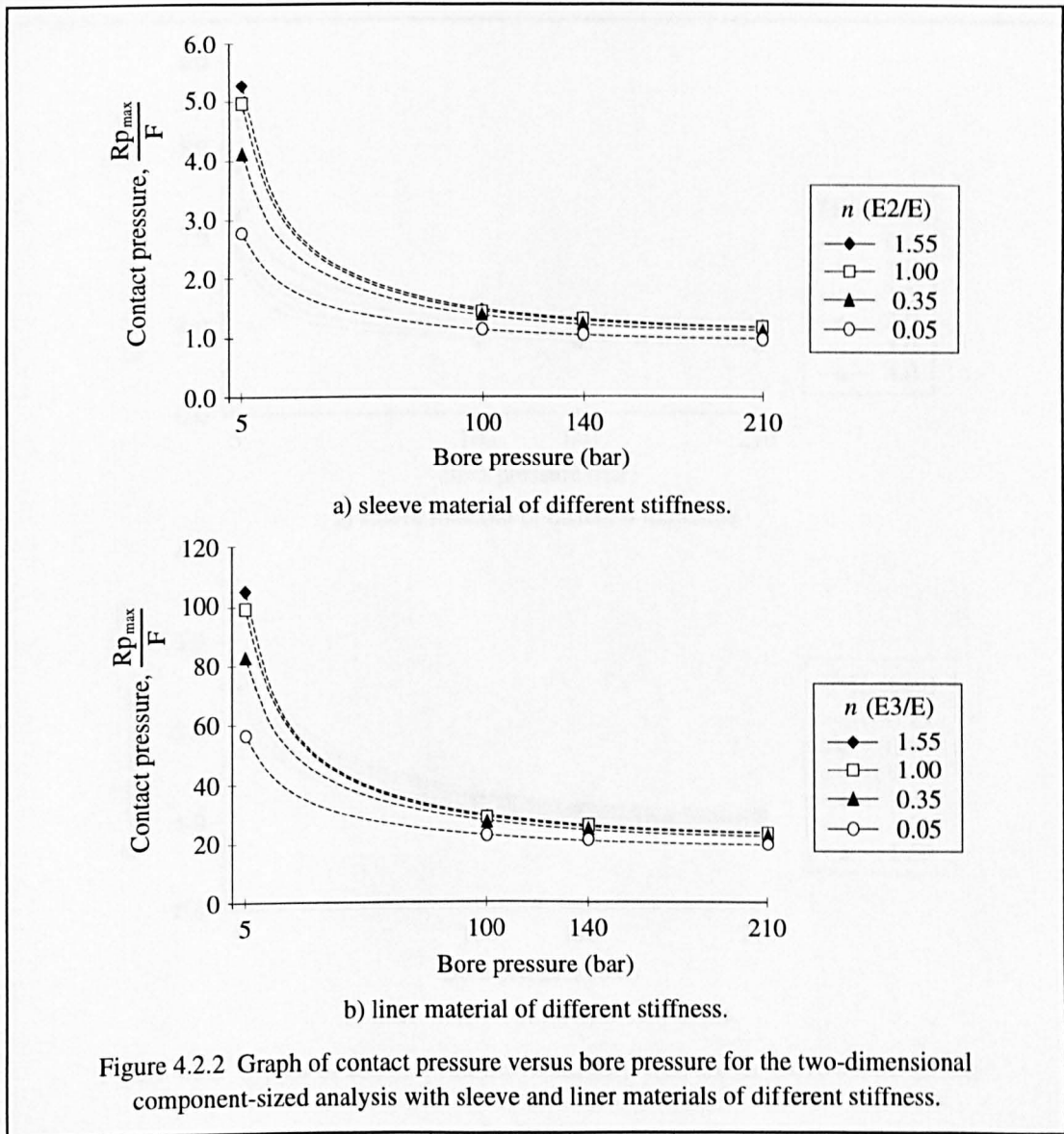
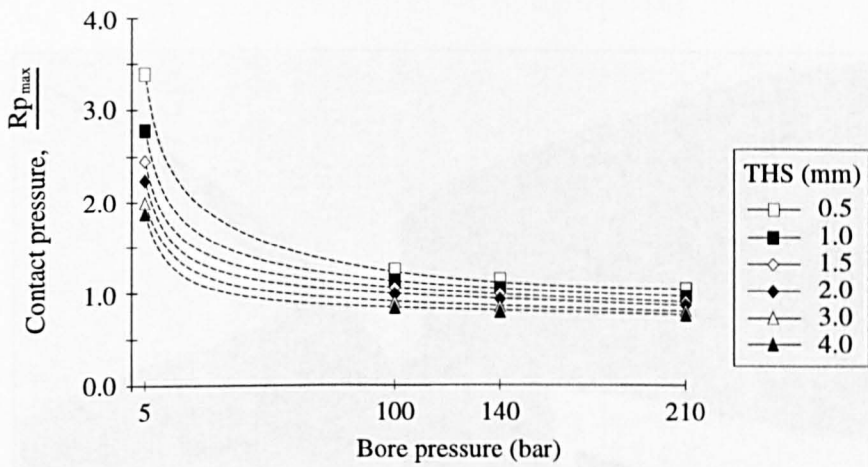
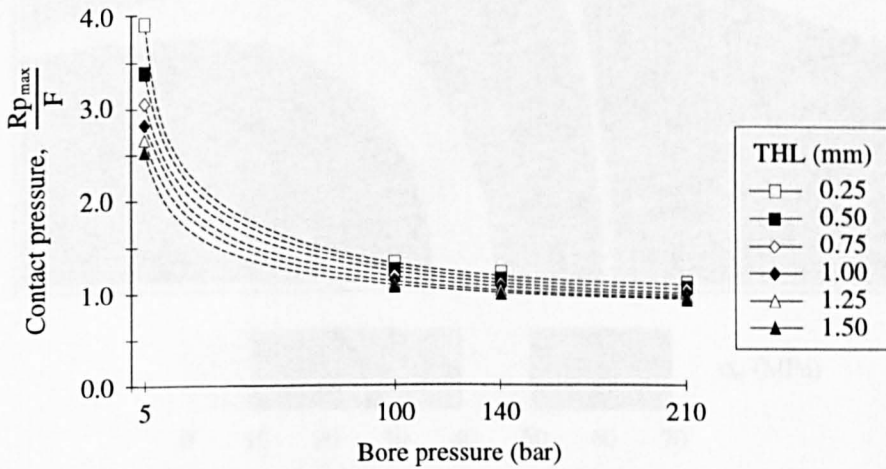


Figure 4.2.3 shows the same quantities as above plotted for sleeves and liners of different thicknesses (see table 4.2.1). The sleeve thickness varied between 0.5 mm and 4.0 mm and that of the liner between 0.25 mm and 1.5 mm. The size of the latter was restricted by the size of the inter-bore width of the cylinder block. The graphs show that, for a sleeve or liner of a more compliant material than the piston and cylinder block, an increased thickness results in a reduced maximum contact pressure. The opposite could be expected to be the case for a stiffer liner or sleeve.

The effect of varying the radial clearance between the piston and cylinder block is shown in figure 4.2.4. As with the verification model, a smaller radial clearance results in a reduced maximum contact pressure and vice versa. As can be seen from table 4.2.1, one analysis was conducted on a model with three different material properties corresponding to a PSZ piston in a 1mm PEEK-lined, steel cylinder block. Figure 4.2.5 shows the stress contours in the model, the load corresponding to a bore pressure of 140 bar.



a) sleeve material of different thickness.



b) liner material of different thickness.

Figure 4.2.3 Graphs of contact pressure versus bore pressure for the two-dimensional component-sized analysis with sleeve and liner materials of different thickness.

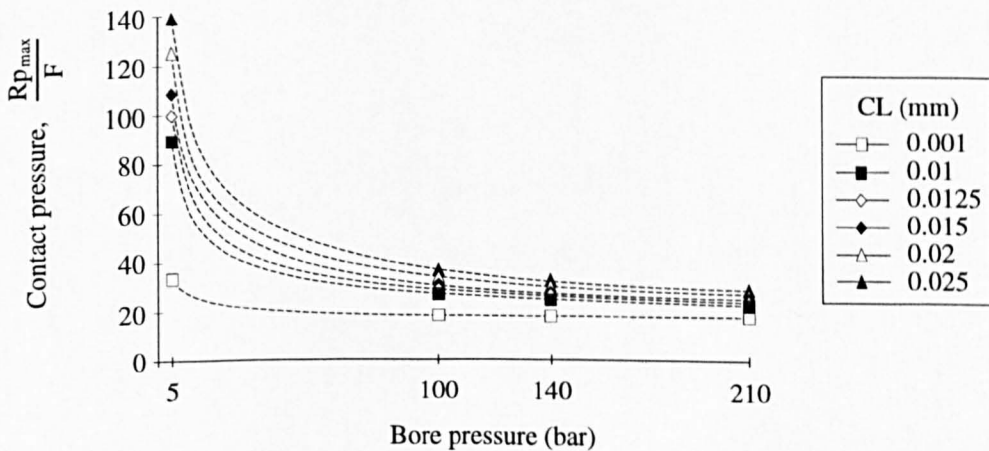


Figure 4.2.4 Graph of contact pressure versus bore pressure for the two-dimensional component-sized analysis with different radial clearances.

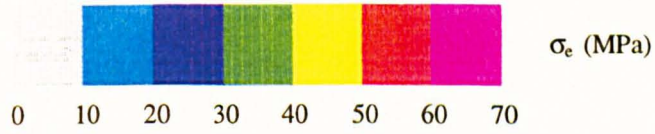
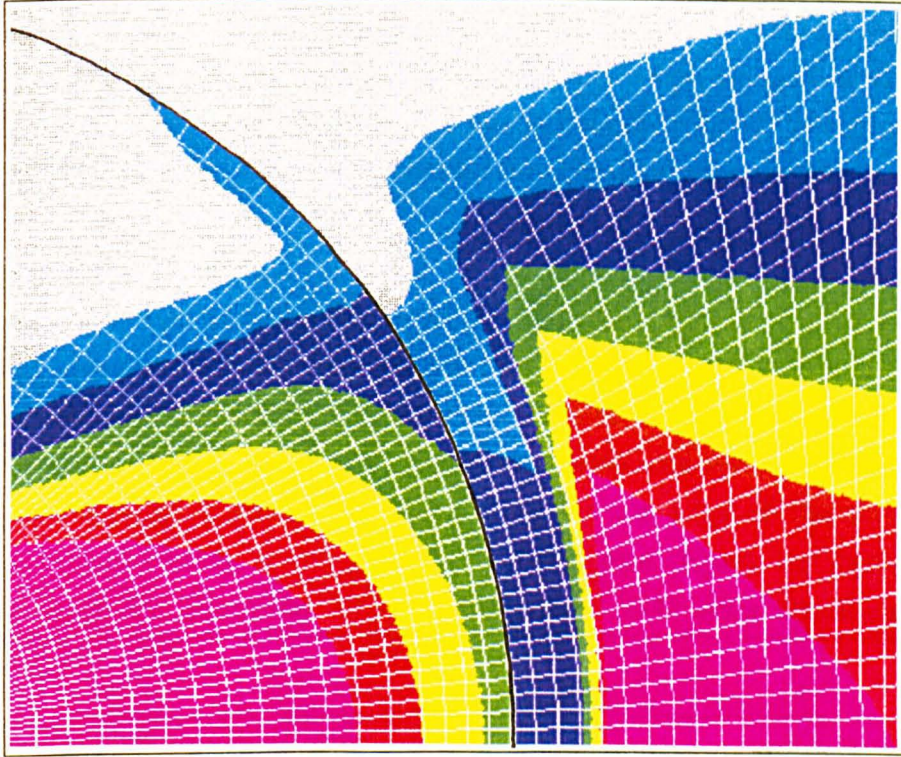


Figure 4.2.5 Stress contours in the model representing a PEEK-sleeved steel piston in a ceramic cylinder block at a bore pressure of 140 bar.

4.3 AXISYMMETRIC VERIFICATION ANALYSIS

Axisymmetric models representing a sphere in an infinite spherical cavity were created to verify the method against known solutions before using it to obtain the contact pressure distribution between the piston ball and slipper seat in an axial piston pump, in the same way as was done for the cylindrical case above.

4.3.1 Models and analyses

Figure 4.3.1 shows an axisymmetric representation of a sphere in a spherical cavity. The model was meshed using first order axisymmetric elements with gap elements connecting the nodes between the components. A force was applied to the model at the centre of the sphere. Nodes along the axisymmetric axis were constrained from moving in the x-direction and the nodes along the top edge of the cavity were constrained from moving in the y-direction as indicated. Again, the figure is not drawn to scale: the dimension X1 is approximately 1000 times dimension R1 to

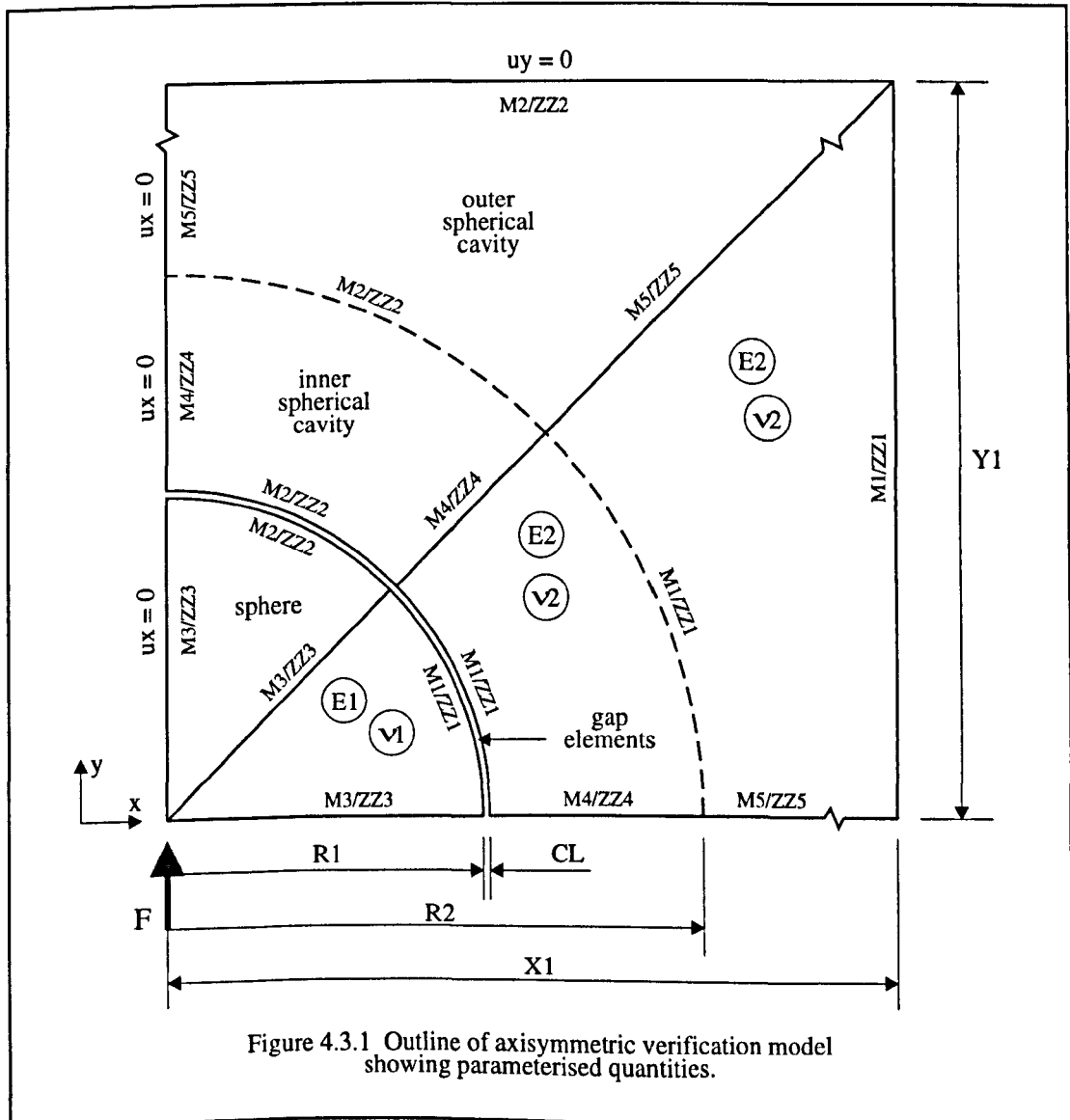


Figure 4.3.1 Outline of axisymmetric verification model showing parameterised quantities.

simulate an infinitely large spherical cavity. Once again several series of analyses were undertaken to establish the effects of load, F, material properties, E1 and E2 and clearance, CL on the contact size and pressure distribution between the sphere and cavity and these are shown in table 4.3.1.

CL (mm)		Young's modulus, E (GPa)					
		10	50	100	200	300	500
Load, F (N)	5	0.1	0.1	0.1	0.1	0.1	0.1
		0.01	0.01	0.01	0.01	0.01	0.01
		0.001	0.001	0.001	0.001	0.001	0.001
	50	0.1	0.1	0.1	0.1	0.1	0.1
		0.01	0.01	0.01	0.01	0.01	0.01
		0.001	0.001	0.001	0.001	0.001	0.001
	250	0.1	0.1	0.1	0.1	0.1	0.1
		0.01	0.01	0.01	0.01	0.01	0.01
		0.001	0.001	0.001	0.001	0.001	0.001
	500	0.1	0.1	0.1	0.1	0.1	0.1
		0.01	0.01	0.01	0.01	0.01	0.01
		0.001	0.001	0.001	0.001	0.001	0.001
	2500	0.1	0.1	0.1	0.1	0.1	0.1
		0.01	0.01	0.01	0.01	0.01	0.01
		0.001	0.001	0.001	0.001	0.001	0.001

Table 4.3.1 Axisymmetric verification analyses.

4.3.2 Results and discussion

Figure 4.3.2 shows graphs of load against contact angle for various values of Young's modulus and clearance size for the finite element analyses undertaken using axisymmetric solid and gap elements. The contact angle, α , was taken as the mean angle between the last closed gap element and the first open gap element. The mesh density was the same as for the two-dimensional verification contact models described in Section 4.1. Hence, from 0° to 45° the gap elements were at intervals of 1.25° and from 45° to 90° at intervals of 2.5° . Curves are fitted between the points on the graphs as shown to indicate trends. As the load increases the contact angle increases, for a given value of Young's modulus, E, and clearance, CL. Likewise, a more compliant material and a smaller radial clearance results in an increased contact angle.

Figure 4.3.3 shows combined results from the graphs in figure 4.3.2, obtained by plotting the dimensionless quantity $\frac{P}{R * CL * E}$ against contact angle. The symbols and dashed line indicate results from the finite element analyses and the solid line results using Hertz theory. The finite element analysis results agree with the Hertz

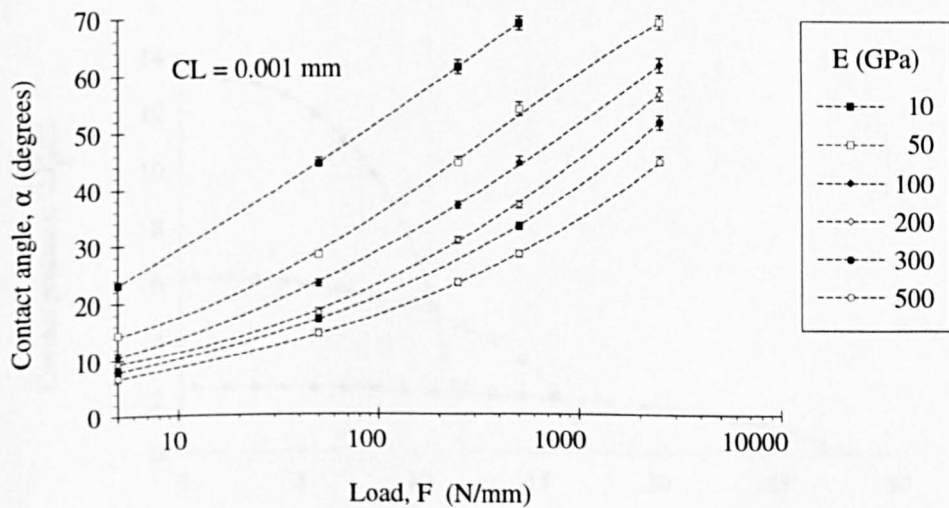
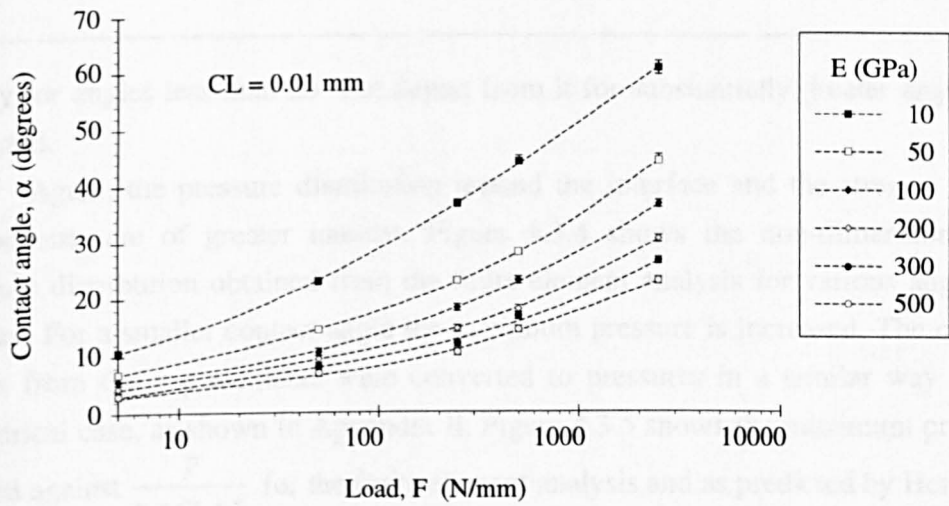
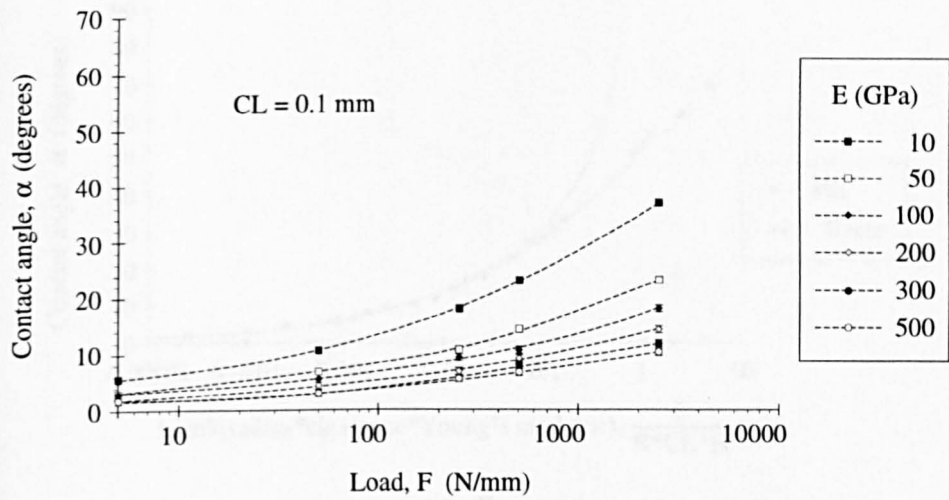


Figure 4.3.2 Graphs of load versus contact angle for the axisymmetric verification analysis.

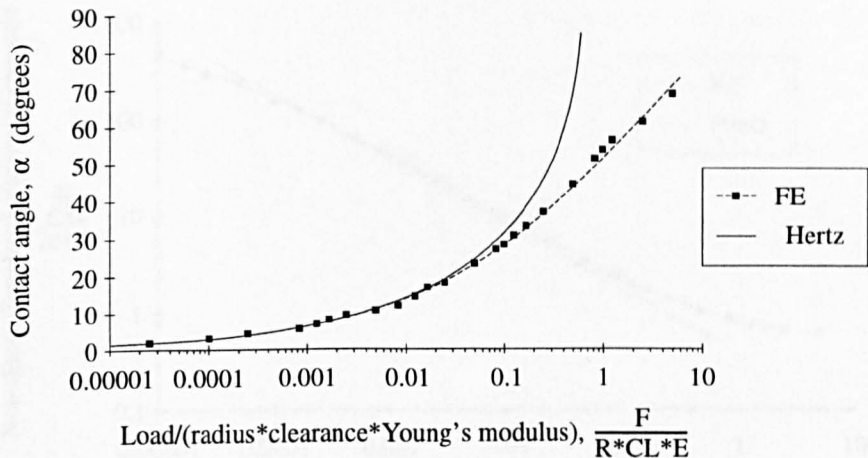


Figure 4.3.3 Graph of contact angle versus $\frac{F}{R \cdot CL \cdot E}$ for the axisymmetric verification analysis.

theory for angles less than 20° but depart from it for substantially greater angles, as expected.

Again, the pressure distribution around the interface and the stresses in the components are of greater interest. Figure 4.3.4 shows the non-dimensionalised pressure distribution obtained from the finite element analysis for various angles of contact. For a smaller contact angle the maximum pressure is increased. The contact forces from the gap elements were converted to pressures in a similar way to the cylindrical case, as shown in Appendix II. Figure 4.3.5 shows the maximum pressure plotted against $\frac{P}{R \cdot CL \cdot E}$ for the finite element analysis and as predicted by Hertz.

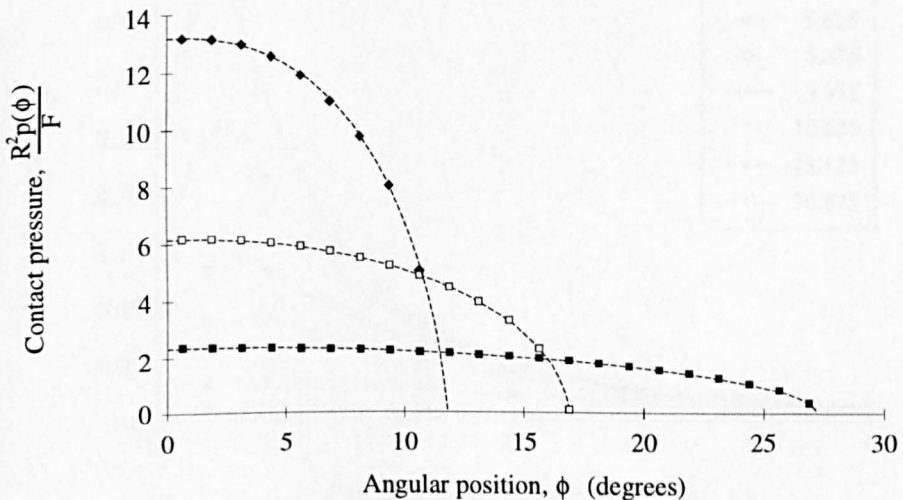
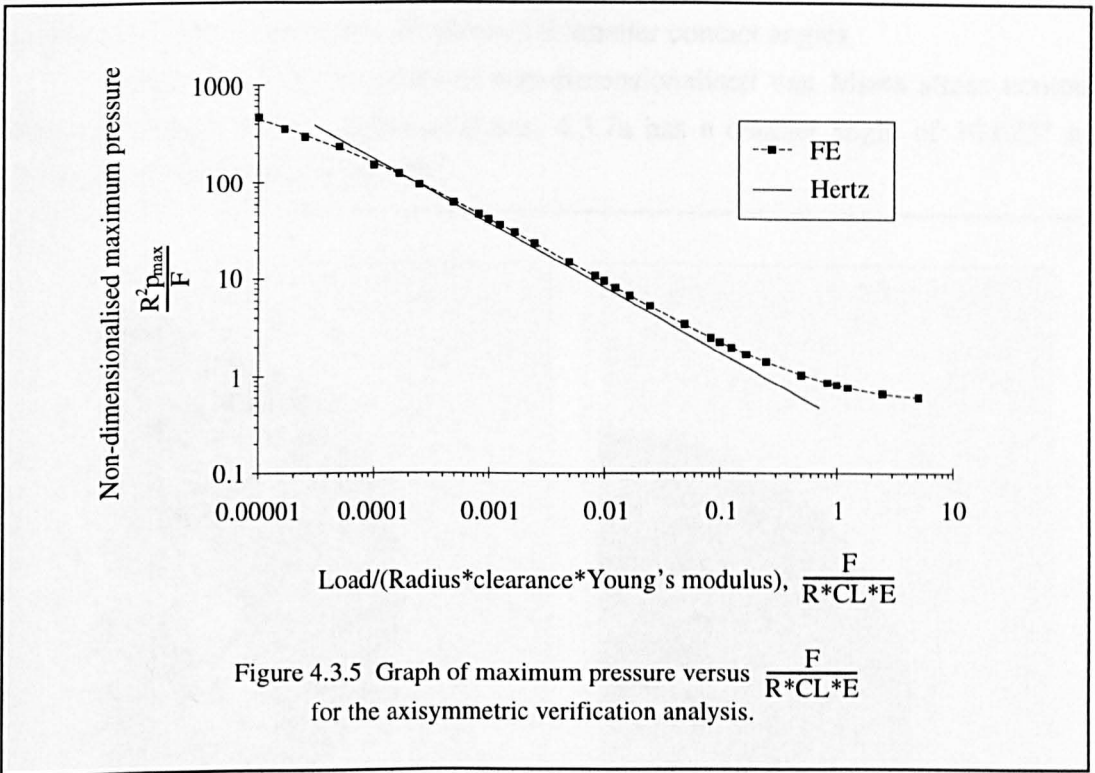
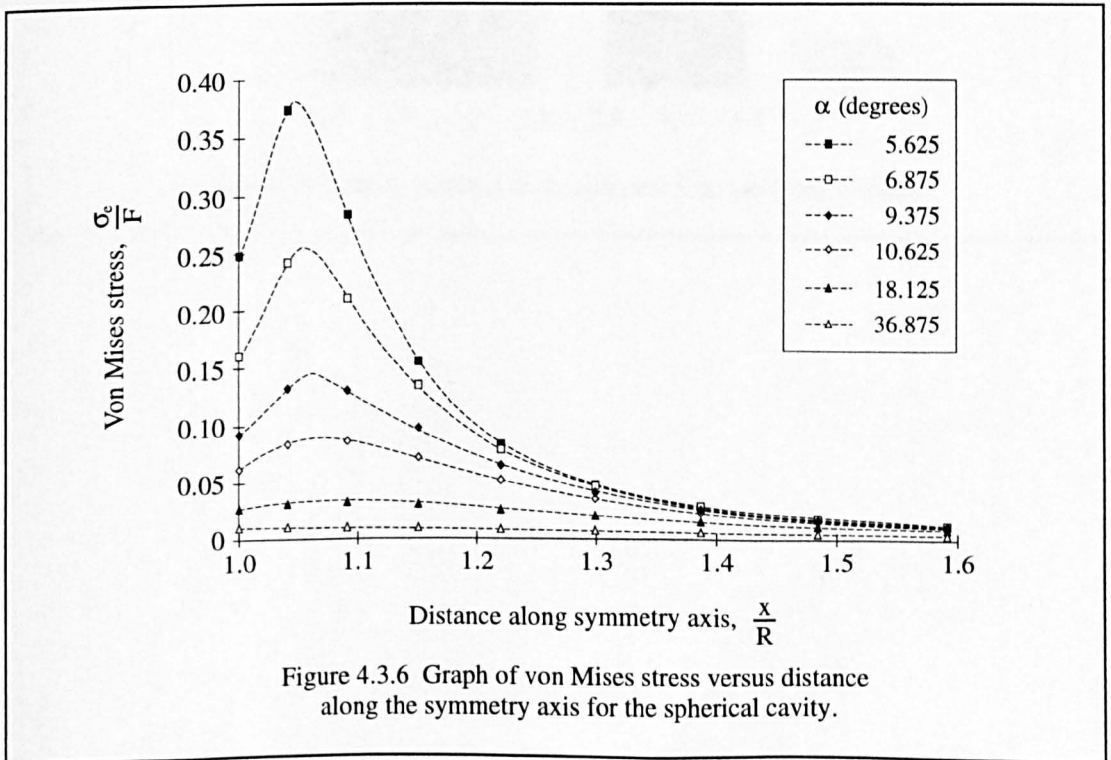


Figure 4.3.4 Graph of pressure versus angular position for the axisymmetric verification analysis.

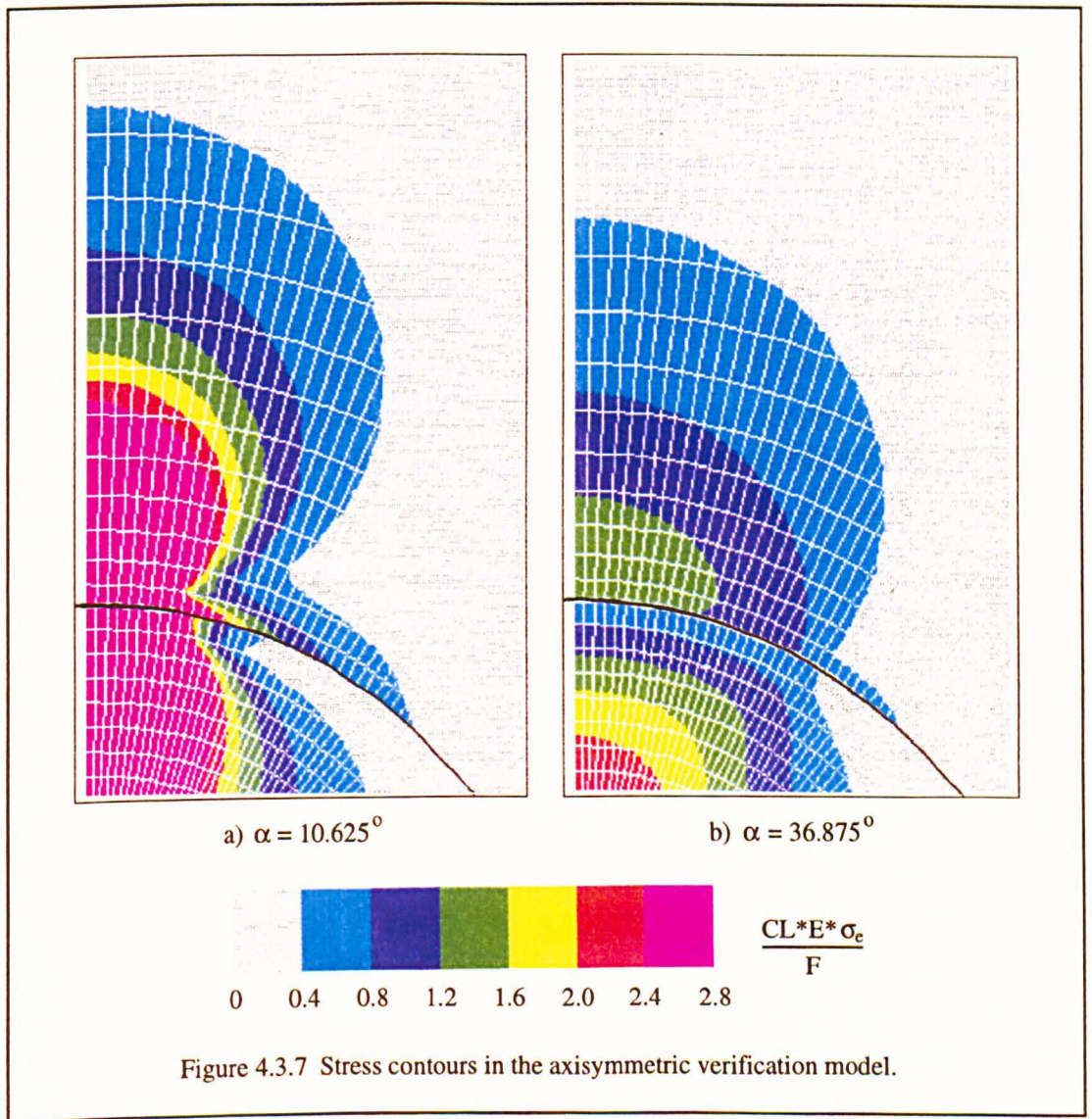


The finite element analysis departs from Hertzian analysis for lower maximum pressure, as expected. However, it also departs from the prediction for higher maximum pressures which probably would be improved with a finer mesh density in this region. Figure 4.3.6 shows von Mises equivalent stress in the spherical cavity along the axis of symmetry. Dashed lines are fitted between the points and, as with the cylindrical case, the mesh density needs to be finer to predict the position of



maximum stress with more confidence for smaller contact angles.

Figure 4.3.7 shows plots of non-dimensionalised von Mises stress contours for two sample finite element analyses, 4.3.7a has a contact angle of 10.625° and 4.3.7b a contact angle of 36.875° .



4.4 AXISYMMETRIC COMPONENT-SIZED ANALYSIS

The results from the axisymmetric verification contact models showed that the finite element method using gap elements to model the interface between the components gave a good prediction of the contact angle and pressure distribution when compared with available analytical methods. The same method was thus used for the component sized models with the addition of a material area to allow the effects of using a lining, or seat, material in the slipper.

4.4.1 Models and analyses

As with the cylindrical case once the method was verified by comparison with known solutions, it was used to determine the contact size and pressure distribution between components of an axial piston pump, namely the piston ball and slipper seat. Figure 4.4.1 shows an outline of the model. The addition of the slipper seat region to the model allows the effects of changing the material properties and thickness of this

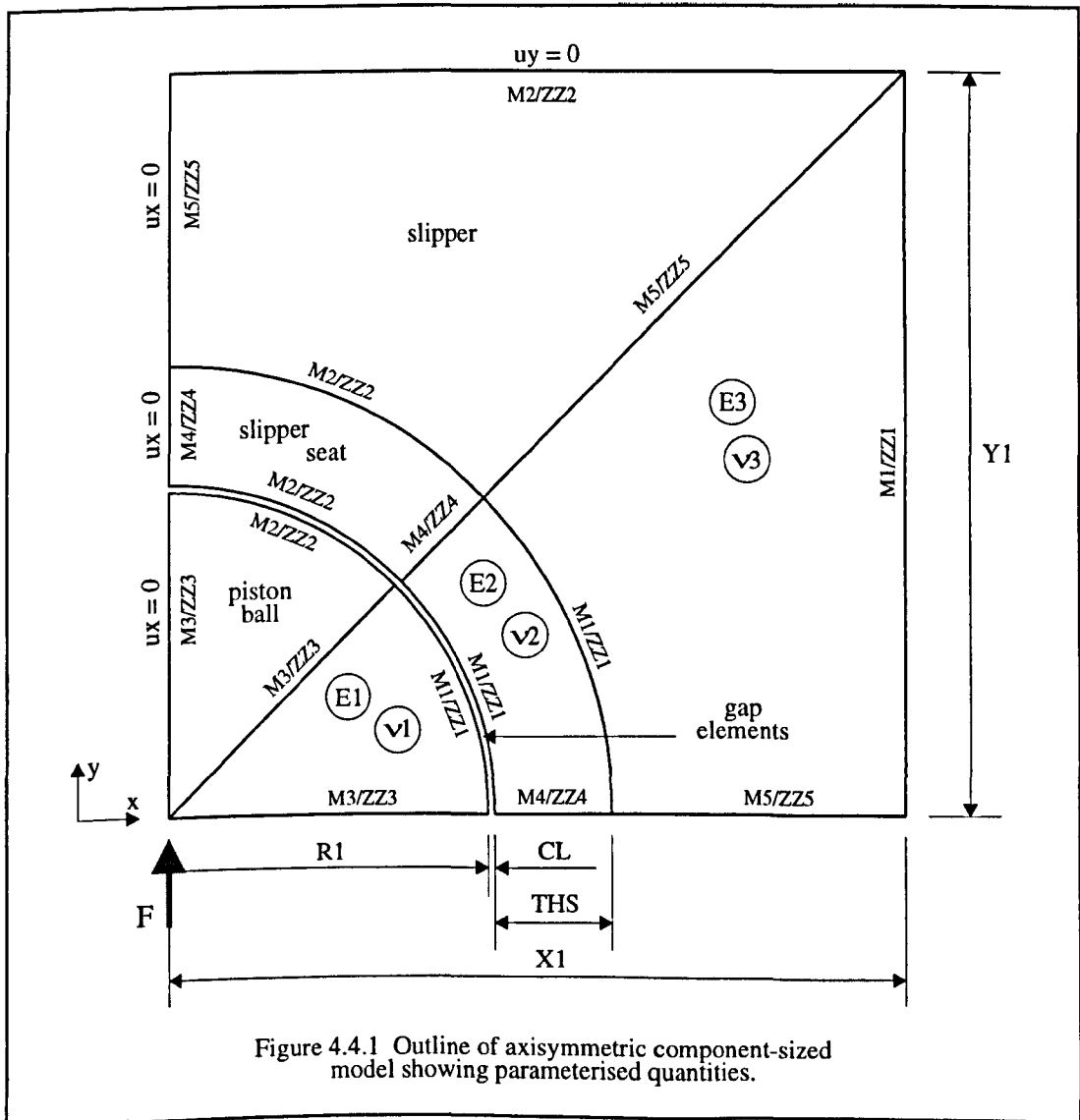


Figure 4.4.1 Outline of axisymmetric component-sized model showing parameterised quantities.

	E1 (GPa)	v1	E2 (GPa)	v2	E3 (GPa)	v3	CL (mm)	THS (mm)
different seat materials	200	0.3	200	0.3	200	0.3	0.0065	1.725
	200	0.3	210	0.25	200	0.3	0.0065	1.725
	200	0.3	70	0.3	200	0.3	0.0065	1.725
	200	0.3	310	0.28	200	0.3	0.0065	1.725
	200	0.3	10	0.4	200	0.3	0.0065	1.725
different seat thickness	200	0.3	10	0.4	200	0.3	0.0065	2.0
	200	0.3	10	0.4	200	0.3	0.0065	1.5
	200	0.3	10	0.4	200	0.3	0.0065	1.0
	200	0.3	10	0.4	200	0.3	0.0065	0.5
different radial clearance	200	0.3	10	0.4	200	0.3	0.01	1.0
	200	0.3	10	0.4	200	0.3	0.003	1.0
	200	0.3	10	0.4	200	0.3	0.001	1.0
	200	0.3	10	0.4	200	0.3	0.0001	1.0
	200	0.3	10	0.4	200	0.3	0.0	1.0

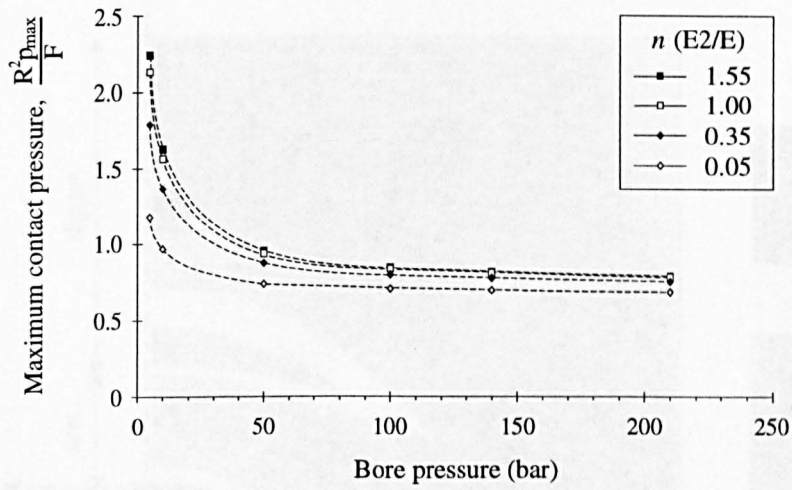
Table 4.4.1 Parameter combinations for the axisymmetric component-sized models.

component to be assessed. Again several series of analyses were undertaken and these are summarised in table 4.4.1.

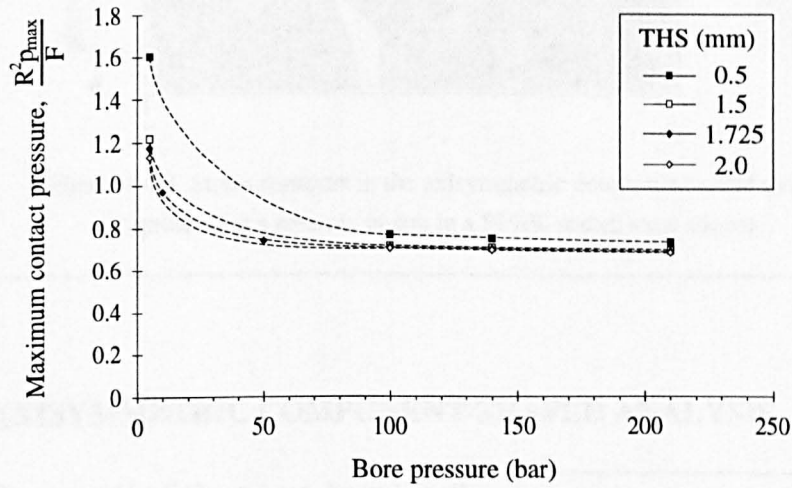
4.4.2 Results and discussion

Figure 4.4.2 shows graphs of bore pressure versus non-dimensionalised maximum contact pressure for seats of different stiffness and thickness and for different radial clearances. For seats of different stiffness the ratio n refers to the Young's modulus of the seat to the Young's modulus of the piston ball and slipper. As the seat material became stiffer the maximum contact pressure increased. Compliant slipper seats between 0.5 mm and 2.0 mm thick were considered and as expected as the thickness increased the maximum contact pressure became less indicating a greater contact angle. However, for loading equivalent to bore pressures over 100 bar there was little difference between a 1.5 mm thick seat and one of 2 mm. Again, as the clearance between the components increased the maximum contact pressure increased.

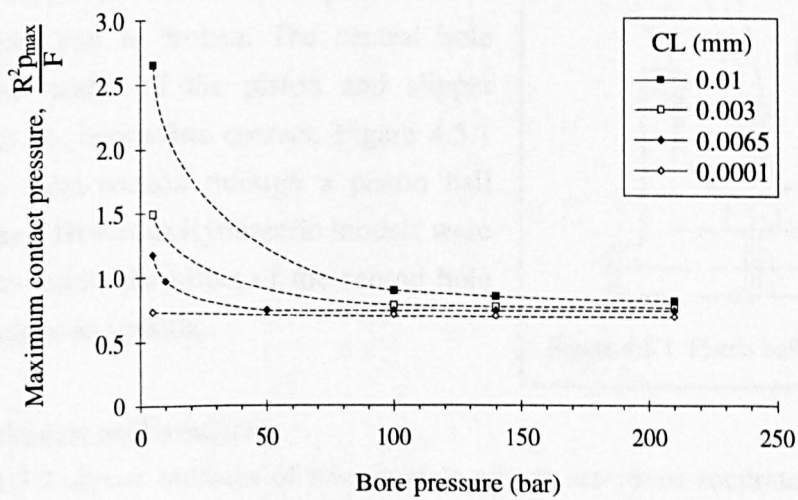
In addition to the analyses above, models with three different material properties were considered, for example, modelling a ceramic piston ball in a PEEK-lined steel slipper. Figure 4.4.3 shows the von-Mises stress contours for such an example at 140 bar. The contact angle between the components was 78.75°.



a) seat material of different stiffness.

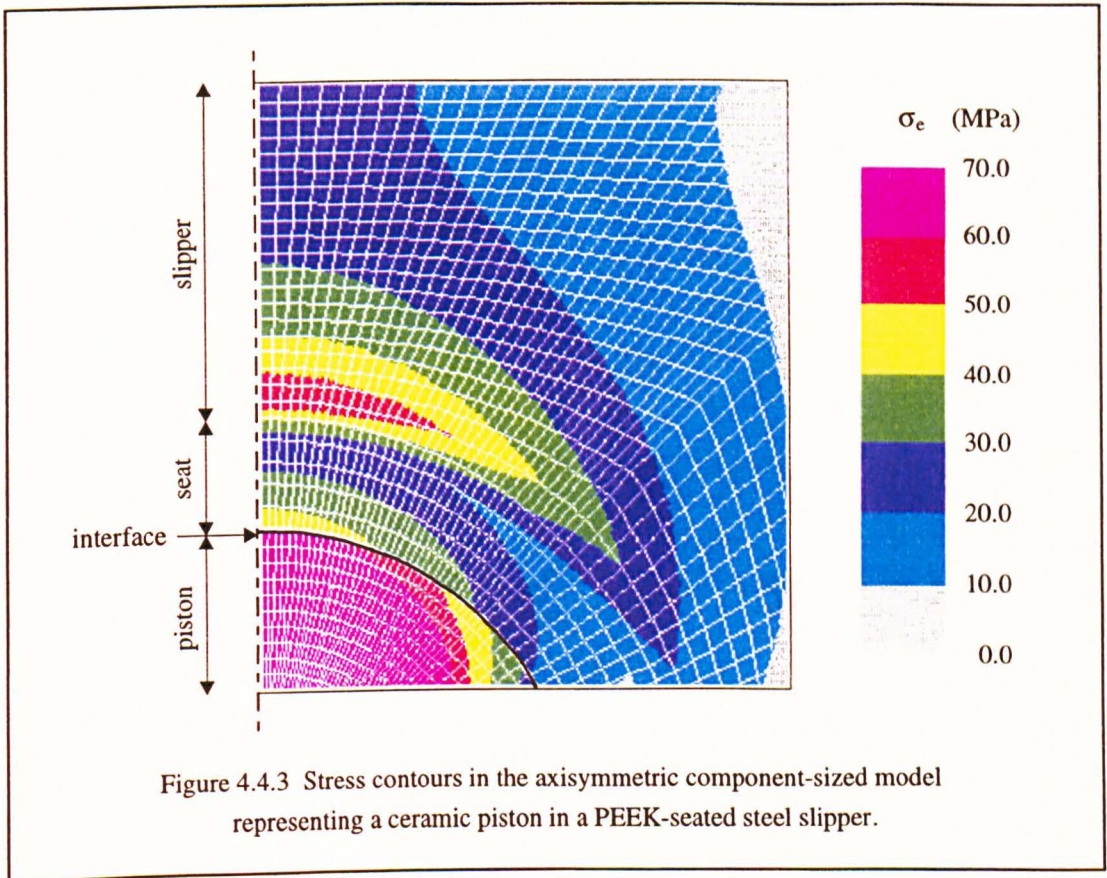


b) slipper seat of different thickness.



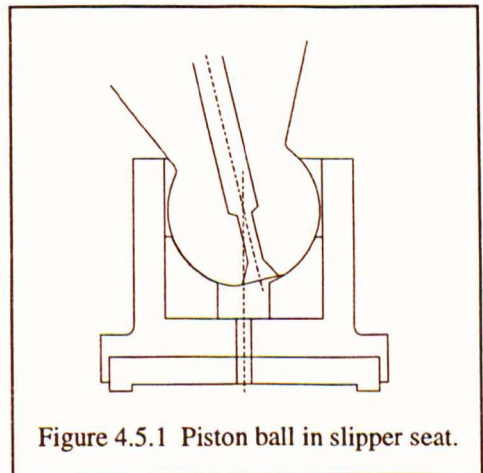
c) different radial clearance.

Figure 4.4.2 Graphs of maximum contact pressure versus bore pressure for the axisymmetric component-sized analysis.



4.5 AXISYMMETRIC COMPONENT-SHAPED ANALYSIS

Unlike the contact of the piston barrel in the cylinder block the contact of the piston ball in the slipper seat is broken. The central hole down the centre of the piston and slipper results in an incomplete contact. Figure 4.5.1 shows a cross-section through a piston ball and slipper. Hence, axisymmetric models were created to assess the effect of the central hole in the slipper and piston.



4.5.1 Models and analyses

Figure 4.5.2 shows outlines of two models which are more accurate axisymmetric representations of a slipper ball in a slipper seat. The minor differences in the hole configuration correspond to two different designs of slipper. Several runs were undertaken to assess the effect of the incomplete contact on the contact size and resulting pressure distribution.

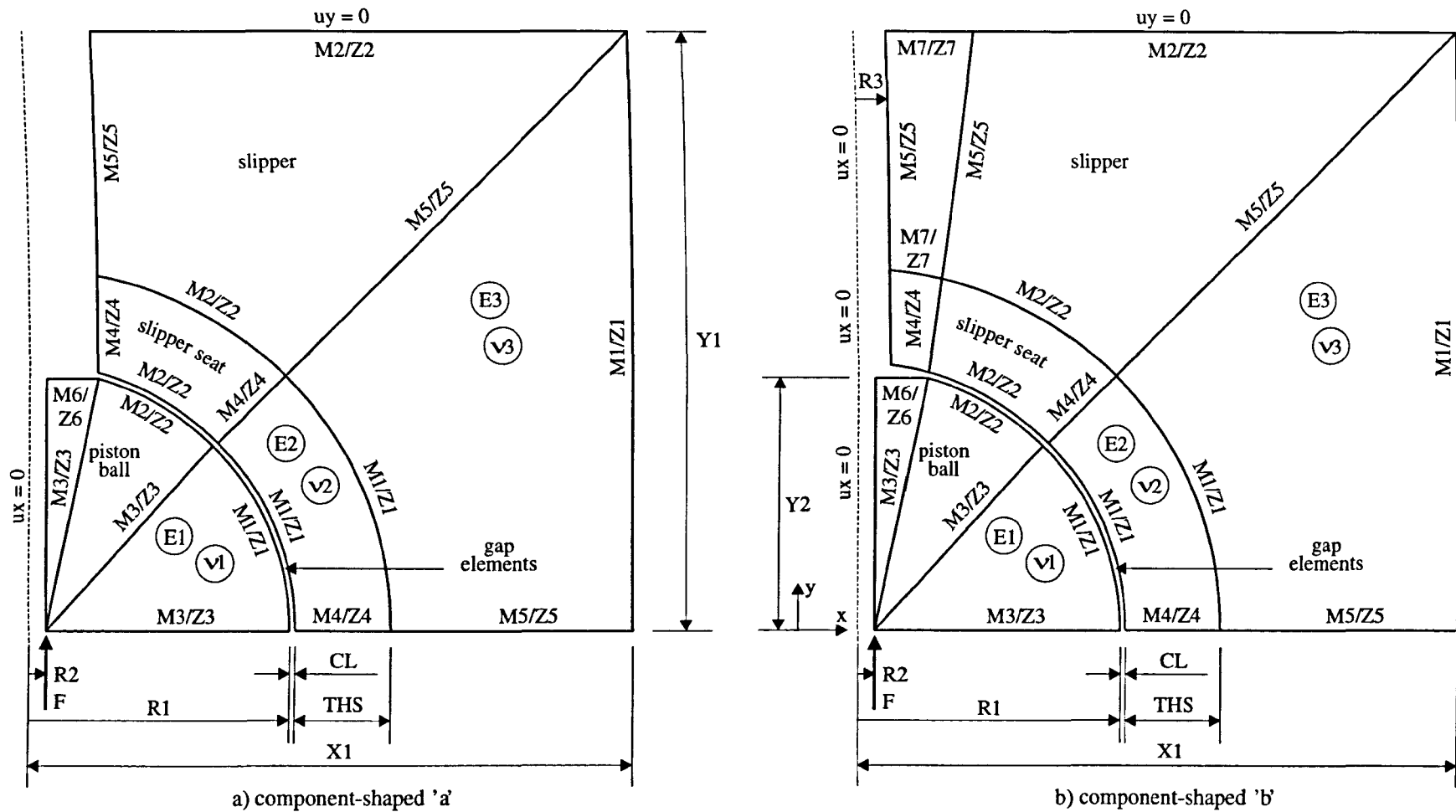
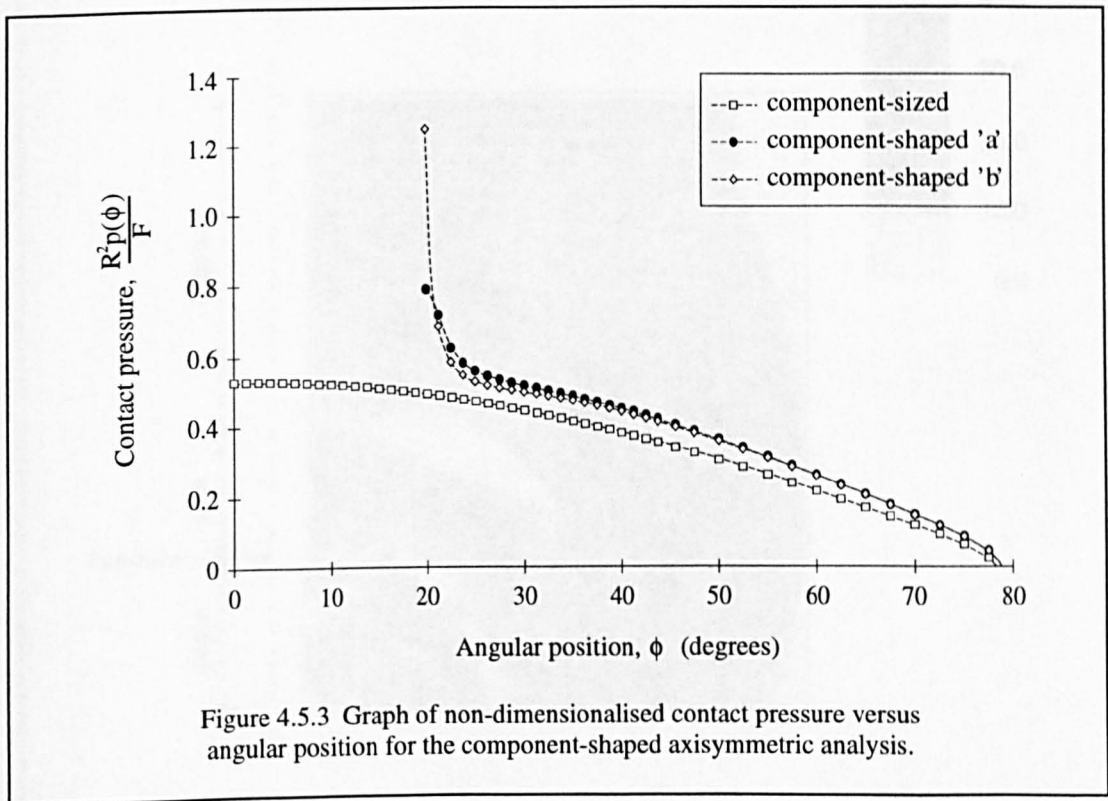


Figure 4.5.2 Outline of axisymmetric component-shaped models showing parameterised quantities.

4.5.2 Results and discussion

Figure 4.5.3 shows a graph of the non-dimensionalised contact pressure versus angular position around the interface between the piston ball and slipper seat for the two component-shaped axisymmetric models and the equivalent component-sized model analysed in Section 4.4. As can be seen the central holes result in a high pressure at the edge of contact but away from this region the contact pressure is not affected greatly, indeed the same number of gap elements closed in each case for the same materials, load and clearance. The slight difference in the contact pressure distribution compared to the equivalent component-sized model is due to the central hole and also to the fact that the load is not applied along the central axis.

Figure 4.5.4 shows the stress contours for the same material, force and clearance as in figure 4.4.3, that is, for a ceramic piston in a PEEK-seated steel piston at a bore pressure of 140 bar. Away from the flat region on the end of the piston ball the stress distribution in the models are very similar.



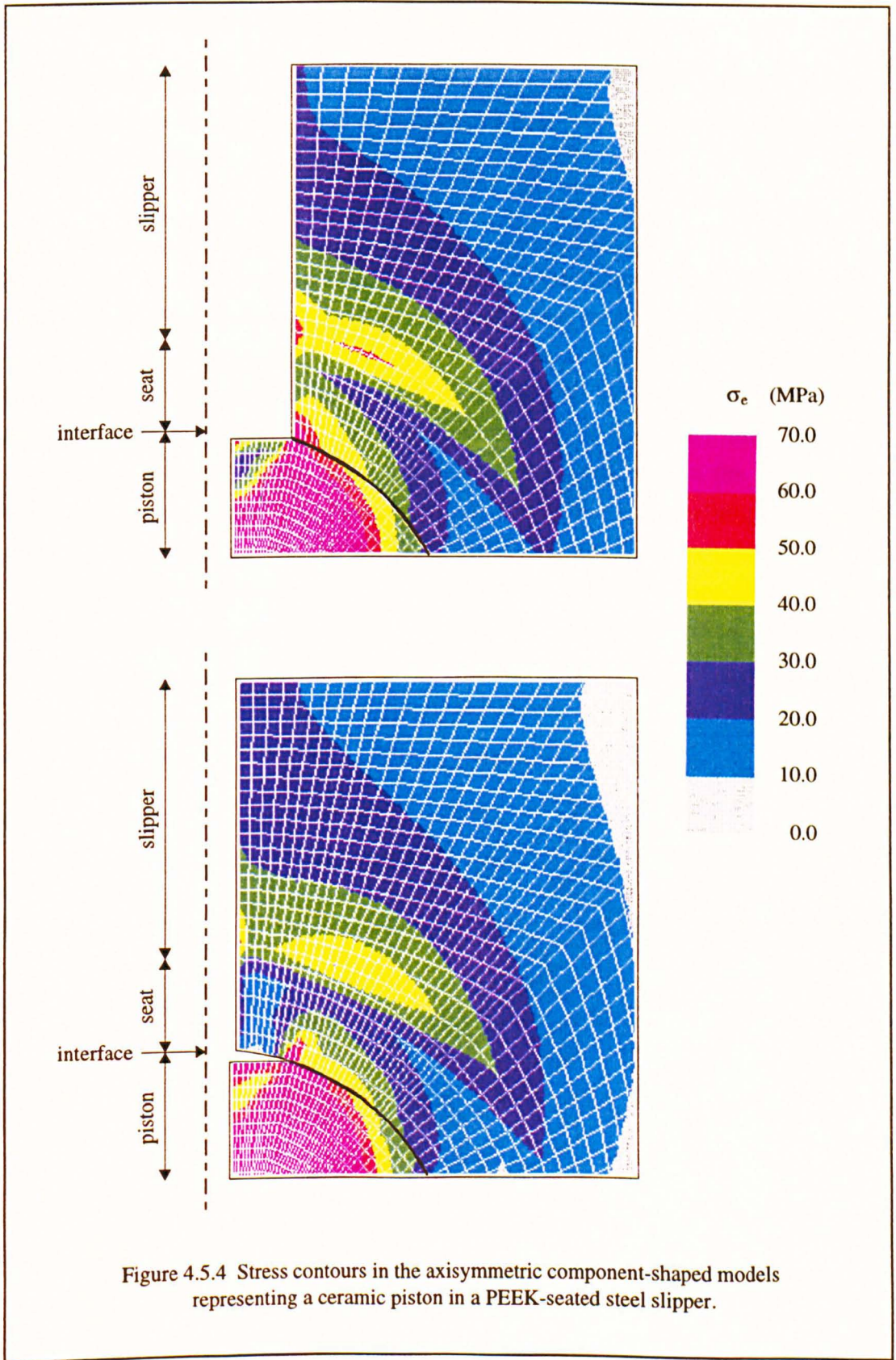


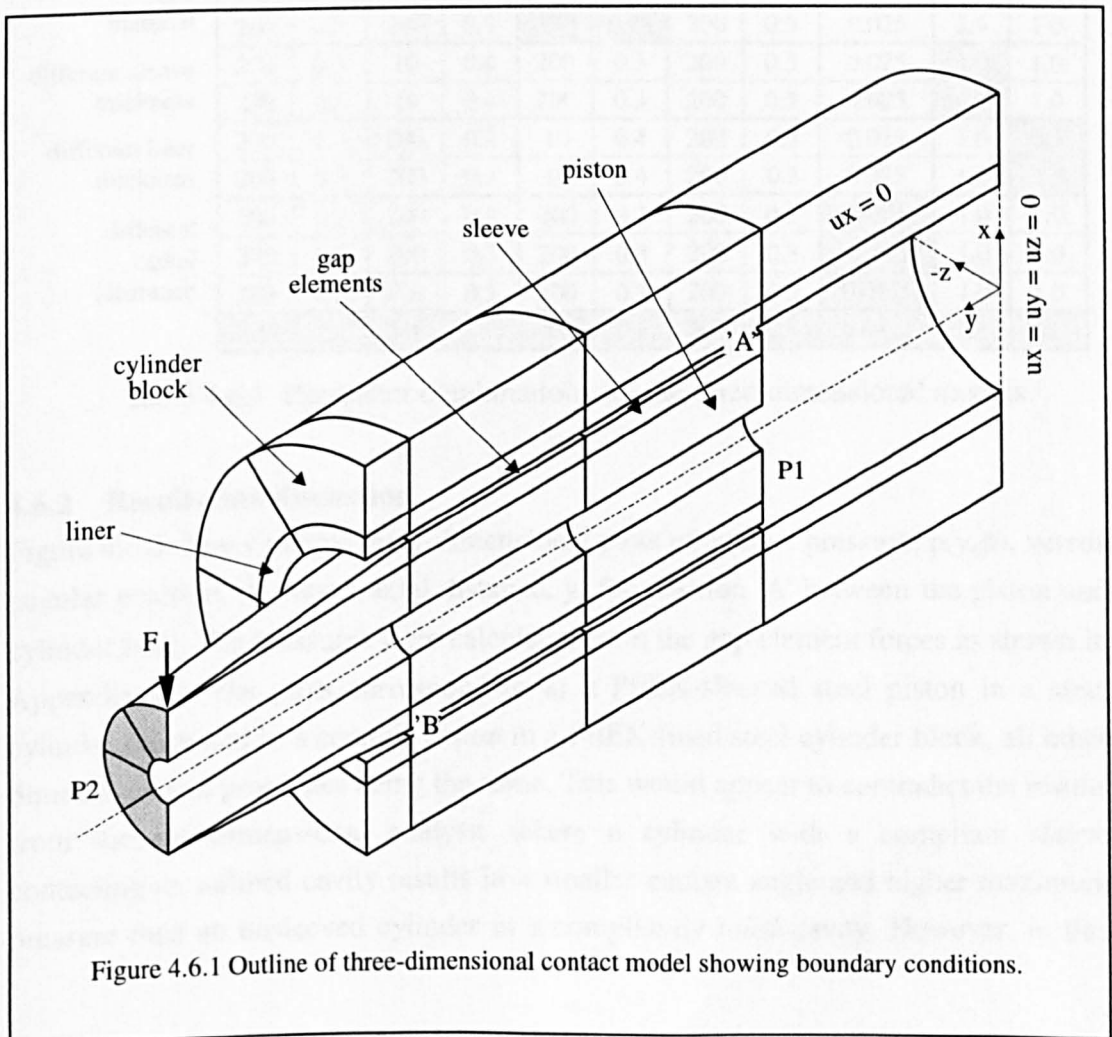
Figure 4.5.4 Stress contours in the axisymmetric component-shaped models representing a ceramic piston in a PEEK-seated steel slipper.

4.6 THREE-DIMENSIONAL ANALYSIS

The three-dimensional model was conducted to determine the contact pressure distribution between a piston and cylinder block bore allowing for the tilting of the piston inside the bore.

4.6.1 Models and analyses

Figure 4.6.1 shows an outline of the three-dimensional contact model and boundary conditions. It is a representation of half a sleeved piston inside a lined cylinder block, taking account of symmetry. It consists of five areas, namely the cylinder block, cylinder block liner, interface, piston sleeve and piston, and is meshed using three-dimensional solid elements and gap elements with no friction. The block and liner are constrained from moving in all three co-ordinate directions at the end furthest removed from the piston, i.e. the swash plate end of the cylinder block. Balanced pressures, P1 and P2, are applied to each end of the piston along its axis and a force, F, in the negative x-direction causes the piston to tilt within the bore. P1 is the bore pressure, determined in the timing analysis, P2 and F are calculated from a



knowledge of the geometry. 'A' and 'B' indicate the areas where the components are expected to contact. Figure 4.6.2 shows the parameters used in the creation of the models. Several analyses were run to assess the effects of changing the bore pressure, material properties, sleeve and liner thickness and clearance size on the contact pressure distribution and size between the components and these are summarised in table 4.6.1. Four load cases were run in each case, corresponding to bore pressures of 100, 140, 180 and 210 bar.

	E1 (GPa)	v1	E2 (GPa)	v2	E3 (GPa)	v3	E4 (GPa)	v4	CL (mm)	THS (mm)	THL (mm)
all materials the same	200	0.3	200	0.3	200	0.3	200	0.3	0.025	2.5	1.0
	100	0.3	100	0.3	100	0.3	100	0.3	0.025	2.5	1.0
	70	0.3	70	0.3	70	0.3	70	0.3	0.025	2.5	1.0
	300	0.28	300	0.28	300	0.28	300	0.28	0.025	2.5	1.0
different sleeve materials	200	0.3	10	0.4	200	0.3	200	0.3	0.025	2.5	1.0
	200	0.3	70	0.3	200	0.3	200	0.3	0.025	2.5	1.0
	200	0.3	310	0.28	200	0.3	200	0.3	0.025	2.5	1.0
	200	0.3	10	0.4	200	0.3	200	0.3	0.0125	2.5	1.0
different liner material	200	0.3	200	0.3	10	0.4	200	0.3	0.025	2.5	1.0
	200	0.3	200	0.3	70	0.3	200	0.3	0.025	2.5	1.0
	200	0.3	200	0.3	310	0.28	200	0.3	0.025	2.5	1.0
different sleeve thickness	200	0.3	10	0.4	200	0.3	200	0.3	0.025	1.0	1.0
	200	0.3	10	0.4	200	0.3	200	0.3	0.025	4.0	1.0
different liner thickness	200	0.3	200	0.3	10	0.4	200	0.3	0.025	1.0	0.5
	200	0.3	200	0.3	10	0.4	200	0.3	0.025	1.0	1.5
different radial clearance	200	0.3	200	0.3	200	0.3	200	0.3	0.001	1.0	1.0
	200	0.3	200	0.3	200	0.3	200	0.3	0.005	1.0	1.0
	200	0.3	200	0.3	200	0.3	200	0.3	0.0125	1.0	1.0
	210	0.25	210	0.25	10	0.4	200	0.3	0.0125	2.5	1.0

Table 4.6.1 Parameter combinations for the three-dimensional models.

4.6.2 Results and discussion

Figure 4.6.3 shows sample three-dimensional plots of contact pressure, $p(y, \phi)$, versus angular position, ϕ , versus axial distance, y , for position 'A' between the piston and cylinder bore. The pressures were calculated from the gap element forces as shown in Appendix IV. The plots correspond to a) a PEEK-sleeved steel piston in a steel cylinder block and b) a ceramic piston in a PEEK-lined steel cylinder block, all other dimensions and properties being the same. This would appear to contradict the results from the two-dimensional analysis where a cylinder with a compliant sleeve contacting an unlined cavity results in a smaller contact angle and higher maximum pressure than an unsleeved cylinder in a compliantly-lined cavity. However, in this

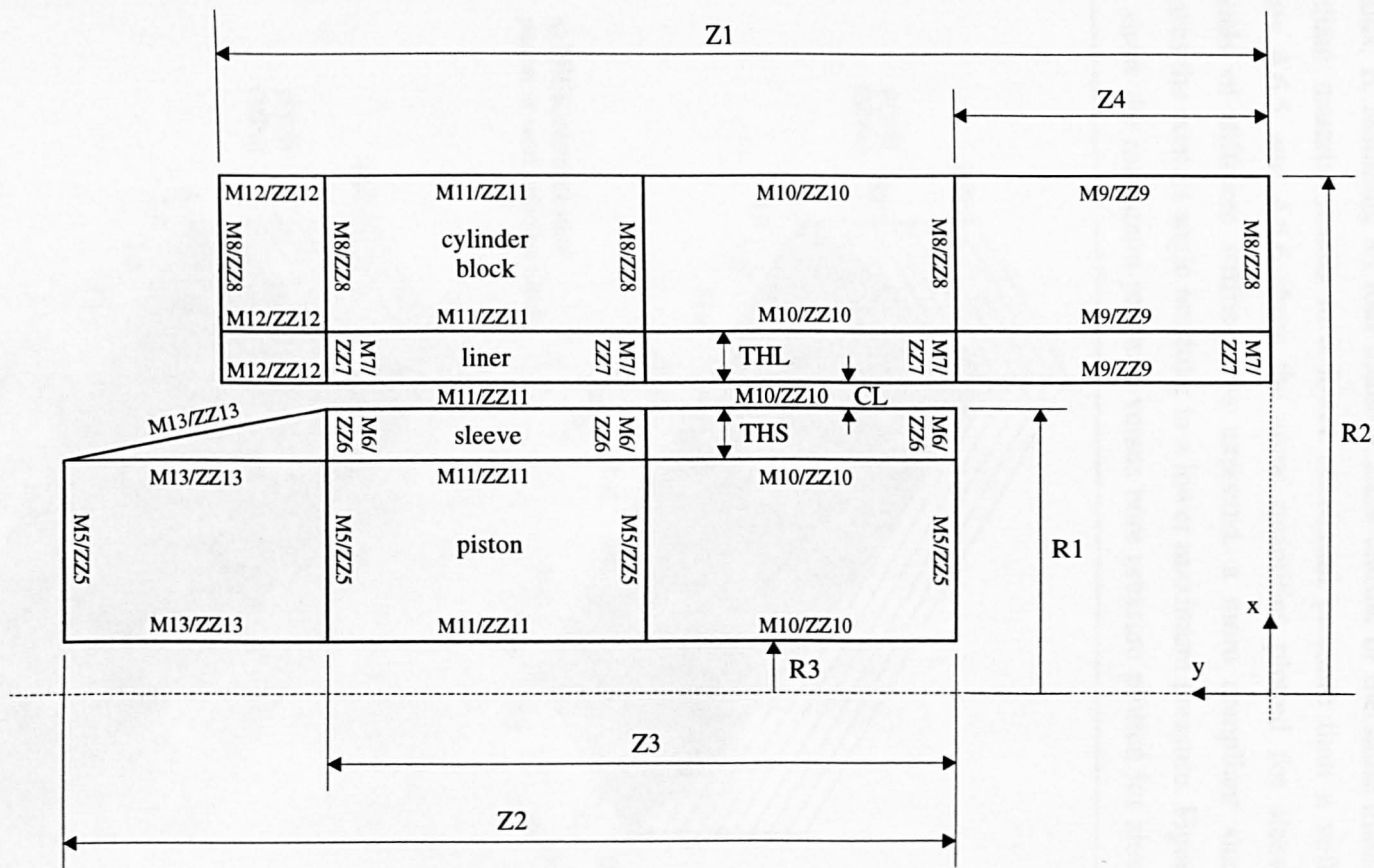
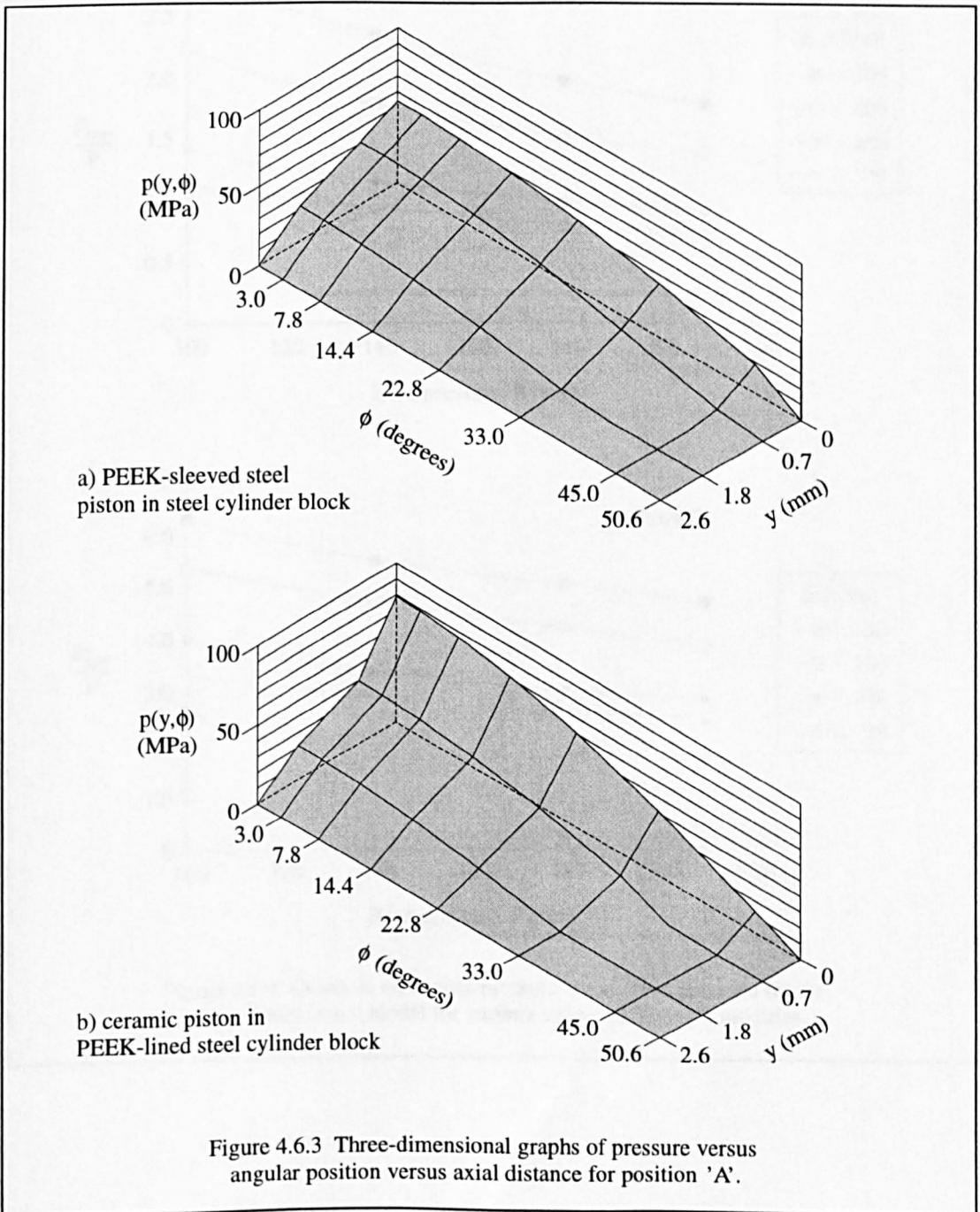


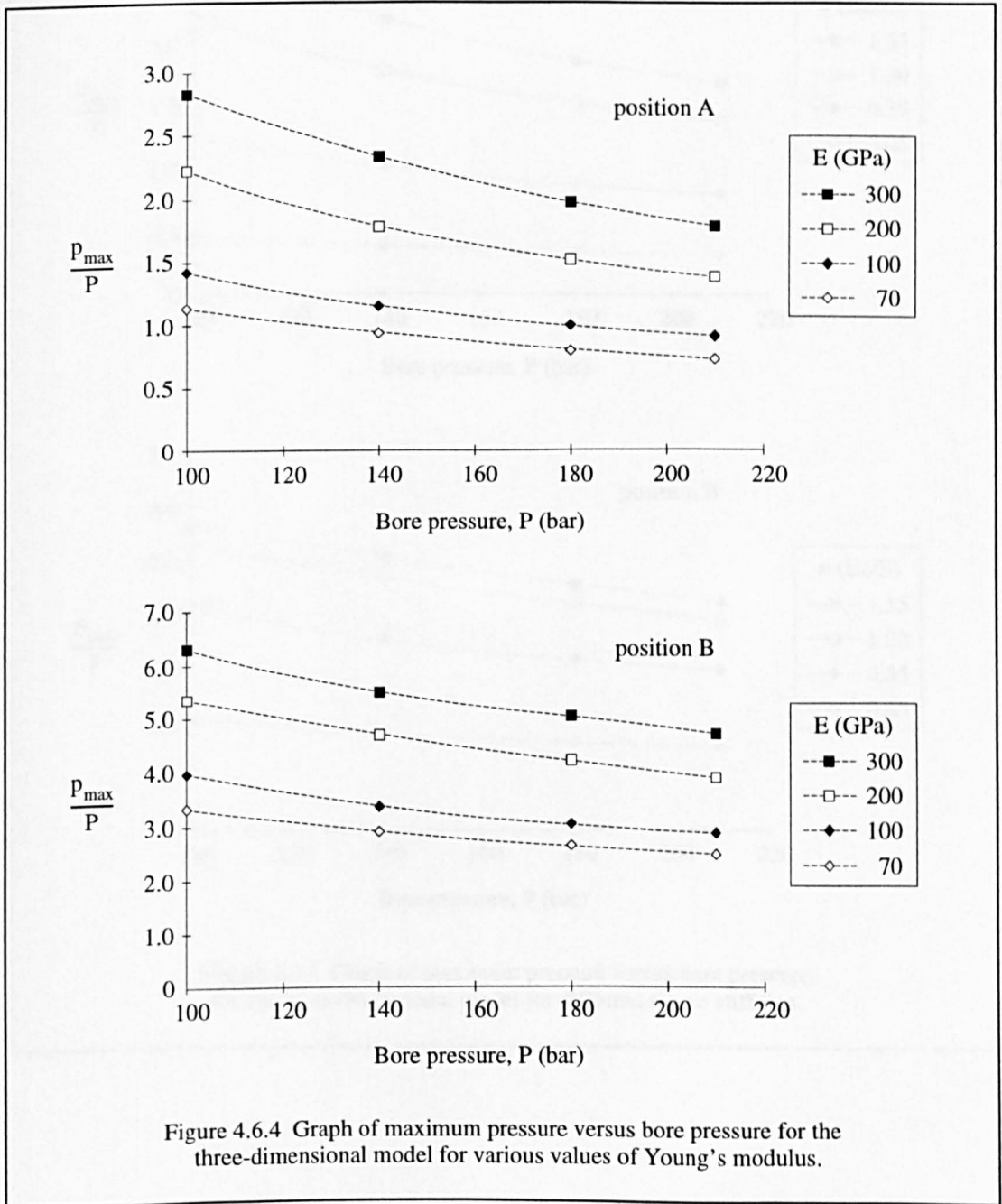
Figure 4.6.2 Outline of three-dimensional contact model showing parameterised quantities.

case the sleeve thickness is much greater than the liner thickness and therefore the results are not directly comparable.

Figure 4.6.4 shows graphs of maximum pressure over bore pressure, p_{\max}/P , versus bore pressure, P , at positions 'A' and 'B' for various values of Young's modulus, E , assuming all four material areas consist of the same material. A more compliant material results in a lower maximum pressure than a stiffer material. Figures 4.6.5 and 4.6.6 show the same quantities plotted for sleeve and liner materials of different stiffness. As expected, a more compliant sleeve or liner increases the contact angle resulting in a lower maximum pressure. Figures 4.6.7 and 4.6.8 show the maximum pressure versus bore pressure plotted for sleeve and liner



materials of different thickness assuming the sleeve or liner is more compliant than the piston of cylinder block. In this case as the thickness of the liner or sleeve increases the maximum contact pressure is reduced. However, if the sleeve or liner was stiffer the situation would be reversed. Figure 4.6.9 again shows the same quantities, this time for different radial clearance. As the radial clearance becomes smaller the contact angle increases thus reducing the maximum contact pressure.



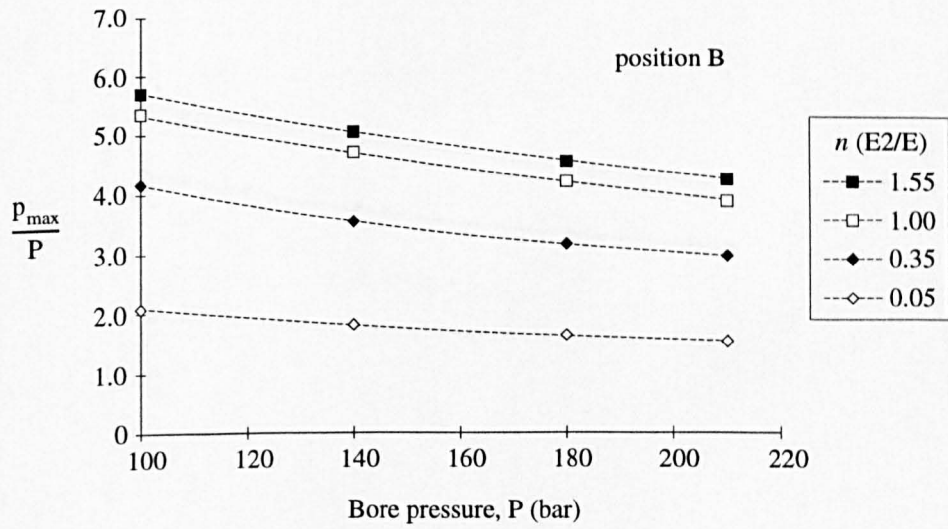
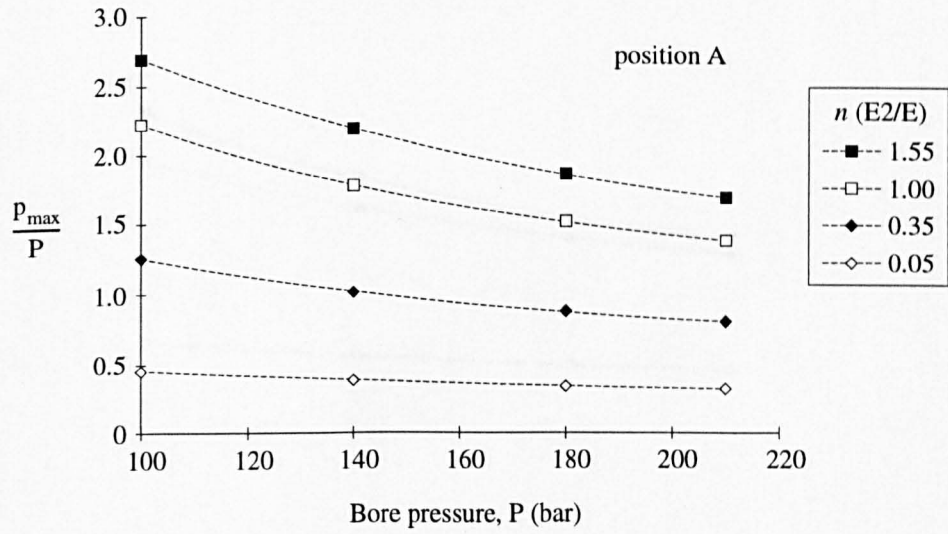


Figure 4.6.5 Graph of maximum pressure versus bore pressure for the three-dimensional model for different sleeve stiffness.

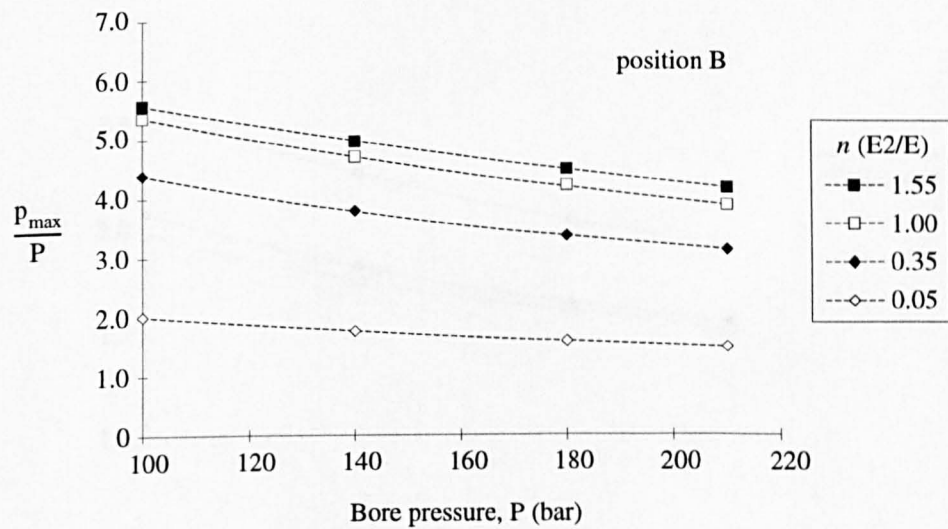
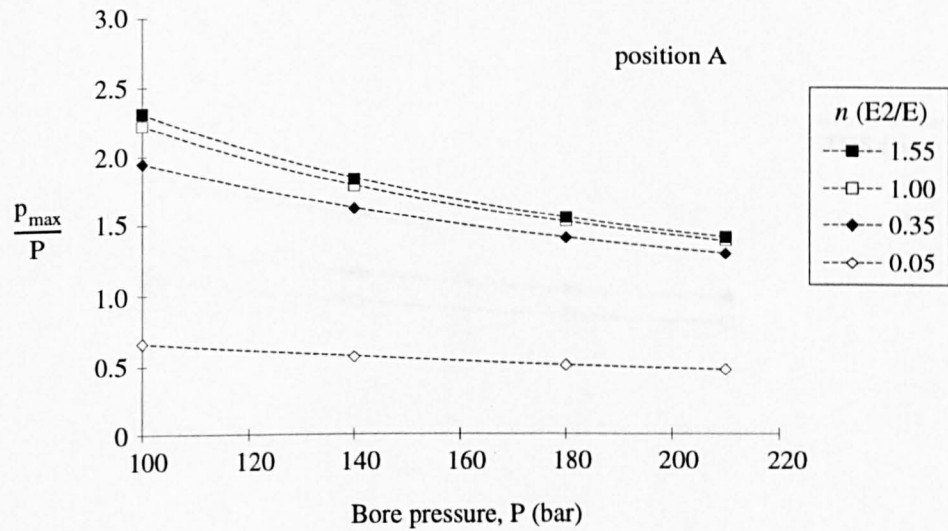


Figure 4.6.6 Graph of maximum pressure versus bore pressure for the three-dimensional model for different liner stiffness.

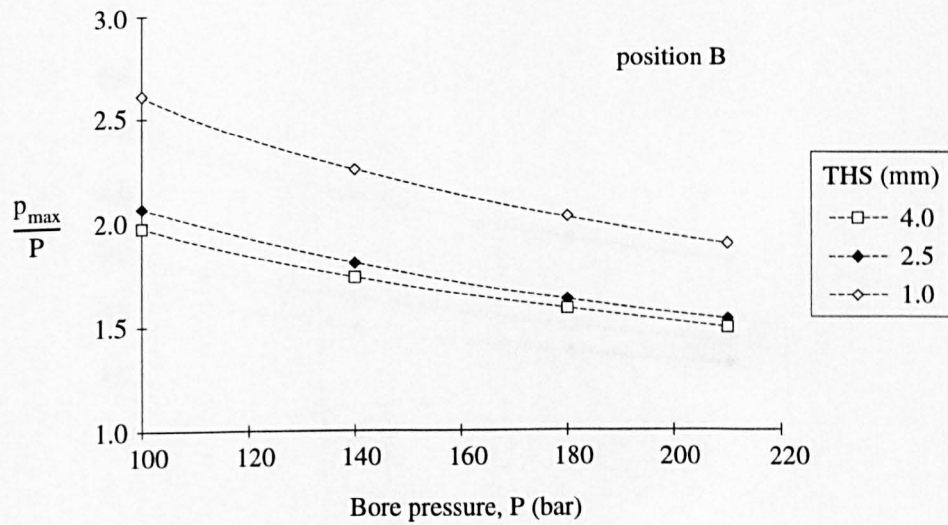
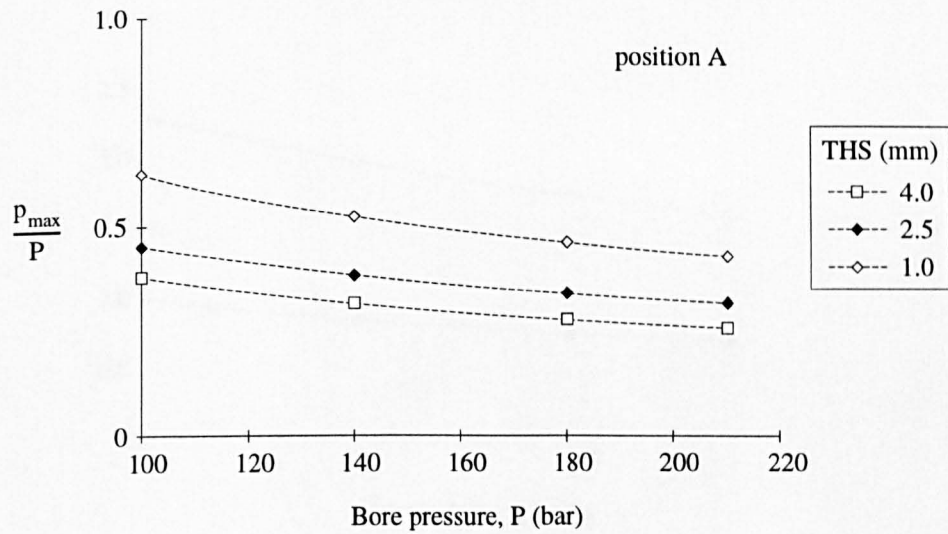


Figure 4.6.7 Graph of maximum pressure versus bore pressure for the three-dimensional model for different sleeve thickness.

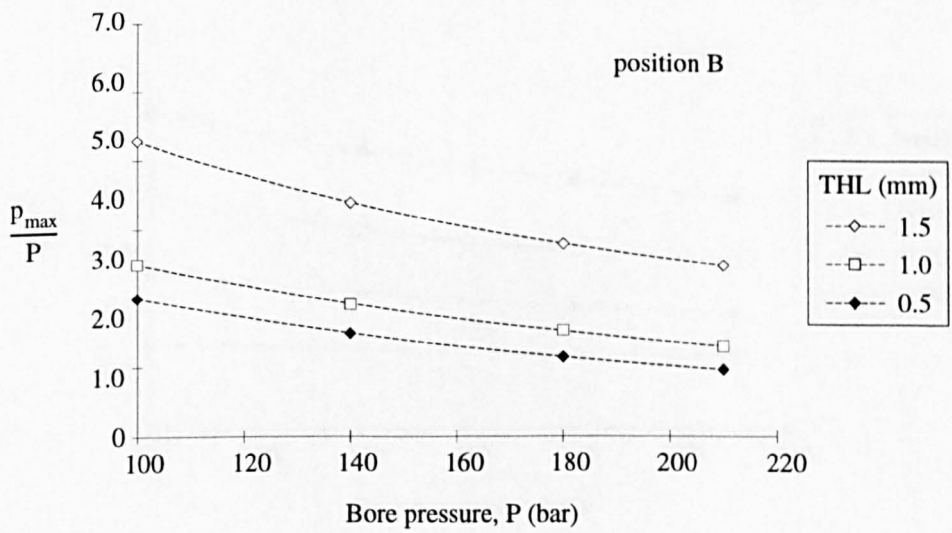
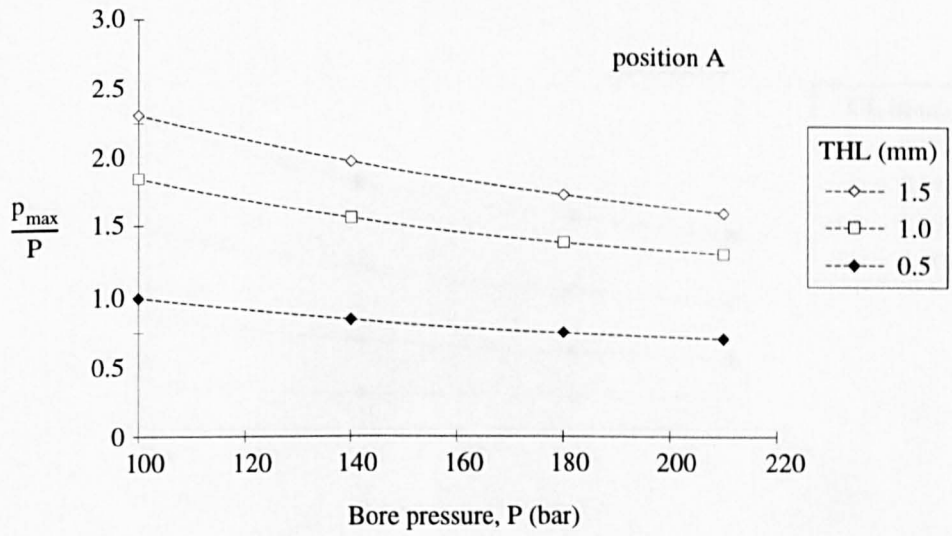


Figure 4.6.8 Graph of maximum pressure versus bore pressure for the three-dimensional model for different liner thickness.

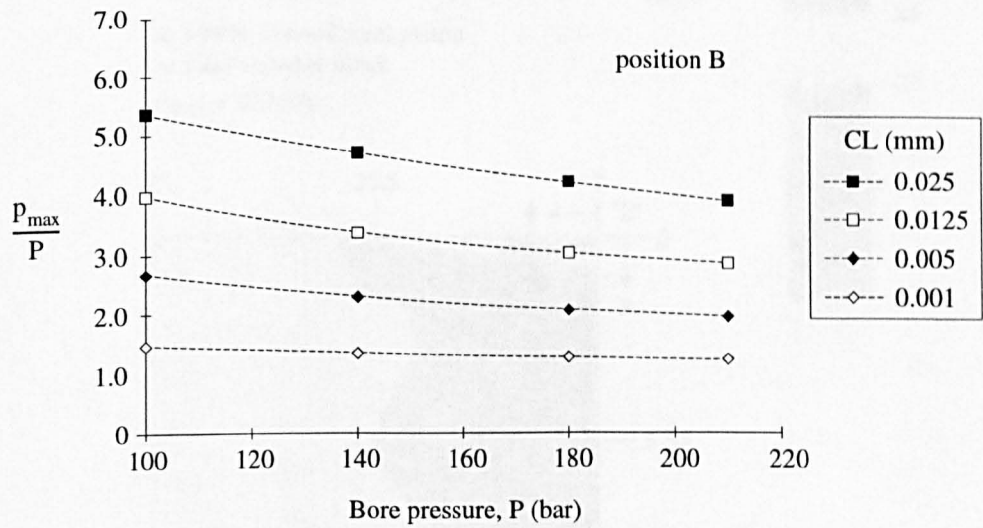
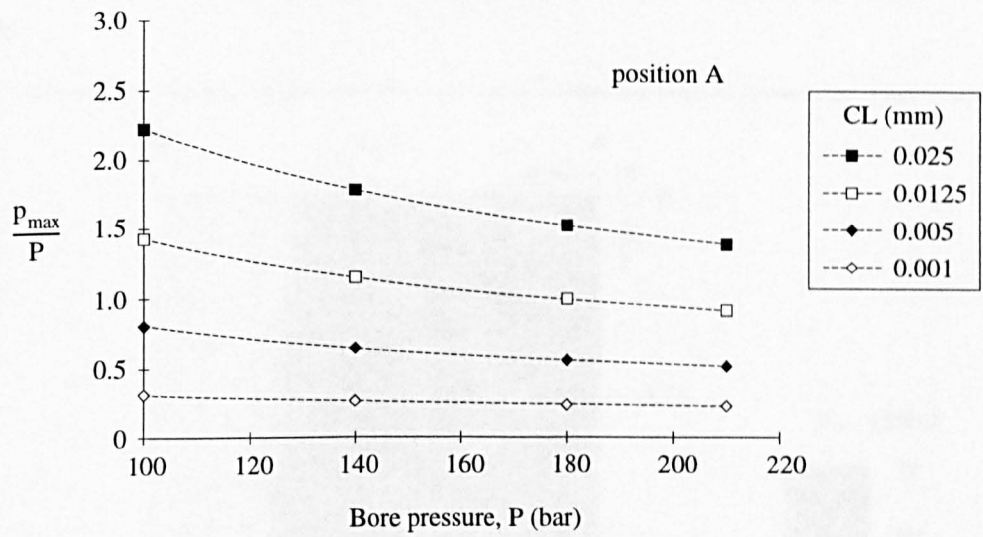
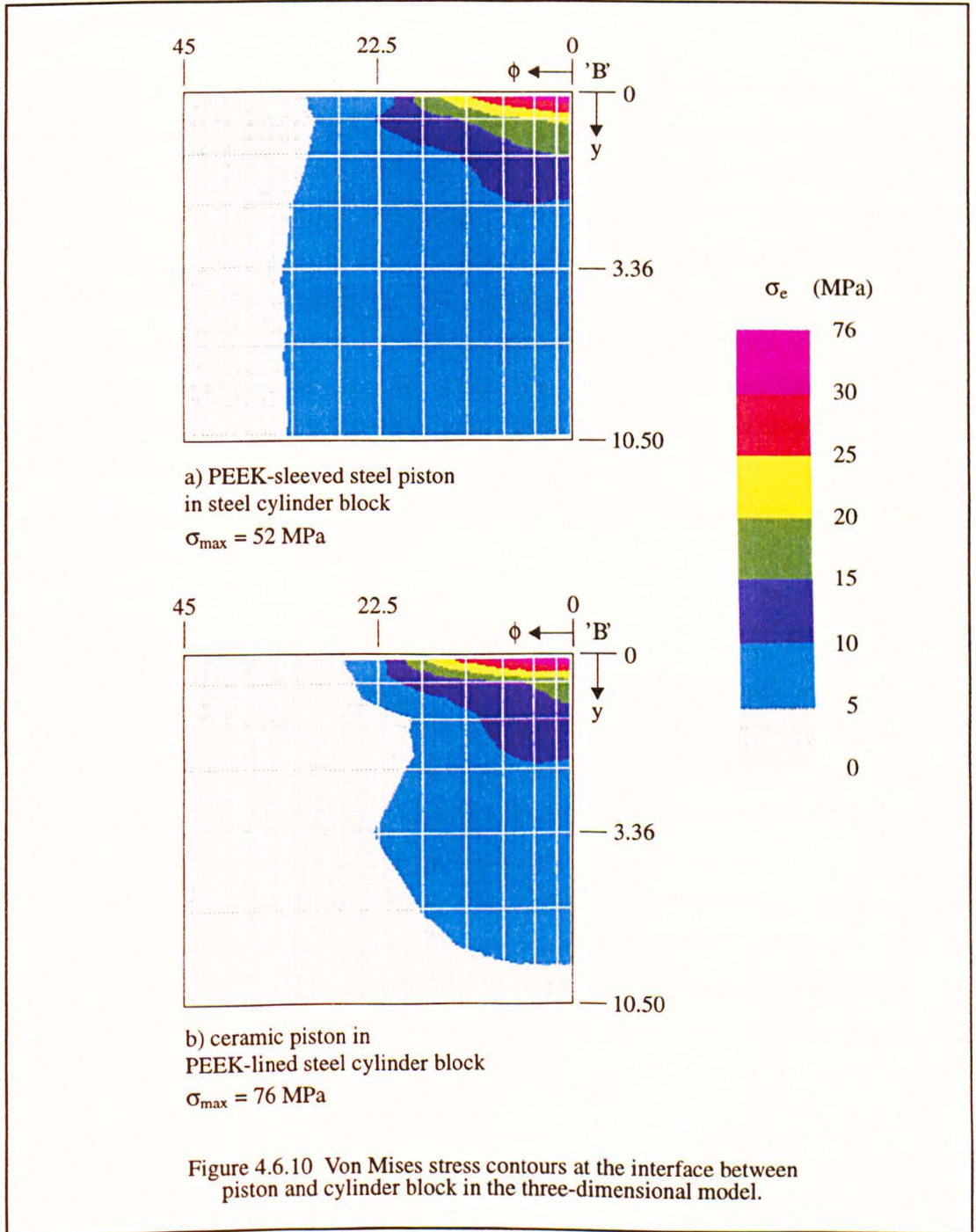


Figure 4.6.9 Graph of maximum pressure versus bore pressure for the three-dimensional model for different radial clearance.

Figure 4.6.10 shows sample plots of the von Mises stress contours around the interface at position B between the two components. The plots correspond to a) a PEEK-sleeved steel piston in a steel cylinder block and b) a ceramic piston in a PEEK-lined steel cylinder block, all other dimensions and properties being the same. The former has a greater contact area and hence a lower contact pressure than the latter.



CHAPTER 5

FINITE ELEMENT ANALYSES - COMPONENTS

5.0 INTRODUCTION

This chapter describes the finite element models and analyses undertaken to obtain a representation of the entire stress distribution in certain key components of an axial piston pump. Most of the analyses were undertaken using component configurations relevant to the Water Hydraulics project at the University of Hull. The contact pressure distributions from the analyses described in Chapter 4 were used as loading on models of the cylinder block, pistons and slippers of the appropriate configuration, i.e. with the same size, materials and clearance. Figure 5.0.1 shows the relationship between the contact models and component models. Separating the contact distribution analysis from the component analysis allowed more complex models to be created than would otherwise have been the case.

Sample results from the analyses are presented in this chapter and a general discussion of the results in Chapter 7.

5.0.1 Model parameterisation and convergence

In each case the model was parameterised to allow all input such as dimensions, material properties, loading, mesh density and element type to be varied with the minimum of additional work. The DISPLAY III pre-processor was used to create the models with session file input, the session file containing the appropriate parameters, and the NISA II finite element package was used to run the analyses.

Model convergence was tested by systematically increasing the mesh density and plotting sample output. The models were assumed to have converged when an increase in mesh density did not result in an appreciable change in the output or the result was acceptably close to a known analytical value. Convergence curves are shown for the models in the appropriate sections.

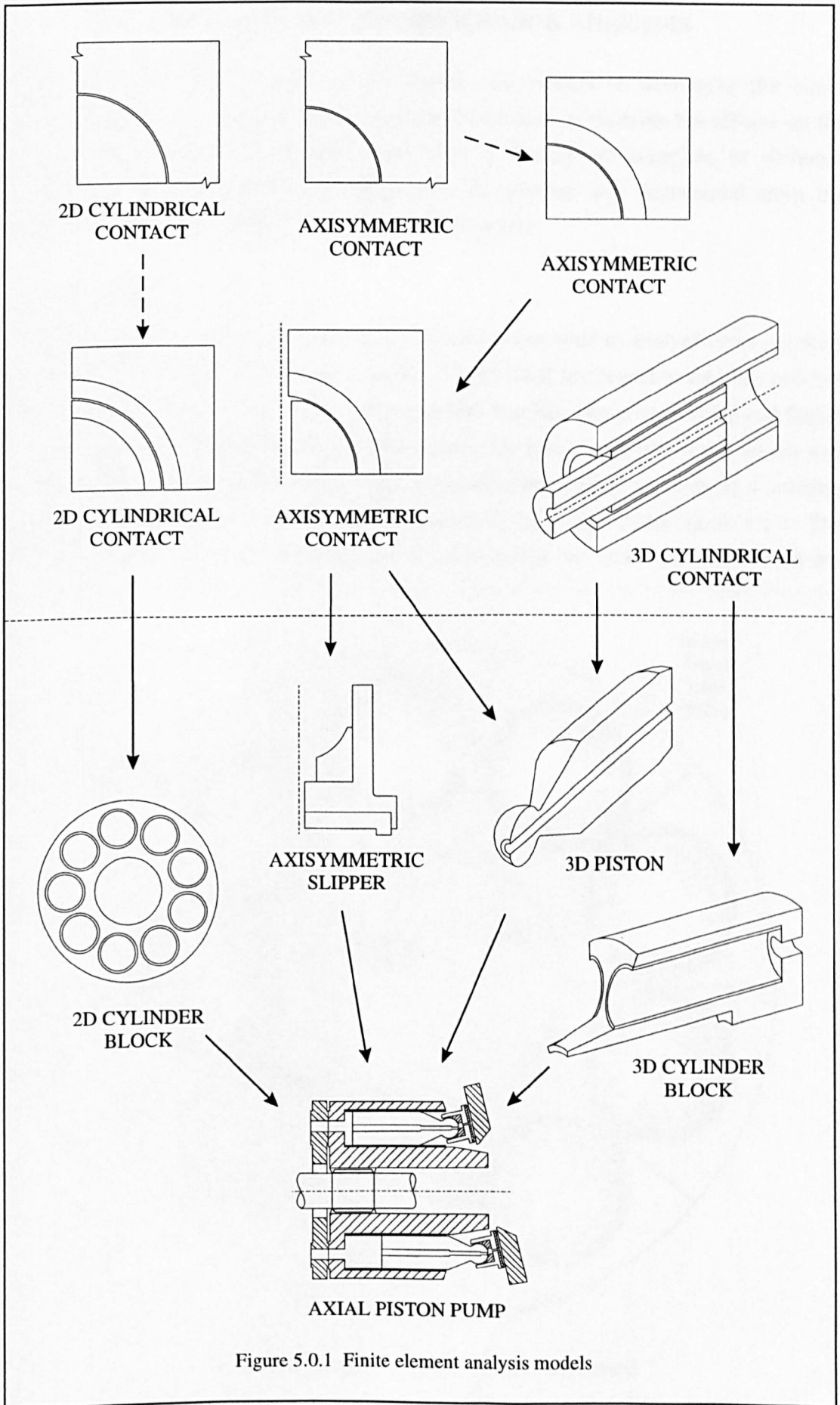


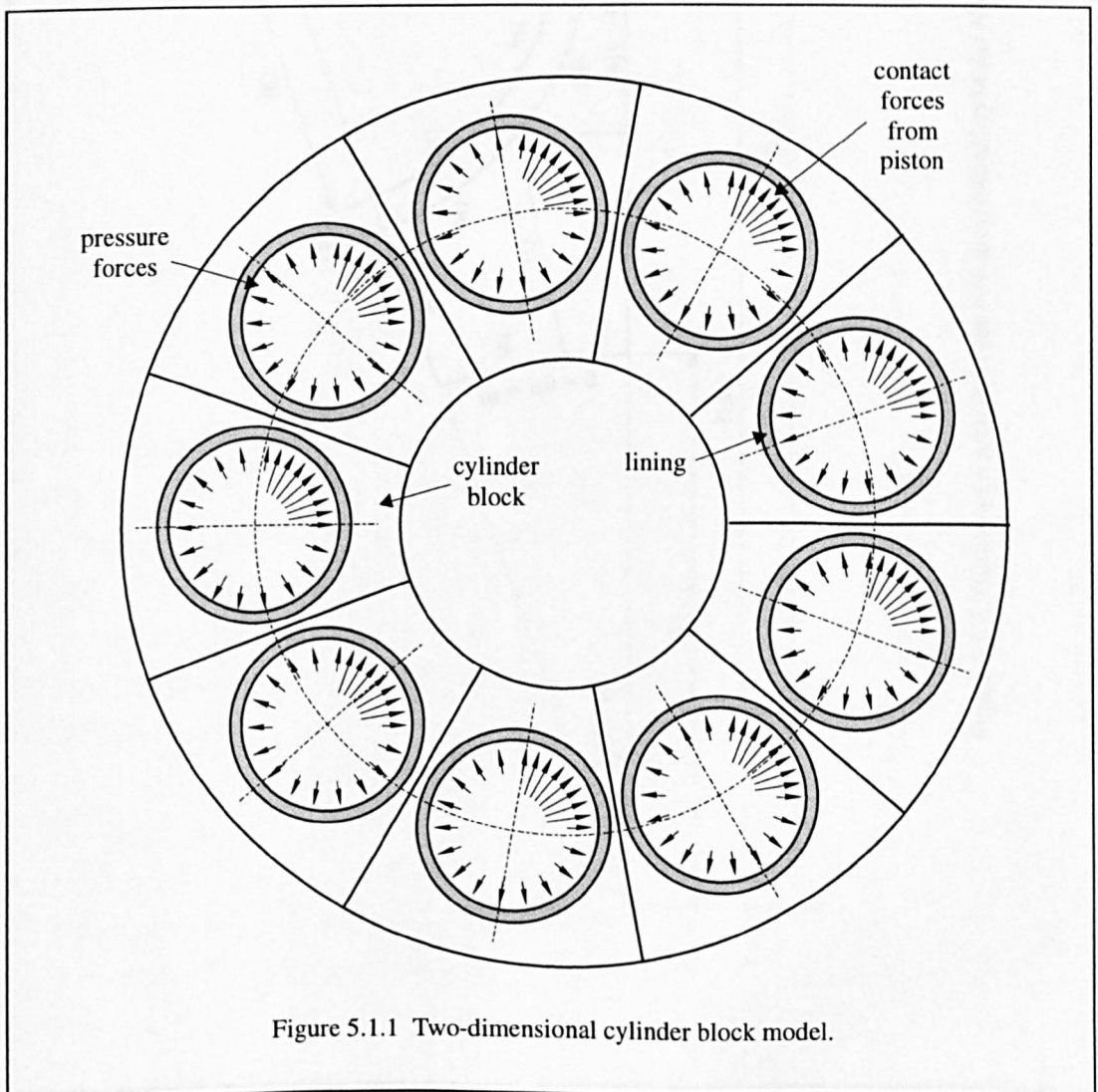
Figure 5.0.1 Finite element analysis models

5.1 TWO-DIMENSIONAL CYLINDER BLOCK ANALYSIS

The two-dimensional cylinder block model was created to determine the stress distribution in cross-sections of the cylinder block and to examine the effects on the stress distribution of lining the bores with a variety of materials of different thicknesses. Contact pressure loading from the pistons was determined from the appropriate two-dimensional component-sized model.

5.1.1 Model

Figure 5.1.1 shows the outline of the model which was used to analyse cross-sections of the cylinder block. The model consists of nine lined bores and as can be seen has rotational symmetry. Each of the nine segments also has planar symmetry and figure 5.1.2 shows the parameterised quantities used in the creation of the model which was meshed using second order plane strain elements. The loading consists of a uniform pressure and contact pressures from the pistons as indicated in the figure 5.1.1. The uniform pressure and contact pressures are related but the latter also depend on the



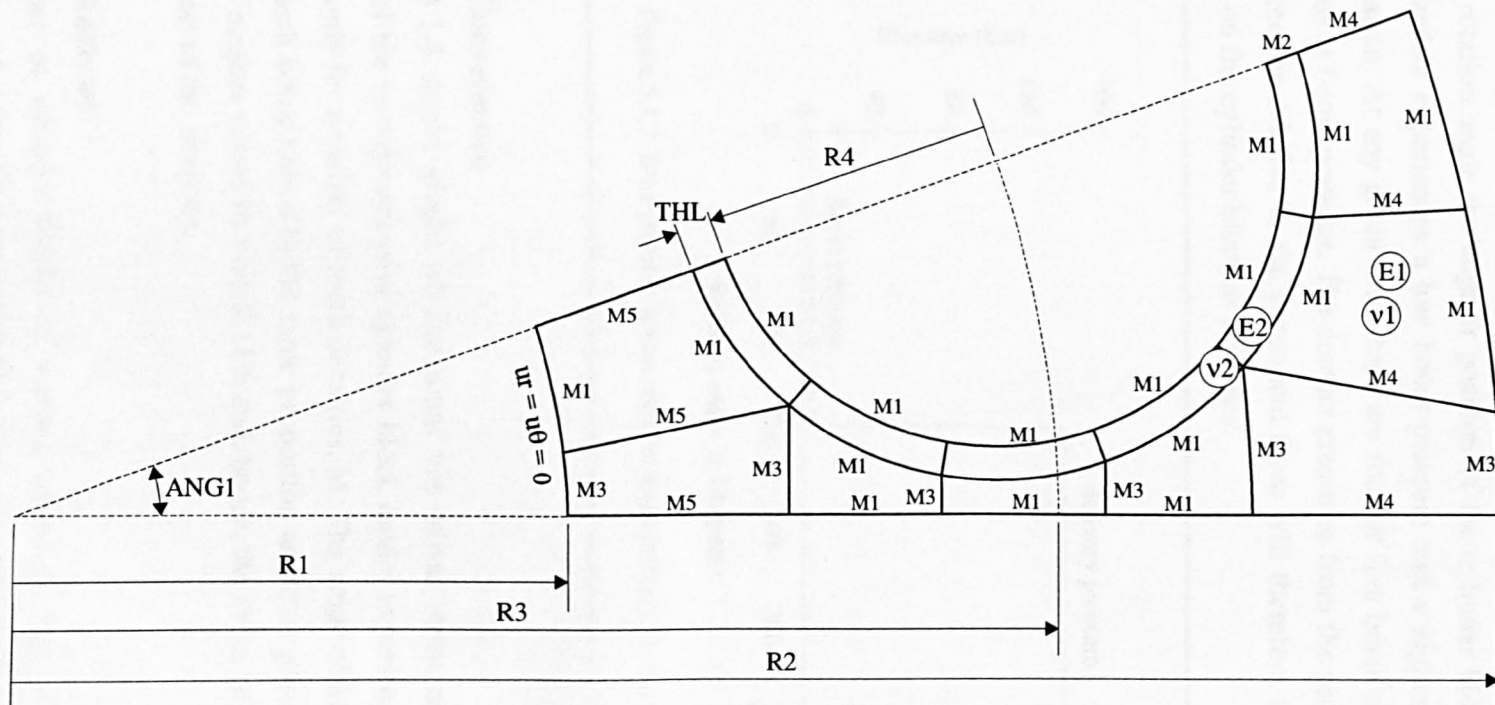
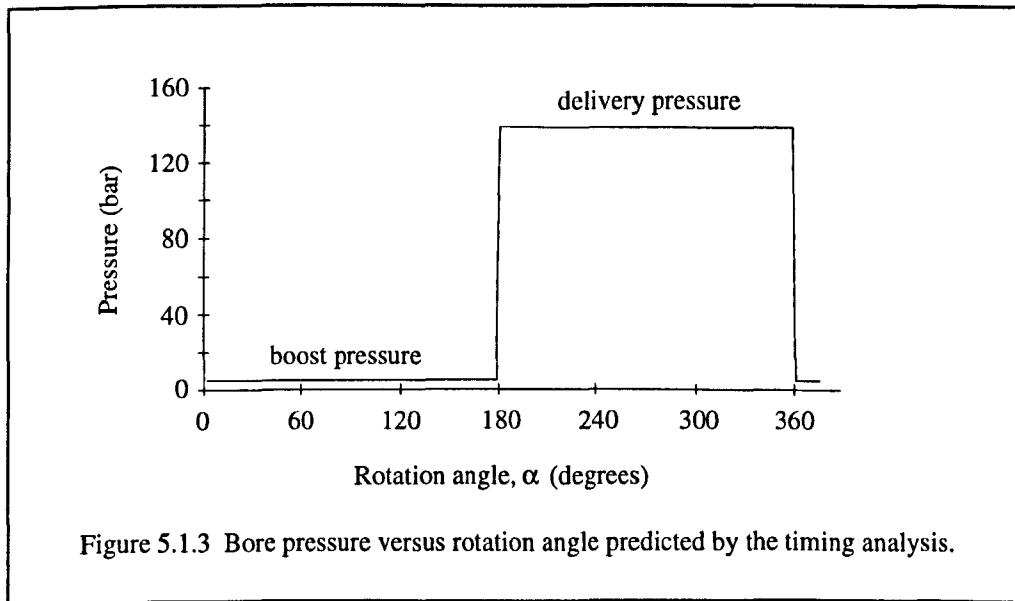


Figure 5.1.2 Outline of a section of the two-dimensional cylinder block model showing parameterised quantities.

material properties, clearance and sleeve or liner thickness.

Figure 5.1.3 shows a graph of pressure versus rotation angle predicted by a timing analysis written as part of the Water Hydraulics project at the University of Hull (Radcliffe et al, 1991). The pressure refers to the uniform pressure in each bore and the rotation angle the angular position of the cylinder block as it rotates. Each bore therefore experiences a low boost pressure and a higher delivery pressure on each rotation. At any given time there are four or five bores at delivery and five or four bores at boost pressure. The contact pressures from the pistons always act in the same direction relative to the pump and these will therefore impinge in a different position on the cylinder block as it rotates.

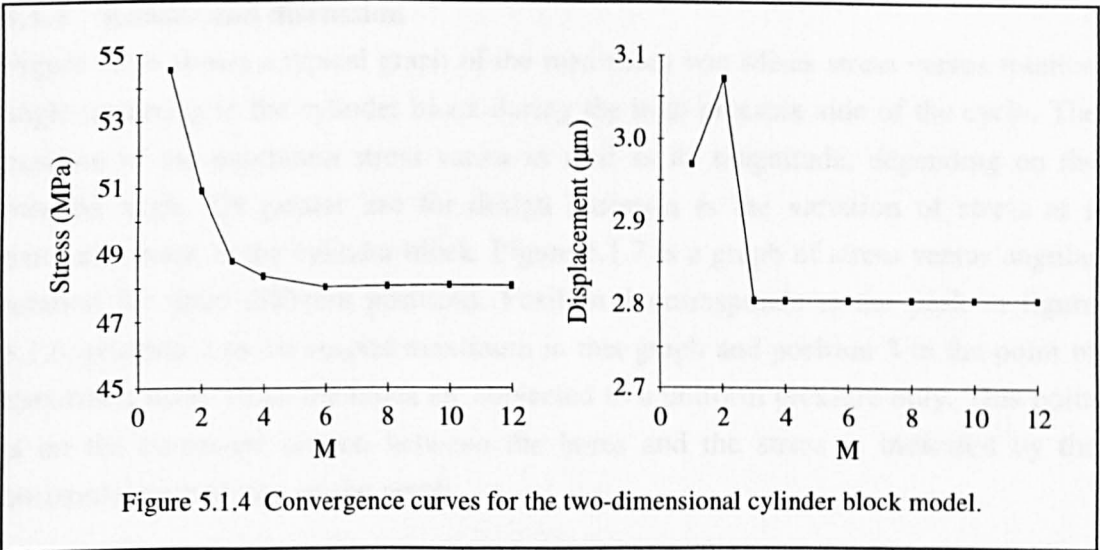


5.1.2 Convergence

Figure 5.1.4 shows graphs of maximum von Mises stress and displacement in a section of the two-dimensional cylinder block model experiencing uniform pressure loading only for a variety of mesh densities, M . The value of M refers to $M1$, the rest of the mesh being varied in the same proportion as far as possible. The stress in the last four meshes varied by only 0.15% and, hence, the mesh with $M1 = 6$ was chosen for the rest of the analyses.

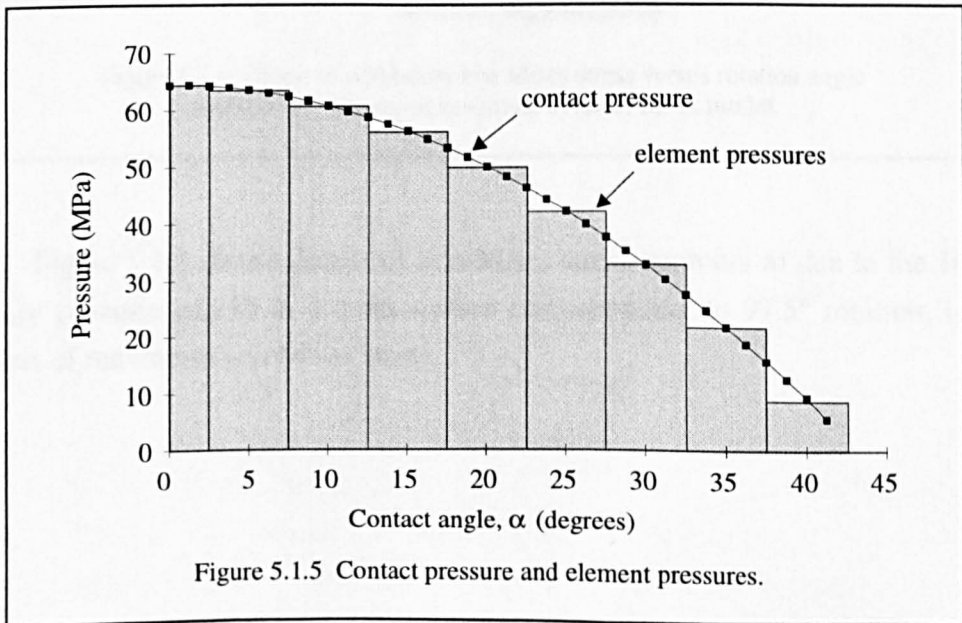
5.1.3 Analyses

A number of cylinder blocks of various materials and with liners of different thickness and materials were analysed for the axial piston pump operating at a variety of pressures. However, the remainder of this section will be concerned with the analysis of a polymer-lined stainless steel cylinder block with ceramic pistons



operating at 140 bar delivery pressure. In this case the boost pressure was assumed to be zero.

From the two-dimensional contact analysis the contact angle for this configuration was shown to be 43.125° with a maximum contact pressure of 64.5 MPa. This was applied to the model as element pressures which are uniform over the face of each element. For the mesh density chosen each bore covers 5° and figure 5.1.5 illustrates how the contact pressure calculated from the gap element forces were approximated by the step-wise element pressures. Several load cases were run corresponding to different angular positions of the cylinder block.



5.1.4 Results and discussion

Figure 5.1.6 shows a typical graph of the maximum von Mises stress versus rotation angle occurring in the cylinder block during the high pressure side of the cycle. The position of the maximum stress varies as well as its magnitude, depending on the rotation angle. Of greater use for design purposes is the variation of stress at a particular point in the cylinder block. Figure 5.1.7 is a graph of stress versus angular rotation for three different positions. Position 1 corresponds to the peak in figure 5.1.6, position 2 to the second maximum in that graph and position 3 to the point of maximum stress when the bores are subjected to a uniform pressure only. This point is on the narrowest section between the bores and the stress is indicated by the horizontal dashed line on the graph.

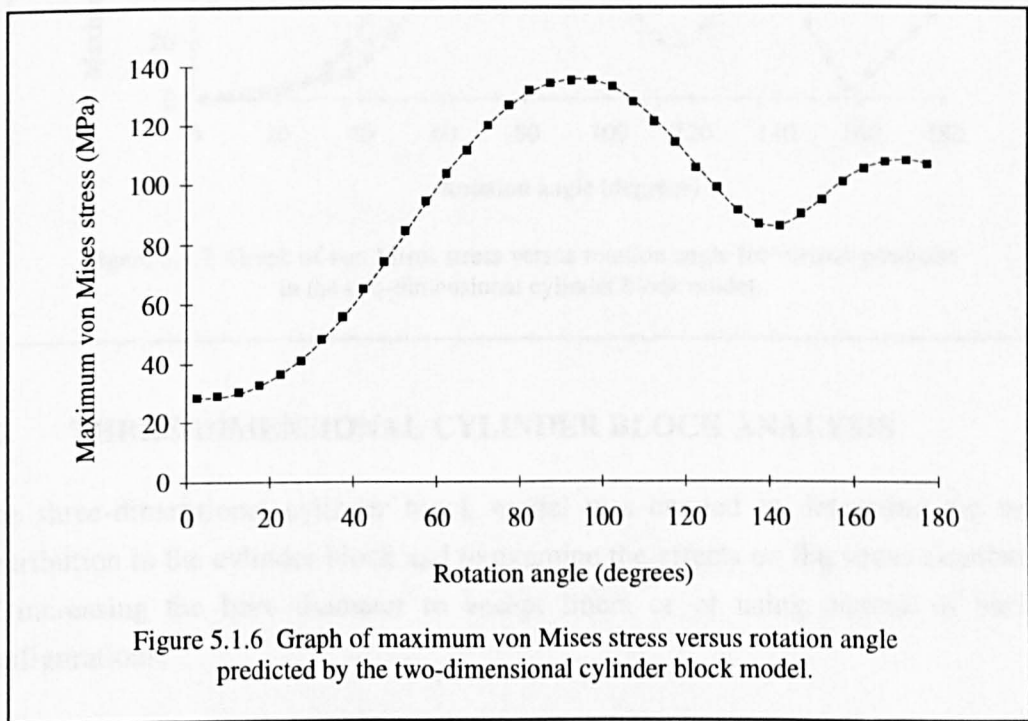
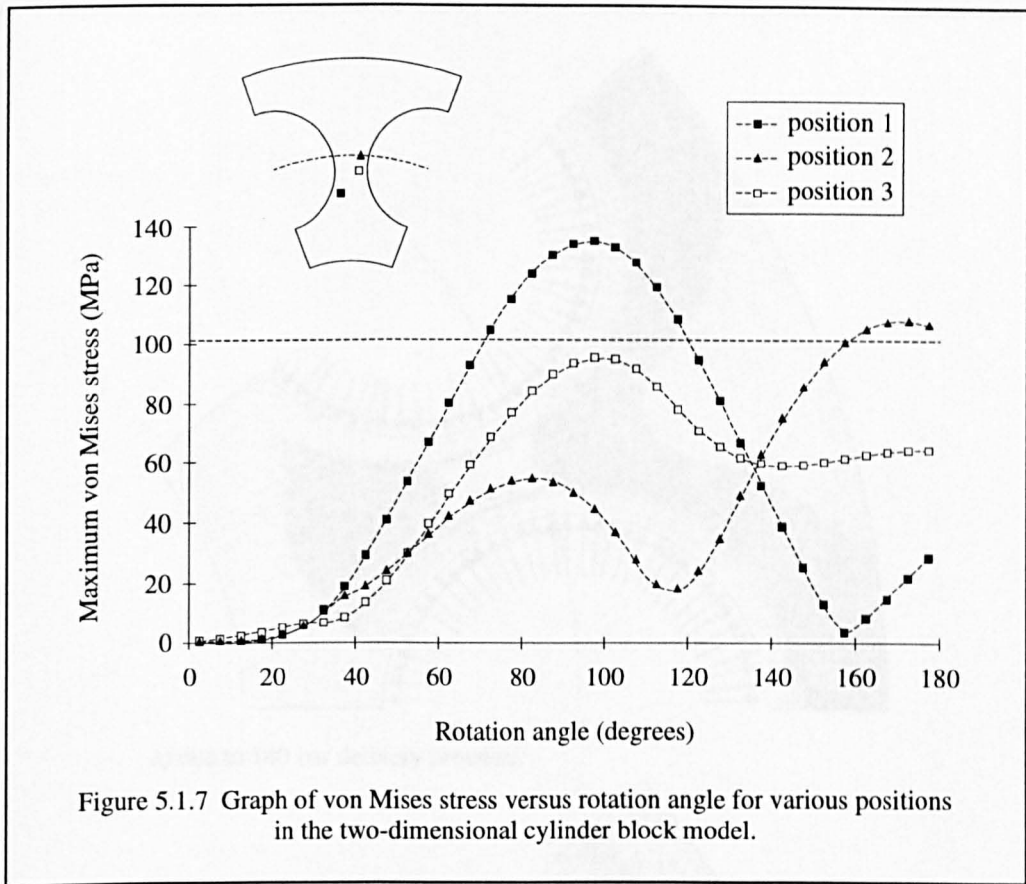


Figure 5.1.8 shows details of von-Mises stress contours a) due to the 140 bar delivery pressure and b) in a cross-section corresponding to 97.5° rotation, i.e. the position of maximum von Mises stress.



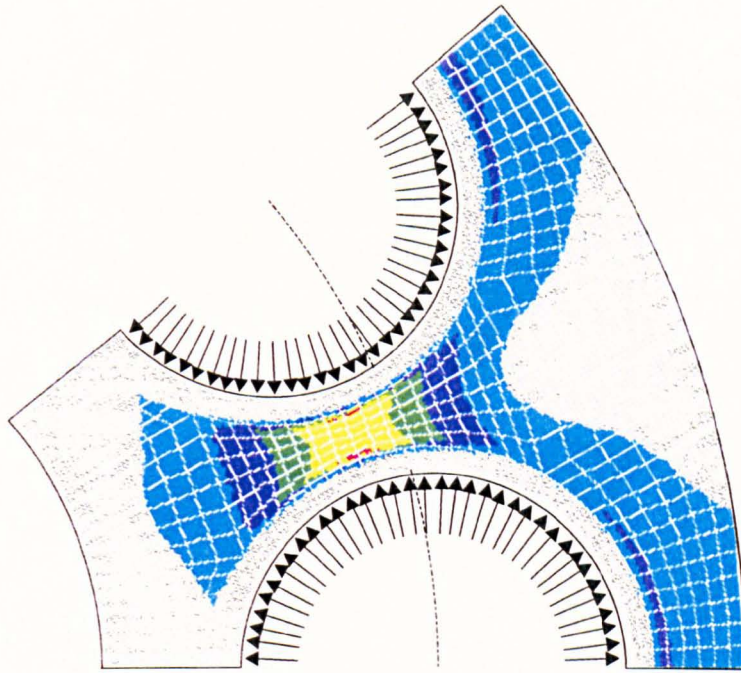
5.2 THREE-DIMENSIONAL CYLINDER BLOCK ANALYSIS

The three-dimensional cylinder block model was created to determine the stress distribution in the cylinder block and to examine the effects on the stress distribution of increasing the bore diameter to accept liners or of using pistons of various configurations.

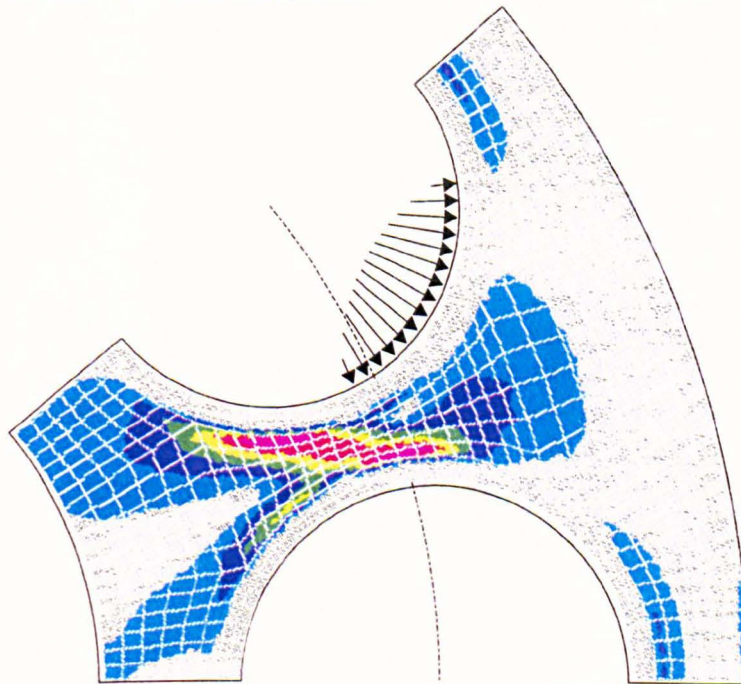
5.2.1 Models

Figure 5.2.1 shows an outline of the three-dimensional cylinder block model with the loading and constraints which were applied. It takes account of rotational symmetry, consisting of two half bores of the cylinder block, and is meshed using second order solid elements. The snout bearing area was constrained from moving in the radial direction and the back face of the block from moving in the z-direction.

A uniform bore pressure, calculated in the timing analysis, was applied to the shaded area shown and contact forces from the pistons were determined using the three-dimensional contact model for the relevant loading and materials. The piston contact pressures were approximated from the contact model results by being applied as uniform pressures over the relevant faces of whole elements as was done for the



a) due to 140 bar delivery pressure.



b) due to contact from pistons.

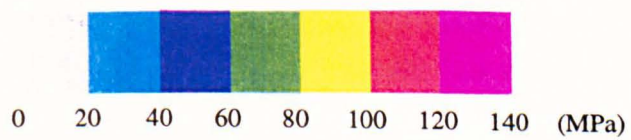


Figure 5.1.8 Stress contours in the two-dimensional cylinder block.

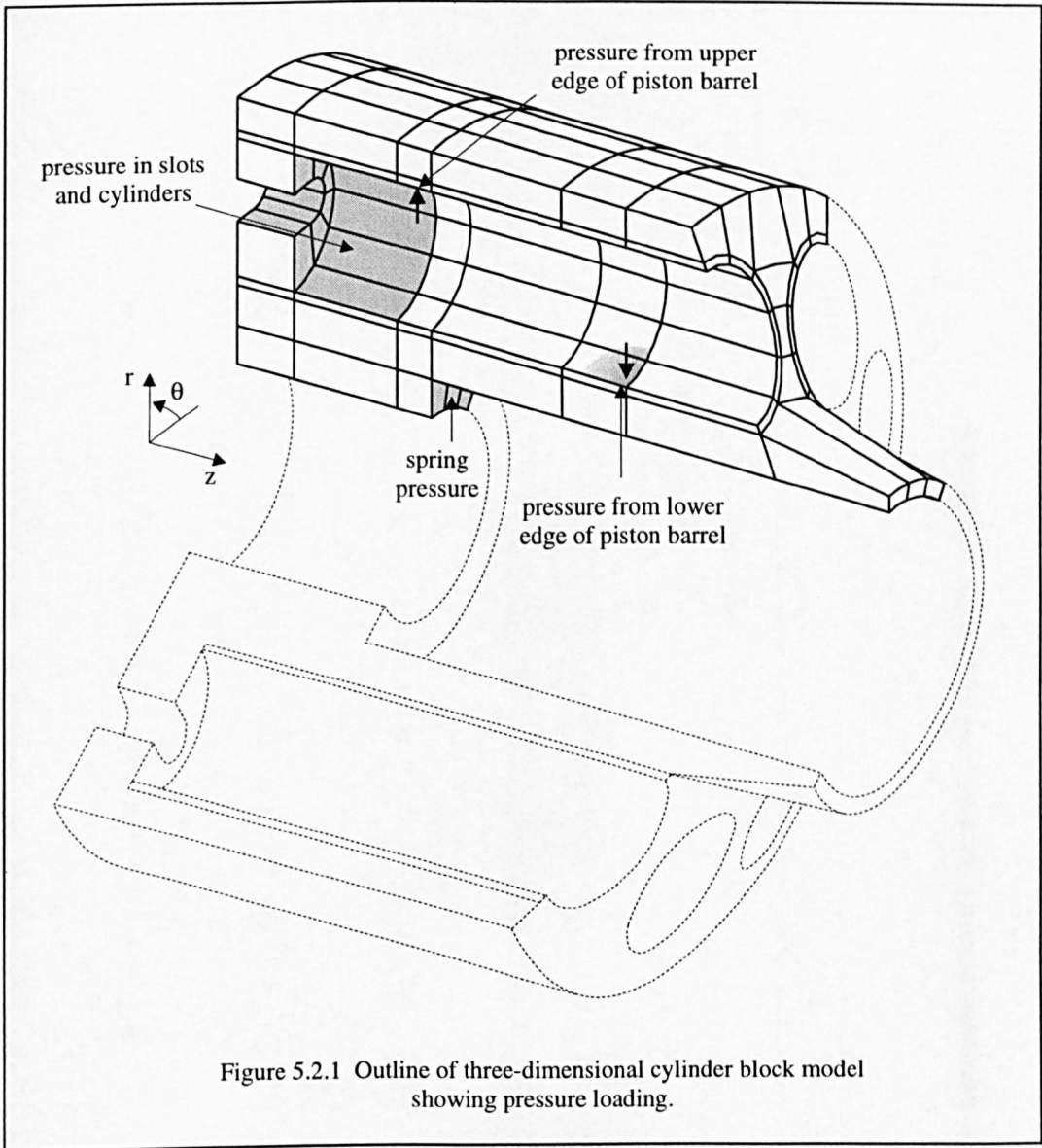


Figure 5.2.1 Outline of three-dimensional cylinder block model showing pressure loading.

two-dimensional cylinder block model. The spring pressure was determined in the force analysis program (Radcliffe et al 1991). Figure 5.2.2 shows the parameters used in the creation of the model.

5.2.2 Convergence

Figure 5.2.3 shows graphs of von Mises stress and displacement in an unlined three-dimensional cylinder block model for a variety of mesh densities, M . The stress in the last two meshes varied by 0.03% and, hence, the mesh corresponding to $M = 6$ was chosen for the rest of the analyses as this allowed more sensitivity in the application of the contact stresses.

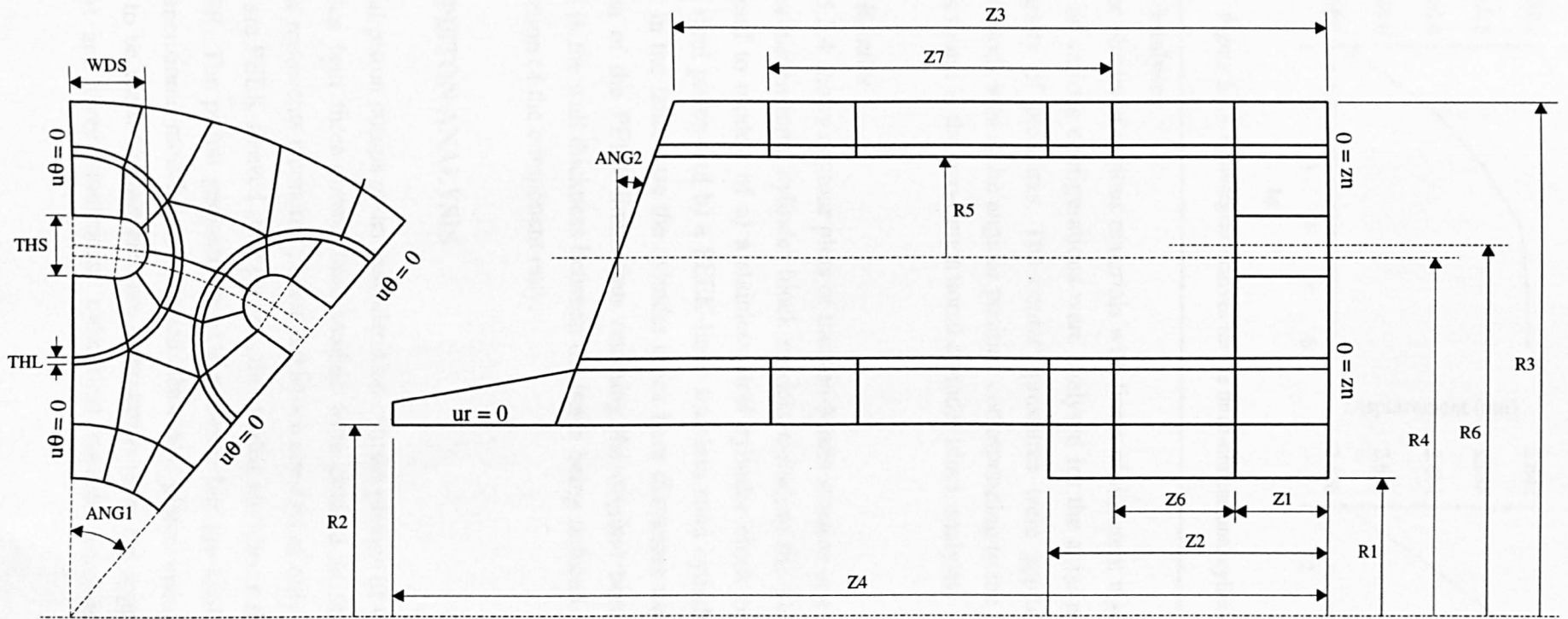
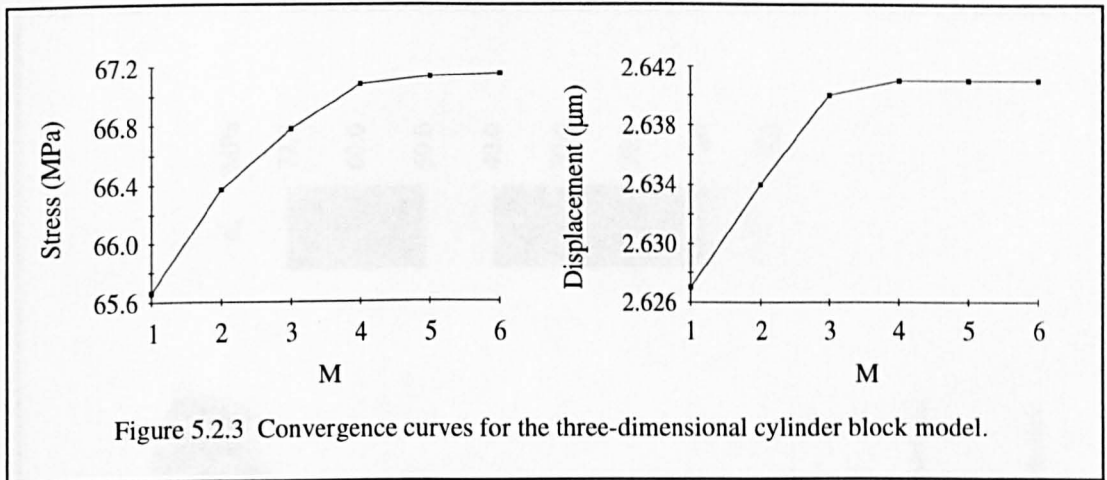


Figure 5.2.2 Outline of three-dimensional cylinder block model showing parameterised quantities.



5.2.3 Analyses

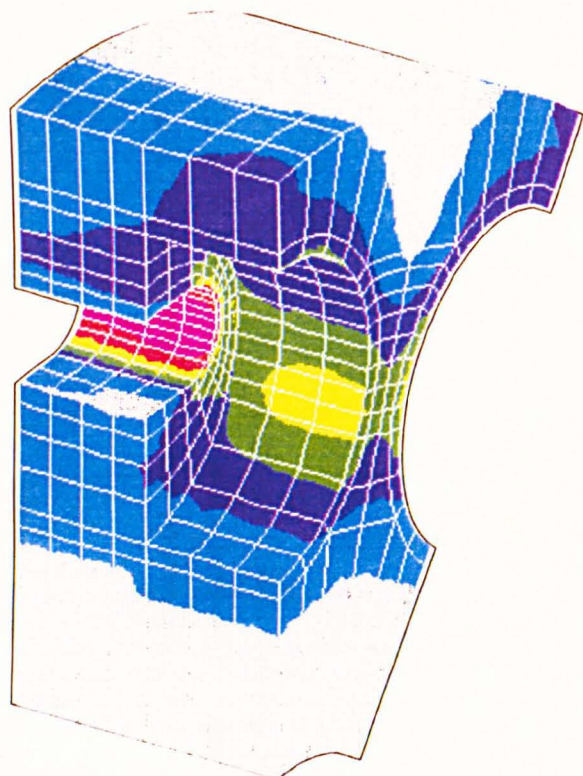
Cylinder blocks of various materials with liners of different thickness and containing pistons of various configurations were analysed for the axial piston pump operating at a variety of pressures. The contact pressures were applied assuming that the cylinder block was at the angular position corresponding to the position of maximum stress as found in the two-dimensional cylinder block analysis.

5.2.4 Results

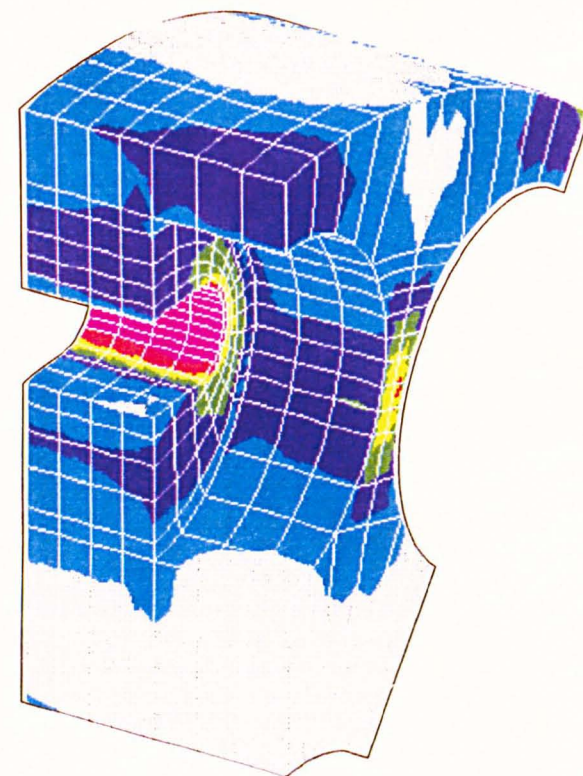
Figure 5.2.4 shows contour plots of the von-Mises stresses in a cross-section through the three-dimensional cylinder block models including the kidney ports. The plots correspond to models of a) a stainless steel cylinder block contacted by a PEEK-sleeved steel piston and b) a PEEK-lined stainless steel cylinder block and ceramic pistons. In the latter case the cylinder block bore diameters were increased to allow inclusion of the PEEK liners thus retaining the original bore size. However, this resulted in the wall thickness between the bores being reduced. The figure shows the steel portion of the component only.

5.3 PISTON ANALYSIS

The axial piston pumps under consideration contain pistons of various configurations and hence four three-dimensional models were created as shown in figure 5.3.1. Piston 'a' represents a ceramic piston and hence consists of only one material; pistons 'b' to 'd' are PEEK-sleeved steel pistons, the shaded sections in the figure representing the PEEK. The piston geometry is axisymmetric but the loading is not and hence three-dimensional models were created. However, planar symmetry does allow half models to be used. Contact pressure information from the appropriate axisymmetric spherical and three-dimensional cylindrical models were applied to the piston models.



a) steel cylinder block with PEEK-sleeved steel pistons
 $\sigma_{\max} = 69.2 \text{ MPa}$



b) PEEK-lined steel cylinder block with ceramic pistons
 $\sigma_{\max} = 72.0 \text{ MPa}$

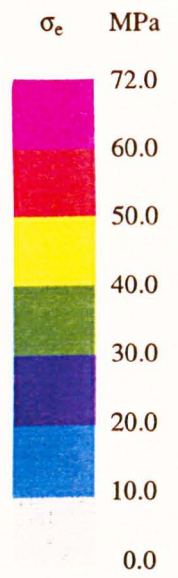
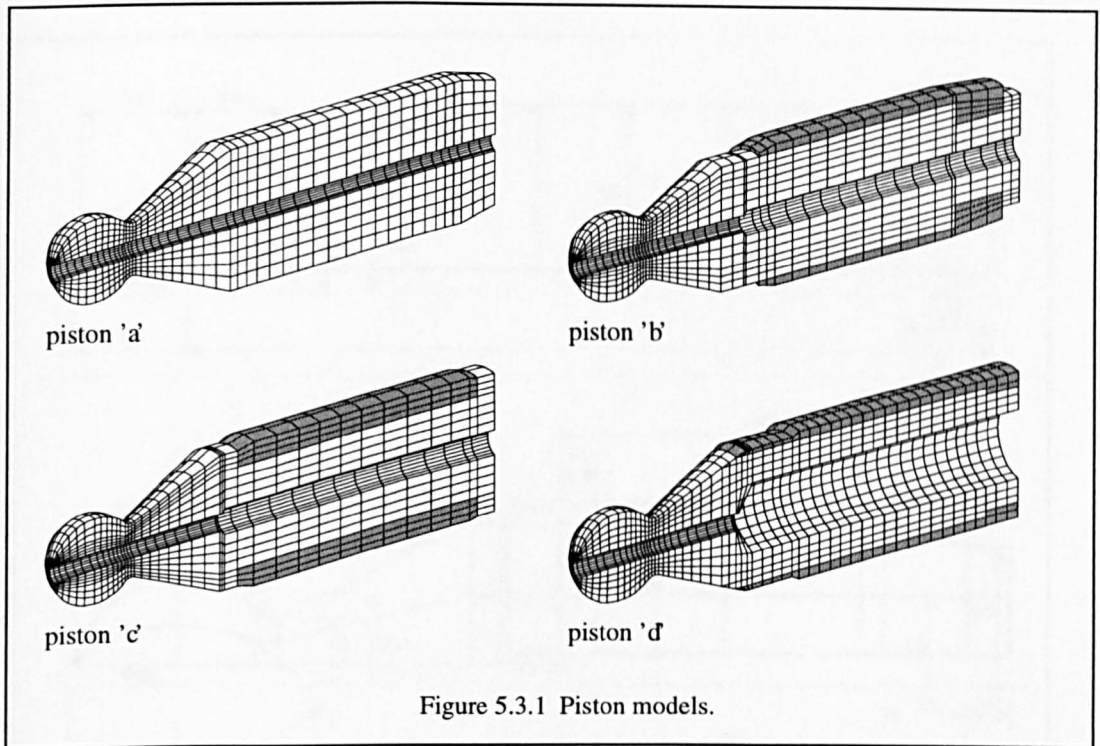


Figure 5.2.4 Von Mises stress contours in a detail of the three-dimensional cylinder block model.



5.3.1 Models

Figure 5.3.2 shows the parameterised quantities relevant to each of the four piston models, each with a different sleeve configuration. The models were meshed using second order solid elements and figure 5.3.3 illustrates the pressure loading and displacement constraints for a typical piston. As with the three-dimensional cylinder block the contact forces were approximated by being applied over the relevant faces of whole elements. The end of the piston furthest from the ball was constrained from moving in the x-direction and nodes along the axis $y = 0$ at the same end from moving in the y-direction.

5.3.2 Convergence

Figure 5.3.4 shows a graph of the von Mises stress at the neck of a typical piston. The value of M refers to the mesh density at the neck of the piston and the rest of the mesh is varied in the same proportion as far as possible.

5.3.3 Analyses

Each of the piston configurations was analysed for a variety of material properties, contacting cylinder blocks with or without liners and, with the exception of piston 'a', for different sleeve thicknesses. Contact pressures, determined from the three-dimensional and axisymmetric contact models, were applied for a variety of bore pressures.

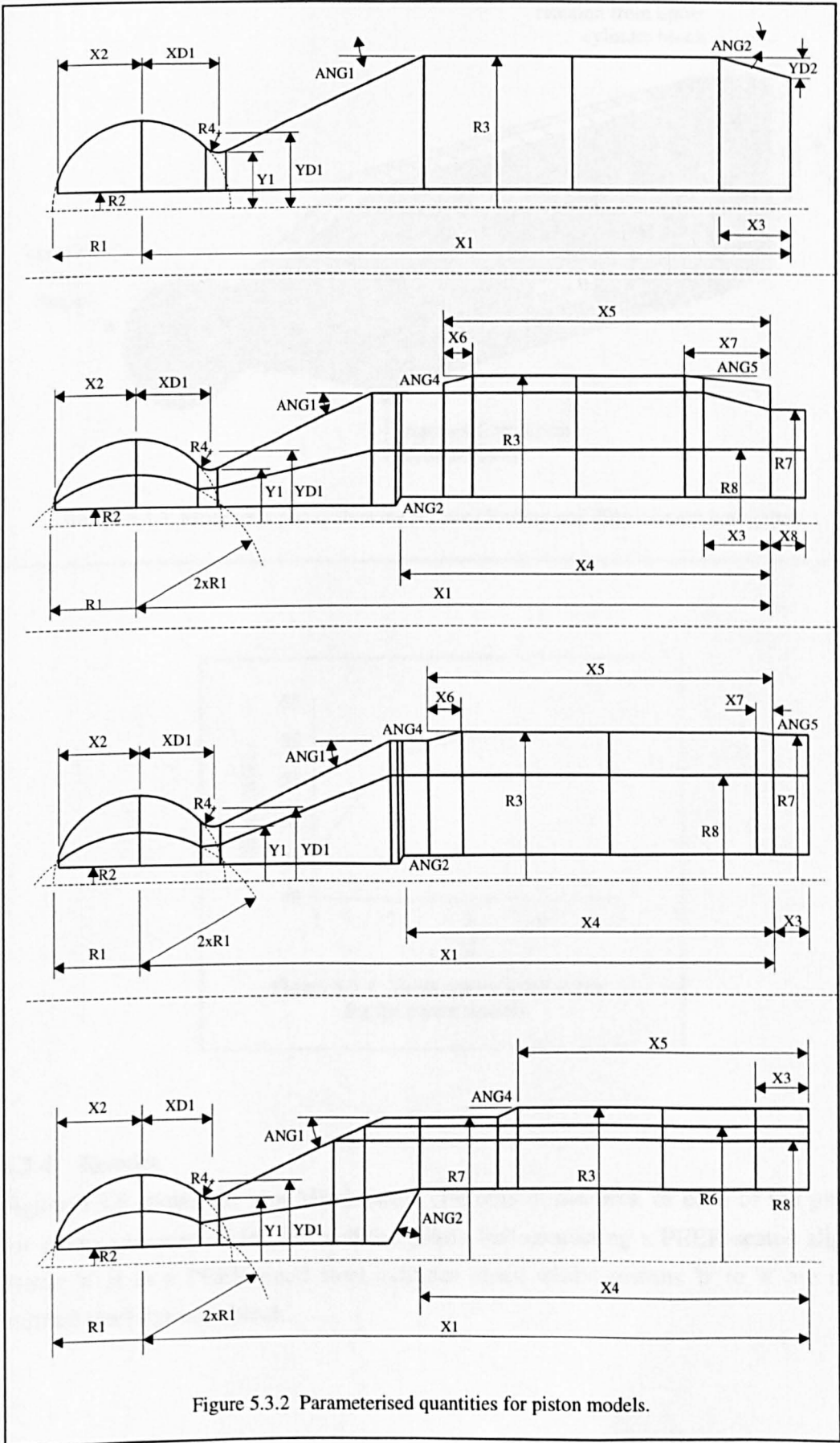
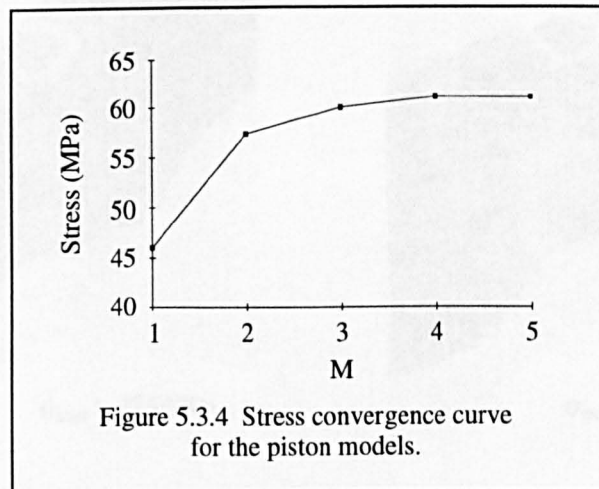
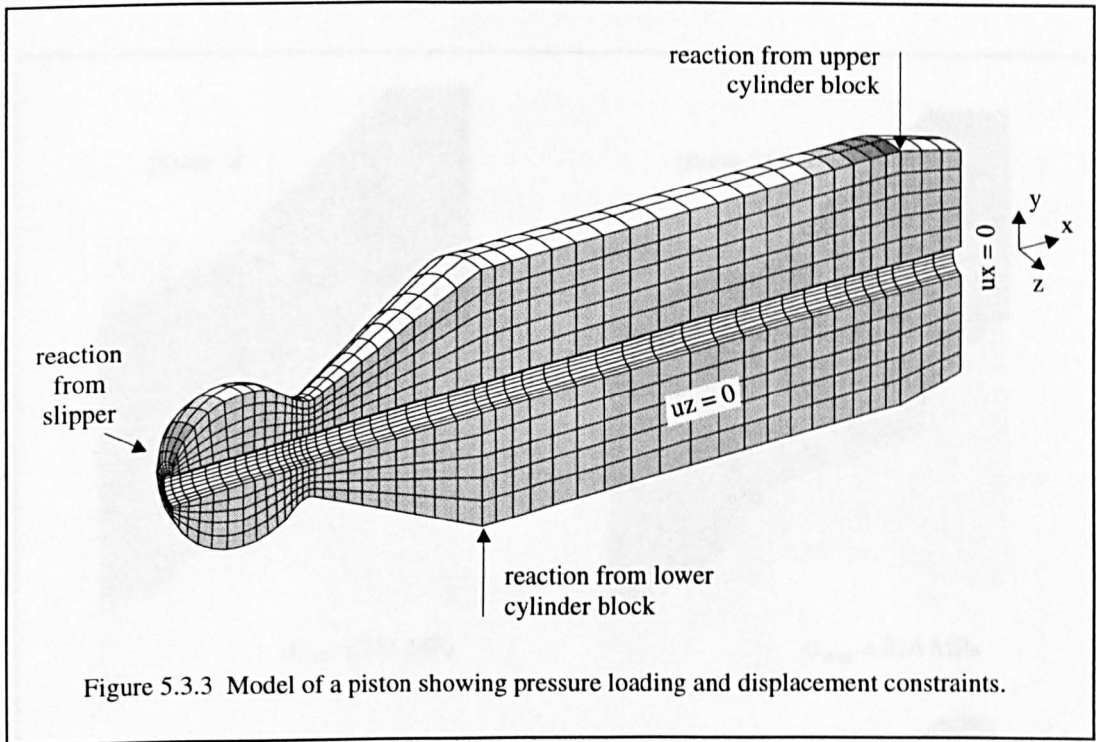


Figure 5.3.2 Parameterised quantities for piston models.



5.3.4 Results

Figure 5.3.5 shows the von Mises stress contours at the neck of each of the pistons for a bore pressure of 140 bar and the piston ball contacting a PEEK-seated slipper. Piston 'a' is in a PEEK-lined steel cylinder block whilst pistons 'b' to 'd' are in an unlined steel cylinder block.

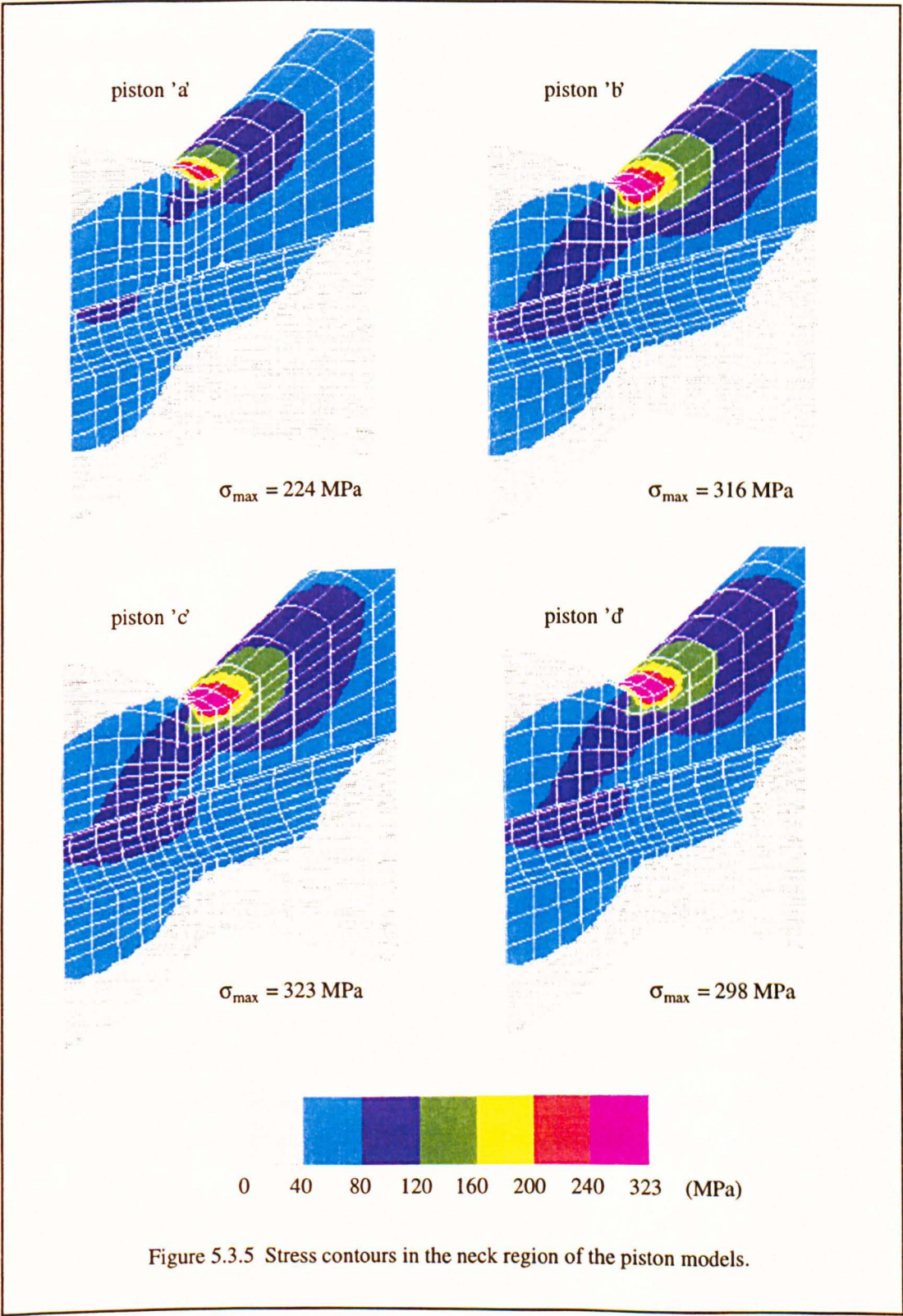


Figure 5.3.5 Stress contours in the neck region of the piston models.

5.4 AXISYMMETRIC SLIPPER ANALYSIS

The axisymmetric slipper models were created to determine the stress distribution in slippers in an axial piston pump and the consequences on the distribution of changing various parameters. Two designs of slipper were considered, sketches of which are shown in figure 5.4.1, and contact pressure loading from the piston ball applied as determined from the appropriate axisymmetric component-shaped analysis.

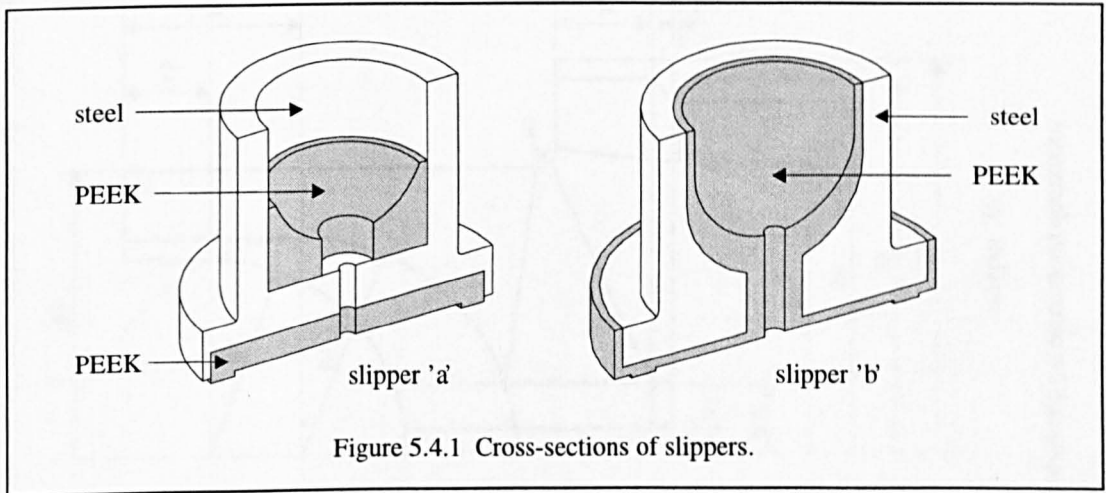


Figure 5.4.1 Cross-sections of slippers.

5.4.1 Models

Figure 5.4.2 shows outlines of the two designs of slipper with dimensional parameters. The models are meshed using second order axisymmetric elements and are constrained from moving in the y-direction on the bottom of the lands.

5.4.2 Convergence

Figure 5.4.3 shows stress convergence curves for the slippers. There is a 1.0% and 0.8% difference between the maximum stress in the last two meshes for slipper a and slipper b respectively and hence a mesh density of 12 was chosen for the remainder of the analyses. These meshes are shown in figure 5.4.4. The grey and white areas represent the different materials, PEEK and steel respectively.

5.4.3 Analyses

Pressure loading was applied to elements in the seat area of the slippers as determined in the axisymmetric component-shaped contact model for the same materials, radius, radial clearance and bore pressure. Analyses were conducted to determine the effects on the maximum stress of changing the loading and various parameters such as the radius R2, the wall thickness in slipper 'a' (R9-R8) and the moulded seat depth in slipper 'b' (Y3-Y2).

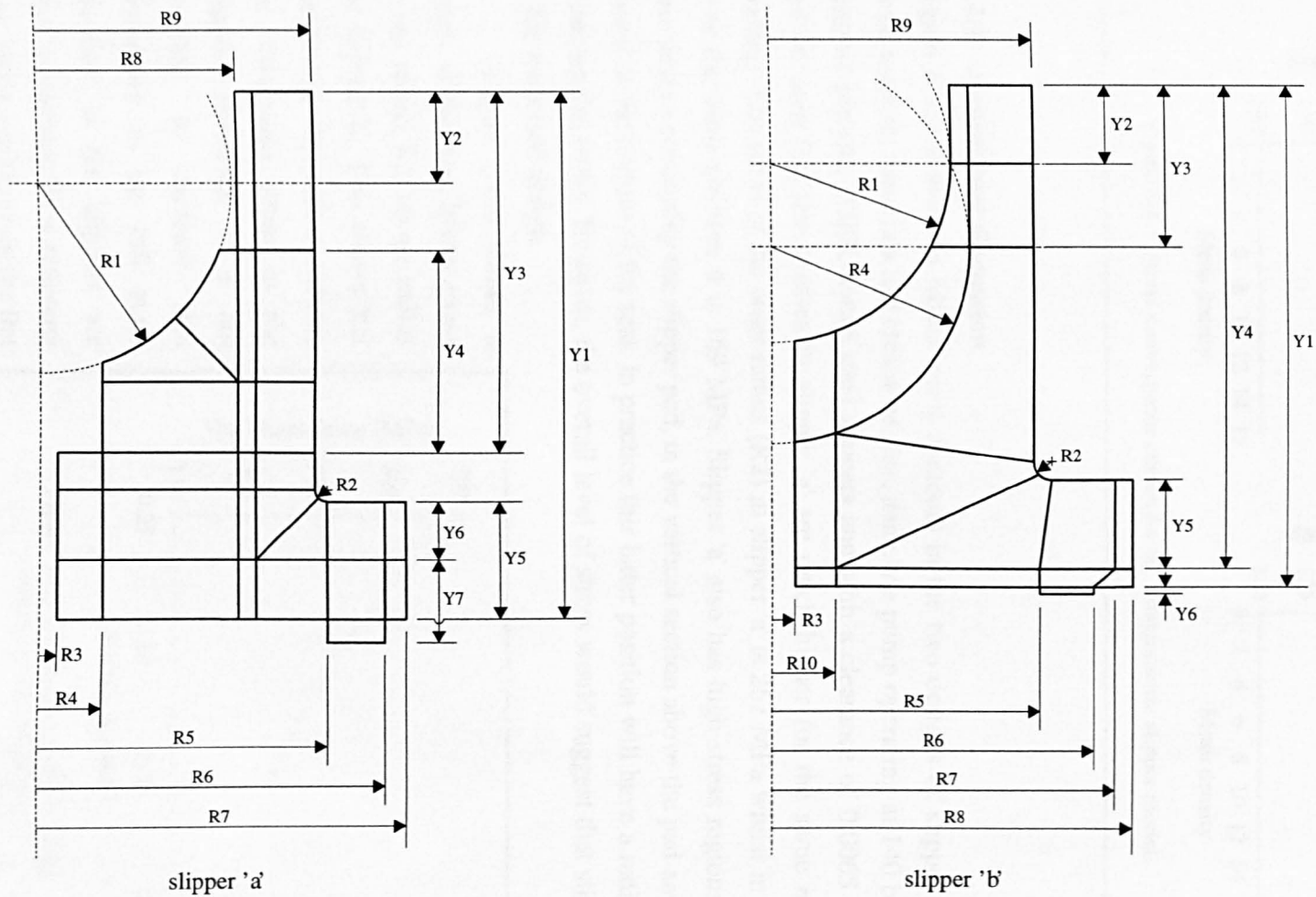


Figure 5.4.2 Outline of axisymmetric slipper models showing parameterised quantities.

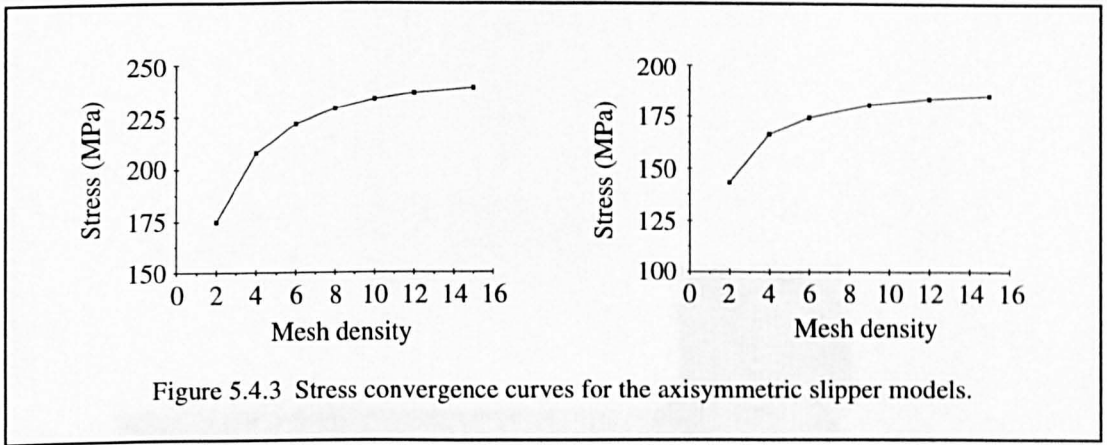


Figure 5.4.3 Stress convergence curves for the axisymmetric slipper models.

5.4.4 Results and discussion

Figure 5.4.5 shows von Mises stress contours in the two designs of slipper for the same loading, materials and clearance size, namely a pump operating at 140 bar with ceramic pistons, PEEK-seated steel slippers and with a clearance of 0.0065 mm. It can be seen that the stresses in slipper 'a' are much higher for the same nominal loading. The stress at the outer radius (R2) in slipper 'a' is 267 MPa whilst in slipper 'b' at the same position it is 169 MPa. Slipper 'a' also has high stress regions in the thin section containing the slipper pad, in the vertical section above the pad and at the corner at the bottom of the seat. In practice this latter position will have a radius thus reducing the stress. However, the overall level of stress would suggest that slipper 'b' is the preferred design.

Figure 5.4.6 shows a graph of the von Mises stress at the radius R2 versus radius for slipper 'a'. This shows that increasing the radius reduces the maximum stress in the slipper. However, it is not possible to increase this dimension to the full outer diameter as the slippers are held in position by a retaining ring which impinges on the flat surface at height Y5.

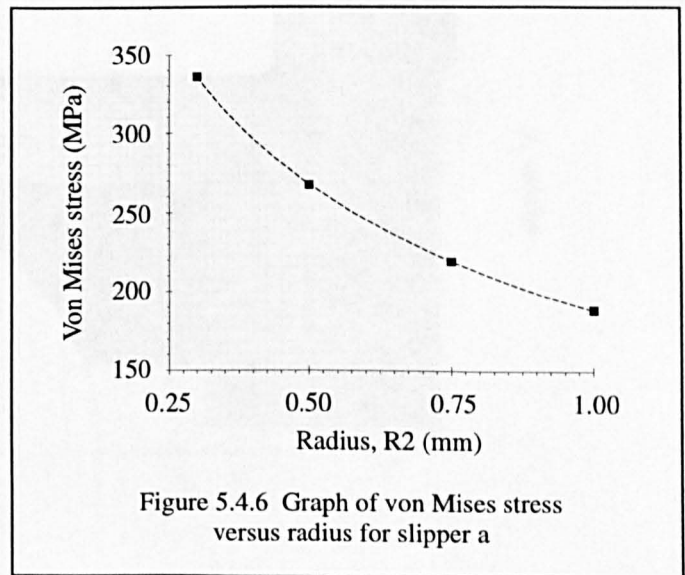


Figure 5.4.6 Graph of von Mises stress versus radius for slipper a

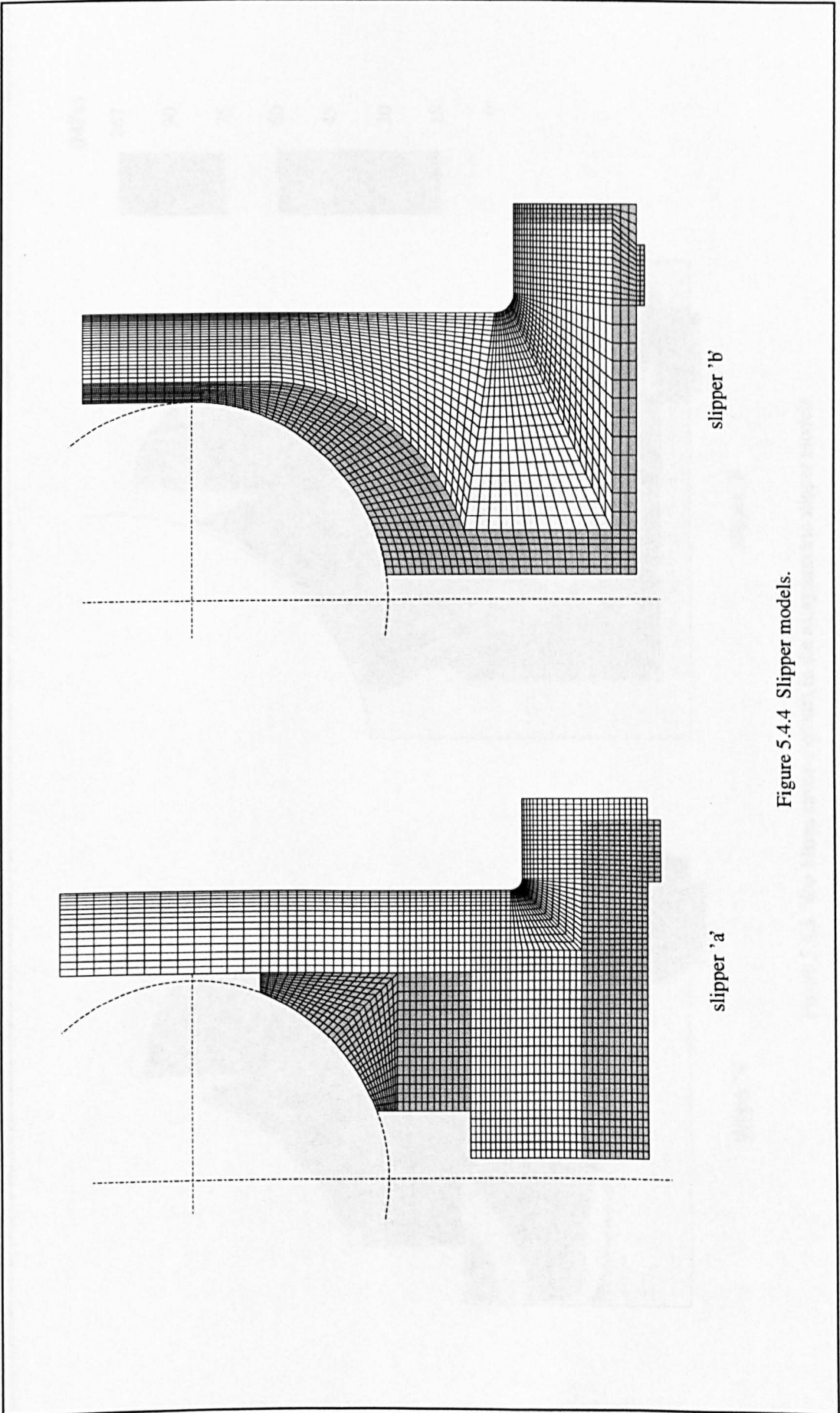


Figure 5.4.4 Slipper models.

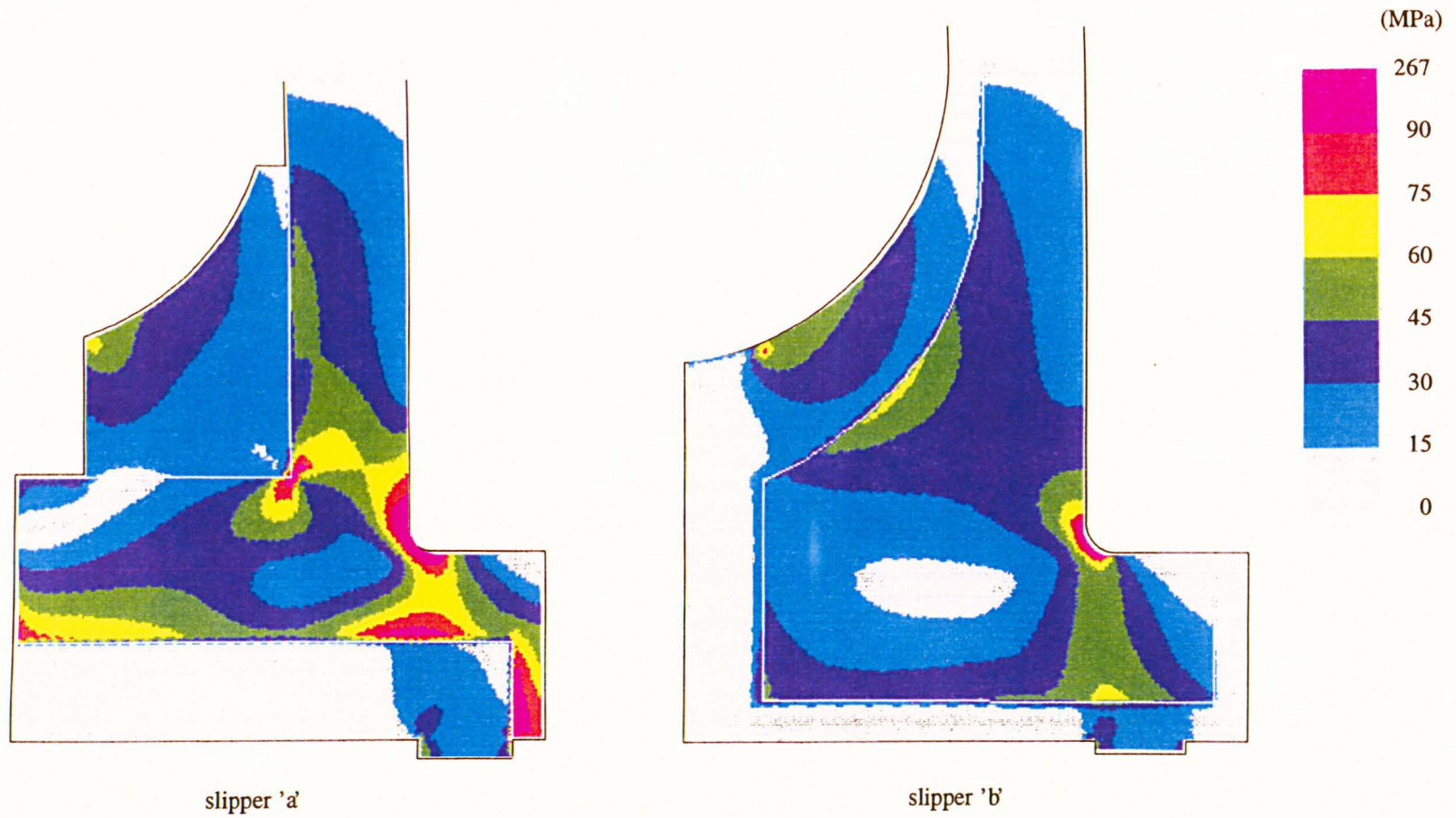


Figure 5.4.5 Von Mises stress contours in the axisymmetric slipper models.

CHAPTER 6

ANALYSIS OF CERAMIC COMPONENTS

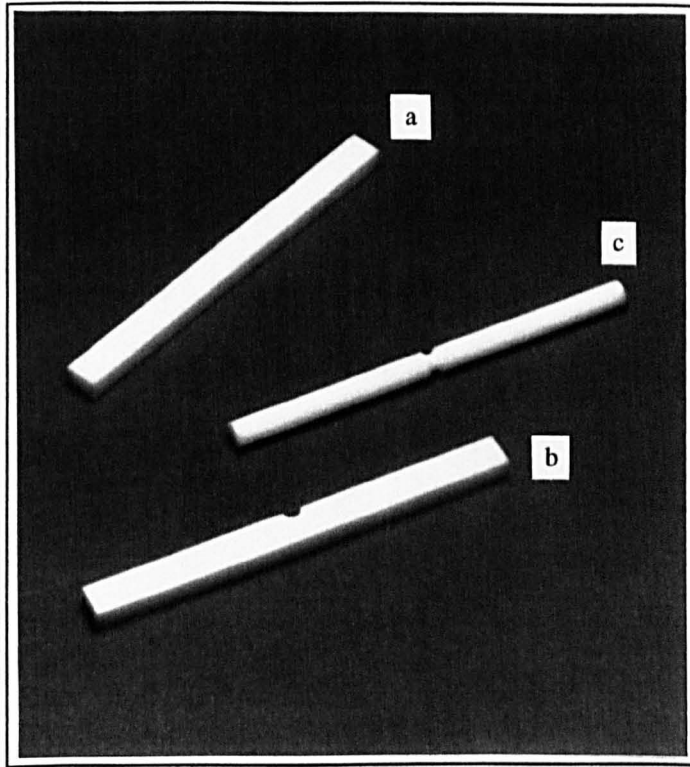
6.0 INTRODUCTION

This chapter describes some of the work undertaken to analyse specimens and components made from advanced ceramic materials. It aims to find the most appropriate statistical analysis method to use when designing components made from partially stabilised zirconia (PSZ) ceramic. The CARES (Ceramic Analysis Reliability Evaluation of Structures) program, as described in Chapter 3, was used for the statistical analyses. The specimens and components were modelled using the ANSYS finite element analysis program and the element volumes and stresses translated to a form suitable for CARES by using the ANSCARES program. The ceramic specimens were tested at the British Gas facilities in Loughborough and Killingworth.

Four-point bend, or flexure, testing provides a relatively easy and inexpensive way of testing the large number of specimens required for a statistical analysis. It is generally proposed that material data derived from these simple, uniaxial tests can be applied in the design of complex three-dimensional components. This research examines the viability of that approach by analysing and predicting the probability of failure of a number of specimens with more complex geometries and stress states than the simple flexure bars. All the available analysis methods and flaw shapes are being considered and compared for both volume and surface flaws. The long term aim of the work is to allow the accurate and reliable design of complex components, such as the ceramic pistons and cylinder block.

6.1 SPECIMEN ANALYSIS

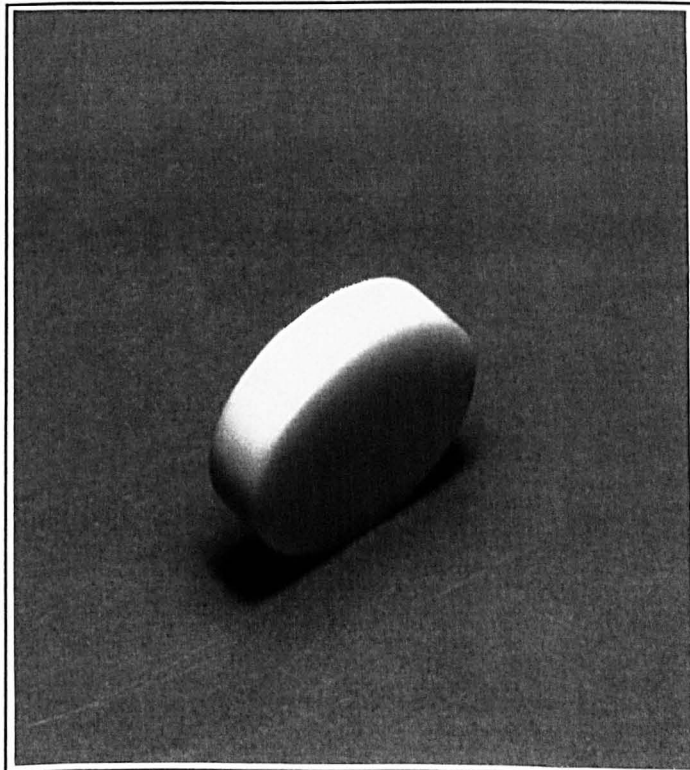
Several specimen configurations with a variety of expected stress distributions were tested to failure to provide data for the ceramic reliability analysis. All the specimens were made from yttria-stabilised zirconia and are shown in figure 6.1.1. Figures 6.1.2 and 6.1.3 show sketches of the specimens with outlines of the finite element models.



a) flexure bar

b) grooved bar

c) grooved rod



d) Brazilian disc

Figure 6.1.1 Photographs of ceramic specimens.

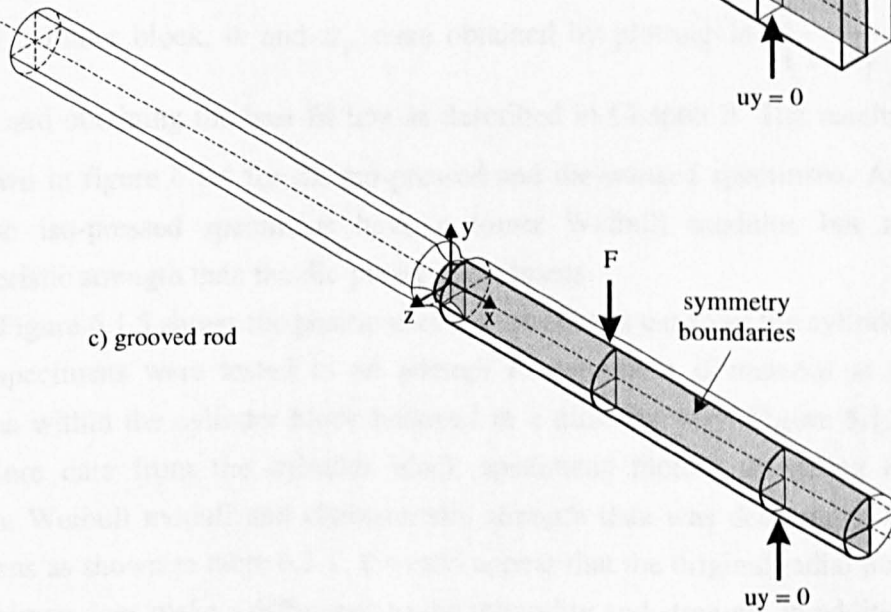
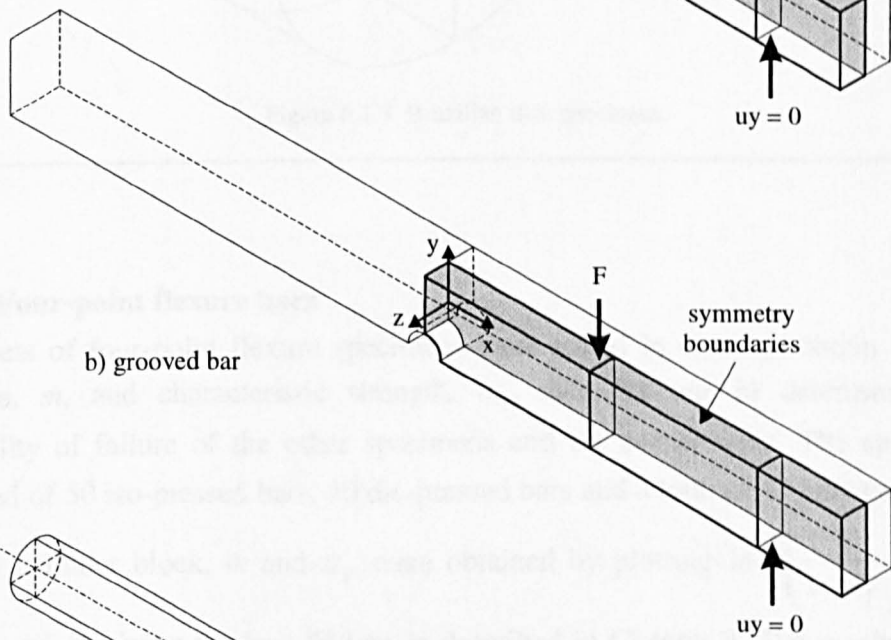
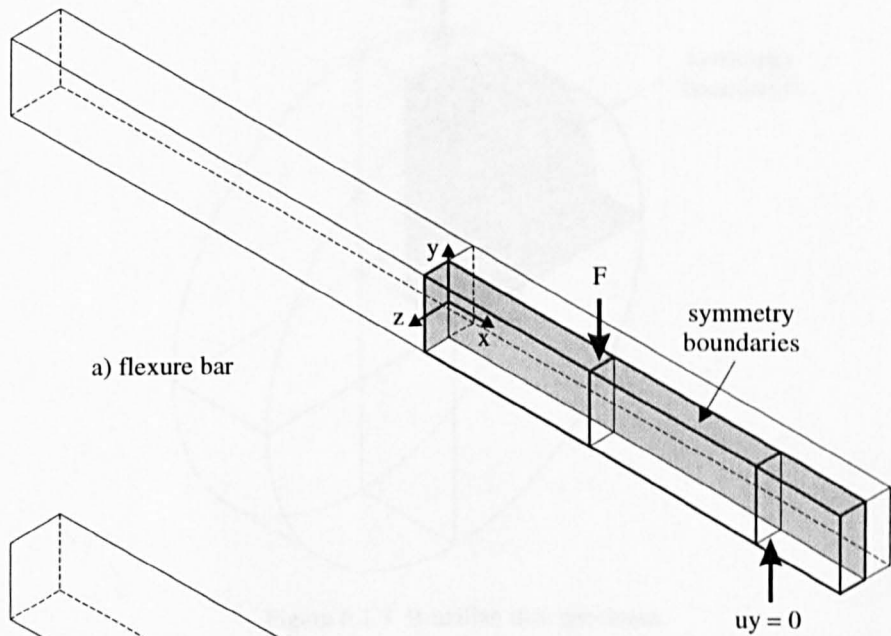
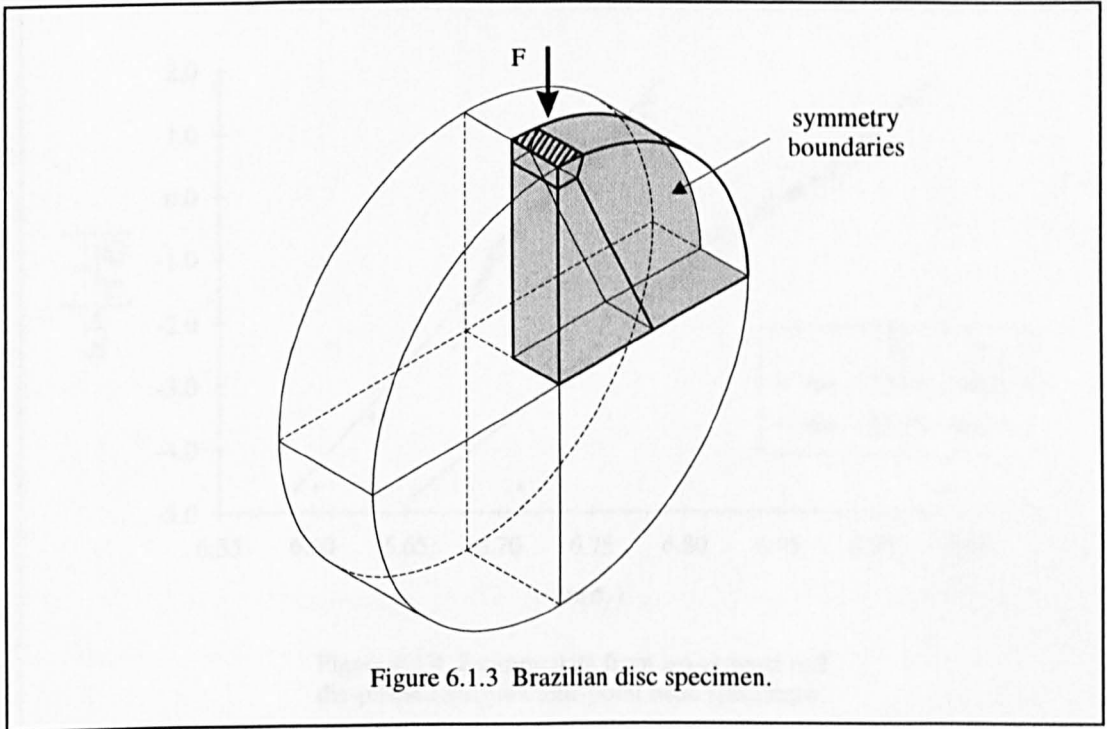


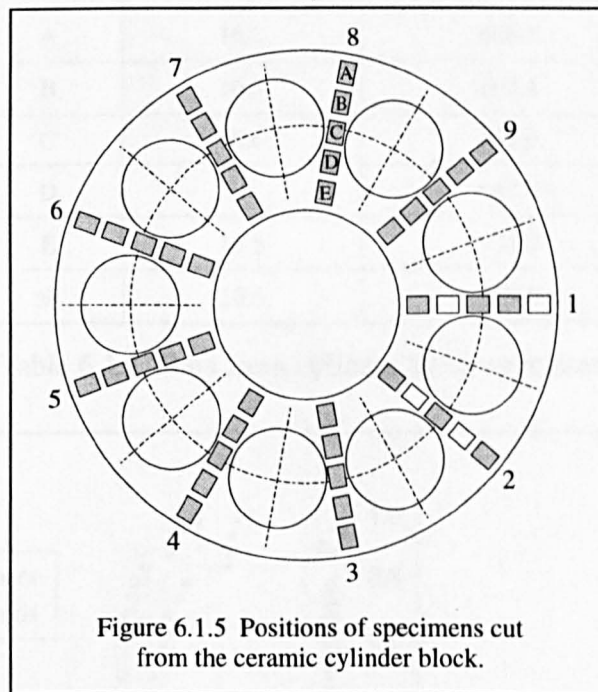
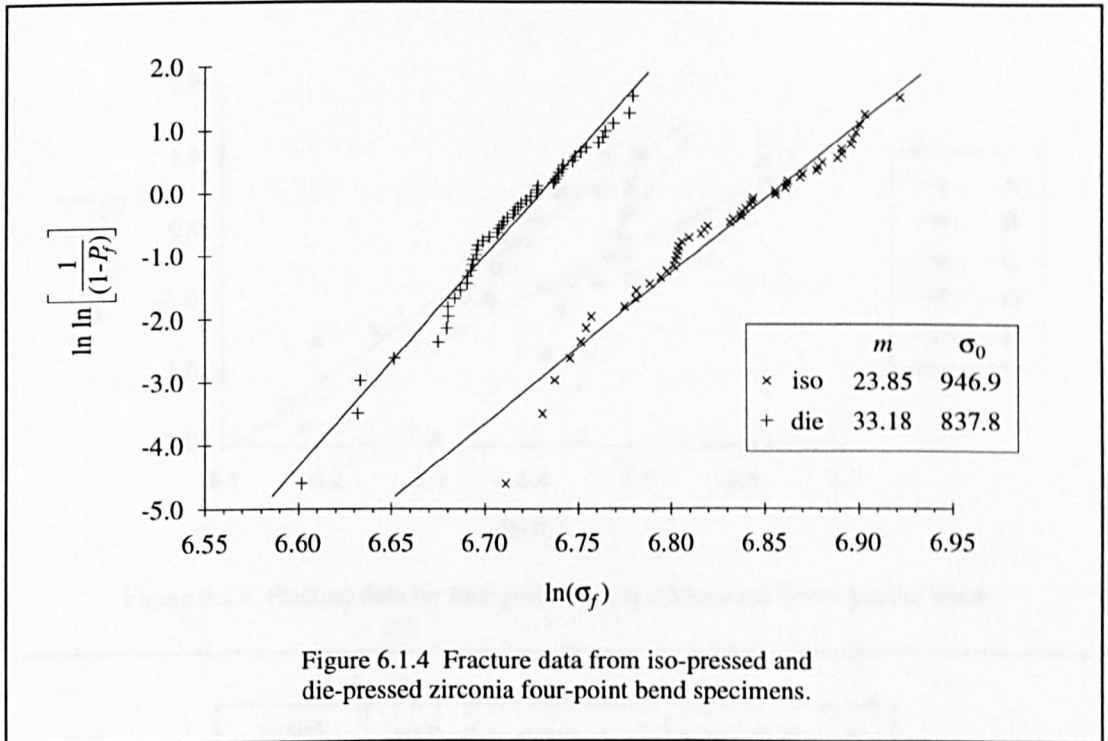
Figure 6.1.2 Ceramic specimens.



6.1.1 Four-point flexure bars

Three sets of four-point flexure specimens were tested in order to obtain Weibull modulus, m , and characteristic strength, σ_0 , data for use in determining the probability of failure of the other specimens and the components. The specimens consisted of 50 iso-pressed bars, 50 die-pressed bars and a total of 41 bars cut from a ceramic cylinder block. m and σ_0 were obtained by plotting $\ln \ln \left(\frac{1}{1-P_f} \right)$ versus $\ln(\sigma_f)$ and obtaining the best-fit line as described in Chapter 3. The results of this are shown in figure 6.1.4 for the iso-pressed and die-pressed specimens. As can be seen the iso-pressed specimens have a lower Weibull modulus but a higher characteristic strength than the die-pressed specimens.

Figure 6.1.5 shows the positions of the specimens cut from the cylinder block. These specimens were tested in an attempt to determine if material at different positions within the cylinder block behaved in a different way. Figure 6.1.6 shows the failure data from the cylinder block specimens plotted according to radial position. Weibull moduli and characteristic strength data was determined for these specimens as shown in table 6.1.1. It would appear that the original radial position of the specimen does make a difference to the reliability and strength. In addition it can be seen that the strength values are much lower than for either the die-pressed or iso-pressed specimens. There are several possible reasons for this and these will be discussed in Chapter 7.



6.1.2 Other specimens

Figure 6.1.7 shows the failure data for the grooved bar, grooved rod and Brazilian disc specimens. The grooved bars and rods were tested in the same test rig as the four-point flexure bars and the Brazilian discs in diametral compression using flat hardened steel plattens as shown in figure 3.6.4.

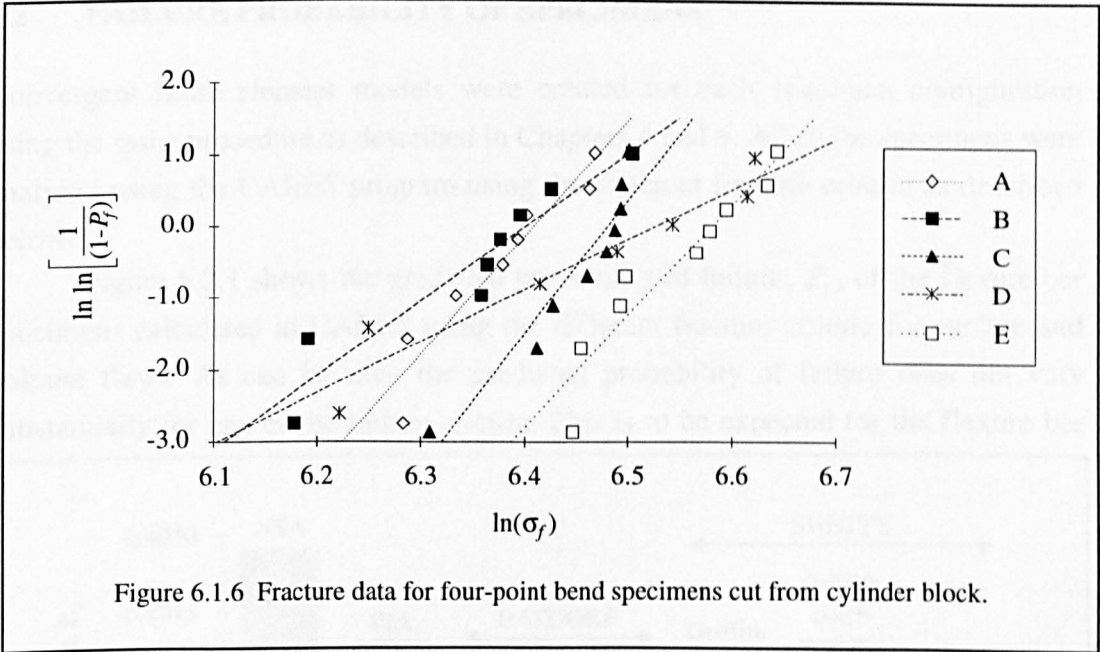


Figure 6.1.6 Fracture data for four-point bend specimens cut from cylinder block.

radial position	Weibull modulus m	Characteristic strength σ_0
A	16.2	608.1
B	10.3	603.4
C	18.6	652.9
D	7.1	683.4
E	15.5	721.0
all	10.5	659.9

Table 6.1.1 Data from cylinder block specimens.

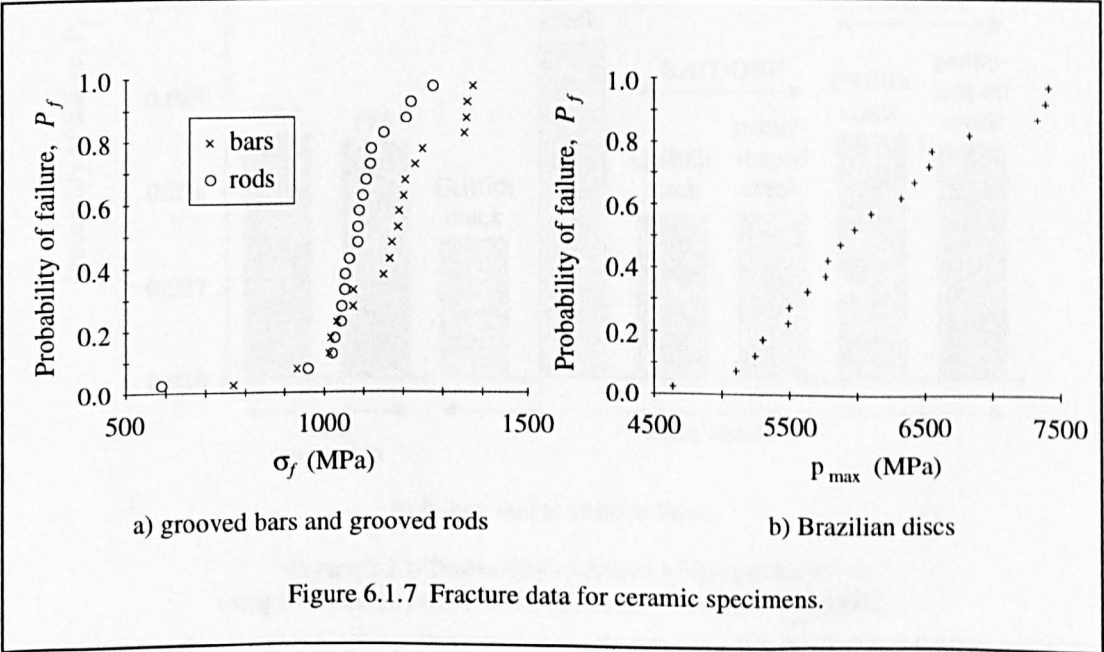


Figure 6.1.7 Fracture data for ceramic specimens.

6.2 FAILURE PROBABILITY OF SPECIMENS

Convergent finite element models were created for each specimen configuration using the same procedure as described in Chapters 4 and 5. All of the specimens were analysed using the CARES program using the different fracture criteria as described below.

Figure 6.2.1 shows the predicted probability of failure, P_f , of the flexure bar specimens calculated in CARES using the different fracture criteria for surface and volume flaws. As can be seen the predicted probability of failure does not vary substantially for any of the failure criteria. This is to be expected for the flexure bar

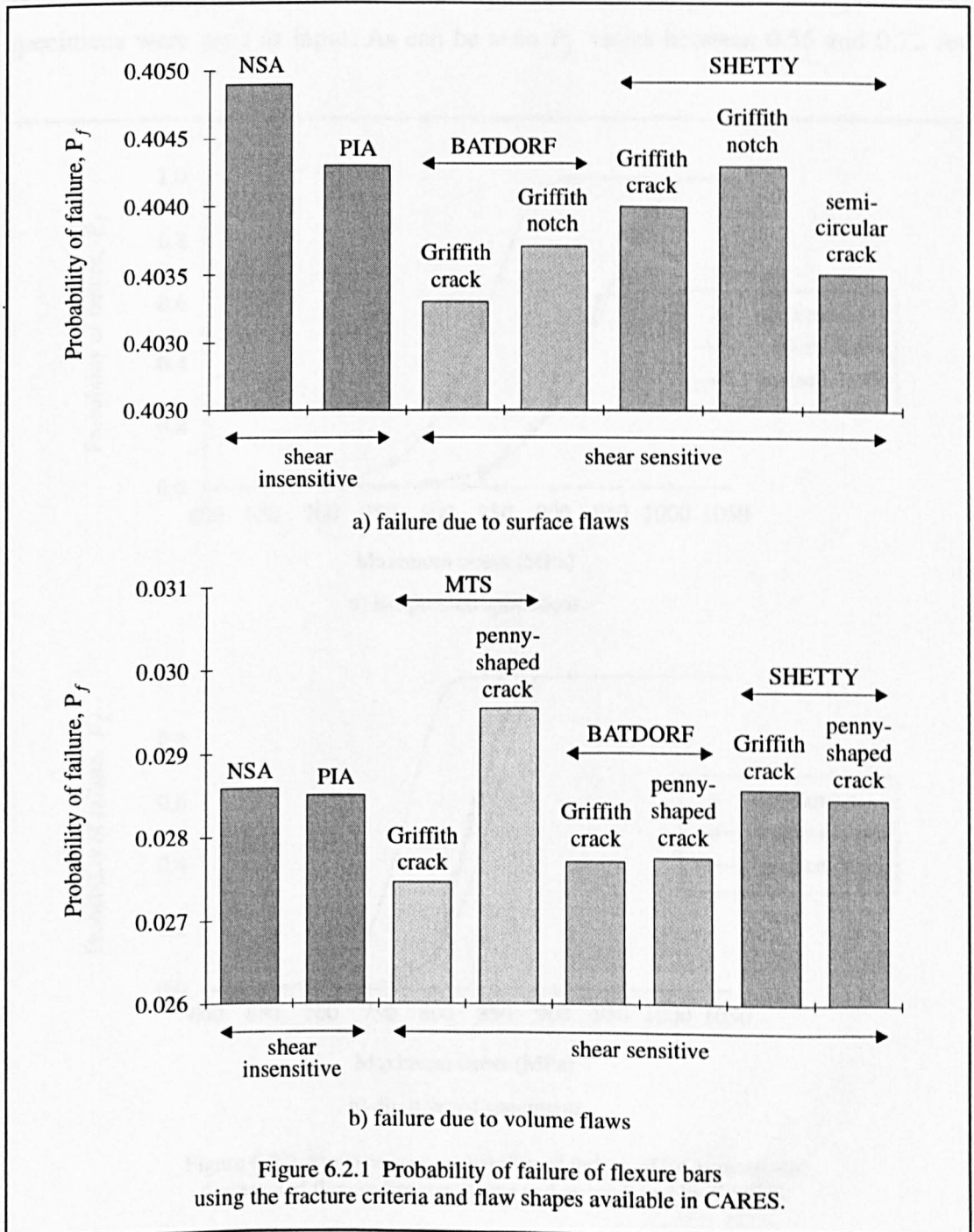
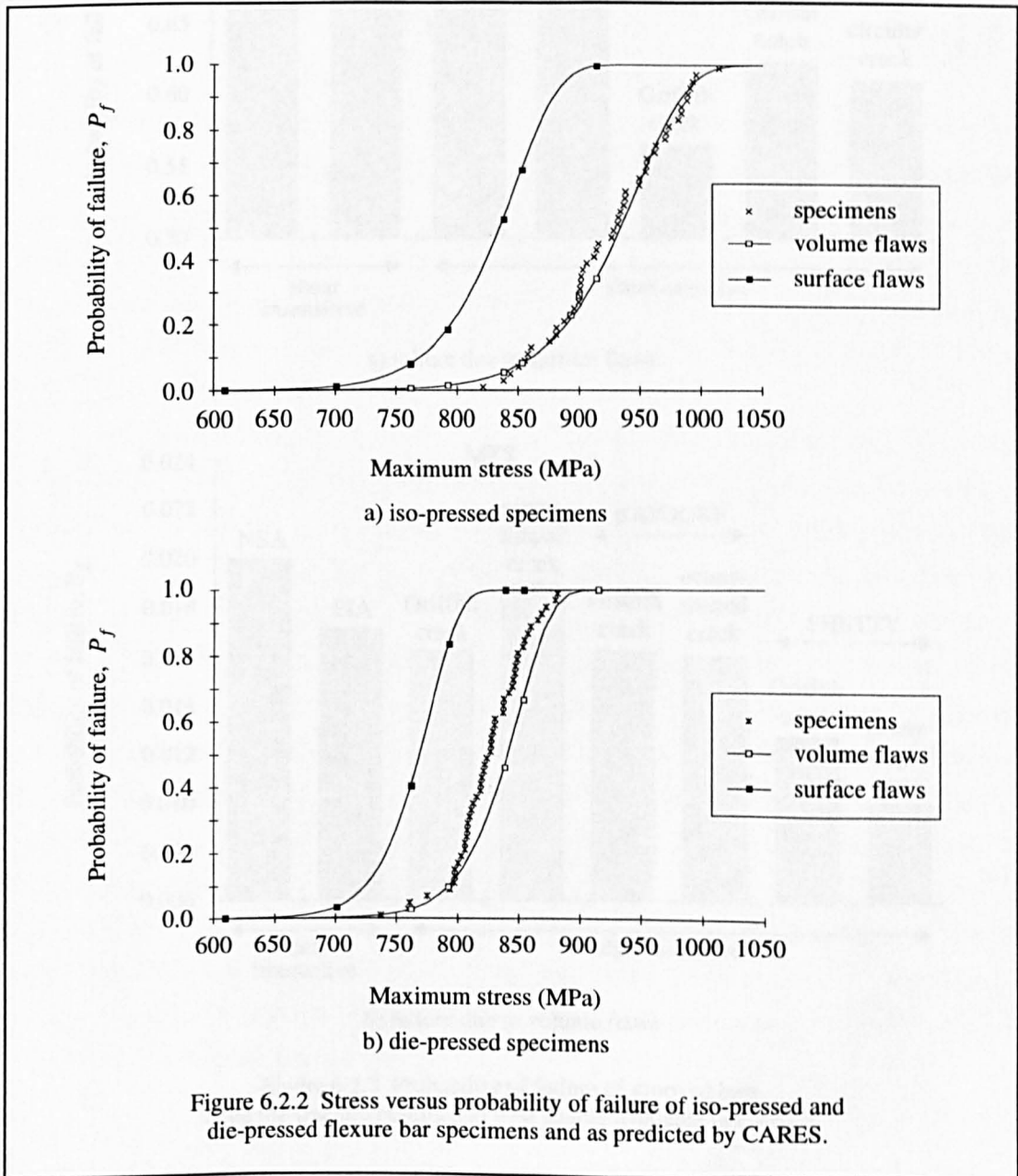


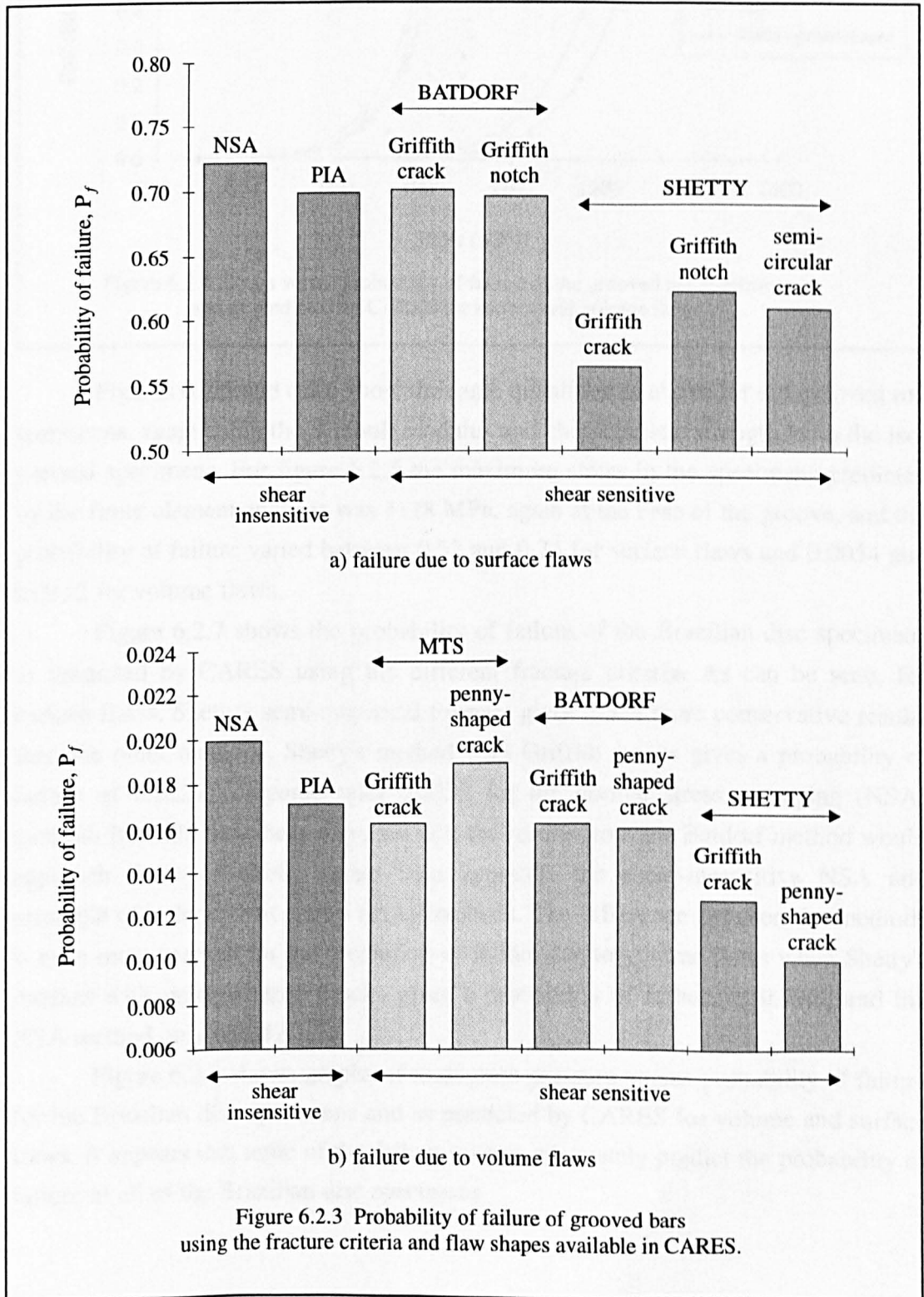
Figure 6.2.1 Probability of failure of flexure bars using the fracture criteria and flaw shapes available in CARES.

specimens as the statistical parameters are based on the failure of these specimens. Figure 6.2.2 shows graphs of maximum stress versus probability of failure for the iso-pressed and die-pressed specimens and as predicted by CARES for surface and volume flaws. The latter prediction more closely matches the failure of the specimens.

Figure 6.2.3 shows the predicted probability of failure, P_f , of the grooved bars calculated in CARES using the different fracture criteria and flaw shapes for surface and volume defects. In each case the maximum stress in the bar predicted by the finite element analysis is 1027 MPa and occurs at the base of the groove. The Weibull modulus and characteristic strength from the iso-pressed four point bend specimens were used as input. As can be seen P_f varies between 0.56 and 0.72 for



surface flaws and 0.01003 and 0.01995 for volume flaws. Figure 6.2.4 shows a plot of P_f versus maximum stress for the grooved bar specimens and as predicted by CARES using the normal stress averaging method (NSA), Shetty's method with semi-circular cracks and with Griffith cracks for surface flaws and the NSA method and Shetty's method with penny-shaped cracks.



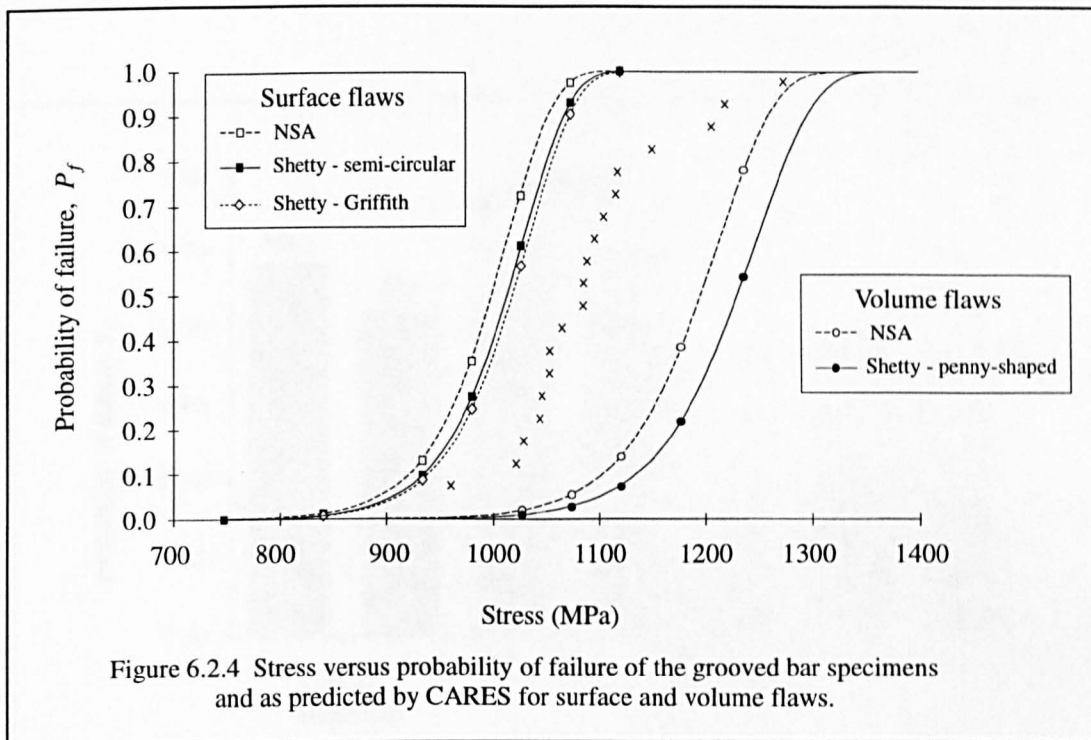
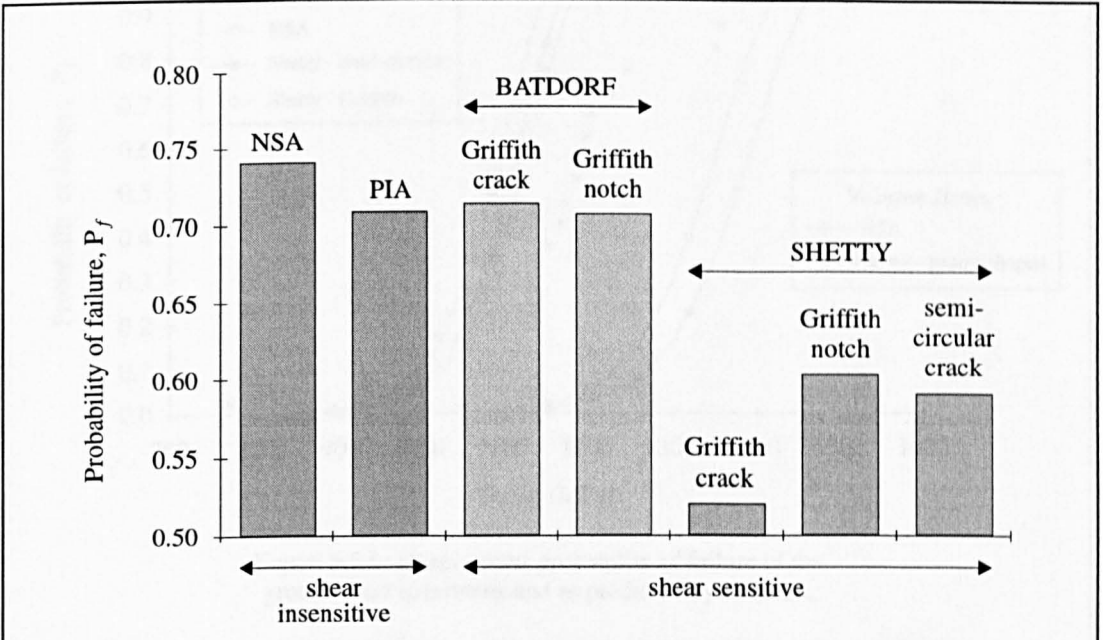


Figure 6.2.4 Stress versus probability of failure of the grooved bar specimens and as predicted by CARES for surface and volume flaws.

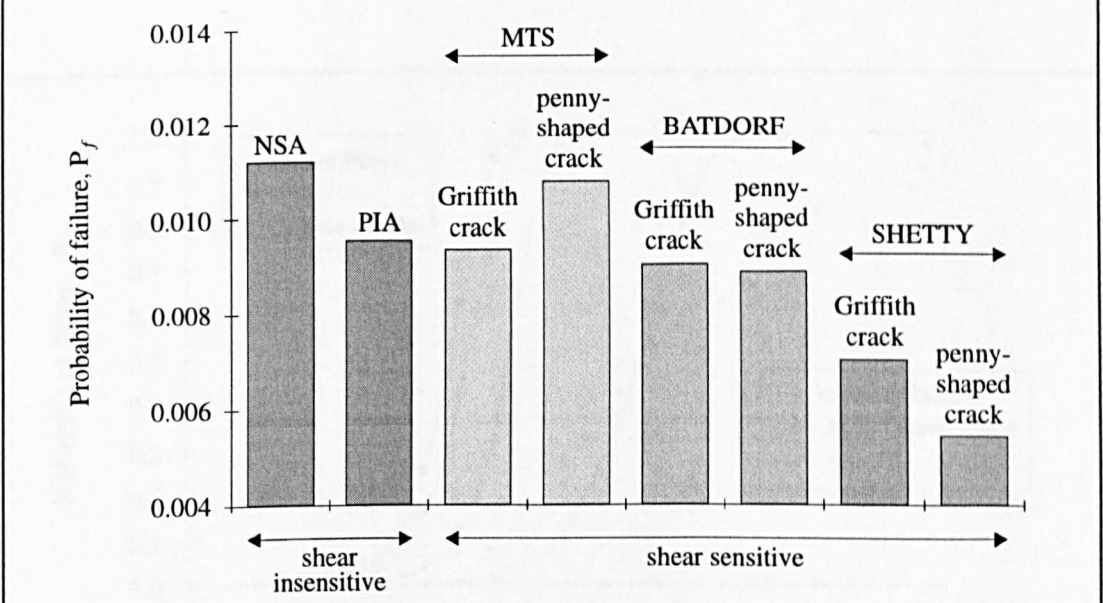
Figures 6.2.5 and 6.2.6 show the same quantities as above for the grooved rod specimens, again using the Weibull modulus and characteristic strength from the isopressed specimens. For figure 6.2.5 the maximum stress in the specimens predicted by the finite element analysis was 1118 MPa, again at the base of the groove, and the probability of failure varied between 0.52 and 0.74 for surface flaws and 0.0054 and 0.0112 for volume flaws.

Figure 6.2.7 shows the probability of failure of the Brazilian disc specimens as predicted by CARES using the different fracture criteria. As can be seen, for surface flaws, Shetty's semi-empirical formula gives much more conservative results than the other methods. Shetty's method with Griffith cracks gives a probability of failure of 0.6227 compared with 0.1238 for the normal stress averaging (NSA) method. It would have been expected that the results from the Batdorf method would approach those of Shetty rather than approach the shear-insensitive NSA and principle of independent action (PIA) methods. The difference between the methods is even more marked for the prediction of failure due to volume flaws when Shetty's method with penny-shaped cracks gives a probability of failure of 0.9922 and the NSA method only 0.0047.

Figure 6.2.8 shows graphs of maximum pressure versus probability of failure for the Brazilian disc specimens and as predicted by CARES for volume and surface flaws. It appears that none of the failure criteria adequately predict the probability of failure of all of the Brazilian disc specimens.

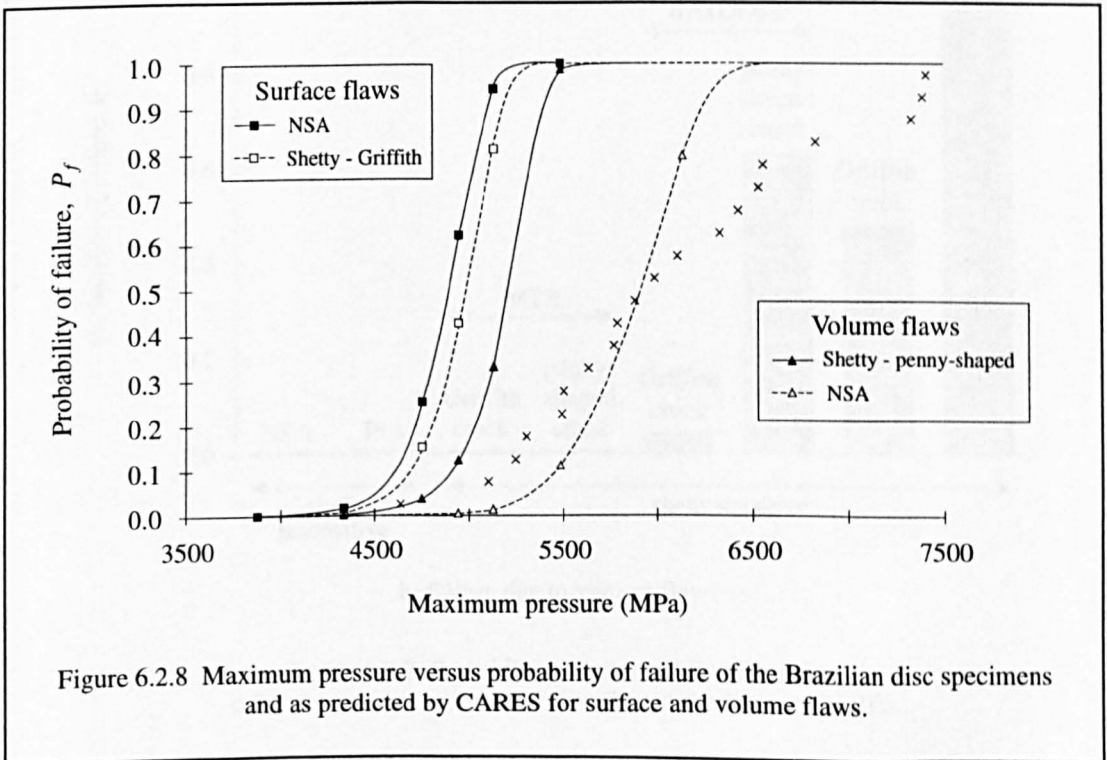
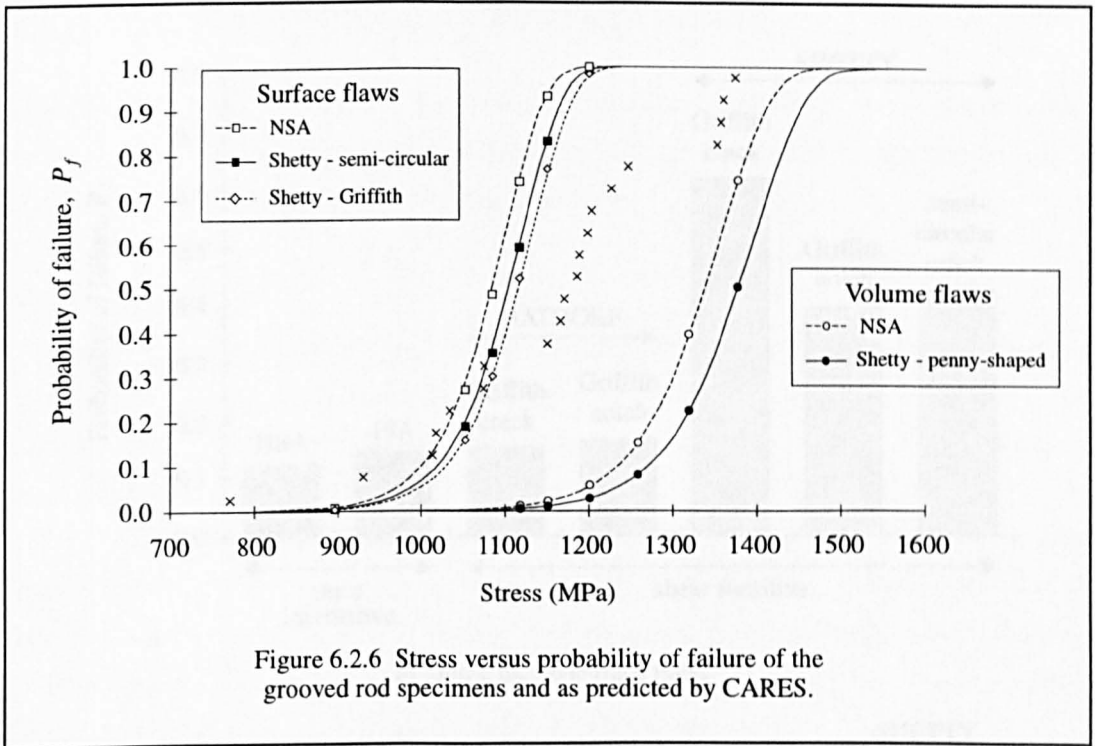


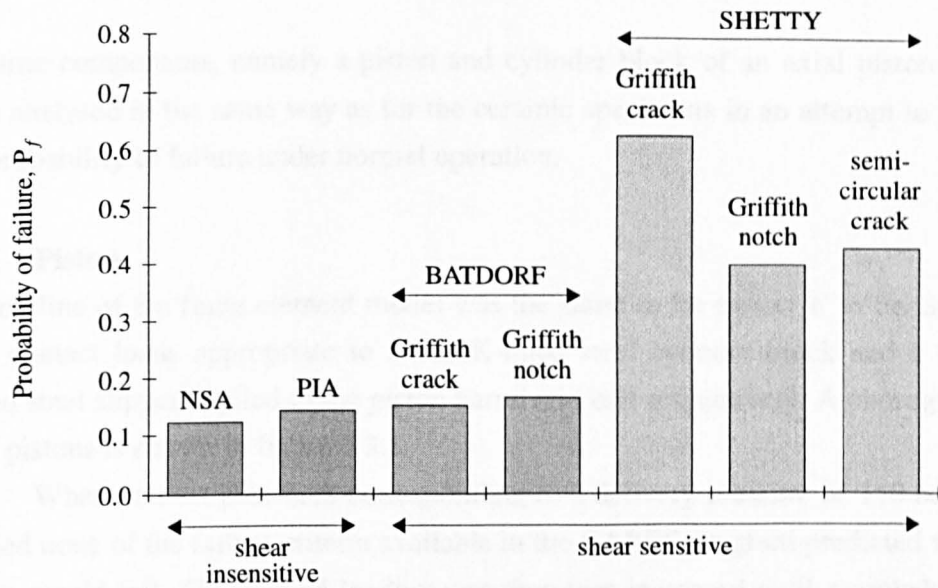
a) failure due to surface flaws



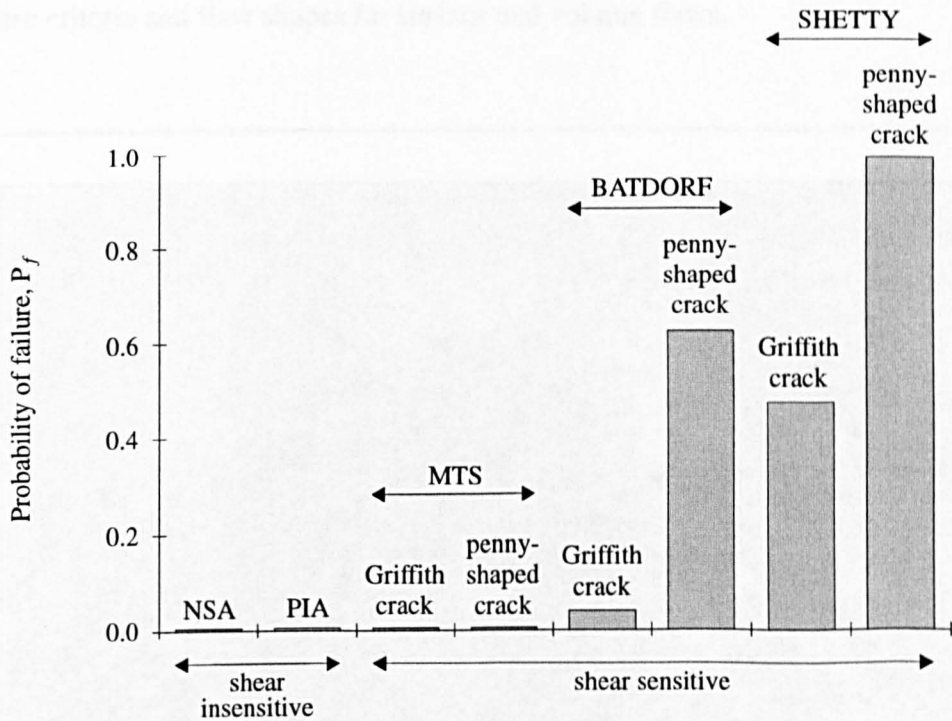
b) failure due to volume flaws

Figure 6.2.5 Probability of failure of grooved rods using the fracture criteria and flaw shapes available in CARES.





a) failure due to surface flaws



b) failure due to volume flaws

Figure 6.2.7 Probability of failure of Brazilian discs using the fracture criteria and flaw shapes available in CARES.

6.3 FAILURE PROBABILITY OF COMPONENTS

Ceramic components, namely a piston and cylinder block of an axial piston pump, were analysed in the same way as for the ceramic specimens in an attempt to predict the probability of failure under normal operation.

6.3.1 Piston

The outline of the finite element model was the same as for piston 'a' in Section 5.3, with contact loads appropriate to a PEEK-lined steel cylinder block and a PEEK-seated steel slipper applied to the piston barrel and ball respectively. A photograph of such pistons is shown in figure 6.3.1.

When contact pressures corresponding to a delivery pressure of 140 bar were applied none of the failure criteria available in the CARES program predicted that the piston would fail. The applied loading was therefore increased until a probability of failure was predicted. Figure 6.3.2 shows the probability of failure for the various fracture criteria and flaw shapes for surface and volume flaws.

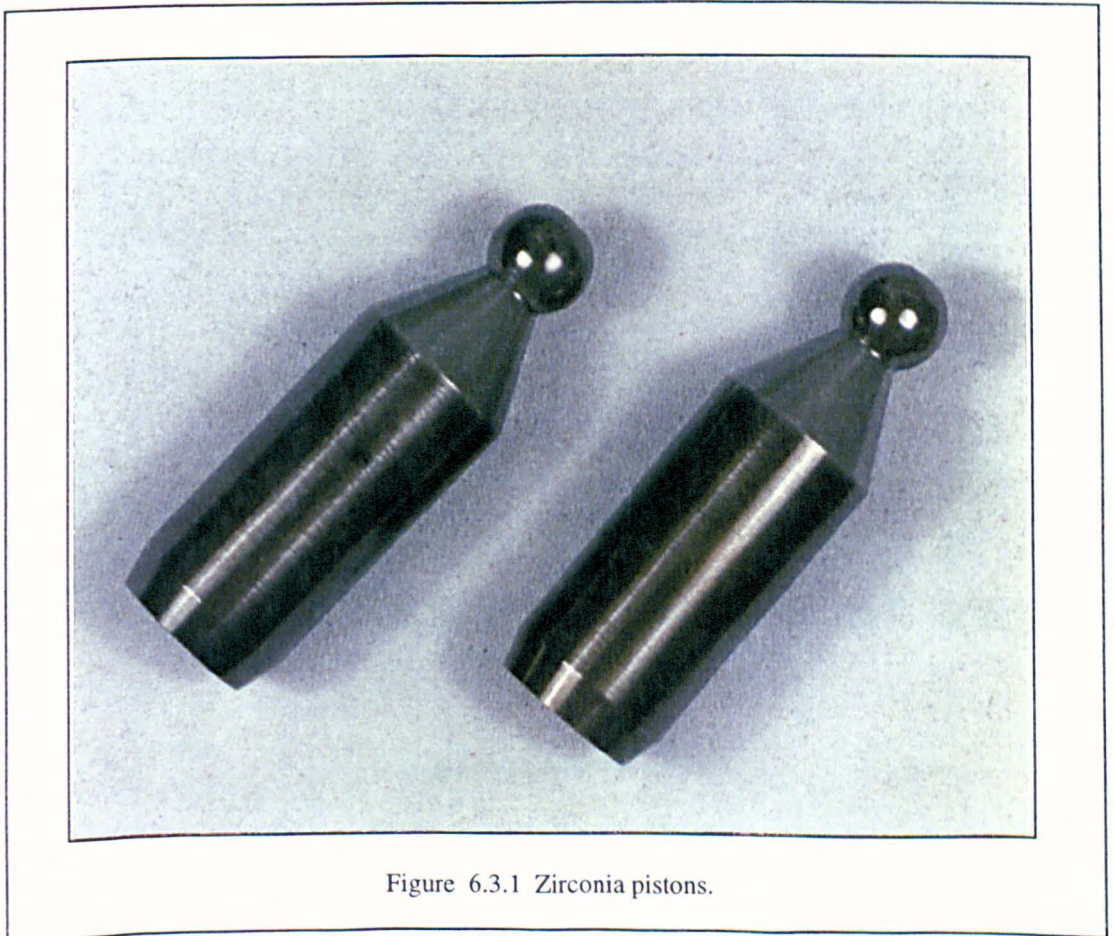
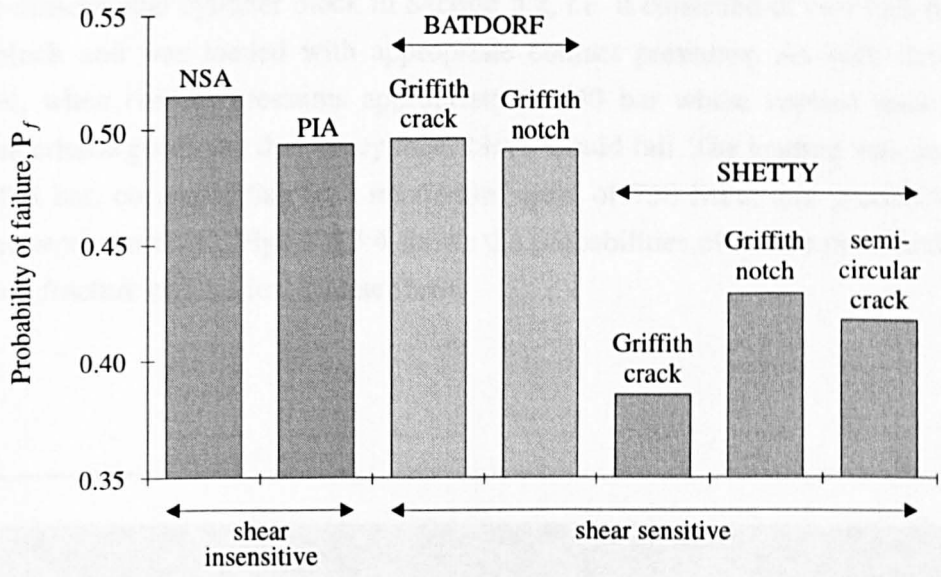
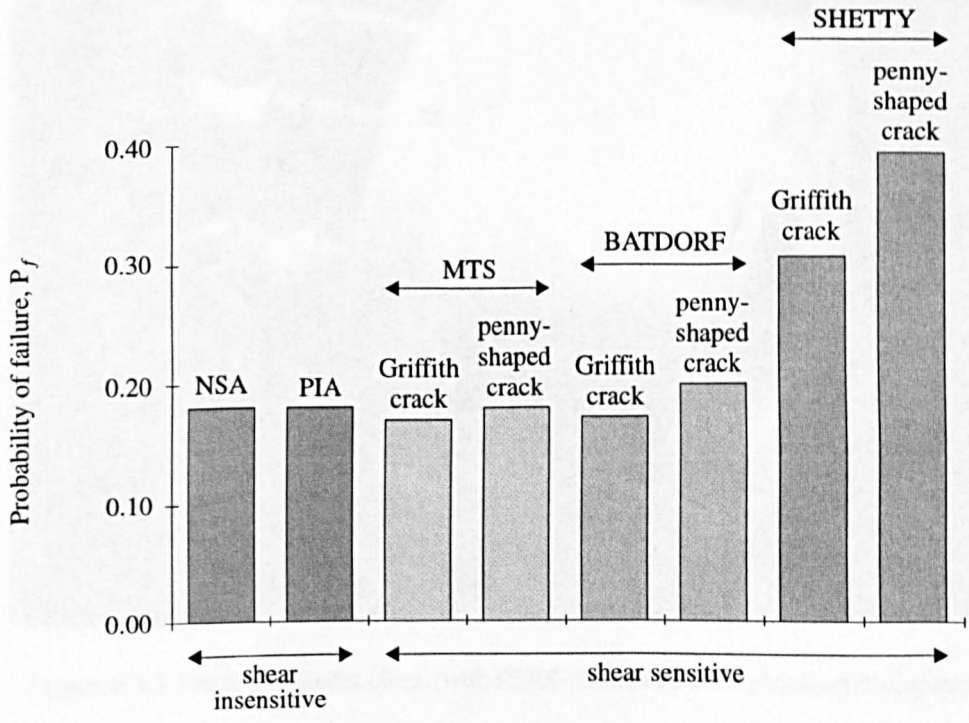


Figure 6.3.1 Zirconia pistons.



a) failure due to surface flaws



b) failure due to volume flaws

Figure 6.3.2 Probability of failure of a ceramic piston using the fracture criteria and flaw shapes available in CARES.

6.3.2 Cylinder block

Figure 6.3.3 shows a photograph of a ceramic cylinder block with PEEK-sleeved ceramic pistons. The outline of the finite element model was the same as for the three-dimensional cylinder block in Section 5.2, *i.e.* it consisted of two half bores of the block and was loaded with appropriate contact pressures. As with the piston model, when contact pressures appropriate to 140 bar were applied none of the failure criteria predicted that the cylinder block would fail. The loading was increased to 1475 bar, corresponding to a maximum stress of 730 MPa, and probabilities of failure were predicted. Figure 6.3.4 shows the probabilities of failure predicted by the various fracture criteria for volume flaws.

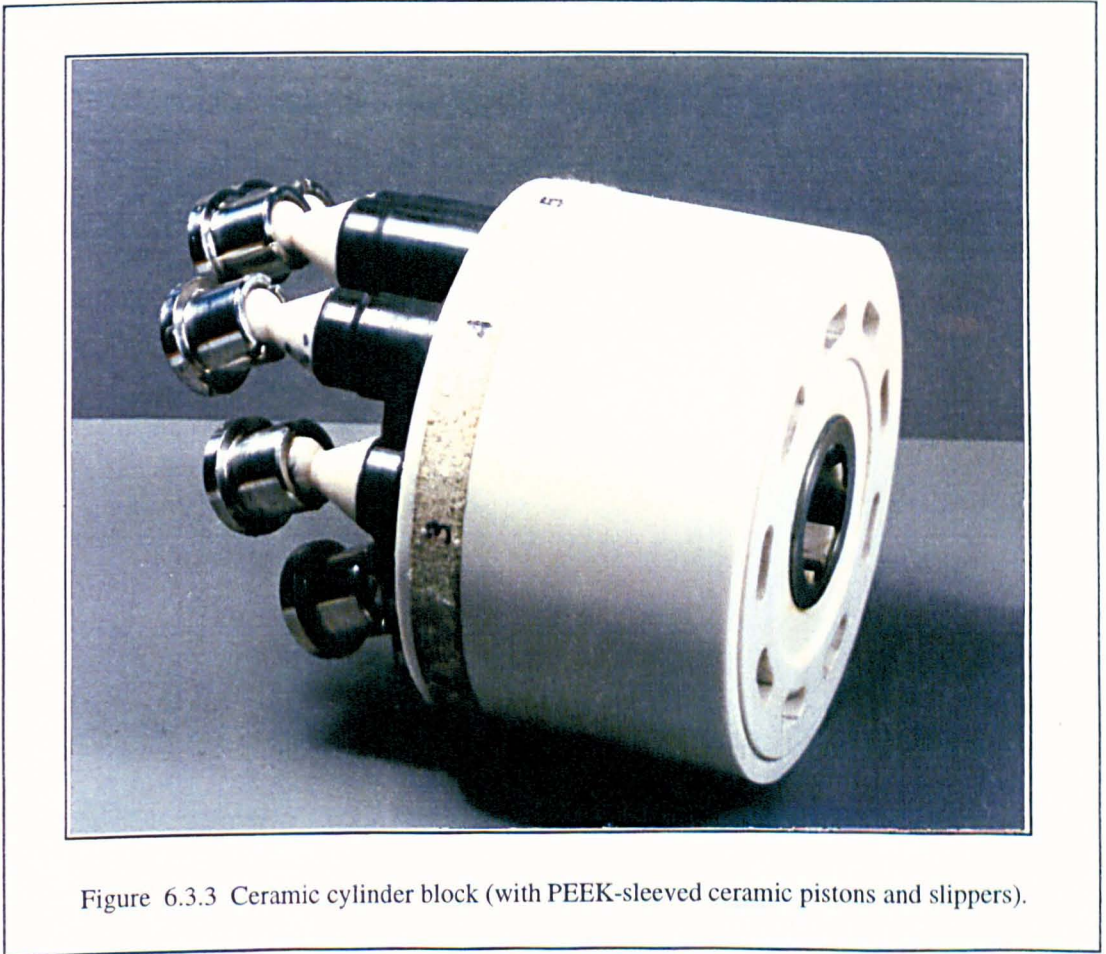
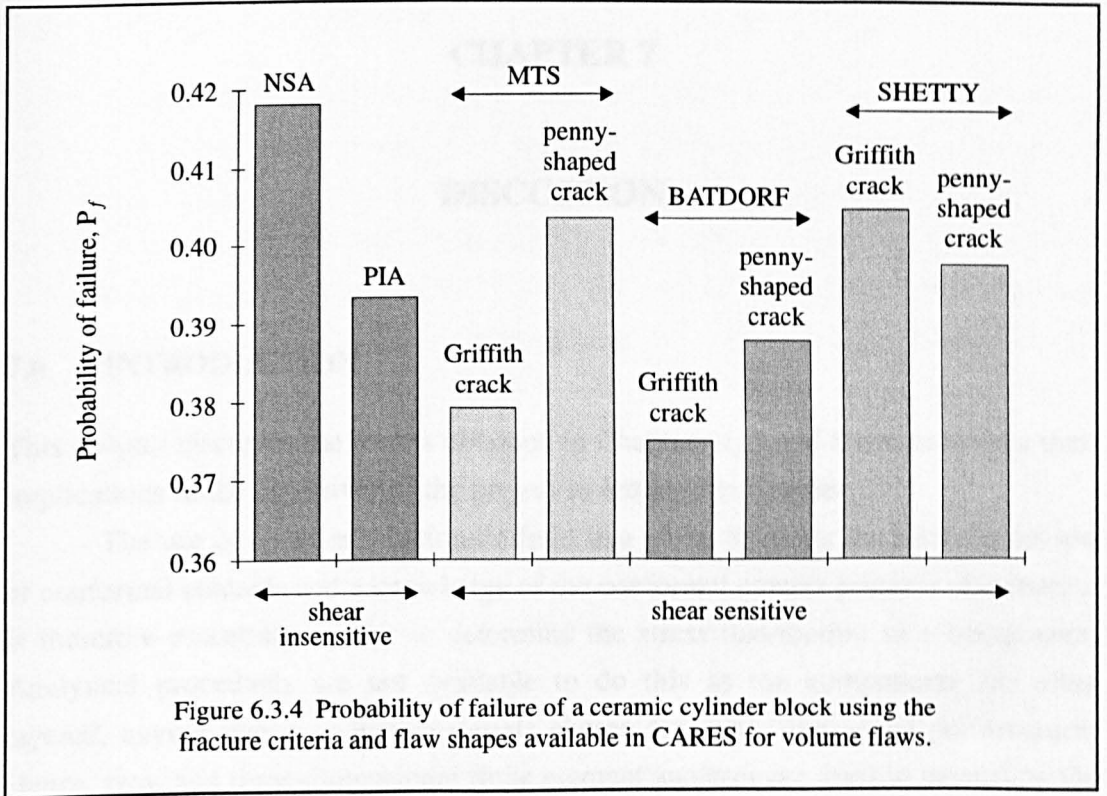


Figure 6.3.3 Ceramic cylinder block (with PEEK-sleeved ceramic pistons and slippers).



CHAPTER 7

DISCUSSION

7.0 INTRODUCTION

This chapter discusses the results obtained in Chapters 4, 5 and 6 and considers their implications to the objectives of the project as outlined in Chapter 1.

The use of water as a hydraulic fluid in a pump or motor necessitates the use of conformal contacts and a knowledge of the conformal contact pressure distribution is therefore essential in order to determine the stress distribution in a component. Analytical procedures are not available to do this as the components are often layered, having sleeve or liner materials chosen for their tribological performance. Hence, two- and three-dimensional finite element analyses are used to determine the contact pressure distribution between cylindrical and spherical conformally contacting layered components. Some preliminary discussion of these results was conducted in Chapter 4, in particular, with respect to verification of the models with known analytical solutions, and thus will only be summarised here.

The stress distribution in layered, conformally contacting, axial piston pump components was then determined in Chapter 5, using the contact pressure distributions from the previous two- and three-dimensional contact analyses as loading. Although the results have not been proven by strain gauging specimens they have been proven by comparison with other published results, extensive convergence checking and some comparison with actual failed components.

Advanced engineering ceramics have been employed in the adaptation of a pump for use with sea-water. Several statistical methods have emerged which attempt to determine a probability of failure of a ceramic component from a knowledge of the strengths of samples of the same material. The results from the above finite element analyses provided a convenient way of determining the stress distribution in the entire component as required by the statistical methods. Chapter 6 described the use of the computer program CARES (Ceramic Analysis and Reliability Evaluation of Structures) which was used in an attempt to determine the most appropriate statistical method for calculating the probability of failure of PSZ components from specimen strength data. A discussion of the results of this is also undertaken in this chapter.

7.1 CONTACT ANALYSIS

The finite element method, using gap elements, has proved to be a useful way of determining the contact size and pressure distribution between conformally contacting components. When layers of material, having different stiffnesses, are used in such components there are no analytical methods available and finite element analysis proves even more useful. Two- and three-dimensional cylindrical and axisymmetric analyses have been conducted and the whilst some of the results may appear to be obvious in a qualitative sense, this approach has allowed the effects to be quantified and this will be discussed below.

7.1.1 Cylindrical contact

In two dimensions comparisons are made between the analytical results of Persson (1964), who analysed the problem of a circular disc contacting an infinite cylindrical cavity, and Hertz whose results are valid for small contact angles only, due to the assumptions made in his analysis.

Numerous finite element analyses were conducted to assess the effects of load, F , Young's modulus, E , and clearance between the cylinder and cavity, CL . The results closely match those predicted by Persson despite the step-wise nature of the contact angle in the finite element analysis. As expected, the results compare well with Hertzian analysis for contact angles less than about 12° but above this they diverge markedly. Figure 4.1.3 showed the separate effects of F , E and CL on the contact angle. Increasing the force, reducing the stiffness and reducing the radial clearance all result in a greater contact angle. It can also be concluded from these graphs that at relatively small loads, of for example 10 N, a change in the stiffness of the material has a greater effect on the contact angle the smaller the clearance, but that at much higher loads, say 5000 N, the opposite is the case.

As previously stated the pressure distribution around the contact interface is of greater interest than the contact angle alone and it has also been shown, in figure 4.1.7, that an excellent agreement is obtained between that predicted by finite element analysis and Persson's analytical model. This graph shows a different relationship between the variables in different regions, approaching that of Hertz for values of $\frac{F}{CL * E} \leq 0.1$. However, for values of $\frac{F}{CL * E} \geq 5$ the non-dimensionalised maximum pressure, $\frac{R_{p_{max}}}{F}$, approaches a constant value of 0.6.

For dissimilar materials, that is, when the cylinder and cavity are composed of different materials the results from the finite element analysis agree with those of Persson and Chen and Marshek (1988). In this case it is found that a hard cylinder

contacting a soft cylindrical cavity results in a higher contact angle than a soft cylinder contacting a hard cavity.

When considering components which have sleeve or liner materials of different stiffness to the bulk materials analytical methods are inappropriate. Finite element analyses were therefore undertaken to assess the effects on the contact angle and hence, the contact pressures, of using different sleeve or liner materials and of changing the clearance between the components. The above was done with dimensions and material properties appropriate to those which might be used in the axial piston pumps under consideration.

It was shown in figure 4.2.2 that using a sleeve or liner of a stiffer material does not affect the contact angle to nearly the same degree as using a more compliant sleeve or liner material. The contact angle was shown to increase as the sleeve or liner thickness increased provided the material was more compliant. The opposite effect would be observed for a stiff liner or sleeve material.

The contact between a piston and cylinder block in an axial piston pump is further complicated by the tilting of the piston in the bore. For that reason a three-dimensional model was created to assess the effects of material properties, sleeve and liner thickness, radial clearance and load on the contact pressure distributions in both the radial and axial directions. The limitations on model size did not allow as fine a mesh to be used as for the two-dimensional case. However, by biasing the mesh such that the mesh density was greater in the regions of contact, convergent results were obtained.

Comparing the results from the two- and three-dimensional analyses it can be seen that the general trends, as expected, are the same. Table 7.1.1 shows a comparison of the results from two specific cases, namely a PEEK-sleeved steel piston in a steel cylinder block and a ceramic piston in a PEEK-lined steel block. Three-dimensional plots for these cases were shown in figure 4.6.3. As can be seen reasonably good agreement is obtained between the radial contact angle, α , and the maximum pressure, P_{max} , especially for the first case. The coarser mesh density of the

	PEEK-sleeved steel piston in steel cylinder block		ceramic piston in PEEK-lined steel cylinder block	
	α	P_{max}	α	P_{max}
2D	53.75°	58.5 MPa	40.625°	67.6 MPa
3D	45.0° - 56.2°	54.1 MPa	45.0° - 56.2°	79.1 MPa

Table 7.1.1 Comparison of sample results from two- and three-dimensional contact analyses.

three-dimensional models did not allow the contact angles to be determined with great accuracy. However, the maximum contact pressure was determined with more confidence as illustrated. In addition, the contact pressure distribution in the axial direction is determined by using the three-dimensional model, allowing a much more accurate representation of the contact due to the tilting of the pistons within the bores.

7.1.2 Spherical contact

For the case of a sphere conformally contacting a spherical seat the analytical methods available are more limited than the equivalent expressions for the cylindrical case. For small contact angles, below about 25° , the contact angles predicted by the finite element analysis agrees closely with Hertzian analysis as shown in figure 4.3.3. However, for angles below a few degrees the prediction of the maximum pressure departs from that predicted by Hertz. This is probably due to the fact that for small contact angles the mesh needs to be finer in the contact region. For the application being considered here this is not a problem as much greater contact angles than this are experienced between the piston ball and slipper seat in an axial piston pump.

As with the cylindrical case, analyses were conducted using materials and dimensions appropriate to the pumps under consideration, including the effects of using different seat materials. As with the equivalent cylindrical case, *i.e.* that of using different liner materials, as the seat thickness increases the contact angle increases, provided the seat material is more compliant than that of the slipper. This effect increases the more compliant the seat and the smaller the clearance between the components.

In addition, an attempt was made to determine the contact pressure distribution for discontinuous contact as both the piston ball and slipper seat have a central hole. The results of this showed that a high pressure is found at the edge of contact, quickly approaching that found for unbroken contact. This effect was found for the cylindrical case by Chen and Marshek (1986) who analysed surface depressions on the conformal contact of bearings.

7.2 CYLINDER BLOCK ANALYSIS

Two- and three-dimensional analyses were conducted of the cylinder block of an axial piston pump in order to determine the stress distribution during normal operation. The primary concerns are the maximum stress, the effects on the stresses of using liners of different, usually polymeric, materials and, for the ceramic cylinder block, the stress distribution in the whole block. The two-dimensional model

analysed a cross-section through all nine bores of the cylinder block using contact pressure loading from the appropriate two-dimensional component-sized contact model as loading and allowed a detailed study of the variation of the stress as the cylinder block rotates and the pistons reciprocate within the bores, as shown in figures 5.1.6 and 5.1.7. The latter figure shows the large fluctuations in stress experienced by three different positions in the inter-bore region, thus predisposing the cylinder block to fatigue failure.

The three-dimensional model consisted of two half bores of the cylinder block and used contact pressure loading from the appropriate three-dimensional contact analyses. It can be seen from the three-dimensional stress contour plots in figure 5.2.4 that the highest stress occurs at the kidney ports and that when the bore diameters are increased to allow the inclusion of PEEK liners then the inter-bore stress approaches the kidney port stress.

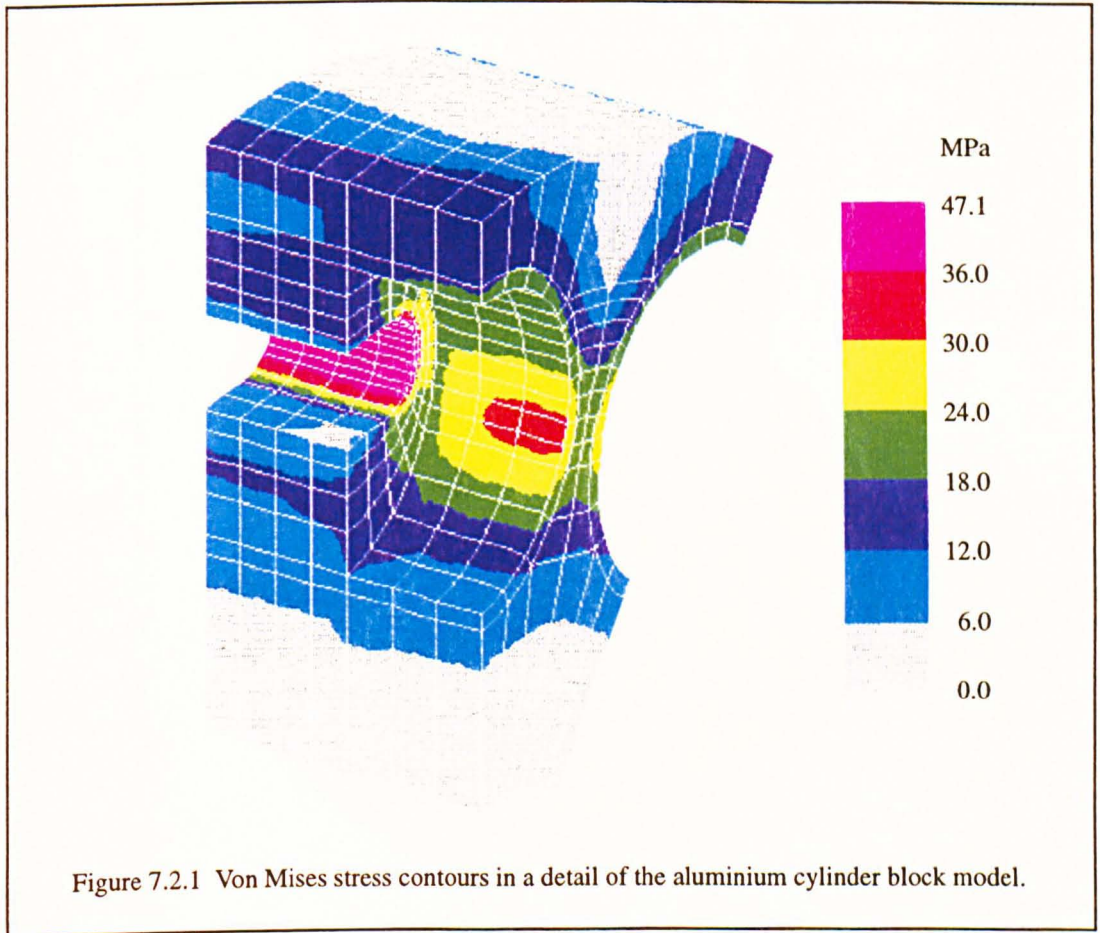
Comparing the results from the two- and three-dimensional analyses it can be seen that the stress predicted by the two-dimensional model is greater than that predicted by the three-dimensional model. This is probably due in a great part to the stiffening effect of the material closing the bore ends (*i.e.* at the porting). In addition, the two-dimensional model assumes that the same load is applied along the whole length of the bore. In the three-dimensional model the maximum delivery pressure is assumed to act only between the porting and the pistons; and the contact pressures from the pistons over a limited axial distance. Hence, the stress levels in the three-dimensional are more representative whilst the two-dimensional model is important in giving a better indication of the fluctuation of stress.

To date, two cylinder blocks have failed: an unlined aluminium alloy block with an anodised coating, and a polymer-lined stainless steel block, providing valuable data to validate the finite element analysis results.

7.2.1 Aluminium cylinder block

Figure 7.2.1 shows the stress contours predicted by the finite element analysis for the unlined aluminium alloy (6082 TF) cylinder block operating with PEEK-sleeved steel pistons. No attempt was made to model the coating which was typically 50 μm thick. The pump unit was operated at pressures up to 100 bar and failure occurred at approximately 18.5×10^6 cycles.

Detailed examination of the failed cylinder block revealed that the coating treatment had completely worn through at the top-dead-centre of piston travel in a number of bores, exposing the relatively soft aluminium substrate underneath. The aluminium itself was then worn to a depth of some 70 μm . Microscopic analysis of the fracture surfaces revealed that a crack originated from the point of maximum



stress in the inter-bore area and rapidly spread up to the kidney port causing catastrophic failure. Figure 7.2.2 shows a photograph of the failed cylinder block with the external cracks clearly visible. The finite element analysis predicts a maximum stress in the inter-bore region of 34.6 MPa for a delivery pressure of 100 bar and contact from PEEK-sleeved pistons. The fatigue strength for uncoated 6082 aluminium alloy is 170 MPa at 50×10^6 cycles (Waterman and Ashby, 1991) which is clearly greater than that predicted. However, the wear step will clearly have introduced a substantial stress concentration which, when combined with the corrosion effects of the water, will greatly increase the likelihood of fatigue failure.

7.2.2 PEEK-lined stainless steel cylinder block

An axial piston pump with ceramic pistons running in a polymer-lined stainless steel cylinder block was developed as part of the Water Hydraulics project as an intermediate step to producing a sea-water pump. The pump was tested for more than 60×10^6 cycles (700 hours) at pressures up to 140 bar on tap water in the laboratory, and then for nearly 15×10^6 cycles at similar pressures on sea-water before failure of the block occurred. When removed from the casing, cracks were visible, as shown in figure 7.2.3.

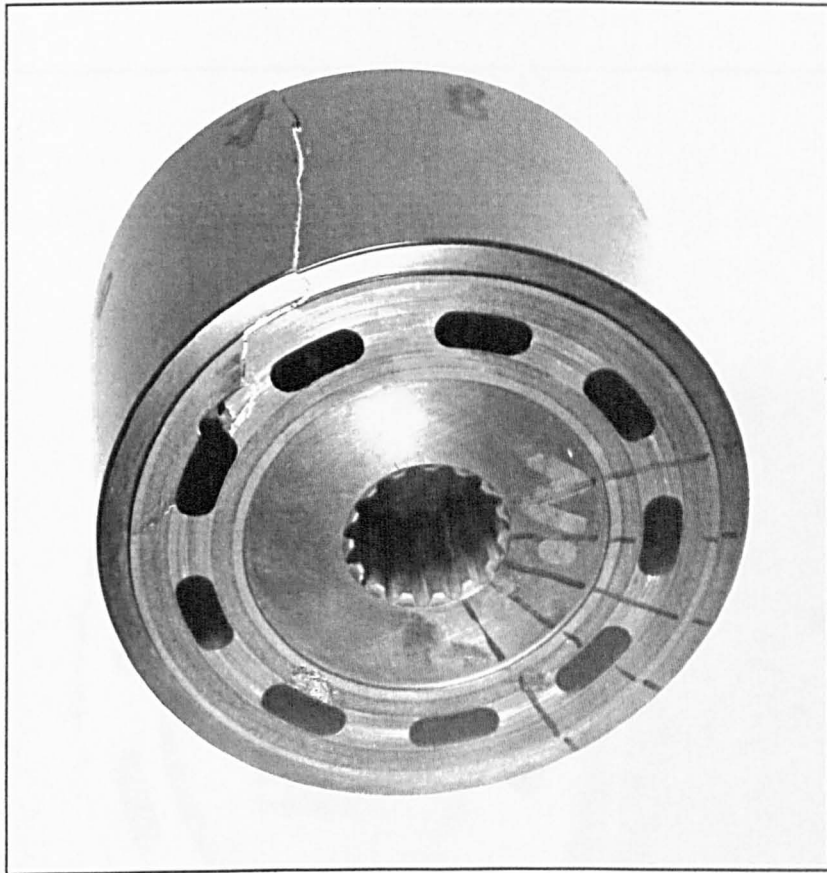


Figure 7.2.2 Failed aluminium cylinder block.

A detailed microscopic examination of the fracture surfaces revealed fatigue cracks originating from the kidney ports of two bores. Subsequently, these two individual cracks linked and it is considered most likely that this led to the formation and propagation of a major longitudinal crack in one of these bores.

The stresses predicted by finite element analysis of a cylinder block of this configuration were plotted in figure 5.2.4b and showed a maximum stress of 72 MPa in the kidney port area. This stress is significantly lower than the 250 MPa limiting fatigue design stress normally expected of 431 stainless steel. This observation, together with multiple initiation of other fatigue cracks, branching, and corrosion product on the fracture surfaces, is consistent with the conclusion that corrosion fatigue was the primary cause of failure of this cylinder block.



Figure 7.2.2 Failed PEEK-lined stainless steel cylinder block.

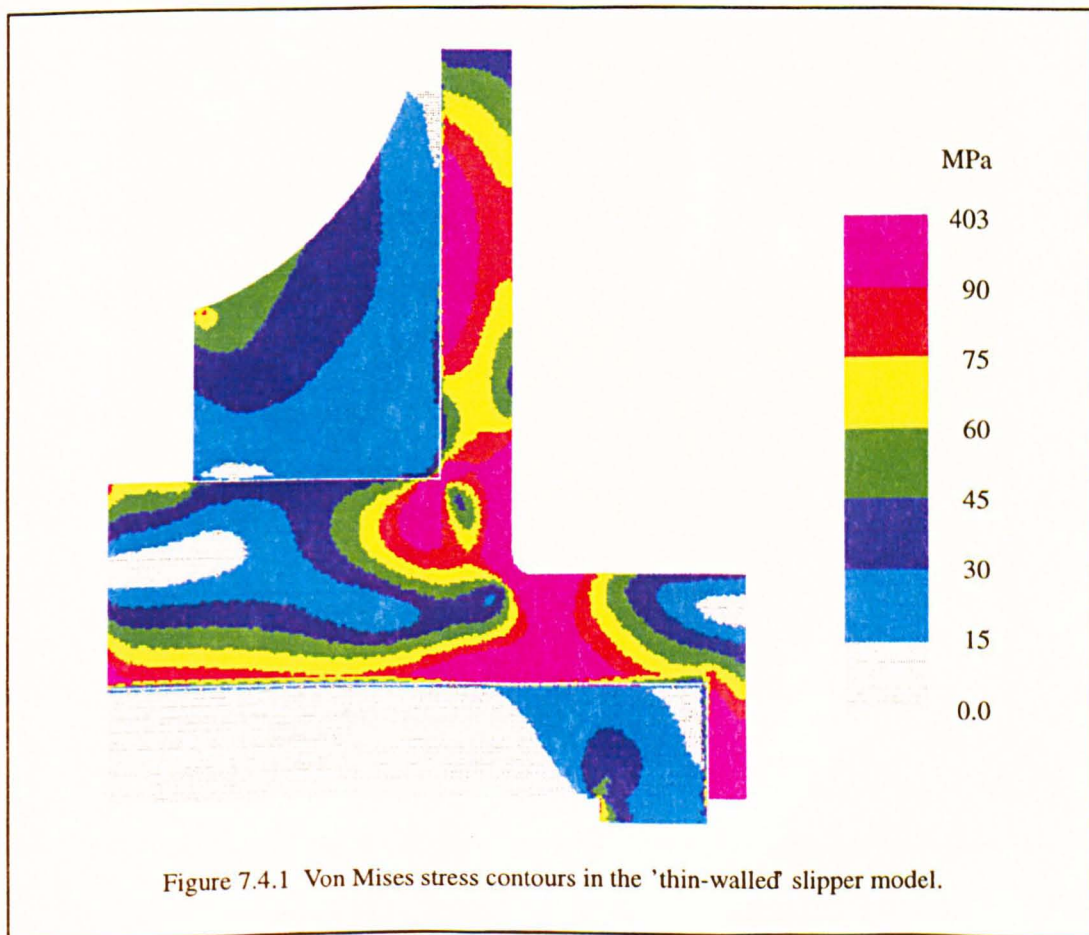
7.3 PISTON ANALYSIS

The stresses in the necks of the pistons are relatively high (figure 5.3.5) and might be expected to lead to a fatigue failure, especially in the corrosive environment of water. However, in practice none of the PEEK-sleeved steel pistons failed.

Two failures of ceramic pistons have occurred during testing although neither happened during normal operation of the pumps. One piston seized in the bore due to overheating, became overloaded and failed at the critical section of the neck identified by the finite element analysis. The other piston failed as a consequence of the fatigue of the PEEK-lined stainless steel cylinder block described in the previous section, again at the neck region. Further, probabilistic analysis of the ceramic pistons is described in Section 7.5.

7.4 SLIPPER ANALYSIS

Section 5.4 considered the analysis of two designs of slipper used in the axial piston pumps. An early version of slipper design 'a' with a thinner wall section failed after running for 117 hours at a pressure of 140 bar. Figure 7.4.1 shows the stress contours



in the slipper assembly predicted by finite element analysis and figure 7.4.2 the fractured slipper with the PEEK seat removed.

Inspection of the slipper revealed a fatigue fracture with the original crack propagation site at the radius at the bottom of the seat. No beach markings were evident indicating uninterrupted crack growth and radial chevrons indicated the route as being from the inside to the outside radius. No obvious internal material defects

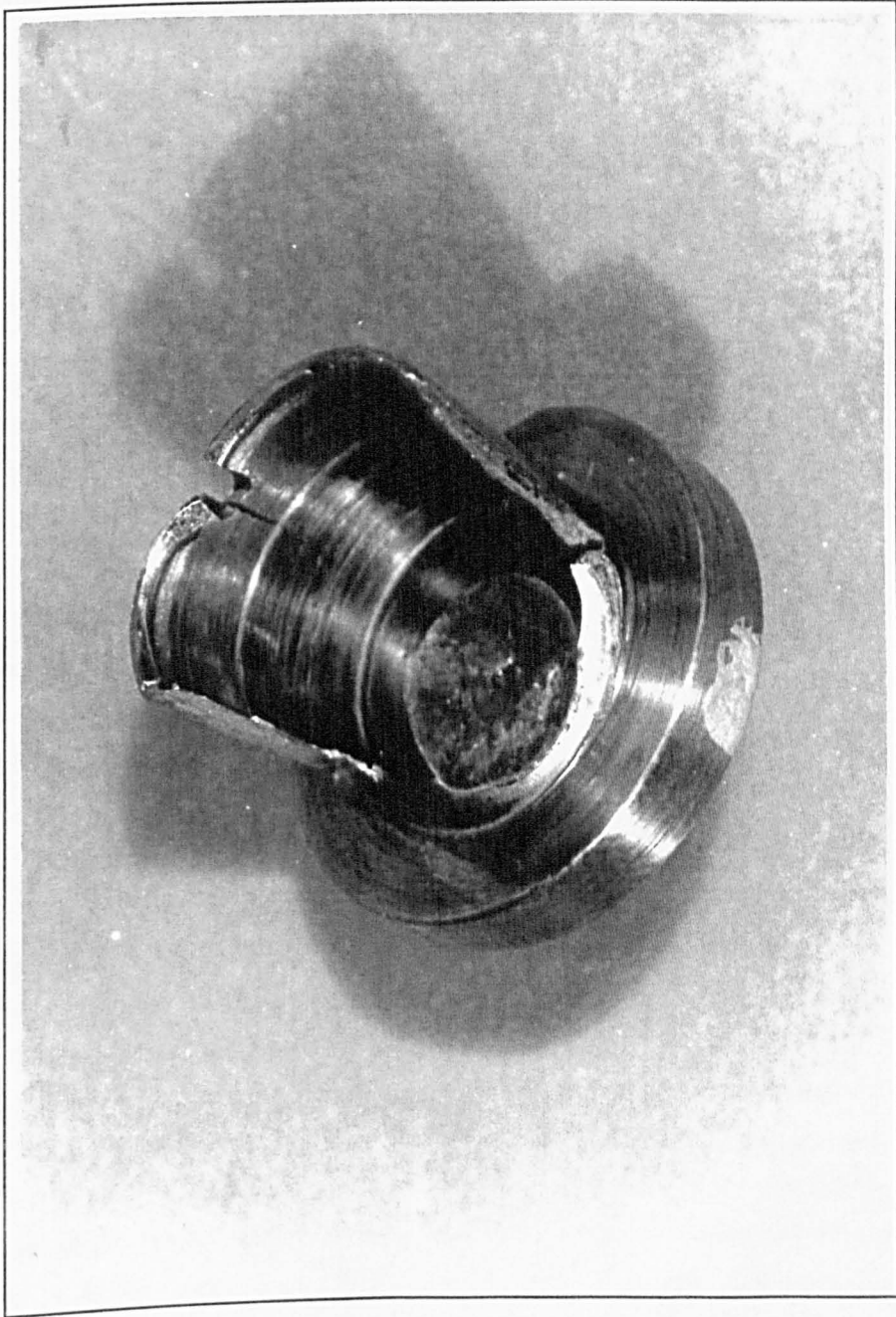


Figure 7.4.2 Failed slipper with PEEK seat removed.

were found. Further investigation revealed that the inner radius was well below specification. The slipper experienced 10×10^6 cycles at a maximum stress of 403 MPa. Subsequent to this failure the wall thickness of the slippers was increased from 1 mm to 2 mm and no more failures were experienced. Figure 5.4.5 showed the stress contours in the slipper after the increase in wall thickness. It can be seen that this resulted in a reduction of the maximum stress from 403 MPa to 267 MPa which is still close to the fatigue strength. It is anticipated that an increase in delivery pressure above 140 bar would lead to more failures and, in this case, it is recommended that slippers of design 'b' be used. These slippers have a greater bulk of steel and the maximum stress is predicted to be 169 MPa at 140 bar bore pressure. However, care must be taken to maintain the depth of the PEEK seat. A model was made with a much thinner seat, predicting a high stress below the edge of contact with the piston ball. A slipper of this configuration failed at this position in service.

7.5 CERAMIC COMPONENT ANALYSIS

This section discusses the results of the statistical analyses undertaken to determine the probability of failure of ceramic specimens and components. Quite a number of papers have been published on isolated work done on the theory of individual methods for the testing and analysis of ceramic specimens, but there has been limited collation and integration of the results. In particular, there is little work on the application and comparison of the different methods to the design of actual engineering components.

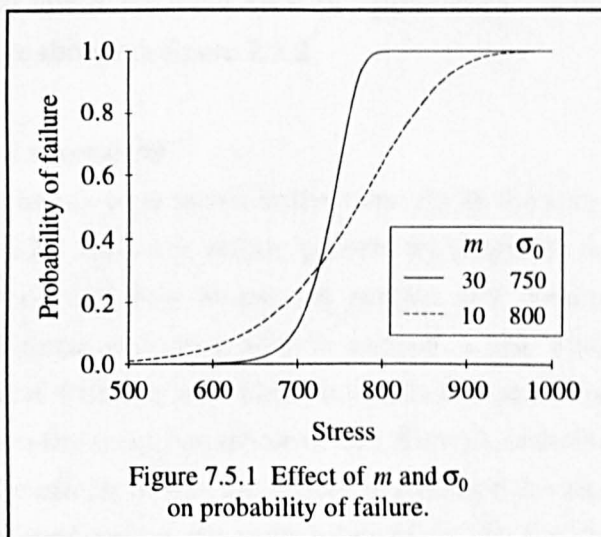
7.5.1 Flexure bar specimens

Two sets of flexure bar specimens were tested and subsequently analysed using the fracture criteria and flaw shapes available in the CARES (Ceramic Analysis Reliability Evaluation of Structures) program. As the Weibull modulus and characteristic strength data used in the statistical analysis was obtained from the failure of these specimens it would be expected that the CARES program would reliably predict their probability of failure. Figure 6.2.1 showed that, for the flexure bars, the failure probability was essentially the same regardless of the failure criterion or crack shape selected. The probability of failure versus stress was shown in figure 6.2.2 for both sets of specimens and as predicted for both volume and surface flaws. The failure of the iso-pressed specimens is reliably predicted if it is assumed that they fail from volume flaws. However, it is usually assumed that four-point bend specimens fail from flaws on, or just beneath, the tensile surface.

The failure of the die-pressed specimens does not appear to be quite so reliably predicted if it assumed that they fail from volume flaws.

An important point for ceramic manufacturers which arises from the failure of the iso-pressed and die-pressed specimens are the values of the Weibull modulus, m , and characteristic strength, σ_0 . A high Weibull modulus indicates a low scatter of strength data of the four-point bend specimens and is taken as resulting in a more reliable material and, therefore, component. However, in this case the higher Weibull modulus of the die-pressed specimens is accompanied by a lower characteristic strength. The higher strength of the iso-pressed bars is a result of the better compaction afforded by the multi-directional iso-pressing compared with the uni-directional die-pressing. For a given application the question must be asked as to whether a higher Weibull modulus

or higher characteristic strength is required. Figure 7.5.1 shows two probability of failure curves, one with a Weibull modulus of 30 and characteristic strength of 750, the other with a Weibull modulus of 10 and characteristic strength of 800. At stresses over 720 the latter material would appear to be the more reliable but below 720 the former material is less likely to fail.



A further set of flexure bar specimens was cut from a ceramic cylinder block and tested to failure. This was to assess the effect of position within the component on the material strength and reliability. Figure 6.1.6 showed the fracture data plotted according to radial position and there does appear to be a difference between the specimens cut from the different positions. The Weibull modulus varied between 7.1 and 18.6 with an overall value for all the specimens of 10.5. However, the value did not increase or decrease with radius and no further conclusions could be drawn. The characteristic strength varied between 603.4 and 721.0 and, apart from positions A and B, increased towards the centre of the cylinder block. This could be due to an increase in the density of the material as the ceramic is pressed from the outside towards a central mandrel. An attempt to scan the cylinder block using x-ray tomography provided no useful results.

The strengths of the specimens cut from the cylinder block were much lower than either the iso-pressed or die-pressed specimens. This could be due to one of several reasons. The material of the cylinder block could be less well compacted than

the relatively small, uniformly-shaped flexure bars; the green machining procedures could introduce flaws or residual stresses and cutting the specimens from the block itself could result in damage. The cylinder block specimens were polished prior to testing but this might not have removed all the cutting defects. For the statistical analysis to be valid the flexure bars must exhibit the same size flaw population and mechanical properties as the component, as outlined in Section 3.5, which might not be true for the reasons given above.

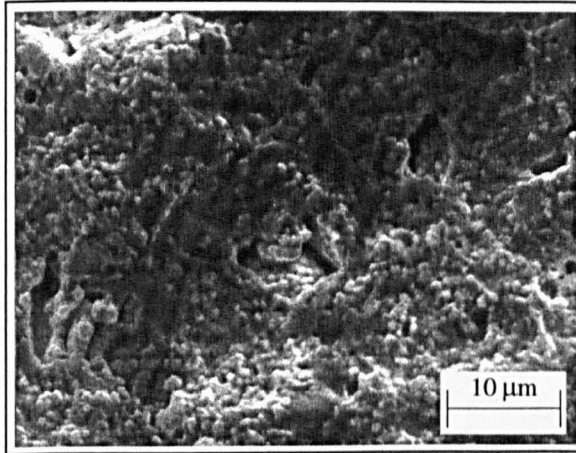
100% fractography of ceramic test specimens, as recommended by Quinn and Morrell (1991), did not prove to be useful in this case. Ytria-stabilised zirconia has a very fine grain structure and examination of the fracture surfaces in a scanning electron microscope, except in a very few cases, did not reveal any visible defects. In some of the specimens which failed at low loads flaws such as agglomerates, pores and impurities were observed. These are shown in figure 7.5.2.

7.5.2 Grooved bar and grooved rod specimens

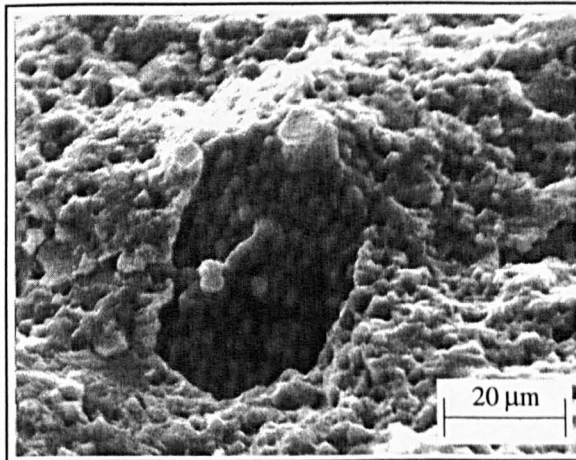
The grooved bar and grooved rod specimens were tested in the same rig as the four-point flexure bars. Figures 6.2.3 and 6.2.5 show the failure probability predicted by CARES for each of the fracture criteria and flaw shapes for surface and volume flaws. For surface flaws the normal stress averaging (NSA) method is the most conservative and Shetty's semi-empirical criterion with Griffith cracks the least. For volume flaws the NSA method is again the most conservative and Shetty's criterion with penny-shaped cracks the least. The effects of this are shown in figures 6.2.4 and 6.2.6 where the maximum stress is plotted versus the probability of failure for the specimens and as predicted by CARES. The failure of the weakest seven of the grooved rod specimens appears to be well predicted by assuming they fail from surface flaws, the strongest four approach the probability of failure due to volume flaws with the remainder lying somewhere between. However, examination of the fracture surfaces using scanning electron microscopy did not reveal any apparent flaws. The grooved bars all failed at stress levels between those predicted for surface and volume flaws and again no defects were detected using scanning electron microscopy.

Figure 7.5.3 shows photographs of the fracture surfaces of a typical grooved bar and grooved rod specimen. In each case machining grooves are apparent and it is probably these grooves which act as fracture initiation sites. The localised stress concentrations which these grooves cause are not modelled by the finite element analysis and therefore not accounted for in the statistical analysis.

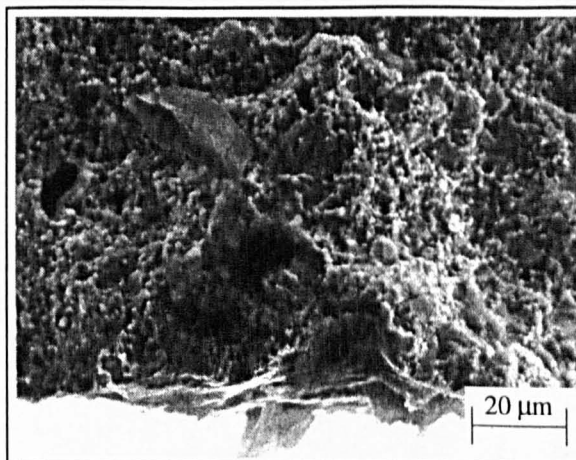
Comparing the failure of the iso-pressed flexure bars with the grooved bars it can be seen that the grooved bars appear to be stronger than the flexure bars. This is



a) agglomerates (iso-pressed zirconia)

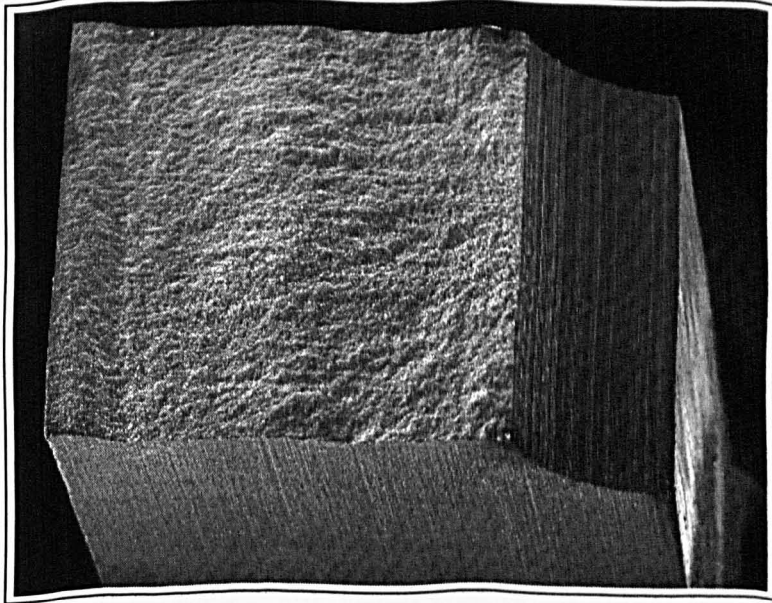


b) pore (die-pressed zirconia)

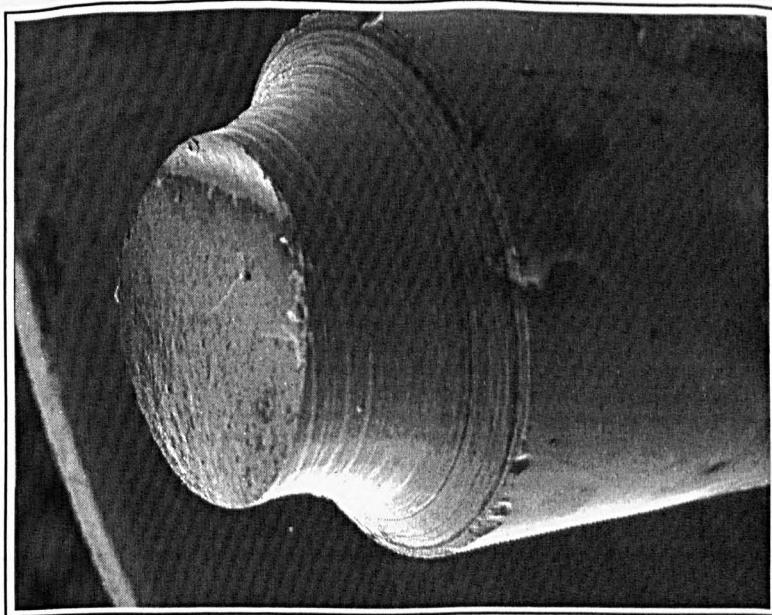


c) impurity (iso-pressed zirconia)

Figure 7.5.2 Flaws in flexure bar specimens.



a) grooved bar



b) grooved rod

Figure 7.5.3 Fracture surfaces in typical grooved bar and rod specimens.

obviously not the case: the grooved specimens failed at lower loads than the flexure bars. The maximum tensile stress in the grooved bars occurs at the base of the groove but the volume of material experiencing this stress is much smaller than the volume of material experiencing the maximum stress in the flexure bars. This is the same effect as is observed when using three-point versus four-point flexure testing.

7.5.3 Brazilian disc specimens

The predicted failure of the Brazilian disc specimens was much more dependent on the failure criterion and crack shape chosen, especially for volume flaws. It can be seen in figure 6.2.7 that the predicted probability of failure varies between 0.05 and 0.99 for volume flaws. However, even this range of values fails to predict the failure of almost half of the specimens and it would appear that none of the failure criteria accurately predicts the failure of components experiencing predominantly compressive stresses.

7.5.4 Failure analysis of components

The failure analysis of the piston and cylinder block predicted that they will not fail from fast fracture at the stress levels experienced during normal operation at 140 bar. However, increasing the loading allowed comparisons to be made between the different fracture criteria and flaw shapes.

For the piston model it can be seen that for surface flaws the prediction of the probability of failure follows the same pattern as the grooved bar and rod specimens. The normal stress averaging (NSA) method is the most conservative and Shetty's criterion with Griffith cracks the least. For volume flaws the same pattern is not followed and Shetty's criterion with penny-shaped cracks is the most conservative and the maximum tensile stress (MTS) method with Griffith cracks the least.

The probability of failure of the cylinder block did not follow the same pattern as any of the specimens tested. The NSA method proved to be the most conservative and the Batdorf method with Griffith cracks the least. The stress levels to cause failure are less than for any of the specimens which can be accounted for by the size effect, i.e. it is more likely that a strength limiting defect is found in a greater volume of material.

British Gas have modified the ceramic cylinder block to use a temporary metal shaft insert. This cylinder block, operating at relatively low pressures, was tested with 1000 μm filtration on sea-water for 100 hours. It is now being tested with a silicon carbide port plate after excessive wear of the PEEK-coated steel port plate was observed. However, this configuration has not been examined here.

CHAPTER 8

CONCLUSIONS

8.0 INTRODUCTION

This chapter summarises the main conclusions of the work, the objectives of which were outlined in Chapter 1, and makes suggestions for further useful work in these areas.

8.1 CONCLUSIONS

The use of finite element analysis with gap elements is a useful way of determining the contact pressure distribution between conformally contacting components. It was shown that this method gives excellent agreement with available analytical methods for the two-dimensional cylindrical and axisymmetric spherical cases, and thus was extended to components constructed of layered materials. Extension to three dimensions, when the contact cannot be accounted for by plane strain or plane stress conditions, was also undertaken. This allowed a much more representative analysis of the contact conditions within an axial piston pump to be made for a variety of sleeved or lined components. No single combination of materials is identified as being the most suitable, rather, the method enables the consequences of choosing materials for their tribological characteristics to be examined. For example, choosing a compliant liner material results in a lower maximum contact pressure than the equivalent sleeved combination. However, in this application, cylinder block liner wear will always occur in the same position whereas piston sleeve wear will be distributed around the circumference of the piston.

The above study allowed the stress distribution in layered, conformally contacting components to be determined by using the resulting contact pressure distributions as loading. Separating the contact analyses from the component analyses allowed more complex component models to be created than would otherwise have been the case.

The final part of the work examined the different probabilistic methods currently available for designing ceramic components in this application. A knowledge of the entire stress distribution in these components is essential and finite element analysis provides the most convenient way to do this. The first part of this work enabled this to be done with confidence as conformal contact pressures cannot be removed from the

stress distribution in the bulk of the component as with point contacts. It can be concluded that no single method adequately predicts the probability of failure of ceramic specimens with more complex stress distributions than four-point flexure bars and that surface finishing methods are as important as the ceramic materials themselves.

8.2 SUGGESTIONS FOR FURTHER WORK

There are several areas of this work where more study would be interesting. Further analysis of the effects of having layered components would prove useful, in particular at the interface between the bulk and layered material. This study has assumed that the layers are always perfectly bonded but this will not always be the case in practice.

More detailed examination of three-dimensional contact would prove useful for a variety of applications including the effects of misaligned components. A single piston test rig is being developed to examine just such effects.

Much more analysis of the structural behaviour of ceramic materials needs to be done before they can be used with the same confidence as metals in situations where their properties can be exploited to the full.

REFERENCES

- Andersson T, Fredriksson B and Persson B G A, (1980)**, The boundary element method applied to 2-dimensional contact problems. *New Developments in Boundary Element Methods*. ed. Brebbia, CML Publishers, Southampton.
- Andreasen J H, (1994)**, Reliability-based design of ceramics. *Materials and Design*, vol. 15, no. 1, pp 3-13.
- Batdorf S B, (1977)**, Some approximate treatments of fracture statistics for polyaxial tension. *International Journal of Fracture*, vol.13, no. 1, pp 5-11.
- Batdorf S B and Crose J G, (1974)**, A statistical theory for the fracture of brittle structures subjected to nonuniform polyaxial stresses. *Journal of Applied Mechanics, Trans ASME*, vol. 41, pp 459-464.
- Batdorf S B and Heinisch H L, (1978)**, Weakest link theory reformulated for arbitrary fracture criterion. *Journal of the American Ceramic Society*, vol.61, no. 7-8, pp 355-358.
- Bathe K-J and Chaudhary A, (1985)**, A solution for planar and axisymmetric contact problems. *International Journal for Numerical Methods in Engineering*, vol. 21, pp 65-88.
- Becker A A and Plant R C A, (1987)**, Contact mechanics using the boundary element method. Proceedings of the *International Conference on Tribology, Friction, Lubrication and Wear*, London, 1-3 July, p 975.
- Bell D A, (1988)**, Measurement of the flexural strength of engineering ceramics. *British Ceramic Transactions and Journal*, vol. 87, pp 33-38.
- Bergman B, (1986)**, How to estimate Weibull parameters. *The Institute of Ceramics, Proceedings 39*, London 17-19 December, pp 175-185.
- Birkby I and Hodgson H, (1991)**, Progress with zirconia ceramics. *Proceedings of the Third European Symposium on Engineering Ceramics*, London, 1989, pp 167-198.
- Boussinesq J, (1985)**, Application des Potentiels a l'Etude de l'Equilibre et du Mouvement des Solides Elastiques. Gauthier-Villars, Paris.
- Brookes C A, Fagan M J, James R D, Kerry P R and McConnachie J, (1995)**, The development of water hydraulic pumps using advanced engineering ceramics. *Proceedings of 4th Scandinavian International Conference on Fluid Power*, 27-29 September, Tampere, Finland.
- Bush D R, (1993)**, Designing ceramic components for structural applications. *Journal of Materials Engineering and Performance*, vol. 2, pp 851-862.
- Buxbaum O, Sonsino C M and Esper F J, (1994)**, Fatigue design criteria for ceramic components under cyclic loading. *International Journal of Fatigue*, vol. 16, pp 257-265.
- Cerruti V, (1882)**, Roma, Acc. Lincei, Mem. fis. mat.
- Chao L-Y and Shetty D K, (1990)**, Equivalence of physically based statistical fracture theories for reliability analysis of ceramics in multiaxial loading. *Journal of the American Ceramic Society*, vol. 73, no. 7, pp 1917-1921.
- Chao L-Y and Shetty D K, (1991)**, Reliability analysis of structural ceramics subjected to biaxial flexure. *Journal of the American Ceramic Society*, vol. 74, no. 2, pp 333-344.
- Chen H H and Marshek K M, (1986)**, The effect of surface depressions on conformal and nonconformal contact pressure distributions. *Journal of Applied Mechanics*, vol. 53, pp 779-784.
- Chen H H and Marshek K M, (1988)**, Effect of clearance and material property on contact pressure in two-dimensional conforming cylinders. *Mechanics of Machine Theory*, vol. 23, no. 1, pp 55-62.
- Chen W T and Engel P A, (1972)**, Impact and contact stress analysis in multilayer media. *International Journal of Solids and Structures*, vol 8, pp 1257-1281.

- Chui Y P and Hartnett M J, (1983)**, A numerical solution for layered solid contact problems with application to bearings. *Trans ASME Journal of Tribology*, vol 105, pp 585-590.
- Claussen N, (1976)**, *Journal of the American Ceramic Society*, vol 59, pp 49-51.
- Devendra K and Syers G, (1990)**, Application of engineering ceramics in gas turbines. *British Ceramic Proceedings*, vol 46, pp 93-112.
- Dworak W and Fingerle D, (1987)**, Ceramic materials for engines. *Journal, Convention papers*, vol. 86, no. 6, pp 170-178.
- Dworak U, Olapinski H and Thamerus G, (1977)**, *Science of Ceramics*, vol 9, pp 543-550.
- Dworak U, Olapinski H and Thamerus G, (1978)**, *Ber. DKG*, vol 55, pp 98-101.
- Edge K A and Darling J, (1986)**, Cylinder pressure transients in oil hydraulic pumps with sliding plate valves. *Proceedings of the Institute of Mechanical Engineers*, vol 200, pp 45-54.
- Edge K A and Darling J, (1989)**, A theoretical model of axial piston pump ripple. *Design, Modelling and Control of Pumps*, (Eds. C R Burrows and N A Vaughan), Research Studies Press.
- Edwards G R, (1989)**, Non-destructive testing of engineering ceramics. *British Ceramic Transactions and Journal*, vol 88, pp 117-123.
- Evans A G, (1978)**, A general approach for the statistical analysis of multiaxial fracture. *Journal of the American Ceramic Society*, vol 61, pp 302-308.
- Evans A G, (1990)**, Perspective on the development of high toughness ceramics. *Journal of the American Ceramic Society*, vol 73, no 2, pp 187-206.
- Ferber M K, Tennery V J, Waters S B and Ogle J, (1986)**, Fracture strength characterization of tubular ceramic materials using simple c-ring geometry. *Journal of Materials Science*, vol. 21, pp 2628-2632.
- Flamant, (1892)**, *Comptes Rendus*, vol 114, p 1465.
- Francavilla A and Zienkiewicz O C, (1975)**, A note on numerical computation of elastic contact problems. *International Journal for Numerical Methods in Engineering*, vol. 9, pp 913-924.
- Giovan M N and Sines G, (1979)**, Biaxial and uniaxial data for statistical comparisons of a ceramic's strength. *Journal of the American Ceramic Society*, vol. 62, no. 9-10, pp 510-515.
- Godfrey D J, (1986)**, Ceramic strength determination with ring loaded disc specimens. *The Institute of Ceramics, Proceedings 39*, London 17-19 December, pp 133-140.
- Goodman L E and Keer L M, (1965)**, The contact stress problem for an elastic sphere indenting an elastic cavity. *International Journal of Solids and Structures*, vol. 1, pp 407-415.
- Griffith A A, (1920)**, *Philosophical Transactions of the Royal Society of London, Series A*, vol 221, p 163.
- Guerra F M and Browning R V, (1983)**, Comparison of two slideline methods using ADINA. *Computers and Structures*, vol 17, pp 819-834.
- Guiu F, Reece M J and Vaughan D A J, (1991)**, Cyclic fatigue of ceramics. *Journal of Materials Science*, vol. 26, pp 3275-3286.
- Gupta P K and Walowit J A, (1974)**, Contact stresses between an elastic cylinder and a layered elastic solid. *Trans ASME Journal of Lubrication Technology*, pp 250-257.
- Harrigan T P and Harris W H, (1991)**, A finite element study of the effect of diametral interface gaps on the contact areas and pressures in uncemented cylindrical femoral total hip components. *Journal of Biomechanics*, vol. 24, no. 1, pp 87-91.
- Hartnett M J, (1978)**, On the axisymmetric contact of closely conforming elastic bodies. Phd thesis, University of Connecticut, USA.
- Hartsock D L and McLean A F, (1984)**, What the designer with ceramics needs. *American Ceramic Society Bulletin*, vol. 63, no. 2, pp 266-270.

- Helgestad B O, Foster K and Bannister F K, (1974)**, Pressure transients in an axial piston hydraulic pump. *Proceedings of the Institution of Mechanical Engineers*, vol 188.
- Hertz H, (1882)**, On the contact of elastic solids. English translation in *Miscellaneous papers by H Hertz*, eds. Jones and Schott, Macmillan, London, 1896.
- Hertzberg R W, (1989)**, Deformation and fracture mechanics of engineering materials. 3rd edition. John Wiley and Sons, USA.
- Heuer A H, Readey M J and Steinbrech R, (1988)**, Resistance curve behaviour of supertough MgO-partially-stabilised ZrO₂. *Materials Science Engineering*, vol A105/106, pp 83-89.
- Hughes T J R, Taylor R L, Sackman J L, Curnier A and Kanoknukulchai W, (1976)**, A finite element method for a class of contact-impact problems. *Computer Methods in Applied Mechanical Engineering*, vol. 8, pp 249-276.
- Ifield R J, (1974)**, The adaptation and development of hydraulic power equipment to operate with 5/95 type non-flammable fluids. Proceedings of Conference on Mining, Quarrying and Tunnelling, Institution of Mechanical Engineers, pp 157-162.
- Irwin G R, (1949)**, Fracturing of Metals, ASM, Cleveland, OH, USA, p 147.
- Irwin G R, (1958)**, Handbuch der Physik, Volume 6, Springer, Berlin, Germany, p 551.
- Johnson K L, (1985)**, Contact Mechanics. Cambridge University Press.
- Kawamoto H, Shimizu T, Suzuki M and Miyazaki H, (1986)**, Strength analysis of silicon nitride swirl chamber for high-power turbocharged diesel engines. in: *Ceramic Materials and Components for Engines*, (edited by Burk W and Hausner H), pp 1035-1042.
- Kerber A and Hofmann H, (1993)**, Improved powders for structural ceramic components. *Ceramic Technology International*, pp 89-92.
- Kim K T and Suh J, (1992)**, Fracture of alumina tubes under combined tension/torsion. *Journal of the American Ceramic Society*, vol 75, no 4, pp 896-902.
- Kokaji A, Uchimura H and Kaji, (1992)**, Fracture strength of silicon nitride under biaxial stresses. *Journal of the Ceramic Society of Japan*, vol. 100, no. 11, pp 1304-1308.
- Kleer G, Richter H, Döll W, Heider W and Röttenbacher R, (1986)**, Strength of SiSiC ceramics - examination of the specimen size effect. *Ceramic materials and components for engines*, (edited by W Burk and H Hausner), Deutsche Keramische Gesellschaft, pp 979-986.
- Knight G C, (1977)**, Application of water-based fluids to hydraulic systems. *Tribology International*, April 1977, pp 105-107.
- Lamon J, (1988)**, Statistical approaches to failure for ceramic reliability assessment. *Journal of the American Ceramic Society*, vol. 71, no. 2, pp 106-112.
- Lamon J and Evans A G, (1983)**, Statistical analysis of bending strengths for brittle solids: a multiaxial fracture problem. *Journal of the American Ceramic Society*, vol. 66, no. 3, pp 177-182.
- Leveson R C, (1974)**, The mechanics of elastic contact with film covered surfaces. *Journal of Applied Physics*, vol 45, no 3, pp 1041-1043.
- Liu S-Y and Chen I-W, (1991)**, Fatigue of yttria-stabilised zirconia: I, Fatigue damage, fracture origins and lifetime prediction. *Journal of the American Ceramic Society*, vol. 74, no. 6, pp 1197-1205.
- Loth W D and Walker C A, (1993)**, Low cost autonomous water injection systems. In: *Low Cost Subsea Production Systems. Advances in Underwater Technology, Ocean Science and Offshore Engineering: Volume 30*, Kluwer Academic Publishers.
- Love A E H, (1929)**, The stress produced in a semi-infinite solid by pressure on part of the boundary. *Philosophical Transactions of the Royal Society A*, vol 228
- Matsui M, (1993)**, Advanced technical ceramics: their potential. *Ceramics International*, vol. 19, pp 9-16.

- Martin M J and Taylor R, (1978)**, Optimised port plate timing for an axial piston pump. *Fifth International Fluid Power Symposium*, pp 51-66.
- Matsuo Y, (1980)**, Transactions of the Japanese Society of Mechanical Engineers, vol 46, pp 605-611. (In Japanese).
- Matthews J R, McClintock F A and Shack W J, (1976)**, Statistical determination of surface flaw density in brittle materials. *Journal of the American Ceramic Society*, vol 59, pp 304-308.
- Mazurkiewicz M and Ostachowicz W, (1983)**, Theory of finite element method for elastic contact problems of solid bodies. *Computers and Structures*, vol. 17, no. 1, pp 51-59.
- Morrell R, (1989)**, Mechanical properties of engineering ceramics: test bars versus components. *Materials Science and Engineering*, vol. A109, pp 131-137.
- Morrell R, (1993)**, Terminology requirements for classification of advanced ceramics. *Ceramics International*, vol 19, no 1, pp 51-54.
- Morton W B and Crose L J, (1922)**, Notes on Hertz' theory of contact problems. *Philosophical Magazine*, vol 43, p 320.
- Mottershead J E, Pascoe S K and English R G, (1992)**, A general finite element approach for contact stress analysis. *International Journal for Numerical Methods in Engineering*, vol. 33, pp 765-779.
- Nemeth N N, Manderscheid J M and Gyekenyesi J P, (1989)**, Designing ceramic components with the CARES computer program. *American Ceramic Society Bulletin*, vol. 68, no. 12, pp 2064-2072.
- Pascoe S K and Mottershead J E, (1988)**, Linear elastic contact problems using curved elements and including dynamic friction. *International Journal for Numerical Methods in Engineering*, vol. 26, pp 1631-1643.
- Pascoe S K and Mottershead J E, (1989)**, Two new finite element contact algorithms. *Computers and Structures*, vol. 32, no. 1, pp137-144.
- Paul B and Hashemi J, (1977)**, An improved numerical method and computer program for counterformal contact stress problems. *ASME Computational Techniques for Interface Problems*. AMD-Vol 30.
- Paul B and Hashemi J, (1980)**, Contact pressures on closely conforming elastic bodies. *Symposium on Solid Contact and Lubrication*, AMD-39, ASME, NY, pp 67-78.
- Persson A, (1964)**, On the stress distribution of cylindrical elastic bodies in contact. PhD thesis, Chalmers Tekniska Högskola, Göteborg, Sweden.
- Quinn GD and Morrell R, (1991)**, Design data for engineering ceramics: a revue of the flexure test. *Journal of the American Ceramic Society*, vol. 74, no. 9, pp 2037-2066.
- Radcliffe P W, (1992)**, Timing of an axial piston pump. Internal report, Department of Engineering Design and Manufacture, University of Hull.
- Radcliffe P W, Fagan M J and McConnachie J (1993)**, Computer aided design of axial piston pumps - a geometry designer. (eds. CR Burrows & KA Edge), Research Studies Press, 1993. Proceedings of the Fifth Bath International Fluid Power Workshop. 16-18 September 1992, England.
- Readey M, (1993)**, Optimised processing of advanced ceramics. *Ceramic Technology International*, pp 47-53.
- Reynard K W, (1993)**, Review of existing classification systems for materials. *Ceramics International*, vol. 19, pp 21-25.
- Richerson D W, (1982)**, Modern Ceramic Engineering. Marcel Dekker Inc, New York.
- Roark R J and Young W C (1975)**, Formulas for Stress and Strain, fifth edition. McGraw-Hill Kogakusha Ltd, Tokyo, Japan.
- Rolf R L and Weyand J D, (1985)**, Structural design of brittle materials. *American Ceramic Society Bulletin*, vol 64, no 10, pp 1360-1363.

- Routledge R, (1876)**, Discoveries and Inventions of the Nineteenth Century. G Routledge and Sons, England.
- Rufin A C, Samos D R and Bollard R J H, (1984)**, Statistical failure prediction models for brittle materials. *AIAA Journal*, vol. 22, no. 1, pp 135-140.
- Salem J A, Manderscheid J M, Freedman M R and Gyekenyesi J P, (1991)**, Reliability analysis of a structural ceramic combustion chamber. presented at the *International Gas Turbine and Aeroengine Congress and Exposition*, Orlando, Florida, USA, 91-GT-155, pp 1-8.
- Schneider S J, (1993)**, Welcome and introduction to the VAMAS workshop on classification of advanced ceramics. *Ceramics International*, vol. 19, pp 5-7.
- Schwartz M M, (1992)**, Handbook of Structural Ceramics. McGraw-Hill, USA.
- Seshadri S G and Srinivasan M, (1981)**, Weibull statistics for expanded ring flexure tests of ceramics. *Journal of Materials Science*, vol. 16, pp 3052-3058.
- Shetty D K, (1987)**, Mixed-mode fracture criteria for reliability analysis and design with structural ceramics. Presented at the *Gas Turbine Conference and Exhibition*, Anaheim, California, USA, pp 1-8
- Shetty D K, Rosenfield A R, McGuire P, Bansal G K and Duckworth W H, (1980)**, Biaxial flexure tests for ceramics. *American Ceramic Society Bulletin*, vol. 59, no. 12, pp 1193-1197.
- Singh K P and Paul B, (1974)**, Numerical solution of non-Hertzian elastic contact problems. *Trans. ASME Journal of Applied Mechanics*, vol. 41, pp 484-490.
- Sinnema S, (1989)**, Aspects of design and stress calculations in engineering ceramics. *Euro-ceramics*, vol 3, pp 3.106-110.
- Solecki R and Ohgushi Y, (1984)**, Contact stresses between layered elastic cylinders. *Trans ASME Journal of Tribology*, vol 106, pp 396-404.
- Stanley P, (1986)**, A probabilistic basis for designing with ceramics. *The Institute of Ceramics, Proceedings 39*, London 17-19 December, pp 167-174.
- Stanley P, Fessler H and Sivill A D, (1973)**, An engineer's approach to the prediction of failure probability of brittle components. *Proceedings of the British Ceramic Society*, vol. 22, pp 453-487.
- Stanley P, Fessler H and Sivill A D, (1976)**, The unit strength concept in the interpretation of beam test results for brittle materials. *Proceedings of the Institution of Mechanical Engineers*, vol. 190, pp 585-595.
- Stefansky W, (1972)**, Rejecting outliers in factorial designs. *Technometrics*, vol. 14, no. 2, pp 469-479.
- Steuermann E, (1939)**, To Hertz's theory of local deformations in compressed elastic bodies. *Comptes Rendus (Doklady) de l'Academie des Sciences de l'URSS*, vol. 25, no. 5, pp 359-361.
- Stürmer G, Schultz A and Wittig S, (1990)**, Lifetime prediction for ceramic gas turbine components. *American Society of Mechanical Engineers, preprint 91-GT-96*, pp 1-7.
- Suresh S, (1991)**, Fatigue crack growth in brittle materials. *Journal of Hard Materials*, vol. 2, no. 1-2, pp 29-54.
- Tangena A G and Wijnhoven P J M, (1988)**, The correlation between mechanical stresses and wear in a layered system. *Wear*, vol 121, pp 27-35.
- Terada Y, Komatsu A, Kanda S, Inokuma M, Makimura M and Nagata Y, (1984)**, Development of high pressure sea water pump. *Naval Architecture and Ocean Engineering*, vol. 22, pp 227-232.
- Thiemeier T, Bruckner-Foit A and Kolker H, (1991)**, Influence of the fracture criterion on the failure prediction of ceramics loaded in biaxial flexure. *Journal of the American Ceramic Society*, vol. 74, no. 1, pp 48-52.
- Tree D J and Kington H L, (1978)**, Ceramic component design objectives, goals and methods. *Ceramic gas turbine demonstration engine program review* (edited by J W Fairbanks and R W Rice), MCIC report MCIC-78-36, pp 41-75.

- Uchimura H, Kakaji A and Kaji M, (1992)**, Evaluation of fast fracture strength of ceramic components under multiaxial stress states. presented at the *International Gas Turbine and Aeroengine Congress and Exposition*, Cologne, Germany, 92-GT-384, pp 1-8.
- Usher, (1994)**, Water powered rescue tools. *Military Firefighter*, vol 21.
- VAMAS, (1993)**, Classification of advanced ceramics - Development of the 1st international system for producer and user industries - Recommendations. *Ceramics International*, vol. 19, pp 59-60.
- Vijayakar S, Busby H and Wilcox L, (1989)**, Finite element analysis of three-dimensional conformal contact with friction. *Computers and Structures*, vol. 33, no. 1, pp 49-61.
- Wallace F B, Stone A J and Nelson N R, (1978)**, Ceramic component design ARPA/Navy ceramic engine program. *Ceramics for high performance applications II* (edited by J J Burke, E N Leno and R N Katz), pp 593-624.
- Waterman N A and Ashby M F (1991)**, Elsevier Materials Selector, volume 2. Elsevier Science Publishers, UK.
- Weibull W, (1951)**, A statistical distribution of wide applicability. *Journal of Applied Mechanics*, vol. 18, no. 3, pp 293-297.
- Wills R R, (1977)**, Structural ceramics. *Research/Development*, vol 28, no 5, pp 30-37.
- Woodward W and Paul B, (1976)**, Contact stresses for closely conforming bodies - application to cylinders and spheres. Technical report no. 2, DOT-TST-77-48, National Technical Information Service.
- Wymer D G, (1979)**, The use of water hydraulics in machines for mechanised gold mining in South Africa. *International Conference on Mining and Machinery*, Brisbane, 2-6 July, pp 320-328.
- Yanagi K, Tsukada Y and Mutoh Y, (1992)**, A geometrical assessment of machined ceramic surface for estimating fatigue strength. *International Journal of Machine Tool Manufacture*, vol. 32, no. 1/2, pp 137-140.
- Yoshinada H, Yamazaki T, Suwa T, Naruse T and Ueda H, (1991)**, Seawater hydraulic actuator system for subsea manipulator. *International Symposium on Advanced Robot Technology (ISART)*, Tokyo, March 5-7.

APPENDIX I

WATER HYDRAULICS PAPERS AND REPORTS

PUBLISHED PAPERS

Brookes CA (1989), Tribological applications of ceramic materials in water hydraulics: problems and potential. Proceedings of the First Bath International Fluid Power Workshop. (eds. CR Burrows & ND Vaughan), Research Studies Press.

McConnachie J, Fagan MJ and Radcliffe PW (1992), Computer modelling of contacting concentric components. Fluid Power Systems, Modelling and Control (eds. CR Burrows & KA Edge), Research Studies Press, 1992, pp 232-246. Proceedings of the Fourth Bath International Fluid Power Workshop, 18-20 September 1991, Bath, England.

Radcliffe PW, Fagan MJ and McConnachie J (1992), Computer modelling and analysis of axial piston pumps. Fluid Power Systems, Modelling and Control (eds. CR Burrows & KA Edge), Research Studies Press, 1992, pp 247-259. Proceedings of the Fourth Bath International Fluid Power Workshop, 18-20 September 1991, Bath, England.

Brookes CA, Green P, James RD, Wallis RL and Kerry PR (1992), Observations on localised plasticity and work-hardening in magnesium oxide crystals during the initial stages of cavitation damage. IMechE conference paper C453/026, pp 139-146.

Radcliffe PW, Fagan MJ and McConnachie J (1993), Computer aided design of axial piston pumps - a geometry designer. (eds. CR Burrows & KA Edge), Research Studies Press, 1993. Proceedings of the Fifth Bath International Fluid Power Workshop. 16-18 September 1992, Bath, England.

Brookes CA, Fagan MJ, James RD, Kerry PR, McConnachie J, and Radcliffe PW (1993), Water hydraulic pumps for a safer and cleaner future. Pumps for a Safer Future, Elsevier. Proceedings of the 13th International Pump Technical Conference. 21-23 April 1993, London, England.

Kerry PR, McConnachie J, Fagan MJ, James RD, Brookes CA and Radcliffe PW (1993). Tribological performance of non-metallic materials for a sea-water pump. Extended abstract - IMechE Water Based Hydraulics Seminar (Tribology Group and Institute of Materials). 23 April 1993, London, England.

Brookes CA, Fagan MJ, James RD, Kerry PR, McConnachie J, and Radcliffe PW (1993), Development of an axial piston pump for water hydraulic systems. IMechE. Proceedings of the 5th International Congress on Fluid Machinery, 17-19 May, 1993, The Hague, Netherlands.

McConnachie J and Fagan MJ (1993), Design and analysis of the cylinder block of an axial piston pump. Proceedings of the 3rd Scandinavian International Conference on Fluid Power (ed. J-O Palmberg), 25-26 May, 1993, Linköping, Sweden.

McConnachie J and Fagan MJ (1993), Computer modelling of layered conformal contact. Contact Mechanics Computational Techniques (eds. MH Aliabadi & CA Brebbia), Computational Mechanics Publications. Proceedings of Contact Mechanics 93, 13-15 July, 1993, Southampton, England.

Fagan MJ and McConnachie J (1993), Modelling and analysis techniques used in the design of axial piston pumps for water hydraulics. Modelling and Simulation (eds. CR Burrows & KA Edge), Research Studies Press, 1994, Proceedings of the Sixth Bath International Fluid Power Workshop, 23-24 September 1993, Bath, England.

Fagan MJ and McConnachie J (1993), Computer aided design and analysis of axial piston pumps. Using computers in the design and selection of fluid machinery. IMechE, 2 December 1993, London.

McConnachie J and Fagan MJ (1994), Finite element analysis of three-dimensional layered conformal contact. Conference on Computational Mechanics in UK - 1994, University of Manchester, 11-12 April 1994. Association for Computational Mechanics in Engineering (UK).

Fagan MJ and McConnachie J (1994), Development of axial piston pumps and motors for water hydraulic systems. Hydraulic Engineering in the Vehicle, SIA Conference, 4-5 May 1994, Angers, France.

Brookes CA, Fagan MJ, James RD, Kerry PR and McConnachie J (1995), The development of water hydraulic pumps using advanced engineering ceramics. Proceedings of the 4th Scandinavian International Conference on Fluid Power (ed. J-O Palmberg), 27-29 September, 1995, Tampere, Finland.

Brookes CA, Fagan MJ, James RD, Kerry PR and McConnachie J (1996), Design and development of an axial piston pump for sea-water hydraulic systems. To be published in the Proceedings of the Conference on Fluid Machinery for the Oil, Gas, Petrochemical and Related Industries, 13-15 May, 1996, The Hague, Netherlands. IMechE.

REPORTS

A preliminary literature review of slipper pad design in axial piston machines. MA O'Donnell, Jan. 1989.

Synopsis of corrosion performance of ceramic coatings. R Field, June 1989.

Preliminary results of ultrasonic cavitation-erosion tests on Mg-PSZ, silicon nitride, PEEK and AISI304 stainless steel. PR Kerry, June 1989.

Design considerations in a swashplate type axial piston machine. MA O'Donnell, July 1989.

Bearing investigation. PR Radcliffe and J McConnachie, Feb. 1990.

Fatigue failure of pistons. PW Radcliffe, Feb. 1990.

The number of pistons in axial piston machines. PW Radcliffe, July 1990.

Surface modification and rolling fatigue tests. August 1990.

F30 pump test - preliminary report. PR Kerry, Nov. 1990.

Finite element analysis of F30 slippers. J. McConnachie, Nov. 1990.

Anderson Longwall, F60 bore and piston sleeve wear. Nov. 1990.

Force analysis of an axial piston pump. PW Radcliffe, Dec. 1990.

Lining of cylinder bores. PW Radcliffe, Feb. 1991.

Hydrostatic piston pads. PW Radcliffe, March 1991.

Materials testing programme - F30 pump test report, pump003, PR Kerry, April 1991.

Thermal expansion of F30 cylinder block. J. McConnachie, April 1991.

Failure report - aluminium F60 cylinder block. PR Kerry, J McConnachie and PW Radcliffe, June 1991.

Background on Hardcor treatment: report I. A Matthews, June 1991.

Study of electroless nickel-phosphorus-silicon carbide composite coating production. MR Kalantary, June 1991.

Analysis of titanium swashplate. PR Kerry, Nov. 1991.

Materials testing programme - F30 pump test report, pump004, PR Kerry and PW Radcliffe, Nov. 1991.

Rolling bearing tests report. Nov. 1991.

Results of ultrasonic cavitation-erosion tests on various grades of stainless steel. PR Kerry, Nov. 1991.

Stresses in the cylinder block of an axial piston pump due to pressure and contact loading. J McConnachie, Feb. 1992.

Materials testing programme - F30 pump test report, pump004, PR Kerry, Feb. 1992.

Timing of an axial piston pump. PW Radcliffe, April 1992.

Materials testing programme - F30 pump test report, pump005, PR Kerry, April 1992.

Materials testing programme - F30 pump test report, pump006, PR Kerry, April 1992.

Materials testing programme - F30 pump test report, pump008, PR Kerry, Oct. 1992.

Cavitating jet rig/F30 test bed design and development. PR Kerry, Nov. 1992.

DTI/JH Fenner Water Hydraulics project Final Report, Section 8.1 Materials programme.

Finite element analysis of a ceramic port plate. J McConnachie and MJ Fagan, Feb. 1995.

Final report of Project 7132 for DTI Offshore Supplies Office, July 1995.

APPENDIX II

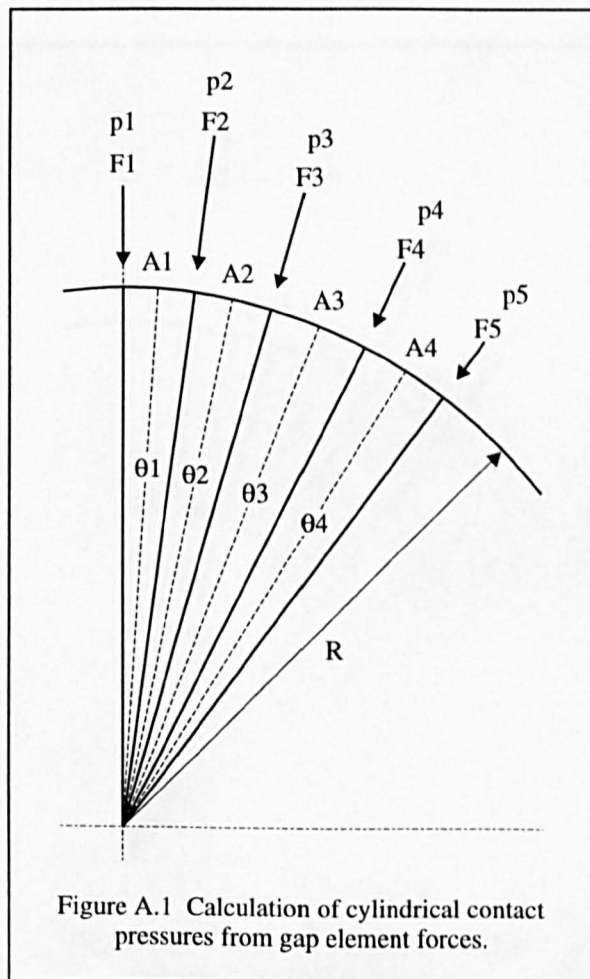
CALCULATION OF CYLINDRICAL CONTACT PRESSURES

The contact pressures, p_n , for the cylindrical contact analysis are calculated from the gap element forces, F_n , as follows:

$$A_1 = 2\pi R \frac{\theta_1}{360}, \quad A_2 = 2\pi R \frac{\theta_2}{360}, \quad A_3 = 2\pi R \frac{\theta_3}{360} \quad \text{etc.}$$

$$p_1 = \frac{2F_1}{A_1}, \quad p_2 = \frac{2F_2}{A_1 + A_2}, \quad p_3 = \frac{2F_3}{A_2 + A_3} \quad \text{etc.}$$

where A_n , θ_n and R are as shown in figure A.1.



APPENDIX III

CALCULATION OF SPHERICAL CONTACT PRESSURES

The calculation of the contact pressures, p_n , from the gap element forces, F_n , for the spherical contact analysis was done as follows:

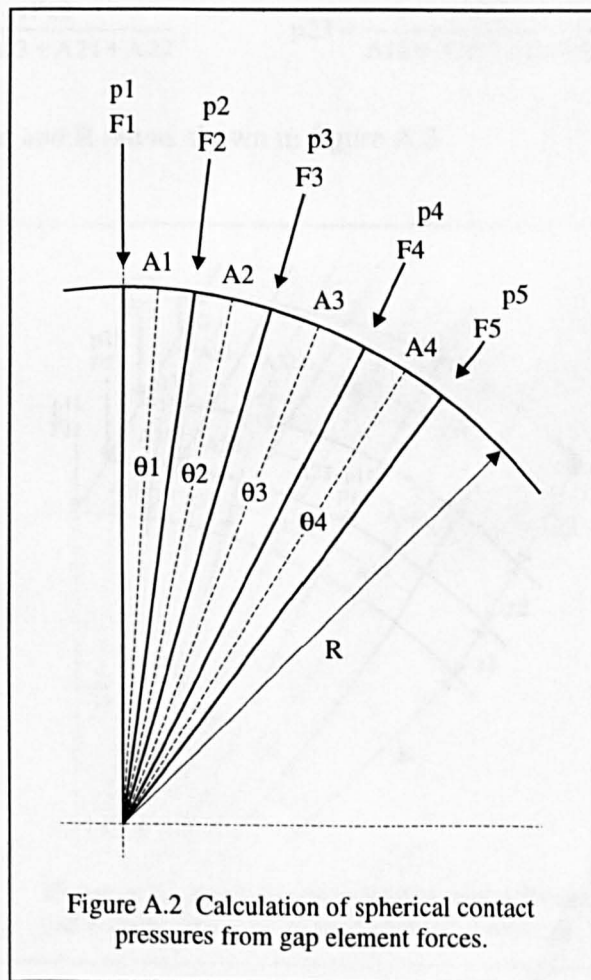
$$A_1 = 2\pi R^2(1 - \cos \theta_1),$$

$$A_2 = 2\pi R^2(\cos \theta_1 - \cos \theta_2),$$

$$A_3 = 2\pi R^2(\cos \theta_2 - \cos \theta_3) \text{ etc.}$$

$$p_1 = \frac{2F_1}{A_1}, \quad p_2 = \frac{2F_2}{A_1 + A_2}, \quad p_3 = \frac{2F_3}{A_2 + A_3} \text{ etc.}$$

where A_n , θ_n and R are as shown in figure A.2.



APPENDIX IV

CALCULATION OF THREE-DIMENSIONAL CONTACT PRESSURES

The contact pressures, p_{nm} , for the three-dimensional contact analysis are calculated from the gap element forces, F_{nm} , as follows:

$$A_{11} = 2\pi Rz_1 \frac{\theta_1}{360}, \quad A_{12} = 2\pi Rz_1 \frac{\theta_2}{360}, \quad A_{13} = 2\pi Rz_1 \frac{\theta_3}{360} \quad \text{etc.}$$

$$A_{21} = 2\pi Rz_2 \frac{\theta_1}{360}, \quad A_{22} = 2\pi Rz_2 \frac{\theta_2}{360}, \quad A_{23} = 2\pi Rz_2 \frac{\theta_3}{360} \quad \text{etc.}$$

$$p_{11} = \frac{4F_{11}}{A_{11}}, \quad p_{12} = \frac{4F_{12}}{A_{11}+A_{12}}, \quad p_{13} = \frac{4F_{13}}{A_{12}+A_{13}} \quad \text{etc.}$$

$$p_{21} = \frac{4F_{21}}{A_{11}+A_{21}}, \quad p_{31} = \frac{4F_{31}}{A_{21}+A_{31}}, \quad \text{etc.}$$

$$p_{22} = \frac{4F_{22}}{A_{11}+A_{12}+A_{21}+A_{22}}, \quad p_{23} = \frac{4F_{23}}{A_{12}+A_{13}+A_{22}+A_{23}}, \quad \text{etc.}$$

where A_{nm} , z_n , θ_m and R are as shown in figure A.3.

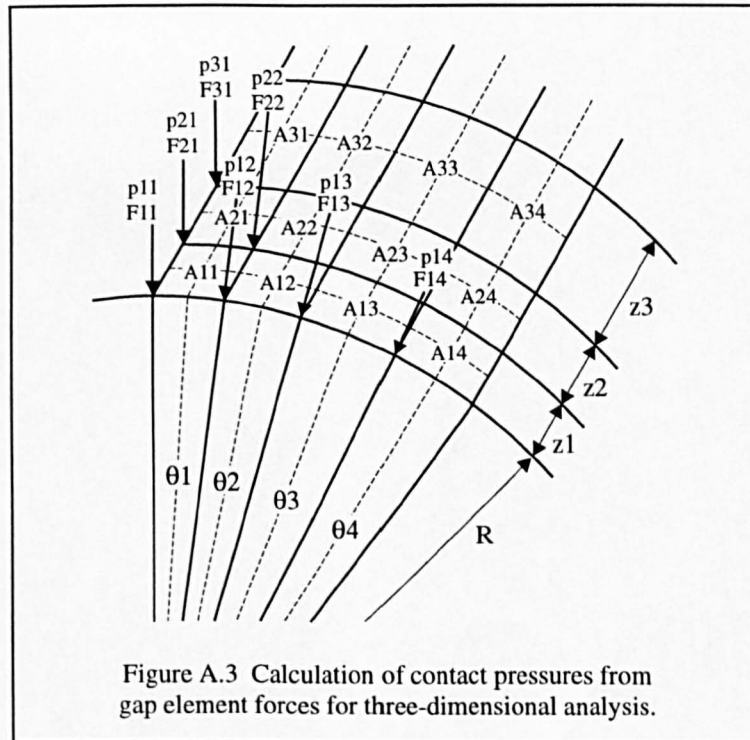


Figure A.3 Calculation of contact pressures from gap element forces for three-dimensional analysis.